

Ultrasonic Additive Manufacturing: Weld Optimization for
Aluminum 6061, Development of Scarf Joints for Aluminum
Sheet Metal, and Joining of High Strength Metals

Dissertation

Presented in Partial Fulfillment of the Requirements for the Degree
Doctor of Philosophy in the Graduate School of The Ohio State
University

By

Paul J. Wolcott, B.S., M.S.

Graduate Program in Mechanical Engineering

The Ohio State University

2015

Dissertation Committee:

Professor Marcelo J. Dapino, Advisor

Professor Amos Gilat

Professor Blaine Lilly

Professor Stephen Niezgoda

© Copyright by

Paul J. Wolcott

2015

Abstract

Ultrasonic additive manufacturing (UAM) is a low temperature, solid-state manufacturing process that enables the creation of layered, solid metal structures with designed anisotropies and embedded materials. As a low temperature process, UAM enables the creation of active composites containing smart materials, components with embedded sensors, thermal management devices, and many others. The focus of this work is on the improvement and characterization of UAM aluminum structures, advancing the capabilities of ultrasonic joining into sheet geometries, and examination of dissimilar material joints using the technology.

Optimized process parameters for Al 6061 were identified via a design of experiments study indicating a weld amplitude of $32.8\text{ }\mu\text{m}$ and a weld speed of 200 in/min as optimal. Weld force and temperature were not significant within the levels studied. A methodology of creating large scale builds is proposed, including a prescribed random stacking sequence and overlap of 0.0035 in. (0.0889 mm) for foils to minimize voids and maximize mechanical strength. Utilization of heat treatments is shown to significantly increase mechanical properties of UAM builds, within 90% of bulk material.

The applied loads during the UAM process were investigated to determine the stress fields and plastic deformation induced during the process. Modeling of the

contact mechanics via Hertzian contact equations shows that significant stress is applied via sonotrode contact in the process. Contact modeling using finite element analysis (FEA), including plasticity, indicates that 5000 N normal loads result in plastic deformation in bulk aluminum foil, while at 3000 N no plastic deformation occurs. FEA studies on the applied loads during the process, specifically a 3000 N normal force and 2000 N shear force, show that high stresses and plastic deformation occur at the edges of a welded foil, and base of the UAM build. Microstructural investigations of heat treated foils confirms that plastic deformation occurs in the bulk of the foil, while previous studies have only identified microstructural changes to the bond interface region.

A methodology for joining aluminum 6061 sheet material 0.076 in. (1.93 mm) thick is proposed based on iterative design studies which identified a scarf joint configuration as viable. Design of experiments studies indicate optimal properties can be achieved using a scarf joint angle of 10° . Room temperature and elevated temperature tensile, and room temperature fatigue testing exhibit joint mechanical properties similar to solid, homogeneous material.

Successful joints were achieved for Al/Ti, aluminum to steel, steel to aluminum, and steel to steel combinations. Mechanical characterization studies of Al/Ti combinations indicate that post-process heat treatments can significantly increase mechanical properties. Microstructural evaluations including electron back scatter diffraction show significant deformation within the softer aluminum layers. Investigations of Al/steel combinations indicate that mostly voidless interfaces occur and that plastic deformation is present in the steel layers only. Steel to steel combinations, while

proven possible, require further work to enhance the consistency of the joints and improve the ability to build larger structures.

To Kara

Acknowledgments

I would like to thank my advisor, Prof. Marcelo Dapino for allowing me the opportunity to work in the Smart Materials and Structures Laboratory. His support and insight have been much appreciated throughout my research. I would like to thank Prof. Stephen Niezgoda, for his assistance in performing electron microscopy and measurements and serving on my committee. I would also like to thank Prof. Blaine Lilly and Prof. Amos Gilat for serving on my committee. Thanks to Prof. Suresh Babu for his insight on materials science and dissimilar joining aspects of this research.

In addition I would like to thank my colleagues in the Smart Materials and Structures Lab, especially Justin Scheidler, Adam Hehr, Chris Pawlowski, Bryant Gengerich, and Matt Scheidt for their help and advice throughout my time here. Their contributions have been invaluable to this work. Thanks to Niyanth Sridharan of the University of Tennessee for his contributions to the microstructural evaluations in this work. Similarly I would like to thank Aslan Miriyev of Columbia University and Prof. Nachum Frage of Ben-Gurion University for their contributions to the dissimilar material joining work. Thanks to Cameron Benedict and Mark Norfolk of Fabrisonic for all their help in learning and troubleshooting the SonicLayer machine.

I would also like to acknowledge the funding sources for my work. This work was supported by the National Science Foundation Industry/University Cooperative

Research Center on Smart Vehicle Concepts, NASA, the Army STTR program (A12a-T004), the OSU Institute for Materials Research, and the Israeli Ministry of Defense.

Vita

September 22, 1987	Born - Lansing, Michigan
June 2005	Diploma, East Lansing High School
May 2009	B.S. Materials Science and Engineering, Cum Laude, University of Michigan
July 2009 - July 2010	Research Metallurgist, General Motors Research and Development
July 2010 - March 2012	Graduate Research Associate, The Ohio State University
March 2012 - 2015	Graduate Fellow, The Ohio State University
June 2012	M.S. Mechanical Engineering, The Ohio State University

Publications

Journal Publications

P.J. Wolcott, C. Pawlowski, L.M. Headings, M.J. Dapino. Seam Welding of Aluminum Sheet Using Ultrasonic Additive Manufacturing System. *Journal of Manufacturing Science and Engineering*. In Review

P.J. Wolcott, A. Hehr, C. Pawlowski, M.J. Dapino. Process Improvements and Characterization of Ultrasonic Additive Manufactured Structures. *Journal of Materials Processing Technology*. In Review

A. Hehr, P. Wolcott, and M. Dapino. Effect of Weld Power and Build Compliance on Ultrasonic Consolidation. *Rapid Prototyping*. 2015 (In Press)

P.J. Wolcott, N. Sridharan, S.S. Babu, A. Miriyev, N. Frage, M.J. Dapino. Characterisation of Al-Ti dissimilar material joints fabricated using ultrasonic additive manufacturing. *Science and Technology of Welding and Joining*. 2015

P.J. Wolcott, A. Hehr, and M. Dapino. Optimized welding parameters for Al 6061 ultrasonic additive manufactured structures. *Journal of Materials Research*, 17 (29):2055-2065, 2014.

P.J. Wolcott, Z. Wang, L. Zhang, and M.J. Dapino. RF patch antenna reconfiguration with Ni-Ti shape memory alloy switches. *Journal of Intelligent Material Systems and Structures*, 24 (B):973-983 2012.

C.D. Hopkins, P.J. Wolcott, M.J. Dapino, A.G. Truog, S.S. Babu, and S.A. Fernandez. Optimizing ultrasonic additive manufactured Al 3003 properties with statistical modeling. *Journal of Engineering Materials and Technology*, 134:011004–1–011004–10, 2012.

P.J. Wolcott, M.J. Dapino, and L. Zhang. Smart switch metamaterials for multiband radio frequency antennas. *Journal of Intelligent Material Systems and Structures*, 22:1469–1478, 2011.

Conference Proceedings

P.J. Wolcott, A. Hehr, and M.J. Dapino. Optimal welding parameters for very high power ultrasonic additive manufacturing of smart structures with aluminum 6061 matrix. *SPIE Conference on Smart Materials and Structures*, San Diego, CA 2014.

P. Wolcott and M. Dapino. Fatigue characterization of ultrasonic additive manufactured aluminum 3003. In *Solid Freeform Fabrication Symposium*, Austin, TX, August 2012.

P.J. Wolcott, M.J. Dapino, Z. Wang, and L. Zhang. Planar RF Antenna Reconfiguration With Ni-Ti Shape Memory Alloys. In *ASME Conference on Smart Materials, Adaptive Structures, & Intelligent Systems*, Scottsdale, AZ, September 2011.

Fields of Study

Major Field: Mechanical Engineering

Studies in Ultrasonic Additive Manufacturing: Dr. Marcelo J. Dapino

Table of Contents

	Page
Abstract	ii
Dedication	v
Acknowledgments	vi
Vita	viii
List of Tables	xv
List of Figures	xviii
1. Introduction	1
1.1 Ultrasonic Additive Manufacturing (UAM)	1
1.1.1 Process Overview	1
1.1.2 Machine Developments	5
1.1.3 Effects of Structural Compliance During UAM Build Process	8
1.1.4 Mechanical Characterization	15
1.1.5 Microstructural Characterization	18
1.2 Sheet Metal Joining	23
1.3 Dissimilar Material Joining	26
1.4 Statistical Techniques in Manufacturing	28
1.5 Problem Statement	31
1.5.1 Dissertation Outline	33
2. Process-Property Relationships and Strength Optimization of UAM Builds	34
2.1 Optimal Process Parameters via Design of Experiments for Al 6061	34
2.1.1 Experimental Methods	35
2.1.2 Results	43

2.1.3	Discussion	50
2.2	Foil Stacking Sequence Study	54
2.2.1	Experimental Methods	54
2.2.2	Results	57
2.2.3	Discussion	59
2.3	Effect of Surface Roughness on Build Quality	61
2.3.1	Experimental Methods	61
2.3.2	Results	63
2.3.3	Discussion	66
2.4	Post-Process Heat Treating Al 6061 UAM Builds	68
2.4.1	Experimental Methods	68
2.4.2	Results	69
2.4.3	Discussion	72
2.5	Summary	73
3.	Analysis of Strength Reduction Due to Process Induced Stresses in UAM Builds	75
3.1	Optimized Builds and Strength	75
3.1.1	Results	79
3.1.2	Discussion	80
3.1.3	Motivation	81
3.2	Sonotrode Contact Modeling	81
3.2.1	Analytical Solution (Hertzian Contact)	84
3.2.2	Finite Element Analysis of Sonotrode Contact	85
3.2.3	Discussion	93
3.3	UAM Applied Loads Model	94
3.3.1	Single Foil Model	95
3.3.2	50 Layer Model	97
3.3.3	Discussion	101
3.4	Microstructural Analysis of Heat Treated Foil	102
3.4.1	Microstructural EBSD	103
3.4.2	Discussion	108
3.5	Summary	110
4.	Sheet Metal Joint Design and Implementation with UAM System	112
4.1	Joint Design with Al 6061	112
4.1.1	Thickness Scoping Trials	112
4.1.2	Design Configuration Development	117
4.1.3	Design of Experiments for Joint Optimization	127
4.1.4	Analysis of Design of Experiments Study	130

4.1.5	Finite Element Modeling of Scarf Joint Angles	139
4.2	Mechanical Characterization of Optimized Joints	142
4.2.1	Room Temperature Tensile Testing	142
4.2.2	High Temperature Tensile Testing	145
4.2.3	Room Temperature Fatigue Testing	148
4.3	Discussion	151
4.4	Seam Joining using Al 2219	153
4.4.1	Discussion	156
4.5	Summary	157
5.	Dissimilar Material Joining with UAM	158
5.1	Al/Ti Joining	158
5.1.1	Experimental Methods	158
5.1.2	Mechanical Characterization	164
5.1.3	Microstructural Evaluations	169
5.1.4	Discussion	175
5.2	Al-Steel Joining	178
5.2.1	Experimental Methods	178
5.2.2	Mechanical Characterization	180
5.2.3	Microstructural Characterization	183
5.2.4	Discussion	188
5.3	Steel-Steel Joining	189
5.3.1	Experimental Methods	189
5.3.2	Microstructural Characterization	198
5.3.3	Discussion	204
5.4	Summary	205
6.	Conclusions and Future Work	207
6.1	Summary	207
6.2	Contributions	209
6.3	Future Work	211
Appendices		
A.	Design of Experiments Data for UAM Al 6061	215
B.	Seam Joining Cross Sections and Design of Experiments Data	220

C. Additional EBSD Images	229
Bibliography	232

List of Tables

Table	Page
2.1 Taguchi L18 orthogonal array including 18 treatment combinations and three levels (low, medium, high) for each of the four parameters investigated: temperature, weld force, weld amplitude, and weld rate.	36
2.2 Parameter levels for each of the treatment combinations.	37
2.3 Parameters for first layer welding.	37
2.4 Sample dimensions for shear and push-pin tests (in mm).	40
2.5 Comparison of push-pin results between parameter sets 4 and 9. . . .	44
2.6 ANOVA results for push-pin testing with mechanical work as response variable.	46
2.7 Optimal weld parameters for Al 6061-H18 as determined by analysis of push-pin tests.	54
2.8 Weld parameters for UAM builds.	55
2.9 Overlap and stacking sequence prescribed for each sample set.	56
2.10 Tensile test results for overlap and stagger study builds showing ultimate tensile strength and elongation at failure.	58
2.11 Push-pin data for textured and nontextured builds.	64
2.12 Averaged results of push-pin testing with varying roughness sonotrodes.	65
2.13 Ultimate tensile strength results for as-built and heat treated UAM samples.	70

2.14	Comparison of UAM samples with solid material references.	70
3.1	Weld parameters for UAM block following optimization.	76
3.2	Tensile test results for out of plane tensile testing.	79
3.3	Material properties of relevant components for modeling.	84
4.1	Welding parameters for 0.032 in. (0.813 mm) thick welds using Al 6061-T6.	116
4.2	Design of experiment for angle, amplitude, and weld speed	128
4.3	Compensated weld parameters for low and high levels of amplitude. .	128
4.4	ANOVA table for tensile strength.	132
4.5	ANOVA table for elongation.	133
4.6	ANOVA table for UTS including interaction effects.	137
4.7	ANOVA table for elongation including interaction effects.	138
4.8	Tukey 95% pairwise comparisons among levels of angle compared with Angle = 5°.	139
4.9	Tukey 95% pairwise comparisons among levels of amplitude compared with low level of amplitude.	139
4.10	Optimal levels for seam welding as determined by DOE.	139
4.11	Room temperature ultimate tensile strength (UTS) test results for as-built Al 6061 joints	142
4.12	Room temperature ultimate tensile strength (UTS) test results for heat treated Al 6061 joints	143
4.13	Room temperature tensile test results of aged-only Al 6061-T6 joints.	145
4.14	High temperature tensile test results of heat treated Al 6061-T6 joints.	146

4.15	Cycles to failure for room temperature fatigue testing.	149
4.16	Weld trials process parameters for Al 2219 material.	154
5.1	Nominal composition (wt%) and ultimate tensile strength (UTS) of materials.	159
5.2	Weld parameters used for Al/Ti joints.	160
5.3	Results of push-pin testing for as-built and heat treated Al/Ti joints.	165
5.4	Results of shear testing for Al/Ti joints.	168
5.5	Weld parameters used for Al 6061 onto 4130 steel joints.	179
5.6	Weld parameters used for 4130 steel onto Al 6061 joints.	180
5.7	Results of push-pin testing for aluminum onto steel joints.	181
5.8	As-received 4130 steel foil to annealed 4130 steel baseplate welding parameters for direct welds to the baseplate.	189
5.9	Weld parameters for steel to steel with nickel interlayer.	192
5.10	Weld parameters for steel to steel with nickel interlayer.	194
5.11	Weld parameters for steel to steel with nickel interlayer.	195
5.12	Weld parameters for steel to steel using annealed 4130 steel foil.	197
A.1	Push-pin results for design of experiments study.	215
A.2	Shear test results for design of experiments study.	217
B.1	UTS test data for design of experiment study of seam welded joints	227
B.2	Elongation test data for design of experiment study of seam welded joints	228

List of Figures

Figure	Page
1.1 Schematic of the UAM components including additive and subtractive stages.	2
1.2 X-ray image of thermal management device with conformal channels (Image taken by Fabrisonic LLC).	3
1.3 Cross section of Ni-Ti embedded into aluminum using UAM [33]. . .	4
1.4 Schematic 1 kW UAM system.	6
1.5 Cross sections from (a) 1 kW UAM welds with Al 3003 and (b) 9 kW UAM welds with Al 6061 [87].	7
1.6 Image of the 9 kW OSU UAM system.	8
1.7 Schematic of the loss of relative amplitude based on stiffness change.	9
1.8 Illustration of the influence of structural compliance on weld input power (energy) for stack of welded aluminum foils: (a) empirically measured average power over steady-state weld zone with first standard deviation as error bars; (b) relation of cantilever beam stiffness as function of length or layers [37].	10
1.9 Illustration of a modal effect in a UAM build [28].	12
1.10 Tape overlap and stagger, i.e., stacking sequence, with potential void filled in via plastic deformation of the tape, as well as schematics for ordered and random stagger sequences.	13
1.11 Block build showing surface variations at tape overlap locations. . . .	15

1.12	Schematic of the peel test setup [52].	16
1.13	Schematic of the push-pin test setup.	17
1.14	Electron back scatter diffraction image of bond interface in UAM Al 3003 [27].	19
1.15	(a) Typical Kikuchi pattern and (b) indexed pattern [29].	21
1.16	Polycrystalline nickel under 1%, 5%, and 10% strain showing (a) grain orientations and (b) integrated misorientation map, with color scale in degrees [12].	22
1.17	Typical tip used for ultrasonic spot welding [5].	25
1.18	Concept for using ultrasonic welding to join two sheet materials. . . .	26
1.19	Cross section of aluminum/copper joint using UAM.	28
2.1	Test strips from push-pin sample manufacturing.	39
2.2	Sample design for shear test.	40
2.3	Gleeble 3800 thermal-mechanical characterization system utilized for push-pin testing. The boxed area illustrates the key test components.	41
2.4	Interlaken load frame utilized for shear testing. The boxed area illustrates the key test components.	42
2.5	Push-pin results for parameter set 4 representing poor interlaminar failure.	44
2.6	Push-pin results for parameter set 9 representing good interlaminar failure.	45
2.7	Main effects plot of push-pin test for each factor.	47
2.8	Interaction plot of force and temperature for push-pin tests.	48
2.9	Shear strength test results for parameter set 6 showing high variability.	49

2.10	Failure surfaces for samples showing failure (a) through multiple layers and (b) through a single layer.	50
2.11	Yield strength versus temperature for Al 6061 with temperatures utilized indicated [3].	53
2.12	Tensile samples machined from UAM build block.	57
2.13	(a) (b) Cross sections of UAM builds showing voids in Sample 1B and (c) cross sections of sample 1D with no voids.	59
2.14	Peak weld amplitude measurement under load during welding. Measurements were taken at the second layer of each stack. Similar weld amplitude levels were utilized to weld all the stacks.	63
2.15	Push-pin results: (a) 14 μm R_a ; (b) 7 μm R_a	65
2.16	Cross section of UAM builds with 7 μm and 14 μm roughnesses. . . .	66
2.17	Dimensions of tensile specimens (in mm).	69
2.18	Microstructure showing precipitate density of (a) T6 heat treated and (b) as-built sample.	71
3.1	Edge effect in a UAM build which occurs due to a lack of weld support. .	78
3.2	Tensile specimen dimensions for out of plane tensile testing (in.). . . .	79
3.3	Cylinder on flat geometry [16], modeling the sonotrode onto baseplate configuration.	82
3.4	Analytical results for contact stress through depth of aluminum. . . .	85
3.5	Sonotrode onto baseplate geometry used for FEA (dimensions in m.). .	86
3.6	Subset of the mesh used for FEA (dimensions in m.).	87
3.7	von Mises stress field for elastic contact FEA (Stress in MPa).	89
3.8	Stress-strain curve for Al 6061-H18 foil.	90

3.9	von Mises stress field with plastic deformation (Stress in MPa).	91
3.10	Zone of plastic deformation due to contact stresses.	91
3.11	Plastic deformation along the depth of the baseplate.	92
3.12	von Mises stress field under 3000 N normal force.	93
3.13	Schematic of applied loads from UAM applied to FEA analysis.	95
3.14	von Mises stress field for half cycle loading on single tape (Stress in MPa).	96
3.15	Plastic deformation zone for half cycle loading on single tape.	97
3.16	von Mises stress field for half cycle loading on 50 layer build (Stress in MPa).	98
3.17	Plastic deformation zone for half cycle loading on 50 layer build.	99
3.18	von Mises stress field for half cycle loading on 50 layer build with fillet.	100
3.19	Plastic deformation zone for half cycle loading on 50 layer build with fillet.	101
3.20	Grain map colored via inverted pole figure of the welded 6061-T4 foil.	105
3.21	Grain map colored via inverted pole figure of the unwelded 6061-T4 foil.	106
3.22	Grain orientation spread analysis of welded 6061-T4 foil.	107
3.23	Grain orientation spread analysis of unwelded 6061-T4 foil.	108
4.1	Knurl patterned sonotrode.	114
4.2	Image of 7 μm horn.	115
4.3	Image of 0.016 in. (0.406 mm) thick scoping trial.	115
4.4	Weld trial using aluminum sheet stock.	117

4.5	(a) Layout for lap joint (b) joint with machined surface and (c) joint with flush surface using foil.	118
4.6	Lap joint showing joining of two sheets.	119
4.7	Weld trial using foil to fill in machined section exhibiting tape tearing due to poor support.	119
4.8	Vacuum chuck and deformed sheet material pressed into chuck channels.	120
4.9	Adapter plate for vacuum chuck.	121
4.10	Lap joint (a) schematic and (b) cross section.	122
4.11	Angled lap joint (a) schematic and (b) cross section.	123
4.12	Scarf joint (a) schematic and (b) cross section.	124
4.13	Scarf joint with side by side welding: (a) schematic and (b) cross section.	125
4.14	Scarf joint with welding on both sides: (a) schematic and (b) cross section.	126
4.15	Image of aluminum film deposited onto horn after joining 0.020 in. (0.508 mm) thick stock material.	127
4.16	Method for machining plates at various angles.	129
4.17	Schematic test specimen for tensile testing (dimensions in inches). . .	130
4.18	Main effects plot for ultimate tensile strength.	132
4.19	Main effects plot for elongation.	133
4.20	Residual plots for UTS.	134
4.21	Residual plots for elongation.	135
4.22	Interaction plots for UTS.	136

4.23	Interaction plots for elongation.	137
4.24	Boundary conditions and loads applied to FEA model.	140
4.25	Horizontal displacement results for each of the five angles modeled (a) 5° (b) 10° (c) 15° (d) 20° and (e) 25°	141
4.26	(a) Representative room temperature tensile test results for as-built and heat treated joints (b) Fracture surface of as-built joint (c) Fracture surface of heat treated joint.	144
4.27	Reference data from MMPDS for elevated temperature tensile strength of Al 6061-T6 [1].	147
4.28	Comparison of high temperature tensile strength of welded test samples to reference and MMPDS data.	148
4.29	Reference data from MMPDS for fatigue testing of Al 6061-T6 material.	150
4.30	Comparison of fatigue performance of welded test samples to reference and MMPDS data.	151
4.31	Cross section of trial 1 with Al 2219.	154
4.32	Cross section of trial 2 with Al 2219.	154
4.33	Cross section of trial 3 with Al 2219.	155
4.34	Cross section of trial 4 with Al 2219.	155
4.35	Cross section of trial 5 with Al 2219.	155
4.36	Cross section of trial 6 with Al 2219.	156
5.1	Arrangement for Al/Ti bilayers.	159
5.2	Setup for shear test including (a) shear specimen drawing (in mm) (b) schematic of shear test loading conditions (not to scale) and (c) image of shear fixture.	163
5.3	Push-pin data for as-built and heat treated Al/Ti joints.	165

5.4	Failure surfaces of Al/Ti push-pin samples for (a) as-built and (b) heat treated samples.	166
5.5	(a) SEM image of failure surface of as-built push-pin sample (b) EDS mapping of aluminum (c) EDS mapping of titanium.	167
5.6	Failed Al/Ti shear test specimens (a) as-built and (b) heat treated. .	168
5.7	Failed shear test specimens (a) as-built and (b) heat treated.	169
5.8	Optical image of Al/Ti bilayers.	170
5.9	(a) SEM image of as-built Al/Ti sample showing diffusion line scan results at multiple scales (b) and (c).	171
5.10	Electron back scatter diffraction image of Al/Ti joint, arrows indicate approximate location of material interfaces.	172
5.11	Electron back scatter diffraction image of (a) aluminum foil and (b) titanium foil, prior to welding.	173
5.12	Diffusion line scan for Al/Ti after heat treatment along smooth interface.	174
5.13	Electron back scatter diffraction image of Al/Ti joint after heat treatment, arrows indicate approximate location of material interfaces. . .	175
5.14	Stress-strain curve for as-received 4130 foil.	179
5.15	Push-pin results for Al 6061 onto 4130 steel.	181
5.16	Failure surfaces of aluminum onto steel samples.	182
5.17	Scanning electron microscopy image of aluminum onto steel joint interface.	183
5.18	Optical image of steel onto aluminum joint interface.	184
5.19	(a) SEM image and (b) diffusion line scan results for Al/Steel joints. .	185
5.20	EBSD of Al/steel interface.	186

5.21 Grain orientation spread for Al/steel joint.	187
5.22 Steel to steel directly to baseplate.	190
5.23 Nugget formations on horn from direct as-received steel foil joining. . .	191
5.24 Steel to steel weld with significant surface coloration.	191
5.25 Weld schematic for joining steel to steel using Ni interlayer.	192
5.26 Steel to steel joint with nickel interlayer.	193
5.27 Steel joining with nickel interlayer and increased normal force.	194
5.28 Steel joining with 1010 steel interlayer.	195
5.29 Stress-strain curve for annealed 4130 foil.	196
5.30 Successful layered build using annealed 4130 foil.	197
5.31 Successful layered build using annealed 4130 foil.	198
5.32 EBSD of as-received 4130 foil.	199
5.33 EBSD of steel joints using Ni interlayers.	200
5.34 EBSD of steel joints using Ni interlayers zoomed in to closer length scale.	201
5.35 Optical microscopy image of steel joint with 1010 interlayer.	202
5.36 EBSD scan of steel joint with 1010 interlayer.	202
5.37 Optical image of six annealed 4130 foil layers welded to steel baseplate.	203
5.38 Optical image crack in annealed 4130 foil welds.	204
B.1 Cross section for weld trial 1.	220
B.2 Cross section for weld trial 2.	220

B.3	Cross section for weld trial 3.	221
B.4	Cross section for weld trial 4.	221
B.5	Cross section for weld trial 5.	221
B.6	Cross section for weld trial 6.	222
B.7	Cross section for weld trial 7.	222
B.8	Cross section for weld trial 8.	222
B.9	Cross section for weld trial 9.	222
B.10	Cross section for weld trial 10.	223
B.11	Cross section for weld trial 11.	223
B.12	Cross section for weld trial 12.	223
B.13	Cross section for weld trial 13.	224
B.14	Cross section for weld trial 14.	224
B.15	Cross section for weld trial 15.	224
B.16	Cross section for weld trial 16.	225
B.17	Cross section for weld trial 1.	225
B.18	Cross section for weld trial 18.	225
B.19	Cross section for weld trial 19.	226
B.20	Cross section for weld trial 20.	226
C.1	SEM image of welded Al 6061-T4.	229
C.2	SEM image of unwelded Al 6061-T4.	230

C.3	Unprocessed grain maps colored via inverse pole figures for welded Al 6061-T4.	230
C.4	Unprocessed grain maps colored via inverse pole figures for unwelded Al 6061-T4.	231

Chapter 1: INTRODUCTION

1.1 Ultrasonic Additive Manufacturing (UAM)

1.1.1 Process Overview

Ultrasonic additive manufacturing (UAM), is a solid-state welding process that uses principles of ultrasonic metal welding to create layered metal structures. Thin metal foils, often on the order of 0.006 in. (152.4 μm) thick, are joined to a baseplate or previous foil layer in a continuous manner to create the final structure. The joining process uses vibrations developed in one or more piezoelectric transducers to create a scrubbing action at the weld interface via transverse motion. This scrubbing action is applied by a horn or sonotrode, which when combined with a normal force, displaces surface oxides, contaminants, and asperities to generate nascent metal surfaces leading to bonding. A schematic of the UAM components is shown in Figure 1.1. Continuous welds are created as the sonotrode rolls along a specified weld path to create each joint. As a continuous process, the layered structure is built on top of, or next to the previously welded layer, depending on the desired component dimensions. Commonly controlled parameters in the process are the normal force, vibration amplitude, and weld speed.

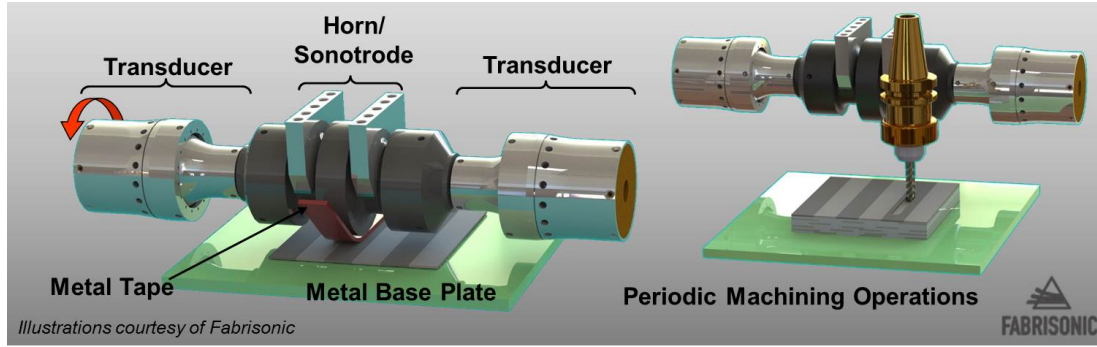


Figure 1.1: Schematic of the UAM components including additive and subtractive stages.

Often, UAM systems are integrated into a CNC machining framework enabling additive and subtractive operations to be performed in tandem. These capabilities enable production of near net shape components in a single system. Another application of this capability is the creation of integrated channel networks, which can be used for thermal management devices [63]. Examples of two such devices are shown in the x-ray image in Figure 1.2. In the device on the left, 10 successive foils were welded to a baseplate, followed by machining passes using the CNC stage to create the channel paths shown. Following machining, 10 welds were laid on top of the channels to create the final structure. In the device on the right, similar welds were conducted, however a cartridge heater was laid into a channel formed in the base of the structure to provide a heat source. Manufacturing of such devices using the UAM process can enable unique channel geometries difficult to achieve using traditional manufacturing techniques, enabling cooling networks to be created that are otherwise not possible using other processes.

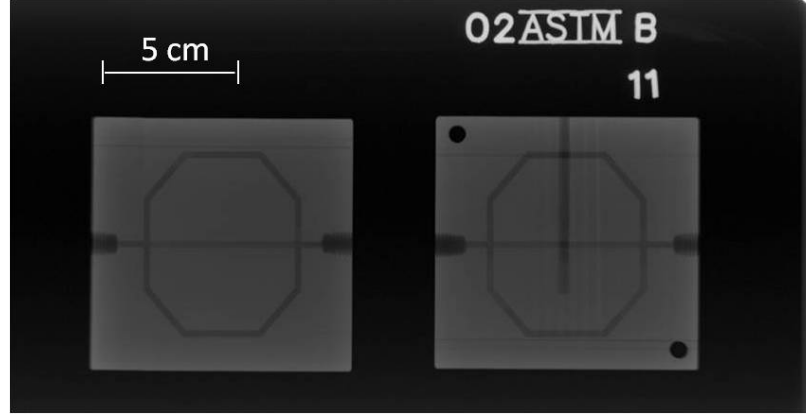


Figure 1.2: X-ray image of thermal management device with conformal channels (Image taken by Fabrisonic LLC.).

A key advantage of the UAM process is that it performs at low temperatures. Transient heat generation during the process has been measured at 30% to 50% of the melting temperature of the base metal when welding aluminum and other materials [53, 71, 79]. The low heat generation allows for the embedding of thermally sensitive components such as sensors, smart materials, and electronics that would otherwise be destroyed in fusion-based joining processes [51, 73]. An example of a Ni-Ti shape memory alloy ribbon embedded into aluminum is shown in Figure 1.3. Fusion based processes would result in significant heating of the Ni-Ti, resulting in annealing of the microstructure, in turn eliminating the memorized shape. The UAM process, operating at much lower temperatures, offers an ideal method of creating composites with integrated Ni-Ti or other smart materials without altering the existing microstructure.

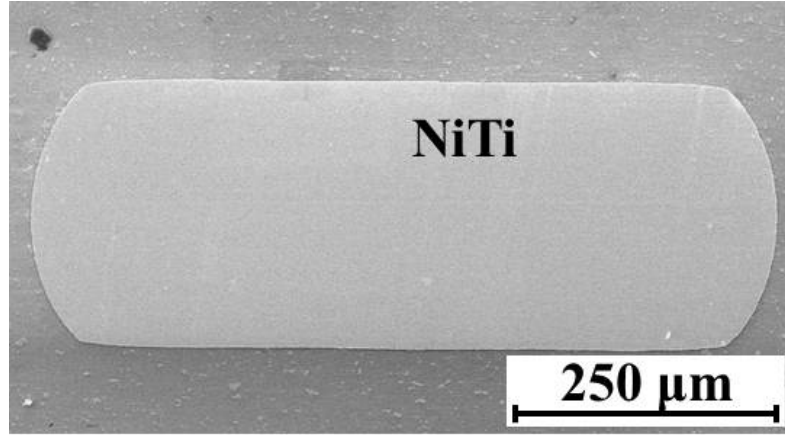


Figure 1.3: Cross section of Ni-Ti embedded into aluminum using UAM [33].

Another advantage of the low temperature nature of the UAM process is the ability to create dissimilar material joints without the production of harmful intermetallic compounds at the joint interface. Laminated builds combining aluminum with either titanium, nickel, tantalum, or copper have been achieved using UAM, as well as other material combinations such as nickel/copper and nickel/silver [41, 64, 65, 82]. It is difficult to achieve robust joints of these combinations in fusion based processes, due to their associated high temperatures. Under high heat, at or near the material melting temperature, brittle intermetallics can form at the interface via diffusion which compromises the mechanical properties of the joint. The low operating temperatures of the UAM process suppresses intermetallic formation, providing a viable joining process for welding dissimilar material combinations.

1.1.2 Machine Developments

Machine design developments have enhanced the available ultrasonic power in the process from 1 kW to 9 kW, significantly enhancing the performance of the UAM technology. A schematic of a typical 1 kW system is presented in Figure 1.4. The 1 kW systems use one piezoelectric transducer to drive the sonotrode motion and are limited to approximately 1500 N normal forces and amplitudes of less than 30 μm . Application of loads greater than 1500 N results in limited sonotrode motion due to lack of ultrasonic power, as well as bending in the weld assembly due to compliance. Such factors limit the scrubbing action applied at the weld interface, thus limiting the design possibilities for UAM components. In 9 kW UAM, two transducers are used on each side of the sonotrode, creating a push-pull effect that significantly increases the displacement and scrubbing power of the sonotrode. The mounting of the assembly has been shifted as well, to apply loading closer to the sonotrode contact area which decreases bending effects and allows more normal load to be applied without detrimental compliance effects. A schematic of the system showing the transducers and load points is shown in Figure 1.1. Available loads for 9 kW systems can be in excess of 10,000 N with vibration amplitudes of up to 50 μm .

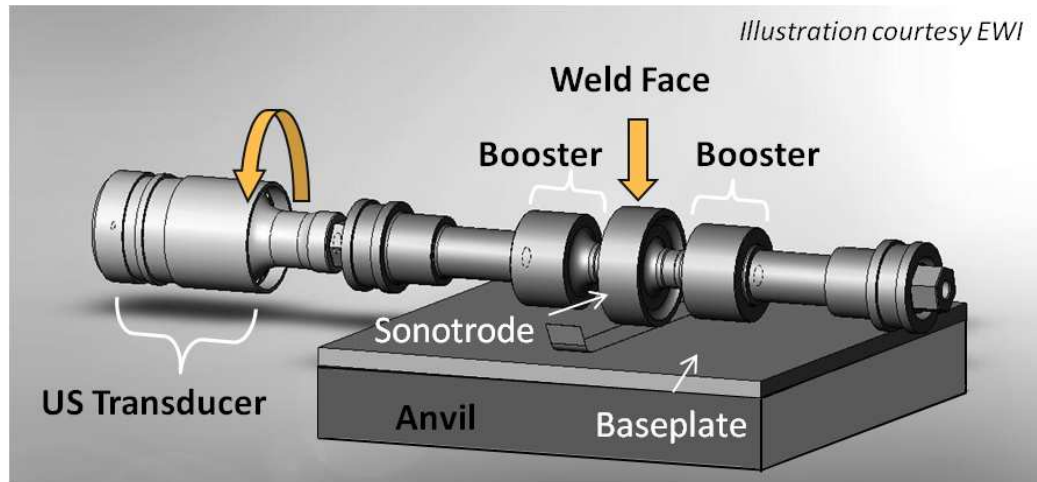


Figure 1.4: Schematic 1 kW UAM system.

These enhancements have increased the material combinations weldable with the process, as well as improved the process overall. Figure 1.5 shows images from typical 1 kW and 9 kW UAM builds using aluminum alloys. Builds using 1 kW UAM often have a prevalence of voids throughout, whereas builds using 9 kW UAM are nearly voidless. Likewise, higher strength alloys can be joined using the process. The 1 kW process is limited to soft aluminum alloys such as Al 1100 and Al 3003, whereas the 9 kW process is capable of joining 2xxx, 6xxx, and 7xxx series aluminum alloys.

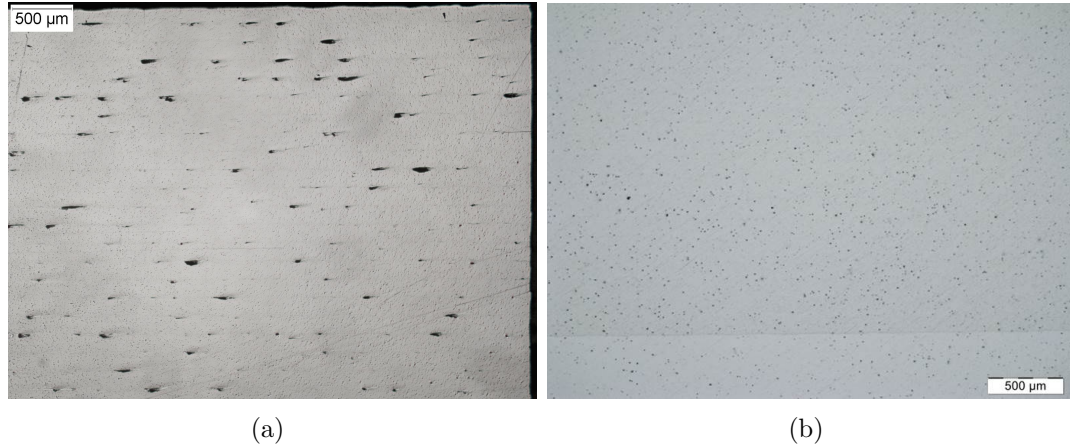


Figure 1.5: Cross sections from (a) 1 kW UAM welds with Al 3003 and (b) 9 kW UAM welds with Al 6061 [87].

A Fabrisonic SonicLayer 4000 system, located at Ohio State University, is used for all joining work in this dissertation. It is a fully automated 9 kW system with additive and subtractive stages. As with other 9 kW UAM systems, the machine can apply normal forces of 10,000 N and weld amplitudes of 50 μm . The system is shown in Figure 1.6. In addition to the 9 kW capabilities, the machine has a laser machining stage for machining of small features. This allows for the creation of small channels, on the order of 50 μm , useful for creating unique thermal management devices and composites with small embedded wires for active or passive applications.

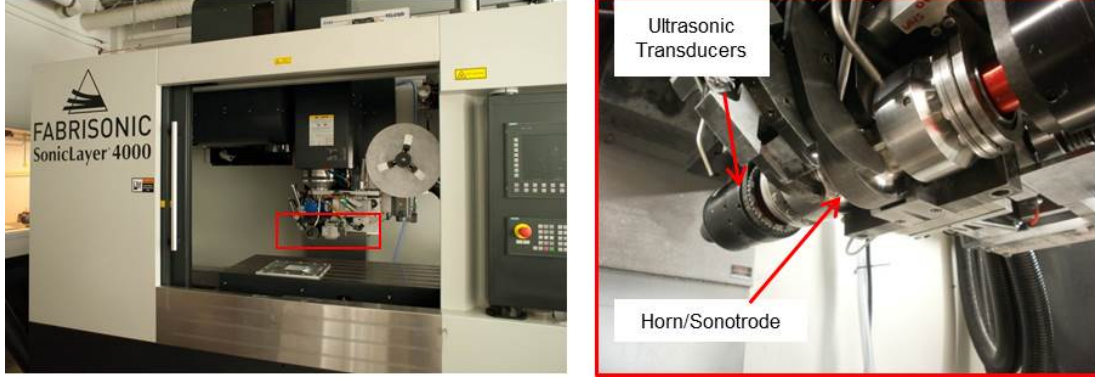


Figure 1.6: Image of the 9 kW OSU UAM system.

1.1.3 Effects of Structural Compliance During UAM Build Process

One of the major elements in the currently accepted weld mechanism for UAM is the amplitude of relative motion between the foil and the workpiece it is to be welded to. This is controlled through the side to side vibration amplitude of the sonotrode, which imparts this motion on the foil to be welded. For consistent welding throughout a UAM build, it is necessary to maintain a constant relative motion between these two pieces. However, as a build is being constructed, the structural compliance changes. Increases in height decrease the stiffness of the workpiece following beam theory. This in turn, has an effect on the relative motion of the foil and workpiece because the workpiece deflects with the loads from the sonotrode. This is shown in Figure 1.7 where the initial relative displacement is represented by δ and the relative displacement due to the compliance of the UAM build is given by α . As the stiffness of the UAM build decreases with height, the relative displacement between the foil and the build decreases. Since amplitude has been shown to have a significant

effect on weld quality [41, 42, 88], the decrease in relative motion could lead to a degradation of weld quality through the height of the build.

The amplitude of the sonotrode motion is controlled through varying the current to the ultrasonic transducers to maintain a constant amplitude via the voltage. As the build stiffness decreases, the required current to maintain a constant amplitude likewise decreases due to a decrease in the reactionary shear force against the sonotrode. Measurements of compliance effects on the ultrasonic power used during welding are shown in Figure 1.8a. As shown, the ultrasonic power decreases as a build progresses, with a roughly 25% drop in power over 20 layers. This correlates with the changes in stiffness of the part as it is built, calculated using beam theory, shown in Figure 1.8b [37].

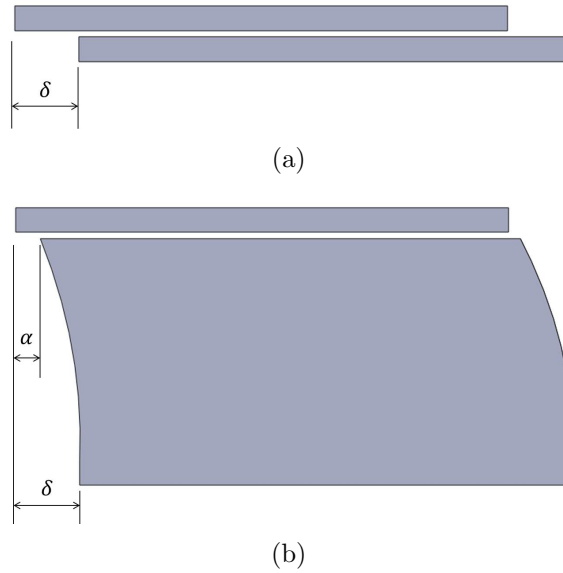


Figure 1.7: Schematic of the loss of relative amplitude based on stiffness change.

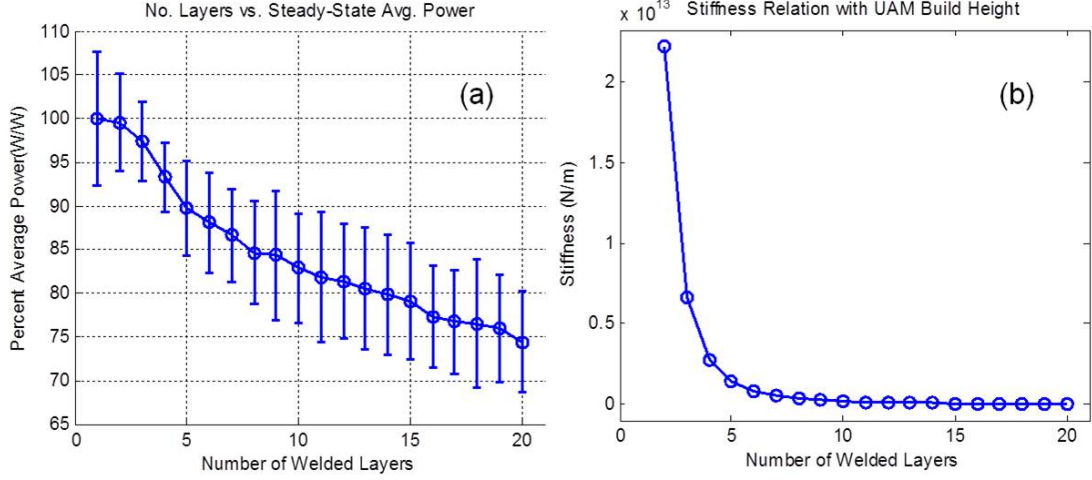


Figure 1.8: Illustration of the influence of structural compliance on weld input power (energy) for stack of welded aluminum foils: (a) empirically measured average power over steady-state weld zone with first standard deviation as error bars; (b) relation of cantilever beam stiffness as function of length or layers [37].

The relationship between weld energy and build height is given by,

$$Energy = F * \delta = \frac{3EI\delta^2}{2(H)^3} \quad (1.1)$$

where F is the shear force applied, δ is the displacement of the sonotrode, E is the elastic modulus of the UAM foil, I is the moment of inertia of the build, and H is the height of the build. Through proper control of the input displacement of the sonotrode, a constant relative motion between the workpieces can be applied and consistent properties can be achieved as a build progresses. However, this methodology has only been proven in an open-loop configuration through manual modification of the input amplitude [37]. Further machine developments will be necessary to incorporate a fully automated control scheme in the build process.

Additional structural effects must be taken into account when creating UAM builds. As a build progresses, the natural frequency of the structure changes with each layer added. Eventually this natural frequency approaches the frequency of the applied ultrasonics, often 20 kHz. Work by Gibert et al. [28], has modeled the structural modes being excited due to the ultrasonics in the UAM process. Their work has shown that as a build approaches a height to width ratio of approximately 0.7, structural modes become excited under resonance and prohibit viable welds. An example of an excited structural mode is shown from their work in Figure 1.9. The motion imparted due to the structural resonance is in the same plane as the applied displacement of the ultrasonics. Due to these common displacements, little to no relative motion between the foil and the structure occurs, resulting in poor bonding. Experimental work by Robinson et al. [69] supports these findings as builds approaching a height to width ratio of 0.7 tend to suffer from poor bonding in the highest attempted layers.

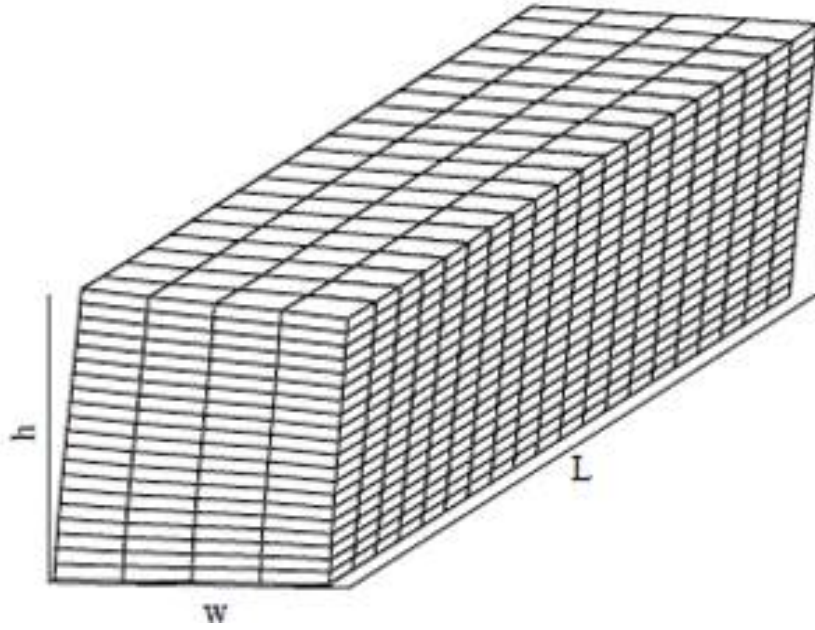


Figure 1.9: Illustration of a modal effect in a UAM build [28].

1.1.3.1 Managing Structural Effects

To combat the degradation in weld quality due to structural effects, the construction of a UAM component must consider the stiffness of the structure throughout the build process to maintain consistent properties. Often a component is built wider than the final dimensions to stiffen the structure and control the natural frequency such that it does not approach a resonance of the applied ultrasonics.

In the creation of UAM parts sized greater than the typical tape width of 1 in. (25.4 mm), tapes must be laid next to one another to generate the full dimensions. This type of layup creates the potential for voids to form at the abutting points. A method of eliminating voids is to overlap tapes slightly when laying up side to side. A schematic of this concept is shown in Figure 1.10, where tapes are laid up next to

one another. If the overlap is too small, the potential for voids increases [66], however if it is too large, build time increases because more tapes will be required to achieve the width dimensions and flash, or excess material, can accumulate at the abutment points making the weld surface uneven.

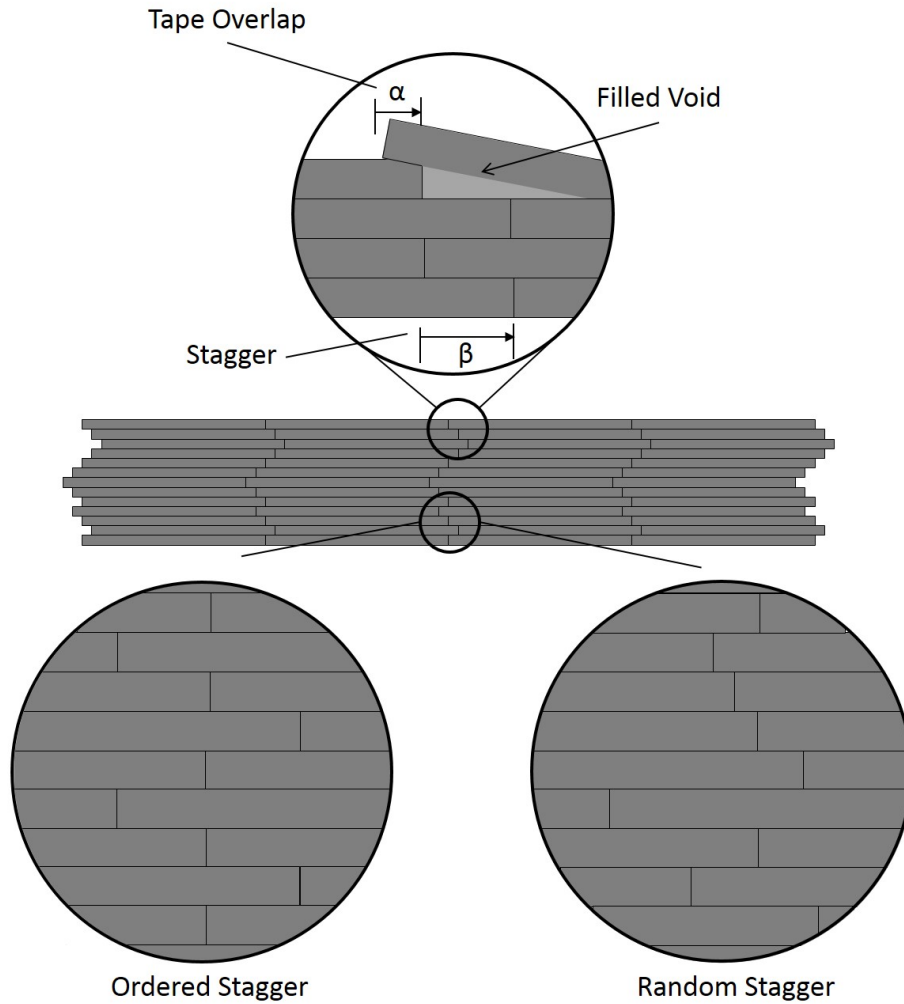


Figure 1.10: Tape overlap and stagger, i.e., stacking sequence, with potential void filled in via plastic deformation of the tape, as well as schematics for ordered and random stagger sequences.

Another production factor that must be addressed is the stacking sequence, or stagger, of layers as they progress higher in the build. If the tapes are all aligned at the same location, the possibility of voids running through a single area greatly increases. Therefore moving the seam location in a brick-like fashion to create a less direct crack path, should a crack develop, is ideal. Many methods of stagger can be implemented, but typical patterns use an ordered, or a random layup, as shown in Figure 1.10.

Previous work conducted by Obielodan et al. [66], studied the effect of the tape to tape overlap and stacking sequence of successive UAM foils on bond quality for 1 kW UAM using Al 3003. Their work showed that a tape to tape overlap of about 0.7 mm and a stacking sequence moving 50% of the tape width was optimal for minimizing voids and providing a consistent tensile strength. The advances in capabilities associated with 9 kW UAM compared to 1 kW UAM specifically with new materials including Al 6061, motivates the need to further investigate tape overlap and stacking.

While tape overlap and stagger practices can reduce voids, as the build progresses material builds up at the overlapped seams and can create uneven weld surfaces. A UAM build is presented in Figure 1.11, showing an example of material build up at the seams leading to uneven weld surfaces. This motivates the use of periodic flattening passes during the build process to create more even weld surfaces as the build advances. However, it is necessary to examine the effect flattening passes have on the mechanical properties of the build, specifically comparing welds on the smoothly machined surfaces to welds on surfaces that have a roughened texture caused by the sonotrode.

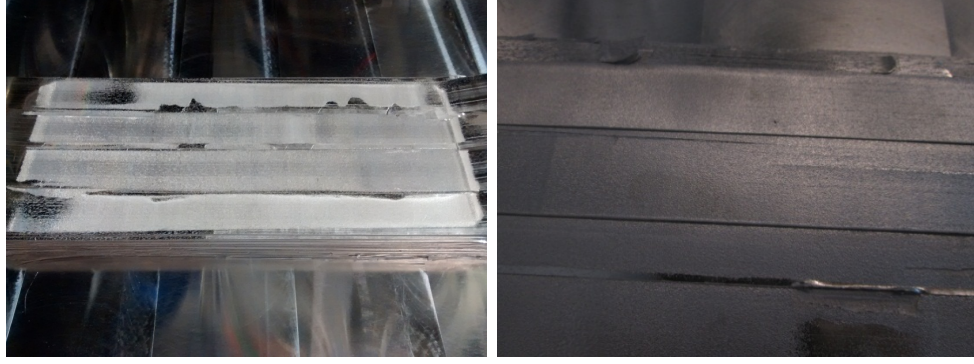


Figure 1.11: Block build showing surface variations at tape overlap locations.

Previous work has indicated that surface roughness can play an important role in joining [25, 47]. Work by Friel et al. [25] in 1 kW UAM indicates that a certain amount of roughness is necessary for optimal joining, but too much roughness can generate large unbonded areas. Their work illustrates that an optimal roughness value may exist for strong bonds while eliminating voids. Work by Ram et al. [47] in 1 kW UAM, indicates that a nearly voidless interface can be achieved when welding on smooth interfaces. However, a voidless interface is not sufficient for achieving optimal mechanical strength [42]. These studies indicate a need to characterize the mechanical strength of 9 kW UAM builds using roughened and smooth interfaces.

1.1.4 Mechanical Characterization

Much of the characterization of UAM builds has been conducted using metallurgical cross sections, quantifying the void content within a UAM build with a metric known as linear weld density (LWD) [47, 53, 65]. An example cross section is presented in Figure 1.5a, where a measurement of the voids along the length of an

interface indicates the LWD. While useful in determining whether voids exist, lack of voids does not guarantee perfect bonding and has been shown to poorly correlate with mechanical tests by Hopkins et al. [42]. Likewise, the polishing process used to prepare such cross sections can provide false indications of bonding through smearing of material over bond interfaces.

To overcome the limitations of LWD in characterization, certain mechanical tests have been used. One of which is the peel test, providing an indication of bond strength through a peeling action which delaminates a single tape from a build or baseplate [53]. A schematic of this test setup is shown in Figure 1.12. This is a useful test in that it provides a mechanical strength metric, but it is comparative in nature, involves a complex stress state, and is limited to test forces up to the strength of the foil being pulled. Therefore, it provides limited information on the bond quality of a UAM part.

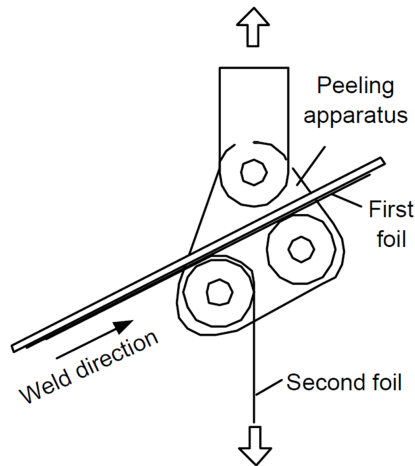


Figure 1.12: Schematic of the peel test setup [52].

Another test of UAM build mechanical strength is the push-pin test, developed by Zhang et al. [89]. This test uses a through pin to press and delaminate a bonded sample, providing a measure of the delamination strength and displacement. The test has been used in multiple instances and provides a good metric of bond strength [82, 87, 89]. A schematic of this test is shown in Figure 1.13. Machining and testing of push-pin samples is relatively quick, providing a simple, easy to carry out test. However, the test is comparative in nature and involves a complex stress state at failure, making it difficult to compare with homogeneous materials as well as being difficult to design with.

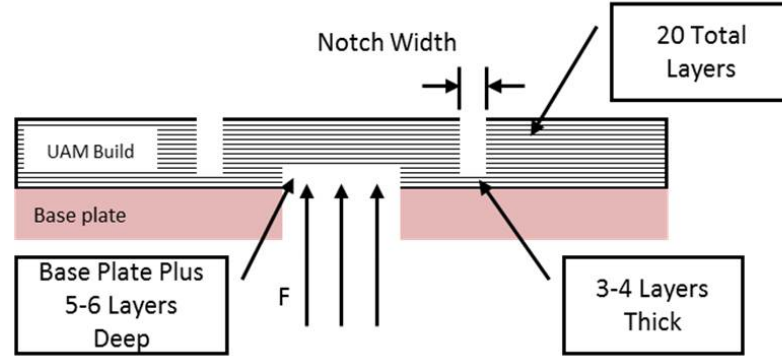


Figure 1.13: Schematic of the push-pin test setup.

Numerous studies have utilized shear strength testing to characterize UAM build strength [41, 42, 67]. Multiple sample designs have been used, with the overarching goal of determining the shear strength of a specific bonded layer. Shear testing provides a strength metric which can be compared to literature values, making it valuable in design. However, in most cases, the shear tests investigated with UAM

do not strictly follow ASTM standards for shear testing due to sample dimension requirements. Creation of full size shear samples using UAM can be prohibitive in terms of cost and time, therefore smaller tests are used which require fewer layers but do not strictly follow standards. Therefore the tests can provide useful information, but considerations must be made to account for variations from accepted standards.

Previous work has shown tensile tests to be a valid method of determining bond quality [19, 41, 42]. Tensile tests provide data for comparisons to literature values which can be used in design. Another advantage is that the failure occurs at the weakest layer within the build, providing a more conservative metric of mechanical strength. However, the cost in time and material associated with building components for such tests is often prohibitive. Also, some of the existing machine structures do not use automated tape feeding, which limits the height at which components can be built due to time and alignment. Therefore tensile tests are not ideal in all cases, however provide the most useful information for design comparisons against traditionally manufactured components.

1.1.5 Microstructural Characterization

The microstructure of UAM built structures has been extensively investigated using optical microscopy, scanning electron microscopy (SEM), focused ion beam (FIB), and transmission electron microscopy (TEM) techniques [19, 27, 49, 58]. Such investigations have shown that, within approximately 15 μm of the bond interface region, an area of small recrystallized grains exists [19, 27, 72]. Figure 1.14 shows an electron back scatter diffraction (EBSD) image of the bond interface in a UAM sample. As is seen within the bond interface, small, mostly equiaxed grains are

observed, whereas the bulk of the foils shows an elongated microstructure from rolling. Likewise, the polar mapping of the grain orientations shows a distinct texture in the bulk due to rolling whereas the interface region is much more equiaxed. This effect has been shown in transmission electron microscopy (TEM) by Johnson [49]. These observations indicate a small recrystallized zone exists within approximately $15\text{ }\mu\text{m}$ of the bond interface, while the remainder of the bulk material is unchanged. The equiaxed grains at the bond interface signify that localized recrystallization is occurring which has been classified as a result of dynamic recrystallization due to deformation and limited heating during processing [78].

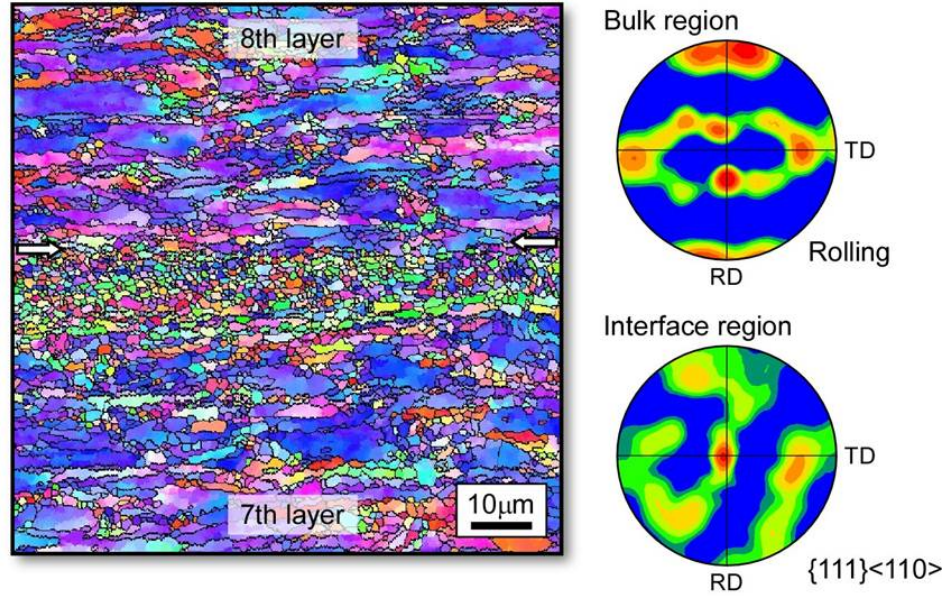


Figure 1.14: Electron back scatter diffraction image of bond interface in UAM Al 3003 [27].

Melting has not been observed in large quantities and transient thermal measurements have shown that the instantaneous temperatures at the bond interface are below melting [53, 79]. Likewise, microstructural evaluations have shown that the oxide layer on the foil stock for welding, is fractured and displaced during the process, though it is unknown whether it is completely displaced [72]. A bond theory has been proposed based on these observations where the shear deformations caused by the ultrasonics fracture and displace surface oxides, creating a driving force for recrystallization within the bond zone and across the interface of the mating foils [72].

Electron Back Scatter Diffraction

Because of the small grain sizes normally associated with UAM structures, typical etching processes are insufficient in exposing grain boundaries for optical microscopy. This has motivated the use of electron microscopy techniques, such as EBSD, which allow for characterization of both the bulk and interface microstructure.

EBSD is a powerful microstructural characterization technique which can provide information on grain size, grain boundary character, grain orientation, texture, and phases. The process works by measuring the diffracted electrons emanating from a sample under an electron beam [30]. When the electron beam interacts with the crystal lattice in the sample, backscattered electrons are diffracted by the crystallographic planes on the surface. The diffracted electrons then undergo constructive and destructive interference which exhibit characteristic patterns known as Kikuchi bands based on the lattice spacing. These electrons then strike a phosphor screen and are detected via a camera. Once the pattern is collected, software is used to identify the characteristic patterns based on the Kikuchi bands exhibited [21]. An example of a typical Kikuchi pattern is shown in Figure 1.15, showing a typical pattern and an

indexed pattern indicating the crystallographic planes characteristic in the material. The characteristic planes are used to identify the phases and orientations present based on the characteristic lattice spacing in a given material.

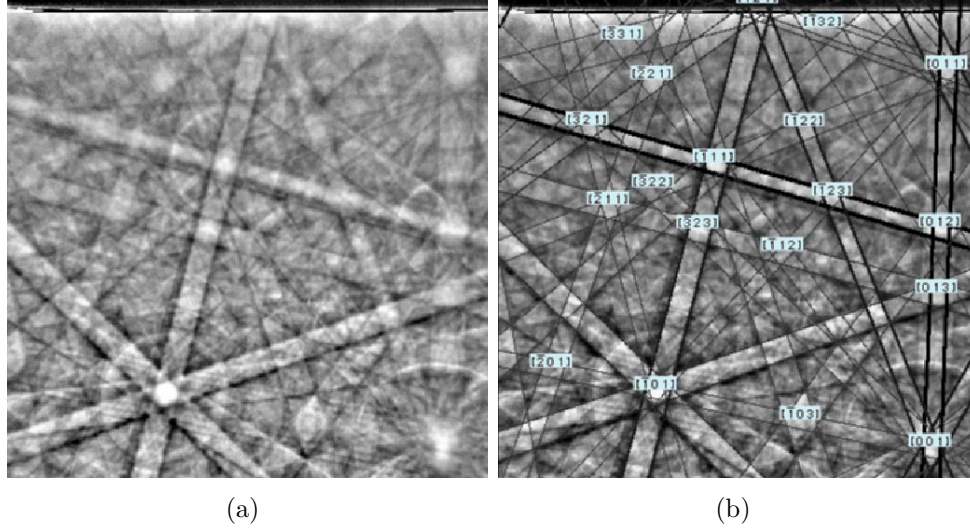


Figure 1.15: (a) Typical Kikuchi pattern and (b) indexed pattern [29].

Because the technique provides information on grain orientation, an indication of the plastic strain within the grains can also be determined. Under plastic deformation, the lattice planes within a grain can rotate several degrees. This grain rotation can then be interpreted in the EBSD measurements to provide information on intragranular strain. An example is given in Figure 1.16, where polycrystalline nickel at various states of strain is presented [12]. In Figure 1.16a, the orientation map indicates deformation bands form within the grains as the strain is increased. In Figure 1.16b, the misorientation of the grains to a given reference is shown, indicated with higher levels of green and red for the higher strain cases. This misorientation within the

grains is associated with an intragranular curvature characteristic of plastic deformation. More information on the techniques used to compute the misorientations can be found in [12].

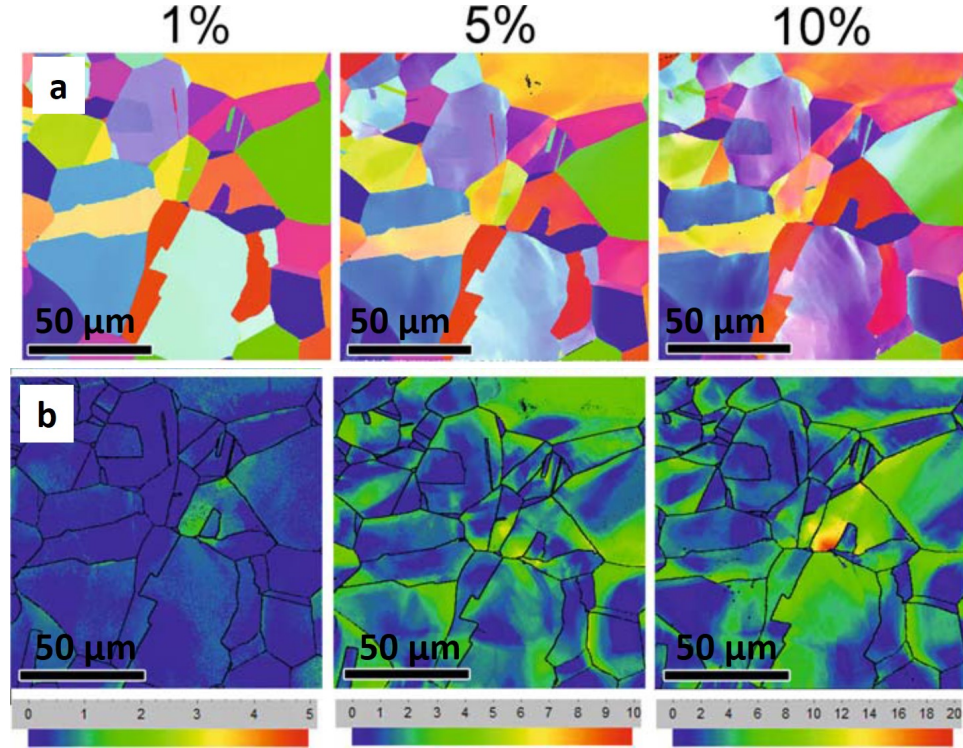


Figure 1.16: Polycrystalline nickel under 1%, 5%, and 10% strain showing (a) grain orientations and (b) integrated misorientation map, with color scale in degrees [12].

While a detailed explanation of all aspects of the technique is beyond the scope of this work, EBSD has proven useful in the examination of UAM structures. A typical image of an EBSD measurement in the UAM process is shown in Figure 1.14. As is seen, the bulk of the tapes is identified via a larger, elongated grain structure, while the interface between foils shows a more equiaxed structure with smaller grain sizes.

This technique has been vital in gaining an understanding of the differences in grain structure through the thickness of UAM welded foils and continues to be useful in understanding new UAM configurations and material combinations. Additionally, in this work, examination of the plastic strain within a UAM build is investigated to better understand the strains applied during the welding process.

1.2 Sheet Metal Joining

There are a variety of techniques for joining sheet materials, including rivets, welding, bolts, fasteners, and many more. For aerospace applications, rivets tend to be used most prevalently due to their applicability to multiple material systems, minimal effect on material microstructure, affinity to investigation via non-destructive evaluation (NDE) techniques, and extensive experience in industry [7]. In certain instances, rivets, or other mechanical fasteners protrude from the surface of the sheet metal. This protrusion can affect flow characteristics for fluids flowing over the sheet, making them prohibitive in specific applications. Flush rivets can eliminate this protrusion but cannot be applied in all joint geometries due to access limitations for in-situ NDE inspections.

Fusion welded joints can provide a flush surface finish, however tend to create a heat affected zone which can degrade the mechanical properties of the material through altering the microstructure [23]. Specifically age-hardenable materials, such as 2xxx and 6xxx series aluminum are prone to such weakening. Heating of such materials can solutionize the precipitates that provide strengthening, leading to a significantly weaker material in the heat affected zone [91]. Solid state techniques,

such as ultrasonic welding, can minimize this property degradation since the associated heating is well below melting.

Ultrasonic spot welding is a technique that has been applied to aluminum sheet joints for automotive applications and proven to be a viable joining solution in certain instances [31, 40]. Ultrasonic spot weld joints using Al 5754 alloy at 2 mm thickness have been achieved using a lap joint configuration without any indications of voids or cracks present [90]. Joints using Al 6111-T4 alloy at 0.9 mm thickness have likewise been successful in generating voidless interfaces [92]. In each case, it has been established that increases in weld energy in the form of weld times, tends toward increases in weld strength [46].

While successful welds can be achieved using the US spot welding process, the roughness imparted by the US spot welding process can be prohibitive in certain applications. A typical weld tip used for US spot welding is shown in Figure 1.17, exhibiting the ridge-like structure used to aid in coupling the tip to the workpiece. Another limitation of the process is that it operates in a discrete manner. Therefore continuous welding operations along the length of given component are not possible.



Figure 1.17: Typical tip used for ultrasonic spot welding [5].

The UAM process operates very similarly to ultrasonic spot welding, where the mechanism of a scrubbing action at the mating interfaces overcomes the barriers to solid state bonding. However the UAM process can operate in a more continuous mode, generating welds along the length of a given joint in a single pass. Similarly, the sonotrodes used in the process impart a much less severe texture, on the order of $7\text{ }\mu\text{m } R_a$. Given these characteristics, UAM equipment is proposed as a method of joining aluminum sheet materials with a flush surface finish.

An example schematic of the concept is presented in Figure 1.18. The concept proposed here will utilize ultrasonic welding to promote bonding of sheet metal on the order of 0.080 in. (2.03 mm) thickness, a significant increase over the current state of the art for UAM processes of 0.006 in. (152.4 μm) thick welds. Because the process

operates at low temperatures, age-hardenable materials will be examined since the process should not affect the material properties therein.

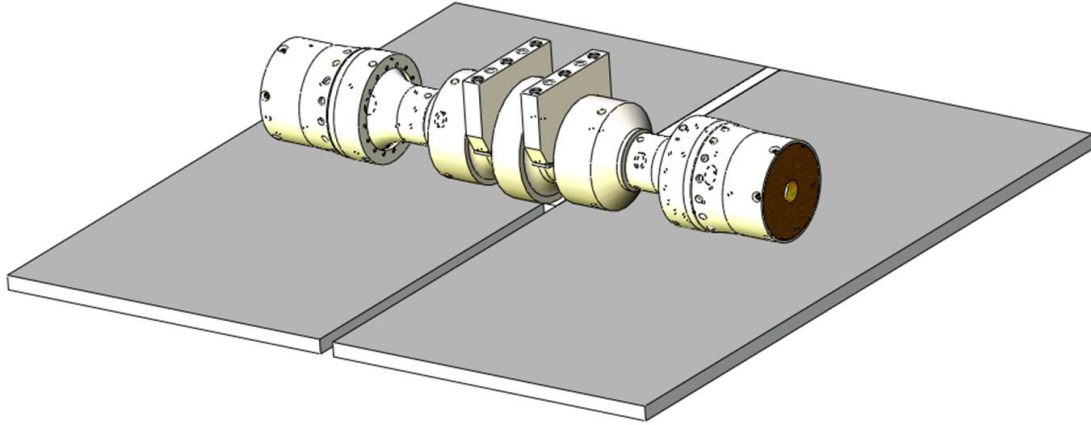


Figure 1.18: Concept for using ultrasonic welding to join two sheet materials.

1.3 Dissimilar Material Joining

Creation of dissimilar material joints is increasingly important as component designs attempt to integrate lightweight parts or tailor specific properties to given applications. For example, parts may require high strength in certain areas while remaining lightweight overall. Such capabilities are becoming of interest in aerospace, naval, railway, and automotive applications [80]. Joining dissimilar materials is often quite complex because successful joints must consider dissimilar melting temperatures, thermal conductivities, mechanical strength, and other material properties. Brittle intermetallics, often generated in the weld zone of typical fusion based welding processes, severely degrade the mechanical properties of the joint [17]. Therefore in certain instances solid state technologies that avoid melting should be considered.

Such processes include ultrasonic welding, explosion welding, friction welding, diffusion welding, and high-frequency resistance welding. Each technique holds its own advantages and disadvantages. Explosion welding for instance, while highly effective, can be costly, requiring significant capital expenses.

Of specific interest in this study are combinations of aluminum to steel, steel to aluminum, Al/Ti, and steel/steel. For joining Al/steel combinations, existing techniques include adhesives, explosive welding, fusion welding, friction welding, and friction stir welding [85]. Adhesives, while viable in certain instances, produce poor specific strength. Fusion welding tends to heat the materials too high and too long to suppress intermetallic formation via interdiffusion, leading to intermetallics such as FeAl, Fe₃Al, and Fe₂Al₅ that create a brittle weld zone [9, 80]. Friction welding, while a feasible solid state process, is limited to specific geometries [14]. Friction stir welding is likewise a possible solution, however the fixturing required can limit the process in certain applications or geometries.

Al/Ti combinations have been proven using diffusion bonding, friction welding, and friction stir welding [15]. Though each of these processes is solid state and therefore below fusion temperatures, intermetallic compounds were shown to exist at the bond interface [15]. Formation of AlTi and TiAl₃ compounds in friction stir welding and diffusion bonding are highly dependent on time and temperature during processing, consistent with diffusion theory [15, 48]. Intermetallics can degrade the strength along the bond interfaces.

Ultrasonic welding is an alternative to existing processes in certain cases. Since the ultrasonic process functions at temperatures below 0.5 the melting temperature (T_m), the driving force for forming brittle intermetallics due to diffusion is significantly

decreased [53]. Diffusion bonding and friction stir welding by contrast, can involve process temperatures of roughly $0.75 T_m$. This increased temperature raises the likelihood for diffusion to occur, leading to a higher driving force for intermetallics to form [57, 76]. Previous work by Truog has proven the UAM process effective for joining aluminum to copper [82]. An example cross section for an aluminum-copper joint is shown in Figure 1.19. Typically achieving this joint can be difficult due to the high thermal conductivity of each material and the potential for intermetallic formations. Other dissimilar joints proven using UAM include Al/Ti, Al/Zn, Cu/Ni, aluminum with metal matrix composites, Al/Ag, Cu/Ag, Cu/Ni, Mo/Al, Ta/Al, and Ni/Stainless steel [32, 41, 50, 65].

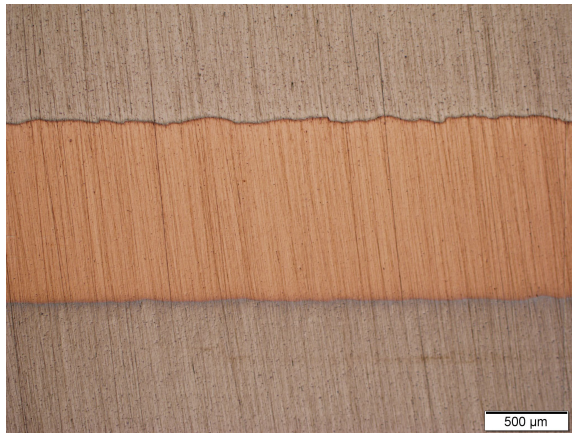


Figure 1.19: Cross section of aluminum/copper joint using UAM.

1.4 Statistical Techniques in Manufacturing

Determination of process variation is of utmost importance in manufacturing. Analyses such as the statistical distribution of given metrics for a production run

requires constant monitoring for quality control and maintaining production tolerances within predefined specifications. The determination of process variation can be achieved using many experimental methods which attempt to glean information from a system based on the input parameters to the system. One strategy is to utilize a best-guess approach which takes advantage of prior knowledge and technical expertise to determine a set of parameters for maximizing a process. This approach, while often successful, often only results in determination of a suitable result, not necessarily an optimized one.

Another approach is a one factor at a time approach which consists of controlled variation of a specified parameter, while holding constant all other parameters to the system. This approach, while able to determine main effects in the system, cannot capture any interaction between the factors in the experiment. Similarly it is a highly inefficient approach which requires a large number of experiments, leading to higher costs.

To determine the affect of several factors in a system, a factorial experiment can be used. This technique, at its core, attempts to glean significant information about a process through a method which minimizes the number of tests or observations required. This type of approach can yield information about main effects and interaction effects, in a relatively small number of experiments or observations. Many types of experimental arrays can be applied such as fractional factorial designs, central composite designs, Box-Behnken designs, Taguchi arrays, and others [10, 11, 81]. The selection of the specific experimental design is dependent on the number of factors being investigated and the desired information from experimentation. Specifics on each design and their selection is beyond the scope of this dissertation, however,

the central concept to each of these experimental designs is gathering pertinent information in the least number of experimental runs. This efficiency is desired for minimizing time and costs for experimentation.

Following experimentation using these approaches, many statistical techniques can be applied to analyze the data. Central to these is the method of least squares, for obtaining estimates of the variation between and within groups of responses to input parameters. Using this approach, a general linear model can be applied which captures the responses of the system to input factors, while also taking into account noise in the system [18]. The generalized linear model takes the form,

$$Y_{ijkt} = \mu + \alpha_i + \beta_j + \gamma_k + \alpha_i\beta_j + \alpha_i\gamma_k + \beta_j\gamma_k + \alpha_i\beta_j\gamma_k + \epsilon_{ijkt} \quad (1.2)$$

where Y is the response of the system, μ is the overall mean, α_i is the effect of the first process input at the i th level, β_j is the effect of the second process input at the j th level, γ_k is the effect of the third process input at the k th level, and ϵ is the noise in the system. Interaction effects including $\alpha\beta$, $\alpha\gamma$, $\beta\gamma$ represent the two factor interaction effects between the three parameters in the system. Similarly a three factor interaction effect including α , β , and γ represents the interaction between all three parameters at the same time. Three factor interactions, while mathematically relevant, can be difficult to interpret physically and can often be ignored due to their insignificance on the process.

Such a model of the system provides information on the main effects and interaction effects of the inputs of the system as well as their significance to the system overall. Treatment contrasts allow for evaluation of the varying levels of a single

parameter to determine the significance of each level's effect on the system. Multiple comparison methods such as Bonferroni, Scheffe, Tukey, Dunnett, and others are techniques which provide comparisons of treatment combinations through confidence interval calculations [22, 70, 84].

Tukey pairwise comparisons specifically, are used to compare the significance of variation from one level to the next [18]. Such comparisons can be used to determine optimal parameters levels for a given response. The comparisons follow the equation,

$$\tau_i - \tau_s \in (\bar{y}_i - \bar{y}_s) \pm \omega_T \sqrt{msE(\frac{1}{r_i} + \frac{1}{r_s})} \quad (1.3)$$

where ω_T is taken from a studentized distribution depending on the data set, y_i and y_s are responses, msE is the mean square error of the response and r_i and r_s are the sample sizes of the given process parameters. When interpreting Tukey pairwise comparison tables, if a comparison range from the lower to higher value includes zero, it is not considered statistically significant. If the comparison range does not include zero, it indicates that a statistically significant difference between two levels is observed at a 95% confidence. Examples of the use of this technique are prevalent throughout the literature when applied to research in engineering, manufacturing, biology, and other sciences [6, 56, 86].

1.5 Problem Statement

While UAM is an appealing technology, research into the mechanical properties of composites built using the technology, expansion of the dissimilar weld envelope, and developments into new weld geometries are all necessary to fully take advantage of its potential. Developments increasing the available ultrasonic power from 1 kW to 9

kW have expanded the possibilities in joint designs and weldable materials. Further developments are required to optimize the process, eliminating voids and maximizing the mechanical strength of joints produced therein. The predominant weld geometry involves a flat lap joint using a metal foil on the order of 0.006 in. (152.4 μm) thick. To expand the design envelope for the technology, other geometries, such as those using thicker foil stock material will require research. Dissimilar material joints, while proven in certain cases, have not been extensively investigated for materials exhibiting hexagonal close packed (HCP) and base centered cubic (BCC) crystal structures, such as titanium and steel. Investigation of the weldability of these materials will provide engineers further design options involving harder materials, as opposed to aluminum alloys often used.

The work in this dissertation pursues a fundamental understanding of the process, allowing for new designs to be considered using the process, enhancing usability, and moving the technology from a niche lab scale to a more applications based scale with relevance to aerospace, automotive, and other industries. Al 6061 foil material will be used as the platform for examining fundamental process-property relationships, while the knowledge and understanding of these relationships can then be extended for other material systems. For joining thicker sheet material, on the order of 0.08 in. (2.03 mm), a methodology is to be developed such that flush, rivetless joints will be created using the UAM process. This capability is expected to provide a higher throughput for builds as well as expand the design space within which the UAM process can operate. Finally, a methodology is to be developed for joining dissimilar material combinations including Al/Ti, Al/steel, and steel/steel. These material systems have

not been formally explored using 9 kW UAM, and such studies will extend the frontier of design possibilities when considering multi-functional structures.

For the first time, optimization of processing conditions for 9 kW UAM will be pursued, thicker joints on the order of 0.076 in. (1.93 mm) will be investigated, and joining with steels will be formally investigated. Such studies will lead to a more fundamental understanding of the process-property relationships for UAM structures. For thicker joints made using UAM, an understanding of the effect of compliance on the relative sliding motion and bond quality will be cultivated through a finite element model. This will provide insight into bond quality and provide an explanation of the thickness limitations which exist in ultrasonic metal welding. Finally an examination of the existing bond mechanisms for dissimilar material combinations will be explored through the grain structures found in UAM bonded structures. This should provide insight into the possibilities for joining material combinations not considered in this study based on their microstructural characteristics.

1.5.1 Dissertation Outline

The outline of this dissertation is organized as follows. Studies on the optimization of UAM welding conditions are presented in Chapter 2, followed by an examination of the stress states and plastic deformation imparted due to the process via modeling and experimentation in Chapter 3. The design and implementation of seam joints using sheet material with the UAM process is presented in Chapter 4. Dissimilar material joints including Al/Ti, aluminum to steel, steel to aluminum, and steel to steel combinations are examined in Chapter 5. Lastly, the significant findings from this work as well as discussion of future work is summarized in Chapter 6.

Chapter 2: PROCESS-PROPERTY RELATIONSHIPS AND STRENGTH OPTIMIZATION OF UAM BUILDS

Introduction

The focus of this chapter is identifying the process-property relationships which govern the strength of UAM built composites, while identifying the optimal strategy for building high strength UAM composites. The first study examines the optimal process parameters for joining Al 6061 foil using a design of experiments approach. A second study examines the foil stacking sequence and proposes an optimized sequence for UAM builds. The third study examines the effect of roughness on UAM builds, specifically the horn roughness and weld effects following flattening passes via machining. Finally the effect of post-process heat treatments on mechanical strength is examined.

2.1 Optimal Process Parameters via Design of Experiments for Al 6061

The purpose of this study is to determine the optimal processing parameters for joining Al 6061-H18 foil using the 9 kW UAM process. A design of experiments (DOE) approach is used, such that multiple processing parameters can be explored

simultaneously. The study uses Al 6061 fully work hardened aluminum which was purchased in the annealed heat treatment and fully work hardened condition, known hereafter as Al 6061-H18. Al 6061 was chosen due its frequent use in industry and strong compatibility with UAM. Samples were manufactured in the Smart Materials and Structures Lab at The Ohio State University on a Fabrisonic SonicLayer 4000 9 kW UAM machine.

2.1.1 Experimental Methods

Sample Manufacturing

The DOE approach uses multiple build strips with varying process parameters to experimentally determine the optimal parameters for welding. Build strips were generated for the DOE following a Taguchi L18 design matrix varying the temperature, weld force, weld amplitude, and weld rate. The design matrix is shown in Table 2.1. The 1, 2, and 3 designations in the table indicate the low, medium, and high levels for each of the parameters within a treatment combination. Execution of this type of design can determine how each parameter affects the mechanical strength of the UAM build in a minimal number of experimental runs. The exact levels for each of the parameters were determined from a pilot study which established the build envelope for the study, with the parameters given in Table 2.2. For amplitude, both the actual sonotrode displacement and the percentage of maximum amplitude set by the machine are listed. The lower limit of parameter levels is where insufficient energy was applied such that welds could not occur, and the upper limit is where too much energy is applied to the foil, causing welding to the sonotrode as opposed to the previous layer. This DOE methodology has been applied to the UAM process for

optimizing process parameters for Al 3003, as well as titanium to Al 3003 and has proven an effective method of optimizing mechanical strength [41, 42].

Table 2.1: Taguchi L18 orthogonal array including 18 treatment combinations and three levels (low, medium, high) for each of the four parameters investigated: temperature, weld force, weld amplitude, and weld rate.

Treatment Combination	Temperature	Weld Force	Amplitude	Weld Rate
1	1	1	1	1
2	1	1	2	2
3	1	1	3	3
4	1	2	1	1
5	1	2	2	2
6	1	2	3	3
7	1	3	1	2
8	1	3	2	3
9	1	3	3	1
10	2	1	1	3
11	2	1	2	1
12	2	1	3	2
13	2	2	1	2
14	2	2	2	3
15	2	2	3	1
16	2	3	1	3
17	2	3	2	1
18	2	3	3	2

Table 2.2: Parameter levels for each of the treatment combinations.

Parameter	Level 1	Level 2	Level 3
Temperature	22.2°C (72°F)	93.3°C (200°F)	-
Force	4000 N	5000 N	6000 N
Amplitude	28.28 μm (60%)	30.47 μm (65%)	32.76 μm (70%)
Speed	84.6 mm/sec (200 in/min)	95.2 mm/sec (225 in/min)	105.8 mm/sec (250 in/min)

Welding was performed with a 7 μm R_a surface roughness sonotrode on 16 in. by 16 in. (0.406 m by 0.406 m) aluminum 6061 base plates with varying thicknesses depending on the mechanical test to be performed. Base plates were constrained with a 16 in. by 16 in. vacuum chuck with a built-in heat plate. Aluminum foils 15/16 in. (23.81 mm) wide and 0.006 in. (0.152 mm) thick were utilized for welding in this experiment. Initial pilot studies indicated that certain parameter sets would not weld well to the smooth aluminum baseplate. For this reason, all first layers were welded with the same parameters, which proved to be viable in pilot testing. Weld parameters are given in Table 2.3. It is hypothesized that the lack of first layer bonding for certain parameter sets is due to minimal surface roughness. This hypothesis was investigated further, with results presented in Section 2.3.

Table 2.3: Parameters for first layer welding.

Parameter	Level
Temperature	93.3°C (200°F)
Force	5000 N
Amplitude	32.76 μm (70%)
Speed	84.6 mm/sec (200 in/min)

The weld strips were built onto four baseplates with nine 15/16 in. wide strips welded onto each plate. Temperature was held constant for each plate during welding, either room temperature or 200°F, while the location on the plate was randomized for each parameter set. Two mechanical tests, push-pin and shear, were conducted after the samples were built. For the push-pin samples, 20 layers were welded onto a 0.5 in. (12.7 mm) thick base plate, whereas for the shear samples, 37 layers of material were welded onto a 0.15 in. (3.81 mm) thick base plate. The number of layers built up for each test was based on the final dimensions of the desired mechanical test. Weld strips were built such that four test specimens could be machined from each strip. A baseplate with weld strips is shown in Figure 2.1. Utilization of solid baseplate material in the sample designs reduced the required number of layers, thus expediting the testing.

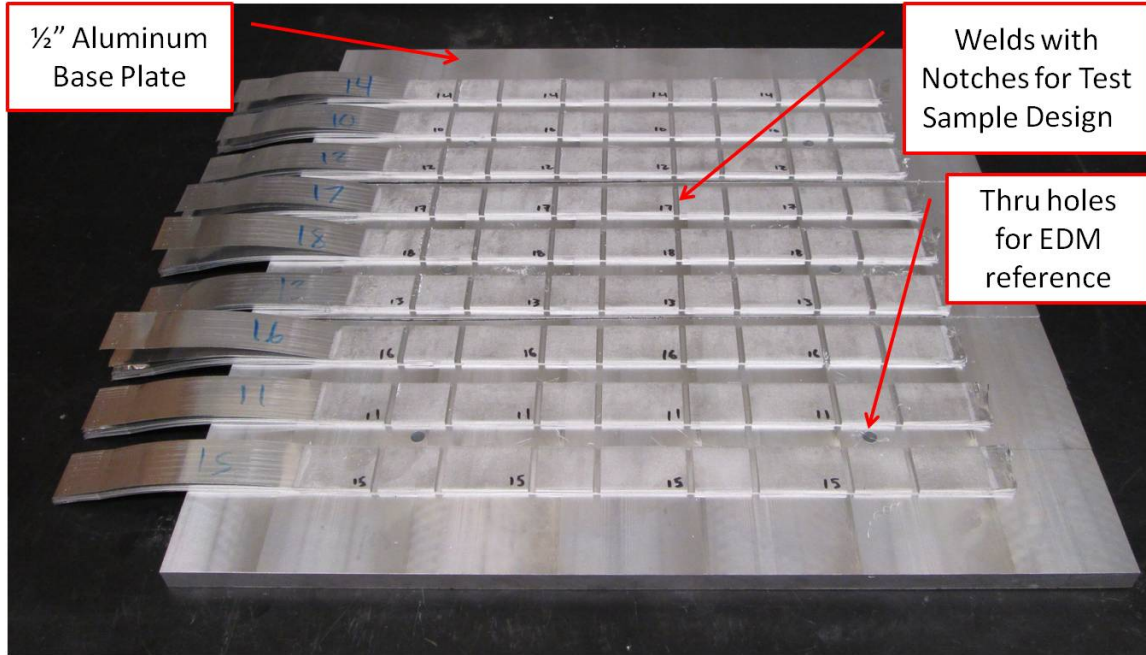


Figure 2.1: Test strips from push-pin sample manufacturing.

After welding, machining was performed using the built-in machining center and external wire electrical discharge machining (EDM). EDM was chosen to partition the samples because it does not introduce large stresses onto the workpiece. After EDM was completed, additional post-machining was performed on a 3-axis mill to final sample dimensions.

Mechanical Characterization

In order to characterize weld performance, out-of-plane delamination resistance and interlaminar shear stress were evaluated. Out-of-plane delamination was evaluated with a push-pin sample while interlaminar shear stress was tested with a custom designed shear sample inspired from ASTM D3165-07. The push-pin sample design

was inspired by Zhang [89] and has been utilized in previous UAM bond assessments [82]. Schematics of the sample designs are presented in Figures 1.13 and 2.2 while sample dimensions for the two tests are given in Table 2.4.

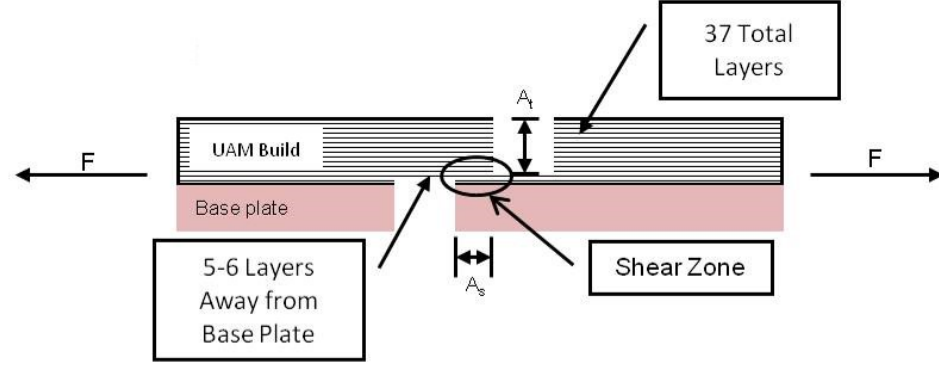


Figure 2.2: Sample design for shear test.

Table 2.4: Sample dimensions for shear and push-pin tests (in mm).

Shear Test		Push-pin Test	
Overall height	9.65	Overall height	15.75
Width	9.65	Width	25.4
A_t	4.826	Notch Width	3.175
A_s	1.6	Pin diameter	10
-	-	Pin depth	13.61

Push-pin testing was conducted on a Gleeble thermal-mechanical system and shear testing was performed on a tensile frame. These machines with detailed test setups are shown in Figure 2.3 and Figure 2.4 respectively. The push-pin samples were manually

positioned close to a mechanical stop which initiates sample loading prior to the start of the test. A pin was then pressed into the sample while load and frame displacement were recorded. A schematic of the push-pin sample is shown in Figure 1.13. All tests were conducted over a travel distance of 10 mm at a rate of 12 mm/min. The manual positioning was done to reduce test time, yet the sample distance from the mechanical stop was not consistent throughout testing. Consequently, samples did not begin to take on load at the same distance for each test. However, this variation in starting distance has no consequence on test results. For shear testing, a load rate of 0.5 in/min (12.7 mm/min) was applied while load and frame displacement were recorded. Load was applied in tension to force a failure along the specified interface. Four samples were tested for both the push-pin and shear tests.

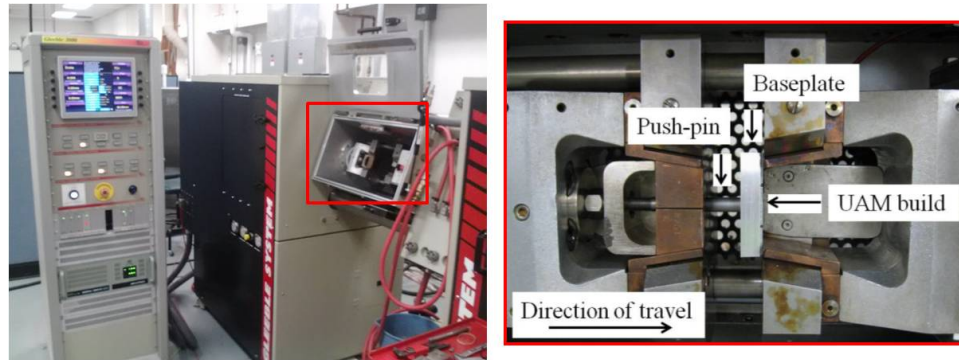


Figure 2.3: Gleeble 3800 thermal-mechanical characterization system utilized for push-pin testing. The boxed area illustrates the key test components.

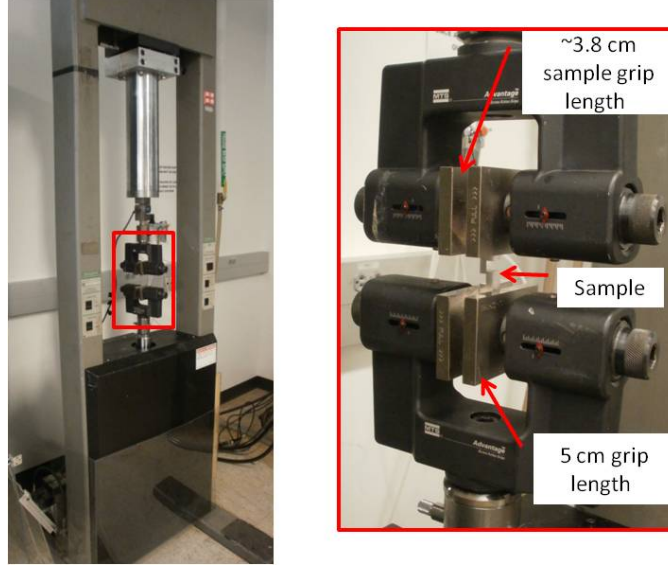


Figure 2.4: Interlaken load frame utilized for shear testing. The boxed area illustrates the key test components.

Statistical Procedures

Following mechanical testing, an analysis of variance (ANOVA) was performed on each set of measurements. The ANOVA is used to test three or more variables for statistical significance within a process. In this case the four parameters listed in Table 2.2 were examined. Main effects plots are then used to indicate the optimal parameter levels for mechanical strength.

The ANOVA uses a generalized linear model with four main effects, with the model equation given by

$$Y_{ijklt} = \mu + \alpha_i + \beta_j + \gamma_k + \delta_l + \epsilon_{ijklt}. \quad (2.1)$$

This linear equation models the dependence of the response variable, Y_{ijklt} , on the levels of the treatment factors [18]. In (2.1), μ is the overall average of the response variable (in this case shear strength or push-pin strength), and α_i , β_j , γ_k , and δ_l represent the effects of each of the process parameters on the mean response. For this study, α_i is the effect of temperature at the i th level on the response while the other factors are fixed. Similarly, β_j , γ_k , and δ_l represent the effects of weld force, amplitude, and weld rate at the j th, k th, and l th levels, respectively, while the other factors are fixed. The error variable, ϵ_{ijklt} , is a random variable with normal distribution and zero mean which denotes any nuisance variation in the response.

2.1.2 Results

2.1.2.1 Push-Pin Testing

Results from two representative push-pin treatment combinations for a poor bond and a good bond are shown in Table 2.5 and Figures 2.5 and 2.6. Complete data sets for the push-pin testing can be found in Appendix A. A poor bond implies that the failure is predominately driven by delamination between layers while a good bond implies that the failure is predominately driven by tensile failure through the layers. Parameter set 4 yields poor bonding and parameter set 9 yields a good bond. Figure 2.5 shows an image of the entire gauge region delaminating, indicating this poor bonding, while Figure 2.6 shows a tensile tearing of layers in a circular pattern consistent with the push-pin dimensions. The failure differences originate from the metallic bond quality because a stronger bond will force the failure progression through the layers while a weaker bond will fail along the joint interface.

Table 2.5: Comparison of push-pin results between parameter sets 4 and 9.

Sample	Set 4 Max Force [kN]	Set 4 Mech. Work [kN*mm]	Set 9 Max Force [kN]	Set 9 Mech. Work [kN*mm]
1	3.56	3.79	3.84	4.94
2	3.03	2.73	3.78	4.50
3	3.08	2.99	3.70	4.74
4	3.27	3.50	3.96	5.44
Mean	3.23	3.25	3.82	4.90
Std. Dev.	0.24	0.48	0.11	0.40

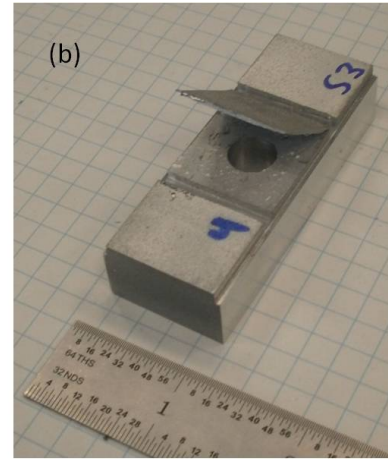
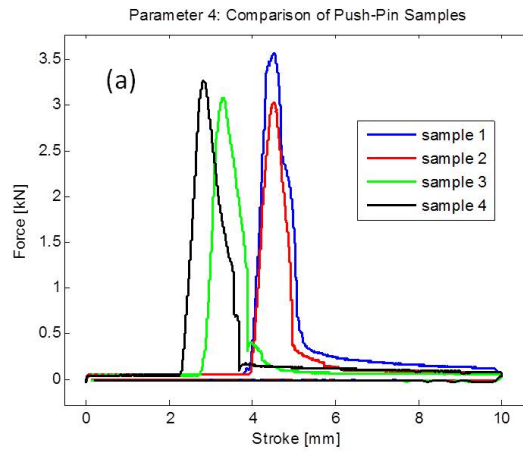


Figure 2.5: Push-pin results for parameter set 4 representing poor interlaminar failure.

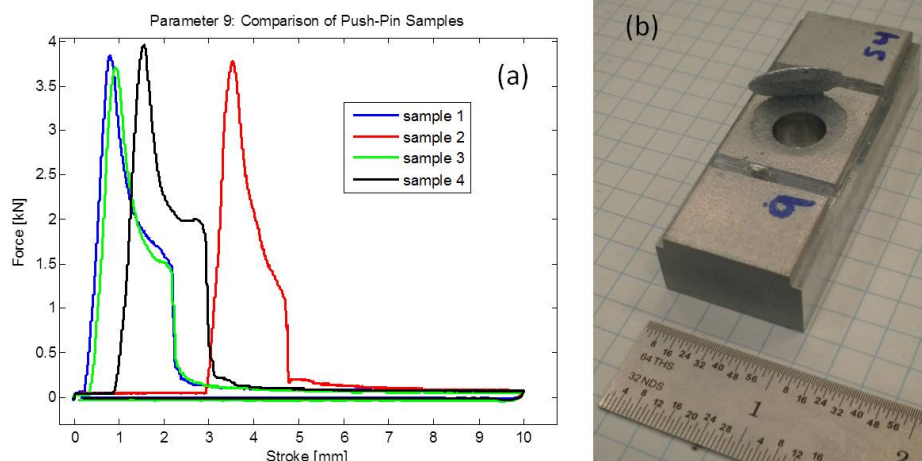


Figure 2.6: Push-pin results for parameter set 9 representing good interlaminar failure.

Although the maximum pushout force during the push-pin test is indicative of bond quality, the mechanical work required for failure is another useful metric, represented by the area under the force-displacement curve [82].

2.1.2.2 Statistical Analysis of Push-pin Testing

An ANOVA study was performed on the results of the push-pin testing utilizing Minitab statistical software. The area under the force-displacement curve, or mechanical work, was used as the response variable. This metric is preferred for the analysis because it provides a good indication of bond quality [82]. ANOVA results are given in Table 2.6. In the analysis, the p-value represents the probability of obtaining a test at least as extreme as the one observed, assuming that the null hypothesis of no trend or no effect is true. Values less than 0.05 were chosen to indicate that a particular source of variation is statistically significant in the process. This means that a source

of variation has a 95% likelihood of being a statistically significant influence on the process. In this case, amplitude and speed are considered significant with p-values of < 0.000 and 0.007 respectively. Both temperature and force have p-values greater than 0.05 and are therefore considered statistically insignificant.

Table 2.6: ANOVA results for push-pin testing with mechanical work as response variable.

Source	DF	Adj SS	Adj MS	F-ratio	p-value
Temperature	1	0.4018	0.4018	0.94	0.337
Weld Force	2	0.3689	0.1845	0.43	0.652
Amplitude	2	19.1955	9.5977	22.39	< 0.000
Weld Speed	2	4.5869	2.2934	5.35	0.007
Error	64	27.4299	0.4286	-	-
Total	71	51.9830	—	—	—

Main effects plots shown in Figure 2.7 visually confirm the ANOVA results. The amplitude plot shows a significant increase in mechanical work with increasing amplitude, while the mechanical work decreases as the speed increases. By comparison, the temperature and force plots indicate very little change in response depending on their level. This indicates that higher mechanical strengths are achieved with increases in amplitude, decreases in speed, and are not dependent on temperature and force within the levels tested in this study.

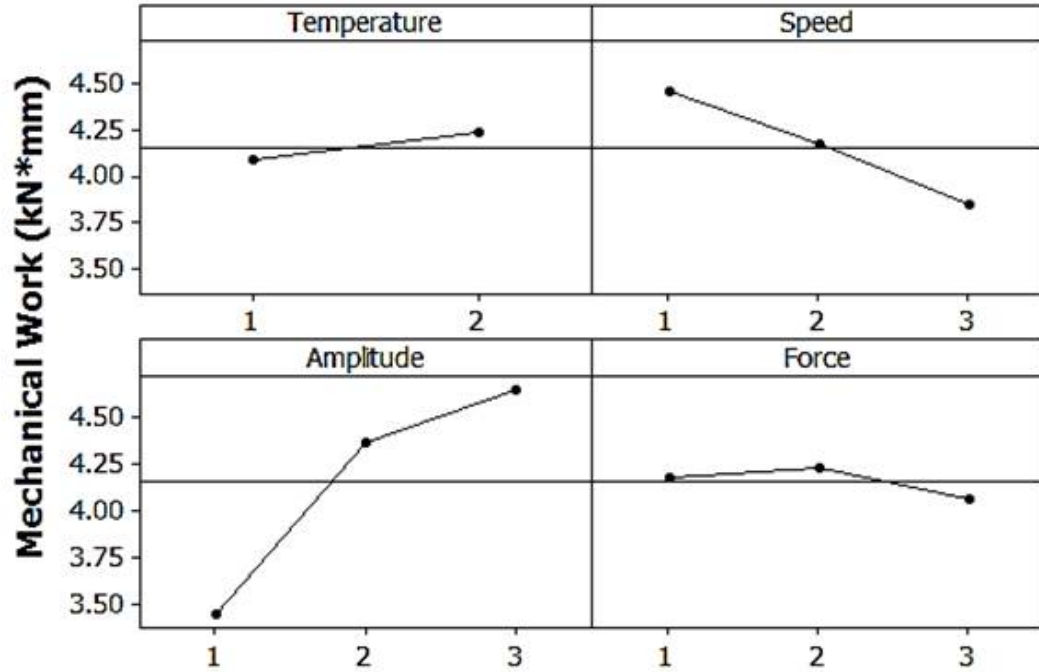


Figure 2.7: Main effects plot of push-pin test for each factor.

The ANOVA test can also be used to quantify interaction effects. Each interaction was investigated, however given the limited degrees of freedom allotted by the Taguchi L18 design matrix, one interaction term was investigated at a time. This investigation (tables not shown for brevity) shows that the temperature-force interaction is the only one that is both significant with $p < 0.001$ and improves the model fit. Overall, the R^2 value for model fit using this interaction is 65%, indicating a relatively good model fit. Figure 2.8 shows the interaction plot between temperature and force. In reading the interaction plot, lines that intersect are an indication of an interaction, whereas roughly parallel lines are indicative of no interaction. The temperature-force plot shown suggests significant interaction at the low force level, with a large difference in

the effect of temperature for the low and medium force levels. However, no interaction is observed at higher force levels, as seen with the roughly parallel curves shown in the interaction plot.

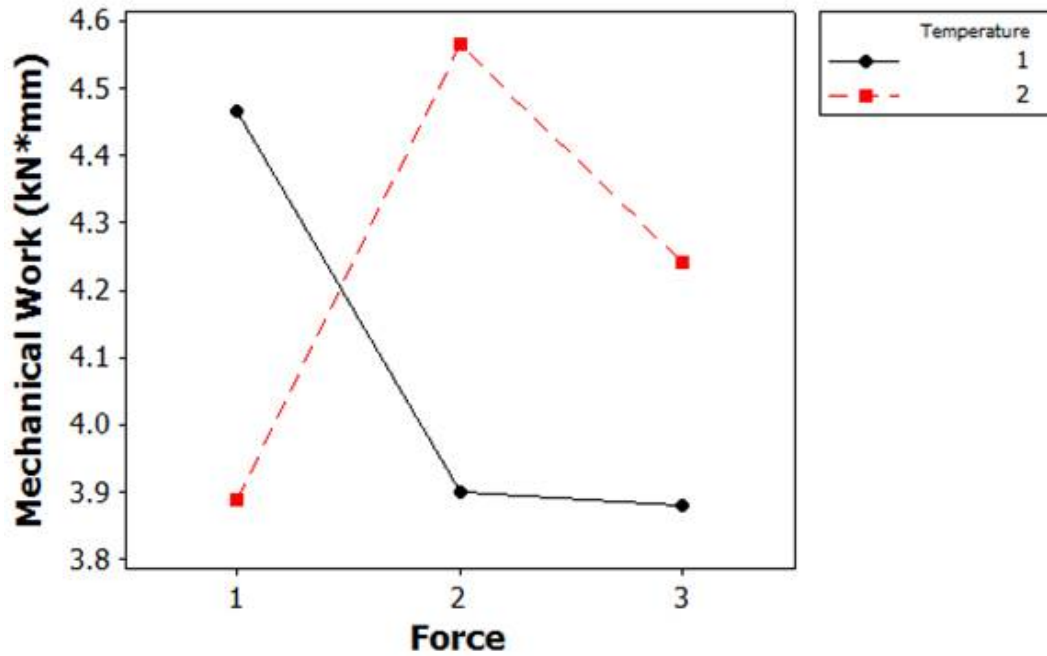


Figure 2.8: Interaction plot of force and temperature for push-pin tests.

2.1.2.3 Shear Testing

The shear tests yielded inconsistent results. A comparison plot for treatment combination 6 is shown in Figure 2.9, while the complete data sets for the shear testing can be found in Appendix A. For this and most other treatment combinations, the ultimate shear stress varies substantially. In certain cases, the failure surfaces provide an indication of the inconsistencies, with higher strength samples failing along a specific interface, while others failed through multiple layers. This is shown in

Figure 2.10. Due to the variability in the data, ANOVA statistical analysis of shear strength testing could not be adequately fit. Attempts at modeling yielded R^2 values of less than 21%. Consequently, these values are not reported. The focus is thus on push-pin data.

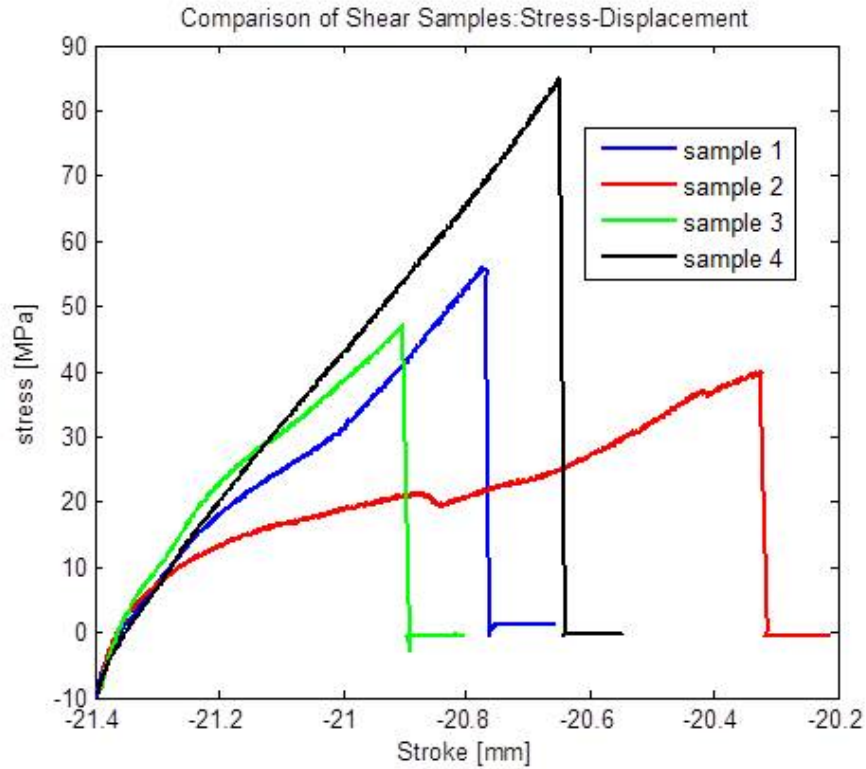


Figure 2.9: Shear strength test results for parameter set 6 showing high variability.

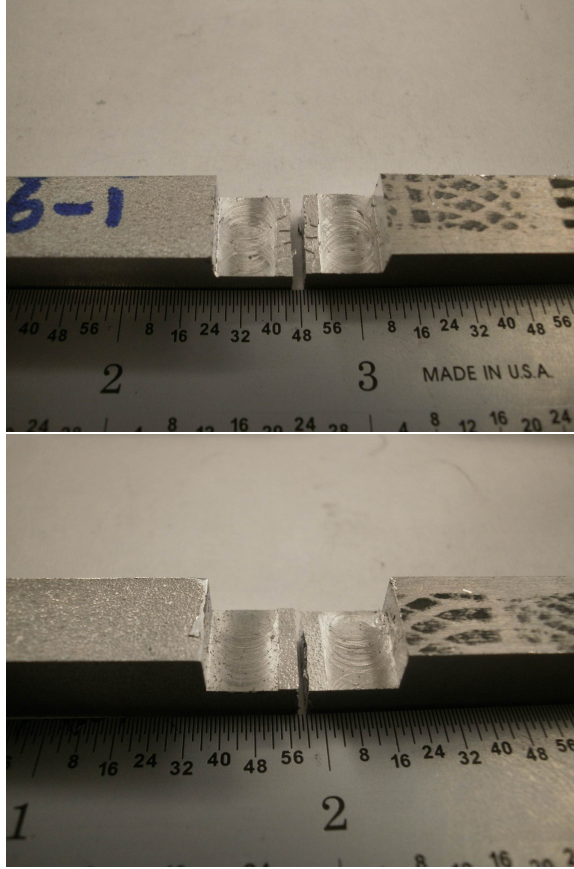


Figure 2.10: Failure surfaces for samples showing failure (a) through multiple layers and (b) through a single layer.

2.1.3 Discussion

Two tests were used in this study, an out-of-plane resistance (push-pin) test and a shear test. The push-pin test was found to yield consistent and informative results that could be modeled with statistical analysis to determine the optimal process parameters for welding Al 6061-H18. A benefit of this technique is that push-pin samples are relatively easy and fast to build, compared to other tests such as out-of-plane tensile tests. This test yields information on the maximum force associated

with failure and the mechanical work (force-displacement) for failure. Although the push-pin test is useful, it has limitations: it is comparative in nature among samples of similar dimensions, cannot be used for comparison with literature values for tensile or shear strength, and entails multiple stress states during failure.

In an attempt to circumvent the limitations of push-pin test data, a shear test was developed to compare against literature values. However, shear testing of UAM samples shows high variability and is prohibitive for statistical analysis. There are a variety of reasons for the data scatter including manufacturing inconsistencies and grip effects. The tests are dependent on the sample dimensions in order to force a failure on a given tape interface. Thus, it is expected that slight variations in sample machining contributes to some of the inconsistencies in the results. Additionally, grip effects are expected to contribute due to difficulties in alignment with the type of grips used in this study. Any misalignment in the test setup could generate a bending load which could also contribute to the data scatter through inconsistencies in the applied stress state on the samples.

Future work could address the issues found with shear tests in this study. An increase in the sample dimensions could decrease the effects of small manufacturing differences by creating more margin of error in the failure loads, however would require more welded layers and therefore time to create the test specimens. A different grip setup could be used to more forcibly grip the samples while alignment plates could be arranged to produce consistent alignment from test to test. With these changes, this test could be useful in the future for comparing the strength of UAM builds to literature strength values.

Nonetheless, sensible ANOVA results were obtained utilizing the push-pin mechanical work response as shown in Figure 2.7 and Table 2.6. As seen in these results, amplitude is the driving and most sensitive variable for a quality weld. This result is expected to be from an enhanced scrubbing action which more effectively disperses oxides and contaminants away from the interface, which in turn improves the strength of the interface by increasing the density of metallic bonding. It cannot be said with confidence if this trend can be extrapolated because defects may be introduced within the structure at higher amplitudes. Yet this variable appears to have a critical correlation with the mechanical strength of UAM builds within the levels tested.

Speed was also found to have a statistically significant effect on strength. A slower speed allows additional time for scrubbing of the interface and therefore increased ultrasonic energy is supplied to the interface. As a result, enhanced dispersion of oxides and contaminants at the interface can be achieved by decreasing the weld speed. Similar to the amplitude observation, it is not known if there will be a point of diminishing returns for decreases in speed.

Temperature was not found to be a significant factor influencing mechanical strength under the conditions tested. Increases in temperature decrease the material flow stress, increasing plastic deformation [62]. However under the current conditions, the differences in temperature tested are relatively insignificant in changing the yield stress of aluminum. Figure 2.11 shows a plot of the yield strength versus temperature for Al 6061 indicating that significant differences in yield strength do not occur until approximately 125°C [3]. The bond quality of UAM structures could therefore depend more heavily on temperature at higher temperature values. Differences in

annealed vs. as-received material as well as changes in strain rates will also change the dependence flow stress on temperature [62]. Therefore temperature could play a more significant role at higher levels or under different material process conditions.

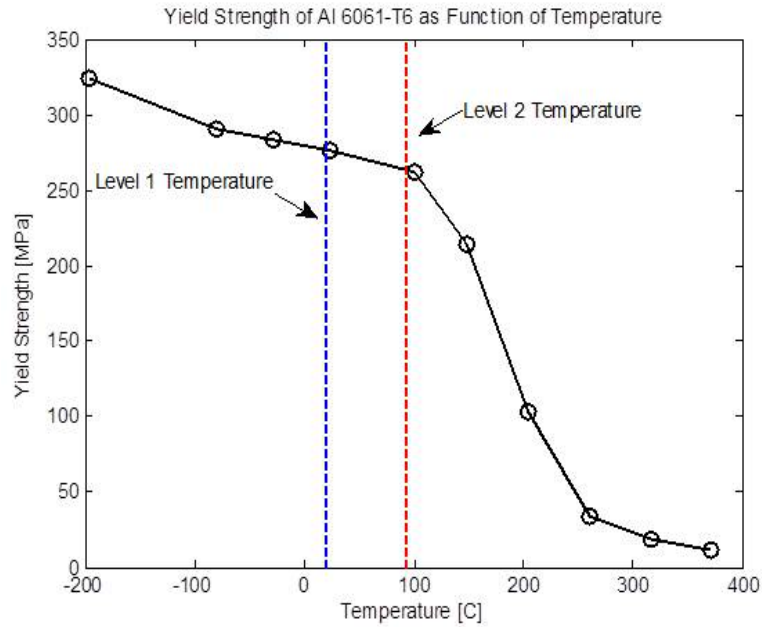


Figure 2.11: Yield strength versus temperature for Al 6061 with temperatures utilized indicated [3].

Finally, weld force was found not to be significant within the range of investigation. This result is inconsistent with previous findings from samples manufactured on other UAM equipment [42]. A couple aspects of the process can be considered, the first of which is asperities. It is possible that force is not influential because asperities have reached a maximum compression point and can no longer collapse to generate bonding. This would indicate that the real contact area between the foils is equal to the nominal contact. A second possible factor is the load range. Previous studies

analyzed much lower loads compared to the loads studied here. Thus, it is possible that load plays a much larger influence in weld quality at lower values. Finally, the loads compared by Hopkins et al. were within a much closer range, with levels varying 200 N. It is possible that the variation in the normal force during the weld process is greater than the variation between levels, and therefore the determination of normal force as a significant factor is an artifact of the statistical analysis of the data used.

In conclusion, it was found that amplitude and speed significantly influence weld quality whereas load and temperature do not exhibit statistical significance within the range of study. After consulting the push-pin statistics, an optimal treatment combination was identified as tabulated in Table 2.7. This treatment combination is composed of levels evaluated in this study.

Table 2.7: Optimal weld parameters for Al 6061-H18 as determined by analysis of push-pin tests.

Parameter	Level
Temperature	RT to 93.3°C (200°F)
Force	4000-6000 N
Amplitude	32.8 μm (70%)
Speed	84.6 mm/sec (200 in/min)

2.2 Foil Stacking Sequence Study

2.2.1 Experimental Methods

In this study, UAM builds were constructed to investigate the effect of tape to tape overlap and stacking sequence on strength. Al 6061-H18 foils, 0.006 in. (0.152 mm) thick, 1 in. (25.4 mm) wide were used; built onto an Al 6061-T6 baseplate. The

weld parameters used for the builds follow previously optimized parameters for Al 6061, presented in Section 2.1 [87] and shown in Table 2.8. All builds were performed at room temperature using a $7\text{ }\mu\text{m}$ R_a roughness sonotrode.

Table 2.8: Weld parameters for UAM builds.

Weld Parameter	Level
Normal Force	5000 N
Amplitude	$32.8\text{ }\mu\text{m}$
Weld Speed	200 in/min (84.6 mm/s)

Two build plates were used to investigate the overlap and stacking, with each of the sample sets summarized in Table 2.9. In plate 1, the stacking remained constant while the tape to tape overlap (α in Figure 1.10) was varied from 0.0015 in. (0.038 mm) to 0.0045 in. (0.1143 mm). In the SonicLayer system, this is achieved by using a constant 1 in. (25.4 mm) wide tape and setting the tape width to varying levels. Tape placement is controlled through the CNC stage of the machine, allowing for tolerances of 0.0005 in. ($12.7\text{ }\mu\text{m}$), with some additional variation due to the foil feeding mechanism in the system. Foil width is held to similarly high tolerances from the supplier.

The specified tape overlaps were selected at levels which provide overlap while minimizing flash, or excess material, at the abutment points. The ordered stacking sequence followed a 0,1,0,-1... sequence as shown in Figure 1.10. The amount of stagger is described by β as shown in Figure 1.10. In plate 2, the tape overlap was held constant while the stacking sequence was varied. Samples A and B were built using similar 0,1,0,-1,0 ordered stacking sequences with varying amounts of

stagger. Build C used random stacking with a maximum stagger value of $\beta = 0.3$ in. (7.62 mm). Build D used ordered stacking with 50% stagger from tape to tape. Stacking sequences were selected such that both randomized and ordered sequences were investigated and the entire design space of stagger values was covered.

Table 2.9: Overlap and stacking sequence prescribed for each sample set.

Sample Set	Overlap (in.)	Stacking Sequence (β in.)
1A	0.0015	Ordered with $\beta = 0.15$
1B	0.0025	Ordered with $\beta = 0.15$
1C	0.0035	Ordered with $\beta = 0.15$
1D	0.0045	Ordered with $\beta = 0.15$
2A	0.003	Ordered with $\beta = 0.1$
2B	0.003	Ordered with $\beta = 0.15$
2C	0.003	Random with $\beta = 0.3$
2D	0.003	Ordered with $\beta = 0.497$ (50% stagger)

Tensile samples were sectioned from the blocks using the CNC stage on the machine following ASTM subsize tensile sample dimensions [45] such that testing occurs across the various tape interfaces, transverse to the welding direction. Examples of samples used in the testing are shown in Figure 2.12. Tensile tests were performed on a 22 kip (98.7 kN) Interlaken 3300 test frame, using a displacement rate of 0.05 in/min (1.27 mm/min) while recording the load to failure.

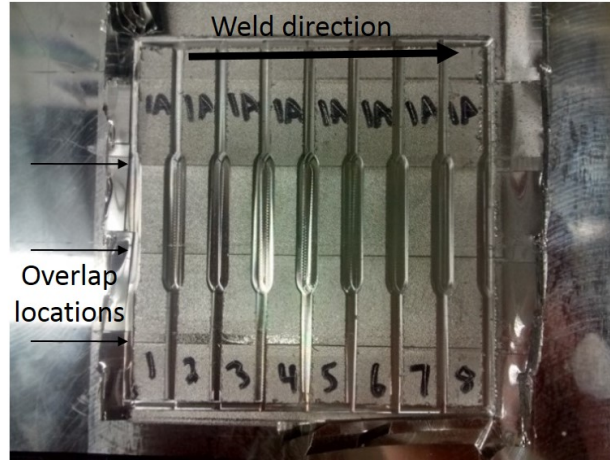


Figure 2.12: Tensile samples machined from UAM build block.

2.2.2 Results

The test results are summarized in Table 2.10. From the results of Plate 1, there is a clear delineation between the first two samples (A-B) and the last two samples (C-D), with samples C and D producing strengths of approximately 210 MPa on average vs. 125 MPa for samples A-B. Results of test data from Plate 2 indicate that sample C resulted in the highest tensile strength, 222.5 MPa on average, compared to the other samples. The elongation results show similar trends, with samples 1C and 1D producing much higher elongation on average than 1A and 1B. Sample 2C also provides the highest elongation to failure among samples from Plate 2.

Table 2.10: Tensile test results for overlap and stagger study builds showing ultimate tensile strength and elongation at failure.

UTS (MPa)								
	1A	1B	1C	1D	2A	2B	2C	2D
	133.1	121.7	202.3	227.1	225.5	185.1	221.7	184.2
	117.7	129.8	214.7	178.8	177.5	196.3	223.9	163.7
	124	144.2	211.4	228.2	185.1	167.7	222	153.6
Mean	124.9	131.9	209.5	211.4	196	183	222.5	167.2
St Dev	7.7	11.4	6.4	28.2	25.8	14.4	1.2	15.6

Elongation (%)								
	1A	1B	1C	1D	2A	2B	2C	2D
	1.15	2.12	5.26	6.76	6.18	4.95	5.79	4.24
	1.13	3.04	5.93	4.85	4.26	4.72	5.23	4.09
	1.08	3.08	6.05	6.34	4.94	4.82	5.06	4.42
Mean	1.12	2.75	5.75	5.98	5.13	4.83	5.36	4.25
St Dev	0.04	0.54	0.43	1	0.97	0.12	0.38	0.17

Optical microscopy shows that voids are found in increasing numbers for the sample sets with lower strengths. Figure 2.13(a-b) shows images of sample 1B where voids are present, while Figure 2.13(c) shows sample 1D and no voids present. The stacking type voids were found in both samples 1A and 1B. The propensity for void formation in sample sets with low overlap, is expected to significantly decrease the mechanical strength of the builds. While significant voids were not found in samples on plate 2, it is expected that weak points may exist at the areas of tape to tape layup and that the propagation of cracks through these weak points leads to decreased strength. Previous work has also shown that void content alone is not a sufficient metric for characterizing bond strength [42], supporting this hypothesis. Sample 2C exhibited the highest strengths in this study and is likely due to a hindrance of crack

propagation through adjoining weak points in the material by creating a tortuous crack path.

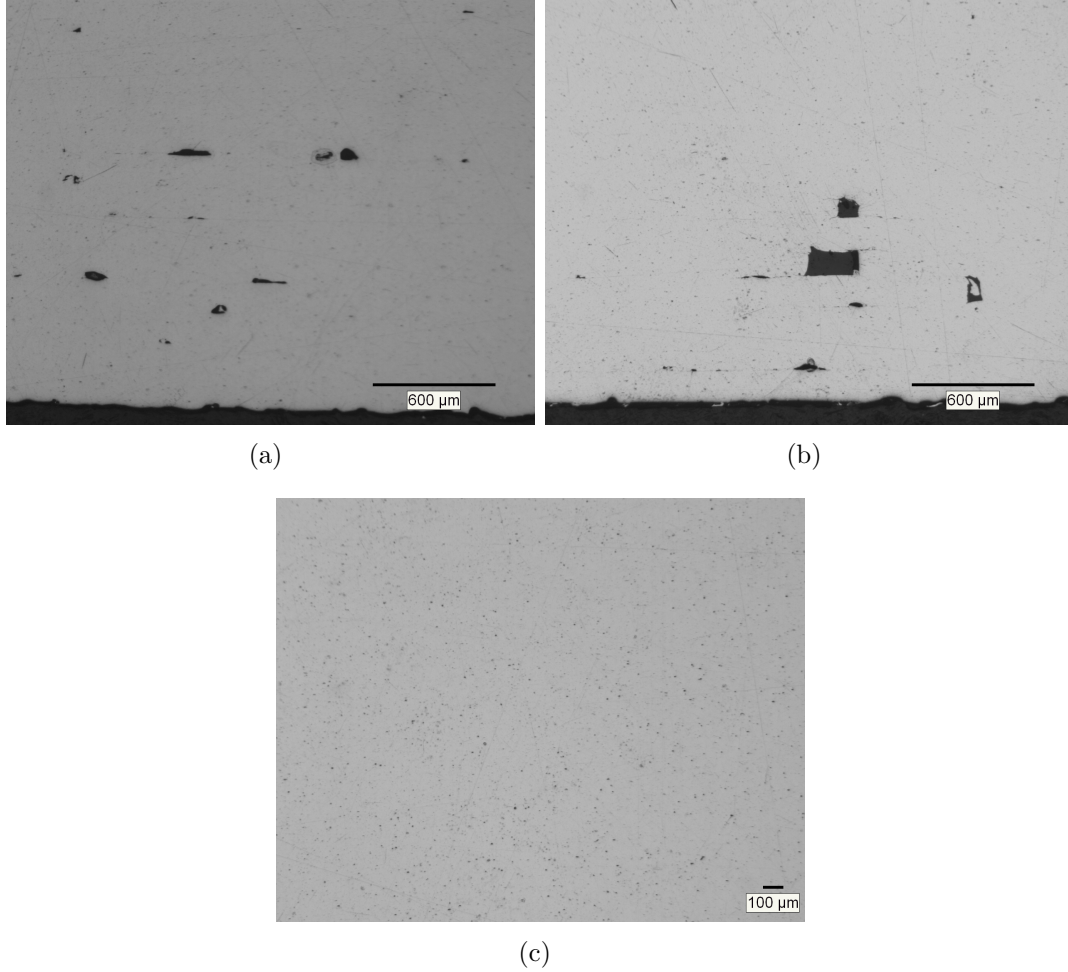


Figure 2.13: (a) (b) Cross sections of UAM builds showing voids in Sample 1B and (c) cross sections of sample 1D with no voids.

2.2.3 Discussion

Based on the test results it is recommended that for UAM block builds, a tape to tape overlap of at least 0.0035 in. (0.0889 mm) be used and that the stacking

sequence follow a random stacking with maximum stagger of 0.3 in. (7.62 mm). The optimal overlap value of at least 0.0035 in. is approximately half the height of the original foil thickness (0.006 in.). This could represent a threshold value whereby the plastic deformation of the foil is able to completely fill the void at the abutting area. Further work using varying thickness foils could be performed to test this hypothesis.

Randomized stacking is shown to produce the highest strength results. It is hypothesized that this is due to a more tortuous crack propagation path. If the abutting points are assumed to be the crack initiation points, failure in the ordered structure would require transmission through only a single layer at a time. In the randomized case, instances of the failure would have to traverse multiple layers, leading to a more complete crack arresting mechanism.

Tape to tape overlap results are consistent with those found by Obielodan et al. in 1 kW UAM [66], which recommend use of overlaps of at least 0.00275 in. (0.07 mm). Stacking sequences recommended by Obielodan et al. use a 50% stagger, however only two stacking methods were investigated, while the study presented here investigated four separate stacking sequences. Of note, these recommendations are based on the testing performed here. A globally optimal value may be achieved through further optimization of these parameters. The recommended stacking sequence proposed is based on the findings from sample 2C, indicating that randomized stacking should be used. However, the magnitude of the proposed stagger may not scale in taller builds where tape flash at the build edge creates areas of poor support leading to inconsistent welds at the build edge. This effect can propagate inward as a build progresses higher, making further welds near the edges difficult. In such circumstances, a random stacking pattern with smaller stagger should be used.

2.3 Effect of Surface Roughness on Build Quality

2.3.1 Experimental Methods

2.3.1.1 Weld Surface Roughness

To study the texture of flattening passes and their effect on UAM strength, builds were conducted with welds onto smooth, freshly machined surfaces and welds onto roughened surfaces. Flattening passes were performed using a carbide insert shell mill within the CNC stage of the UAM machine which creates a smooth surface. Roughened surface samples were built onto surfaces which were textured by vibrating the sonotrode at a low amplitude, similar to welding operations. The roughness of the machined surface is $0.12 \mu\text{m } R_a$ and the roughened surface is $5.7 \mu\text{m } R_a$, measured with a Mitutoyo mechanical probe profilometer. The builds contained flattening passes every third layer, starting at the fifth layer. Each build consisted of 20 total layers such that five flattened surfaces were introduced into each build. All builds were constructed onto a 0.5 in (12.7 mm) thick Al 6061-T6 baseplate with Al 6061-H18 foils 1 in. (25.4 mm) wide and 0.006 in. (0.1524 mm) thick. Weld parameters follow those listed in Table 2.8.

Sample strength was measured via push-pin testing to compare delamination strength and resistance. The measurements in this study were conducted using a Gleeble 3800 thermomechanical frame at room temperature while measuring both push-out force and machine displacement. Mechanical work or energy (force-displacement) was then calculated from the results and used in evaluation of UAM bond strength.

2.3.1.2 Sonotrode Roughness

A second study was performed to determine the effect of sonotrode roughness on weld quality. In this study, samples were fabricated using sonotrodes of 7 μm and 14 μm R_a roughness, respectively. Both sonotrodes were textured with electrical discharge machining to create the desired surface profile. Two 12 in. (30.5 cm) long, 1 in. (25.4 mm) wide build strips 20 layers tall were constructed using each sonotrode, each with identical weld parameters as those listed in Table 2.8. The strips were built onto a 0.5 in. (12.7 mm) thick Al 6061-T6 baseplate, yielding eight total push-pin samples. One of the 7 μm roughness samples was damaged during machining, therefore 15 total samples were tested in this study.

The UAM weld parameters of speed, normal force, and temperature are not a function of welder dynamics during welding. However, weld displacement is a function of welder dynamics due to small amounts of compliance in the sonotrode during welding. To ensure that weld motion was the same for each sonotrode, a Polytec laser vibrometer was utilized to measure velocity during welding operations. Velocity measurements were made at the second layer of each stack and are shown in Figure 2.14. As is shown, peak weld velocity is similar amongst the stacks. Black dashed lines show the approximate bounds of the measurements for comparison purposes. This indicates that the vibration amplitude for the two sonotrodes tested is the same for each set of tests.

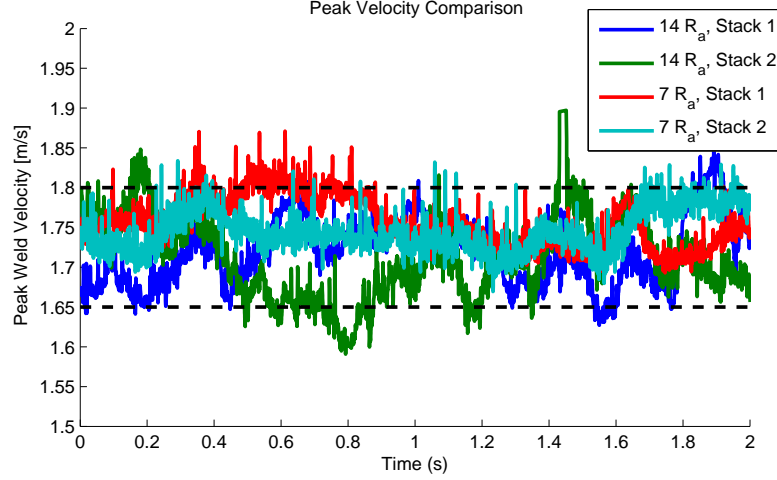


Figure 2.14: Peak weld amplitude measurement under load during welding. Measurements were taken at the second layer of each stack. Similar weld amplitude levels were utilized to weld all the stacks.

2.3.2 Results

2.3.2.1 Weld Surface Roughness

Push-pin test results are provided in Table 2.11. Of note, one textured sample was damaged during test setup and was not tested. The mean peak force for the textured samples (4.42 kN) is similar to the non-textured samples (4.45 kN). However the mechanical work, or energy, of the textured samples shows a difference. The non-textured samples exhibited an average push-out energy of 5.51 kN-mm compared to 4.75 kN-mm for the non-textured samples. In addition to strength improvements, textured samples produce more consistent weld properties than non-textured samples. As shown in Table 2.11, the push-out energy standard deviation for the textured samples is 0.17 whereas the non-textured sample standard deviation is 0.80.

Table 2.11: Push-pin data for textured and nontextured builds.

Sample	Textured		Non-Textured	
	Peak Force (kN)	Energy (kN*mm)	Peak Force (kN)	Energy (kN*mm)
1	4.66	5.32	4.28	3.82
2	4.18	5.47	4.66	5.50
3	4.42	5.74	4.51	5.58
4	-	-	4.35	4.11
Mean	4.42	5.51	4.45	4.75
St Dev	0.20	0.17	0.15	0.80

2.3.2.2 Sonotrode Roughness

Push-pin results comparing the two sonotrode roughnesses are shown in Figure 2.15 and Table 2.12. As seen in the figure and table, the 14 μm samples exhibit a larger peak force than the 7 μm samples. On average, the 14 μm samples yield an average peak force of 5.8 kN while the 7 μm samples have an average peak force of 4.9 kN. The pushout energy is likewise slightly higher for the 14 μm samples vs. the 7 μm samples.

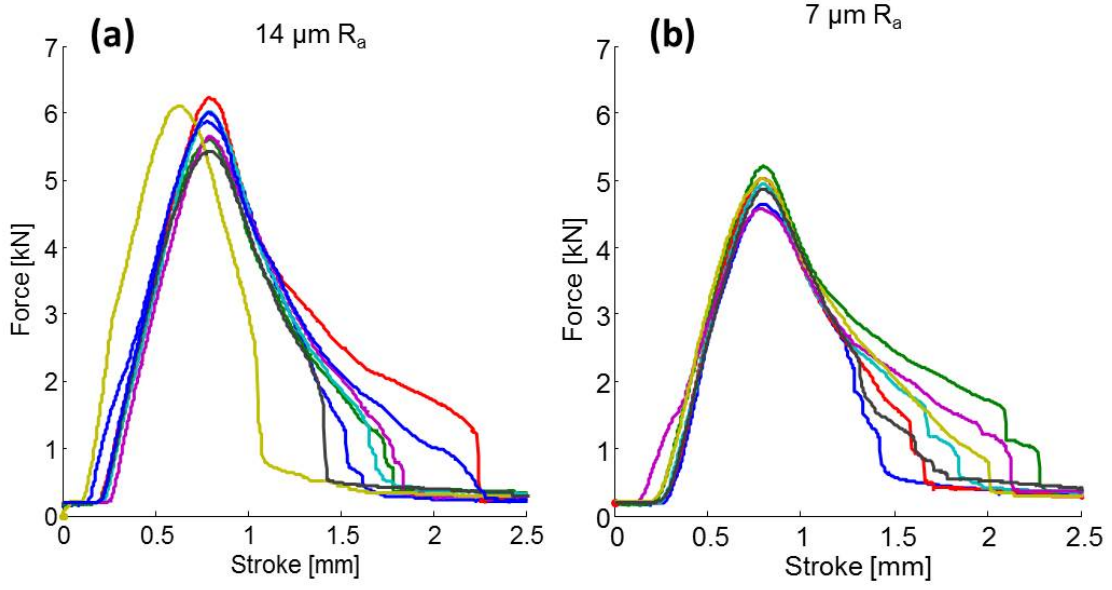


Figure 2.15: Push-pin results: (a) $14 \mu\text{m } R_a$; (b) $7 \mu\text{m } R_a$.

Table 2.12: Averaged results of push-pin testing with varying roughness sonotrodes.

7 μm Roughness		14 μm Roughness	
Max Force (kN)	Energy (kN-mm)	Max Force (kN)	Energy (kN-mm)
4.9	7.3	5.8	7.7

Cross sections of builds from each of the sample sets are shown in Figure 2.16. The baseplate and first welded layer are present in each of the sections. Since the baseplate is Al 6061-T6, it has a slightly different appearance than the welded layers. As is seen, each of the samples appears voidless. The difference in roughness at the baseplate layer is apparent in each of the samples with more roughness shown in the $14 \mu\text{m}$ sample.

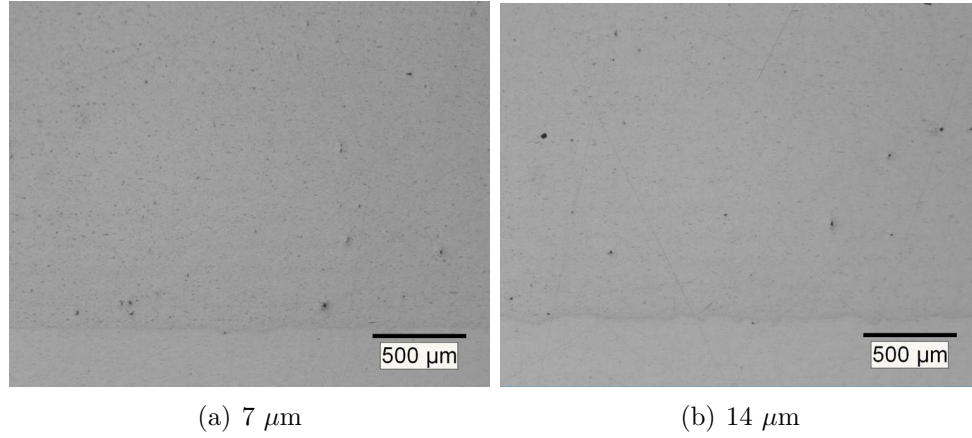


Figure 2.16: Cross section of UAM builds with 7 μm and 14 μm roughnesses.

2.3.3 Discussion

The improvements in weld properties due to surface texturing are believed to originate at the weld interface. It is hypothesized that the increased surface roughness after texturing enhances asperity deformation during welding leading to increases in plastic deformation, oxide dispersal, mixing, and the driving force for dynamic recrystallization. In combination, these factors increase the potential for grain growth across the bond interface leading to improved metallurgical bonding [19]. To further investigate this phenomenon, in depth characterization of the grain structure at the interface will be required.

Based on the push-pin testing, enhanced bond quality can be achieved using a 14 μm R_a roughness sonotrode compared to a 7 μm R_a sonotrode. Li and Soar also noted that rougher sonotrode surfaces produced better bonds using the same UAM processing settings [55]. However, they also reported that rougher surfaces increase the void concentration at weld interfaces. As seen in Figure 2.16, the larger weld

amplitudes and down force of 9 kW UAM eliminates interface voids. However, it is suspected that interface voids can still form during UAM if sonotrodes rougher than $14\text{ }\mu\text{m } R_a$ are used or if lower weld amplitudes and normal forces are utilized. Consequently, selecting an optimal surface roughness for a given material or UAM welding application may be needed, as discussed by Friel et al. [25].

The improved bond quality associated with rougher surfaces is likely to originate in the consolidation at the interface, similar to the effect seen in roughened vs. smooth surfaces. Due to the asperities being larger, more plastic deformation may occur, which would enhance the bonding mechanisms of oxide fracture, dispersal, and increase the driving force for dynamic recrystallization. Push-pin testing showed a greater difference in the peak force of the samples compared to the push-out energy. It is suspected that peak force during push-pin testing is enhanced from the $14\text{ }\mu\text{m}$ sonotrode roughness because it increases the resistance to initial crack formation, while push-out energy is unaffected because it is a measure of the resistance to crack propagation. Further work using mechanical testing and microscopy is required to understand the failure energy differences.

Reporting the magnitude of surface roughness is only part of the surface profile. The statistical distribution of the surface profile is also important. However, this statistical distribution was not extensively measured for the UAM sonotrodes in this study. Further work may be required to understand the influence of asperity distribution on UAM build properties. Also, it may be required to include asperity magnitude and distribution information to more rigorously characterize UAM horn performance. Further the orientation of the weld surface asperities could be of interest, specifically when considering the characteristic texture exhibited after machining operations.

2.4 Post-Process Heat Treating Al 6061 UAM Builds

Previous work has indicated that certain post-process heat treatments can be beneficial for mechanical strength through alterations of material microstructure [75, 82, 87]. In work by Wolcott et. al [87], annealing was performed on samples which were tested using push-pin testing. Results showed strength increases compared to as-built samples. Because Al 6061 is an age-hardenable material, heat treatments can be used to maximize mechanical strength. The objective of this work is to investigate the tensile strength of as-built UAM samples, annealed samples, and samples aged to the T6 condition.

2.4.1 Experimental Methods

To test the effects of heat treatments on out-of-plane UAM tensile strength, a 0.8 in. (20.32 mm) tall UAM block was fabricated using Al 6061-H18 foils 1 in. (25.4 mm) wide and 0.006 in. (0.1524 mm) thick. This build was constructed using the weld parameters in Table 2.8 with a 7 μ m horn, and did not use tape to tape overlaps or flattening passes. From this block, nine cylindrical samples were sectioned using wire EDM avoiding any seam locations. Three samples were annealed, three were treated to a T6 condition, and three samples were tested as-built. Selection of the heat treated samples was randomized along the length of the weld. The specific heat treatment temperatures and settings are summarized below.

For annealing (O): Heat to 413 °C for 2.5 hours, cool at 1 °C/min until 280 °C, then air cool [2]. For T6: Heat to 530 °C for 1 hr to solutionize, quench in water, heat to 160 °C for 18 hours [2]. H18: indicates an as-built condition.

Following heat treatment, samples were machined via CNC lathe to final dimensions for tensile testing. The dimensions for the specimens are based on ASTM standards [45]. Machined specimens were then tested in tension using a 22 kip (98.7 kN) Interlaken 3300 test frame with displacement rate of 0.05 in/min (1.27 mm/min).

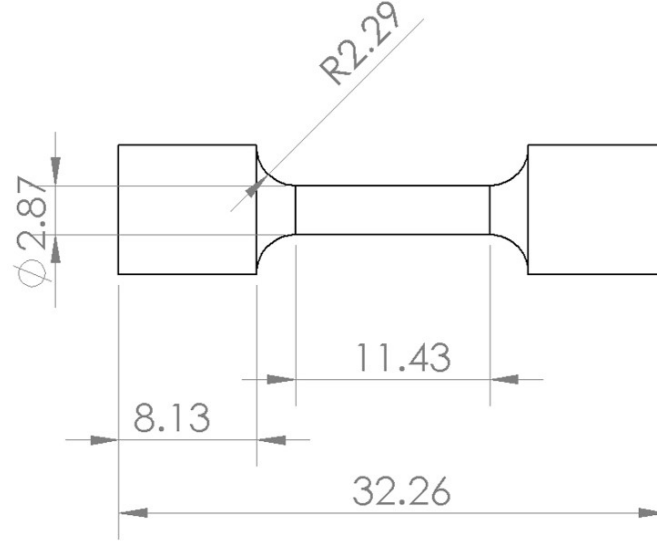


Figure 2.17: Dimensions of tensile specimens (in mm).

2.4.2 Results

Out-of-plane ultimate tensile test results are summarized in Table 2.13. Three tests were performed for each set, though one T6 sample was damaged during test setup. As is shown, the T6 heat treated samples show significant strength increases compared to the as-built samples. In Table 2.14, fractional comparisons to initial foil stock in each of the H18, T6, and O conditions are presented. H18 comparisons used as-received stock tested in tension with no heat treating, while foils for the annealed

and T6 references were processed using the same heat treatment as the samples from the UAM block build and tested. Of note, the elongation values provided are not exact as they represent deflection of the entire load frame measured by the linear variable differential transformer (LVDT). However, the given displacement values can provide useful comparative evaluations. Use of an extensometer was not possible due to the small sample size of the specimens.

Table 2.13: Ultimate tensile strength results for as-built and heat treated UAM samples.

Group	UTS (MPa)	% Elongation
H18	141.7	1.65
H18	123.8	1.1
H18	141.2	1.35
T6	296.8	14.98
T6	303.7	11.26
O	129.2	15.27
O	97.8	6.2
O	124.4	19.7

Table 2.14: Comparison of UAM samples with solid material references.

Group	Avg. UTS (MPa)	Avg. Elo. (%)	Ref. UTS (MPa)	Ref. Elo. (%)	UTS (%)	Elo. (%)
H18	135.6	1.4	266.1	3.1	51	45
T6	300.3	13.1	337.3	12.5	89	105
O	117.1	13.7	121.1	18.6	97	74

Optical microscopy images of a T6 heat treated and as-welded UAM sample are shown in Figure 2.18. The microstructure in each case shows indications of precipitates, typical in Al 6061, with the dark colored precipitates Mg_2Si and the lighter precipitates AlFeSi intermetallics. These precipitates are the primary strengthening mechanism in Al 6061. As can be seen, significantly more precipitates are present in the heat treated sample, compared to the as-welded sample. The increased presence of precipitates is expected to increase the strength of the samples significantly, consistent with mechanisms present in solid material [77]. Further work at higher magnification is necessary to fully characterize the precipitate volume fractions, but these initial studies indicate that the T6 treatment significantly increases the number of strengthening precipitates.

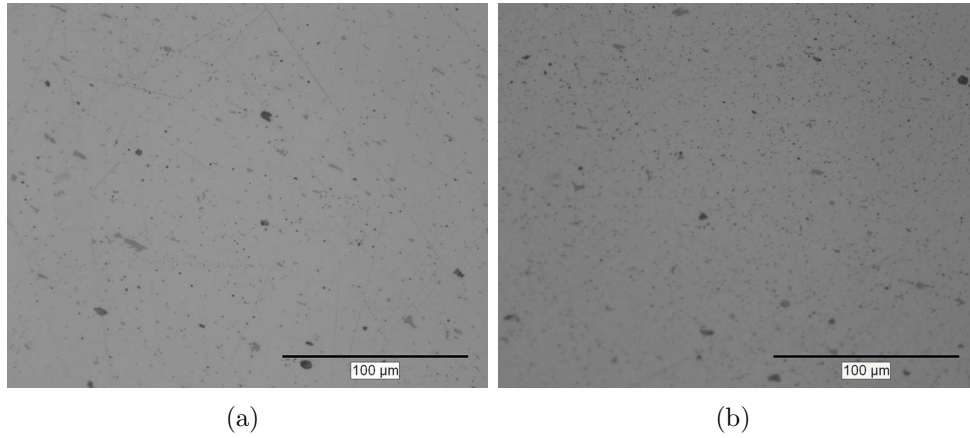


Figure 2.18: Microstructure showing precipitate density of (a) T6 heat treated and (b) as-built sample.

2.4.3 Discussion

The following comments can be made for each of the heat treatment groups:

- H18: For the as-welded group, there is a 50% decrease in strength and a 62% decrease in elongation when compared to the initial Al 6061-H18 foil stock. The decrease in elongation is somewhat expected due to the cold working effect imparted during the UAM process. The decrease in strength, while substantial, is a significant increase over samples made via 1 kW UAM which exhibited strengths on the order of 15% of the parent material [42]. Implementing concepts of periodic flattening passes, rougher sonotrodes, and using recently developed power control concepts [37] could further increase this as-welded UAM build strength.
- T6: The T6 group shows very promising results when compared to homogeneous Al 6061. The T6 condition is the most common form of Al 6061, so the ability to produce welded components with the same temper and mechanical properties is an important benchmark for UAM. Strength of the UAM composites is 89% of the heat treated foil, and the elongation is roughly 105%. While the strength does not exactly match solid material, these metrics show that near T6 properties of UAM composites can be achieved through post process heat treatments.
- Annealed (O): This group, similar to the T6 group, shows promising results when compared to the annealed foils. The strength is 96% of the annealed foil and the elongation is 74%, with a potential outlier failing at 6.2% elongation accounting for the decrease in elongation.

Overall, results indicate that the mechanical properties of UAM structures can be enhanced considerably when a post process heat treatment is applied. These heat treatment results coincide well with the microscopy work of others in Al 3003. In particular, Sojiphan et al. [75] observed that the recrystallized grain structure at weld interfaces in optimized aluminum UAM builds was very stable after heat treating. This stable microstructure results in less defects and defect nucleation sites, which, in turn improves mechanical properties. It was also observed that significant recrystallization and grain growth occurred in the bulk weld foil after heat treating. Heat treating also enhances precipitate distribution and concentration in Al 6061 as shown in Figure 2.18. Consequently, strength improvements are suspected to be a combination of improved precipitate density and microstructure stability. Mitigation of residual stress is also a likely mechanism for strengthening, which is examined in more detail in Chapter 3.

2.5 Summary

Studies were conducted investigating improvements to the UAM process. An optimal stacking and overlap sequence for builds larger than the tape width is proposed which uses random stacking and a tape to tape overlap of at least 0.0035 in. (0.0889 mm). Investigations of the effect of surface roughness on build strength indicate that imparting a roughness on the order of the sonotrode roughness can increase mechanical strength compared to an as-machined (smooth) surface roughness. Use of 14 μm R_a roughness sonotrodes show an improvement in mechanical properties compared to welds made using a 7 μm R_a sonotrode. Heat treatments performed after joining were shown to provide significant increases in mechanical strength with tensile strengths

for the T6 condition approaching 90% of solid material. These improvements are suggested to maximize the strength of future builds, where applicable.

Recommendations for Al 6061-H18 UAM block builds:

- Tape overlap >0.0035 in. (0.0889 mm)
- Random stacking sequence with maximum overlap of 0.3 in. (7.62 mm)
- Conduct surface roughening where applicable
- Utilize 14 μm R_a roughness sonotrode
- Post-process heat treatments to the T6 condition provide the highest tensile strength and should be used when possible

Chapter 3: ANALYSIS OF STRENGTH REDUCTION DUE TO PROCESS INDUCED STRESSES IN UAM BUILDS

This chapter discusses potential causes for low strength in UAM builds, with specific investigation of UAM builds which were created using the improvement studies outlined in Chapter 2. The mechanical strength of the builds was significantly lower than expected, prompting an in depth investigation of the cause. Modeling was conducted to investigate the stresses from UAM applied loads and sonotrode contact conditions. In addition, microstructural investigations were performed to measure the plastic strain due to the UAM process.

3.1 Optimized Builds and Strength

Following the results of optimizing UAM build conditions shown in Chapter 2, builds were constructed to measure their mechanical strength. Optimization concepts used include weld parameters from the DOE study, optimized foil overlap, roughness imparted following flattening passes, and optimized roughness sonotrode. Each concept individually shows improvements in mechanical properties of UAM builds.

A UAM block was produced using these concepts to determine the out of plane tensile strength. The block was made from Al 6061-H18 foil, 0.006 in. ($152.4\ \mu\text{m}$)

thick and 1 in. (25.4 mm) wide using a 14 μm R_a roughness sonotrode. The block was built onto a 0.5 in. (12.7 mm) thick Al 6061-T6 baseplate which was fixtured using a vacuum chuck. A tape to tape overlap of 0.005 in. (0.127 mm) and stacking sequence of 0.1 in. (2.54 mm) stagger between layers was used. Periodic flattening passes were conducted to maintain build flatness, followed by texturing passes such that all welds were performed onto textured surfaces. The weld parameters for the build are shown in Table 3.1 which are based on the optimized parameters outlined in Chapter 2. Conducting consecutive welds numbering in the 100's results in heat buildup in the build due to friction. Therefore, a baseplate preheat of 120 °F was used such that the build maintained a relatively constant temperature throughout the build process.

Table 3.1: Weld parameters for UAM block following optimization.

Parameter	Level
Temperature	51.7 °C (120 °F)
Force	5000 N
Amplitude	32.76 μm (70%)
Speed	84.6 mm/sec (200 in/min)

An early attempt at the block build resulted in a crack at the base layer of the build. This crack occurred shortly after refixturing the baseplate onto the vacuum chuck. Baseplates in the UAM process warp somewhat due to the applied loads from the sonotrode. When refixturing it back onto the chuck, a bending action is applied to the plate which can induce a cracking behavior at the base layer of the build.

Therefore, the build was completed before removing from the vacuum chuck, to avoid bending loads when refixturing the plate.

A transient zone is known to exist in the first second of welding, where the sonotrode amplitude has not reached its steady state value. To minimize the strength reduction effect in this transient zone for the first weld layer, the first layer of the build was made longer than the rest of the build. As the build progressed, trim passes were performed along the perimeter of the block to remove excess tape material and to square the edges along the weld direction. Trim passes help maintain a flat welding surface and remove crack initiation points at the edges of the build which occur due to tape stagger. All trim passes were performed using ball nosed end mills to minimize the stress concentrations surrounding the build edges. Periodically during the build process, the build width was decreased in response to edge effects which can create an uneven weld surface. An example of this effect is shown in Figure 3.1. Edge effects occur due to the layer to layer stagger which forces the foils on the edge to overhang the edge of the build. Perfect welds do not consistently occur at these edge layers, creating areas of poor support for further welds, thus forcing the build to narrow periodically such that a level build surface is maintained.

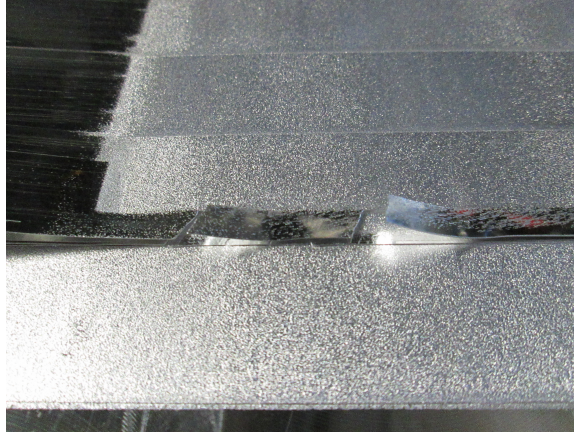


Figure 3.1: Edge effect in a UAM build which occurs due to a lack of weld support.

The build was constructed to a height of 1.1 in. (27.94 mm), with an overall height including the baseplate of 1.59 in. (40.39 mm) Following the build, cylindrical samples were sectioned from the block using wire EDM. Specified samples were heat treated to the T6 condition. Both as-built and heat treated samples were then machined to final dimensions using a CNC lathe. The dimensions of the tensile specimens are shown in Figure 3.2, and were designed to follow ASTM E466 [44], for tensile fatigue testing, though the dimensions are applicable to tensile testing as well. Tensile tests were conducted using an MTS 831 tensile frame with hydraulic grips. Load and frame displacement were recorded until failure.

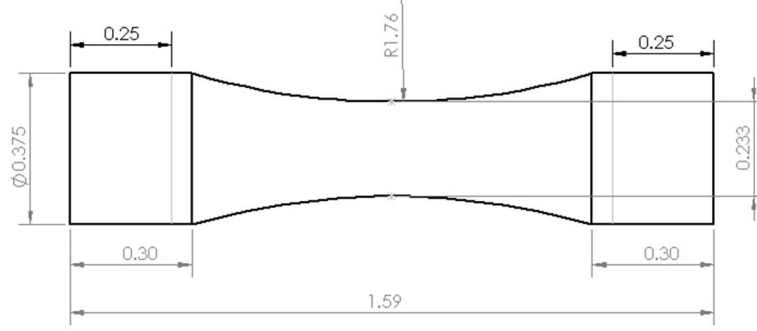


Figure 3.2: Tensile specimen dimensions for out of plane tensile testing (in.).

3.1.1 Results

Results of the tensile testing are presented in Table 3.2. For as-built sample 3, the sample failed immediately upon loading in the grips, with the maximum load at failure recorded. As is shown in the results, the tensile strength of the as-built samples is significantly lower than those presented in Table 2.13, with average UTS values of 56.3 MPa vs. 135.6 MPa. Similarly, the T6 heat treated samples show reduced strength compared to the previous study (236.3 MPa vs. 300.3 MPa).

Table 3.2: Tensile test results for out of plane tensile testing.

Sample	UTS (MPa)
As-Built 1	49.6
As-Built 2	44.1
As-Built 3	19.3
Heat treated 1	214.4
Heat treated 2	244.1
Heat treated 3	250.3

3.1.2 Discussion

Builds were conducted using optimized process parameters (Build B) and non-optimized process parameters (Build A). The builds which utilized optimized welding process parameters resulted in significantly lower as-built strength and marginally lower heat treated strength. The differences in the builds are related to the tape overlap and stagger, use of flattening, and sonotrode roughness. The optimized build used a tape to tape overlap and stagger while build A was constructed without overlaps or stagger, sonotrode roughness for build A was 7 μm vs. 14 μm for build B, and flattening passes were conducted periodically for build B.

The use of these conditions was driven by the results presented in Chapter 2, where each of these conditions was shown to improve mechanical properties. While it was expected build B would result in higher mechanical properties, there are potential reasons why these process conditions would result in reduced strength. The UAM process, especially the 9 kW process, imparts significant loads on a part during the build process. For the case of build B, there are no voids along the material seams due to the tape to tape overlap used. However, in build A, there are voids at seam locations, which add a degree of compliance to the build. This compliance could allow motion of the build itself, thereby reducing the amount of stress applied to the build during processing.

Another difference in the two builds is the utilization and need for periodic flattening passes in build B, whereas flattening passes were not conducted in build A. Because build B used tape to tape overlaps, material built up at seam locations which required machining to maintain flatness, a known effect in the UAM process. While a study was conducted which showed that applying a roughness via the sonotrode

after flattening improves weld quality, it may not exactly match the conditions of a weld layer. Therefore, reduced weld quality could occur at such locations and lower the overall mechanical strength. Therefore there may be a tradeoff in the use of tape overlaps and the number of flattening passes in a UAM build.

3.1.3 Motivation

The differences in build strength between build A and build B and the relatively low as-built mechanical strength of each compared to the as-received foil indicates that further investigation must be performed to determine the effects of processing conditions on build strength. While many causes for the low as-built strength may exist, the focus of this study is on the mechanical loads applied during the UAM process. These include the contact mechanics at the sonotrode foil interface, and applied normal and shear forces which are hypothesized to cause plastic deformation and residual stress in a UAM build resulting in reduced strength.

3.2 Sonotrode Contact Modeling

The UAM process imparts contact stresses on the component being built via the sonotrode. Contact conditions can be modeled using a cylinder on flat configuration with existing analytical solutions described by Hertzian contact mechanics. The purpose of this study is to examine the stress field and deformation in a weld foil caused by sonotrode contact in the UAM process. Plastic deformation and residual stress are of interest since they can degrade build properties. FEA and analytical solutions are used to describe the elastic behavior. The boundary conditions and loads applied in the elastic FEA are then used to implement plasticity within the FEA code.

The analyses performed are for a single static contact, neglecting the rolling of the sonotrode, friction, or shear loads applied during the UAM process.

An image of the cylinder on flat geometry, which is representative of the sonotrode onto a baseplate is shown in Figure 3.3. The geometry creates a line contact along the length L of the sonotrode and a variable contact length, $2b$, in the plane transverse to the weld direction which depends on the geometric and loading conditions.

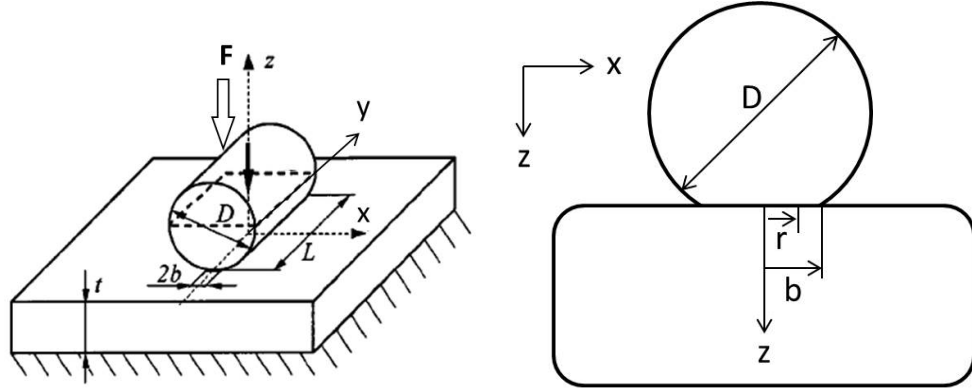


Figure 3.3: Cylinder on flat geometry [16], modeling the sonotrode onto baseplate configuration.

The equations used to describe the contact mechanics analytically were originally developed by Hertz [39], using the following assumptions: 1) the surfaces are continuous, smooth and nonconforming; 2) the strains are small; 3) each solid can be considered as an elastic half-space in proximity to the contact region; and 4) the surfaces are frictionless [8]. Reformulated versions of these equations providing a useful engineering form are provided in [13, 34, 68].

Half of the contact length, as described by Hertzian contact mechanics, is modeled by b in equation 3.1, where F is the normal force, E_1 and E_2 and ν_1 and ν_2 are the elastic modulus and poisson ratio of the cylinder and flat respectively. d_1 is the diameter of the cylinder while d_2 is infinite in the case of a flat contact.

$$b = \sqrt{\frac{2F}{\pi l} \frac{\frac{1-\nu_1^2}{E_1} + \frac{1-\nu_2^2}{E_2}}{\frac{1}{d_1} + \frac{1}{d_2}}} \quad (3.1)$$

The maximum pressure due to the contact is given by p_{max} in equation 3.2 where l is the depth of the cylinder.

$$p_{max} = \frac{2F}{\pi b l} \quad (3.2)$$

The applied pressure along the x-direction due to the contact takes the form of an ellipse and is given by p in equation 3.3, where r is the distance in the x direction on the plane of contact.

$$p = p_{max} \sqrt{1 - \left(\frac{r}{b}\right)^2} \quad (3.3)$$

The stresses in the x, y, and z directions as well as the xz and yz shear directions are provided in equations 3.4-3.8 below, describing the stress field directly beneath the center of the contact through the depth of the materials. The shear in the xy plane is zero. In these equations, z represents the depth beneath the plane of contact.

$$\sigma_x = -2\nu p_{max} \left[\sqrt{1 + \frac{z^2}{b^2}} - \left| \frac{z}{b} \right| \right] \quad (3.4)$$

Table 3.3: Material properties of relevant components for modeling.

Property	Steel (Sonotrode)	Aluminum (Baseplate)
Elastic Modulus (GPa)	200	70
Poisson Ratio	0.3	0.33

$$\sigma_y = -p_{max} \left[\frac{1 + \frac{2z^2}{b^2}}{\sqrt{1 + \frac{z^2}{b^2}}} - 2 \left| \frac{z}{b} \right| \right] \quad (3.5)$$

$$\sigma_z = -\frac{p_{max}}{\sqrt{1 + \frac{z^2}{b^2}}} \quad (3.6)$$

$$\tau_{xz} = \frac{\sigma_x - \sigma_z}{2} \quad (3.7)$$

$$\tau_{yz} = \frac{\sigma_y - \sigma_z}{2} \quad (3.8)$$

For both the analytical and FEA solutions, the sonotrode was modeled using steel, while the baseplate was modeled with aluminum. Material properties used are presented in Table 3.3. The model uses a sonotrode with 1 in. (25.4 mm) width and 3.78 in. (96.01 mm) diameter, both typical dimensions for the UAM process.

3.2.1 Analytical Solution (Hertzian Contact)

Using the Hertzian contact equations, the stress field below the center of the cylinder in the z-direction was computed. As is shown in Figure 3.4, the von Mises stress is greater than the yield stress for the conditions tested, indicating that yielding occurs. The yield stress used is 225 MPa, representative of the foil yield strength. In

addition to the von Mises stress, each stress component is plotted with respect to the depth. As is shown, the shear component has a minimum value within the depth of material, at the same depth as the von Mises maximum, while the other components of the stress have their highest negative values at the material surface. The shapes of these curves are consistent with previous work with the cylinder on flat geometry [13].

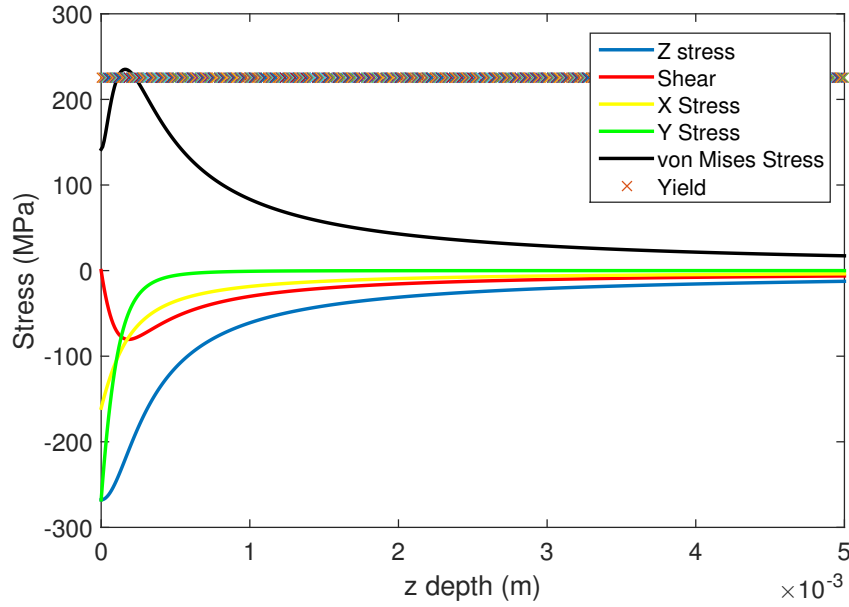


Figure 3.4: Analytical results for contact stress through depth of aluminum.

3.2.2 Finite Element Analysis of Sonotrode Contact

To complement and augment the analytical results, finite element analysis using contact conditions was conducted in COMSOL Multiphysics. The xz plane was modeled for the cylinder on flat configuration using a plane strain condition in the y-direction. The geometry used a sonotrode diameter of 96 mm, or 3.78 in, a common

sonotrode diameter. To minimize computing time, symmetry was used such that half the sonotrode was modeled.

The stress field in the baseplate requires an extremely fine mesh to gather the relevant information at the correct scale; therefore the aluminum layer was modeled using a small volume of material to likewise minimize computing costs. An image of the geometry is shown in Figure 3.5, while an image of a subset of the mesh used for the analysis is shown in Figure 3.6. As is shown, refinements were conducted at the surface of the sonotrode; and to provide the resolution of the stress field in the baseplate, an extremely fine mesh is used.

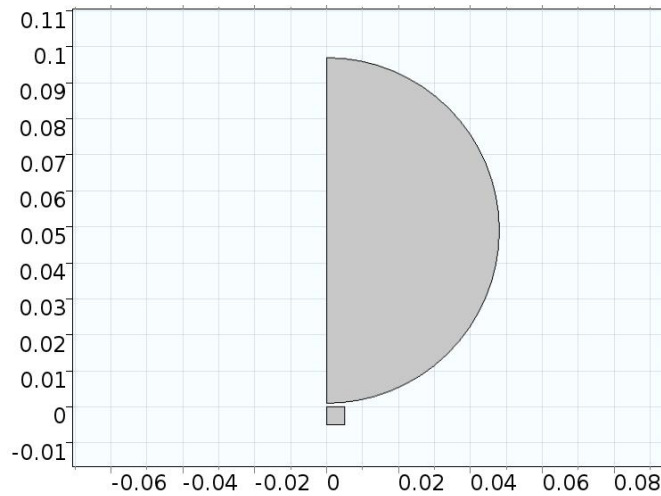


Figure 3.5: Sonotrode onto baseplate geometry used for FEA (dimensions in m.).

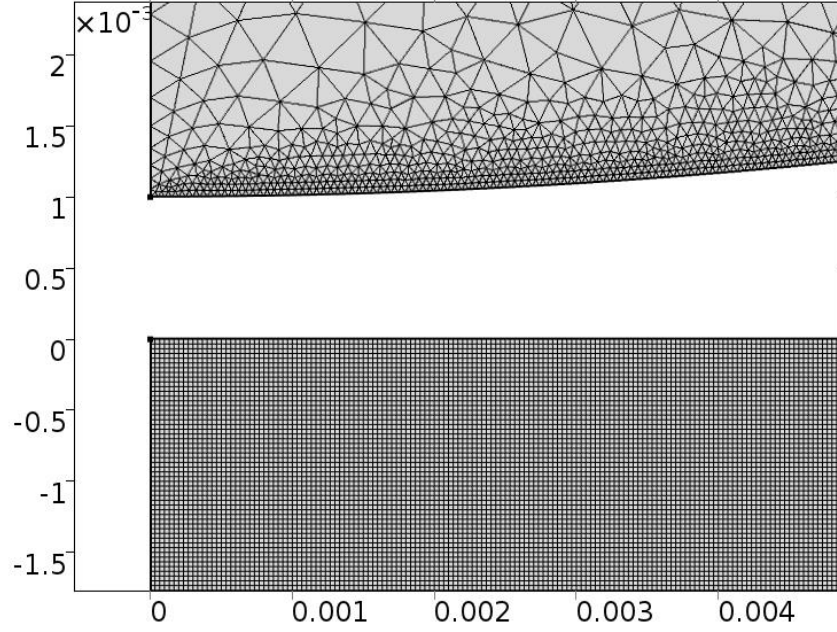


Figure 3.6: Subset of the mesh used for FEA (dimensions in m.).

A symmetry condition was used on the left side of both the sonotrode and baseplate, such that no displacement occurs in the x-direction. The bottom of the baseplate layer was fixed, simulating conditions of the vacuum chuck, while the sonotrode and baseplate were separated by one mm prior to loading. Initial attempts were made to apply the normal force loading of 5000 N through the sonotrode onto the foil via direct loading. However convergence could not be achieved using this method. Therefore displacements were used such that the sonotrode was displaced into the baseplate to create the contact. To achieve the correct normal force according to the loading, iterative studies were performed where the displacement was altered until the z-direction reaction force at the bottom of the baseplate layer was 5000 N.

The model assumes a flat baseplate surface and smooth sonotrode surface to simplify the analysis. Under this construct, it is assumed that loading completely collapses any surface asperities in the aluminum. Because the stiffness of surface asperities is in series with the stiffness of the bulk, the same load is transmitted to each. Therefore the effects of stress in the bulk is constant with respect to any changes in asperity stiffness. In a condition where all asperities are not collapsed, a dynamic loading condition would exist changing the real contact area, but not effecting bulk stresses. The focus of the analysis is on stress effects, not strain, and therefore any potential overprediction of strains is disregarded.

3.2.2.1 FEA Results (Elastic)

The von Mises stress field for the FEA solution is given in Figure 3.7. As is shown, the maximum von Mises stress is found beneath the contact surface, which correlates well with the analytical solution. Similarly, the maximum stress of 239 MPa is greater than the yield stress of the aluminum, indicating that plastic deformation is occurring. This result correlates well with the analytical solution where plastic deformation is also predicted.

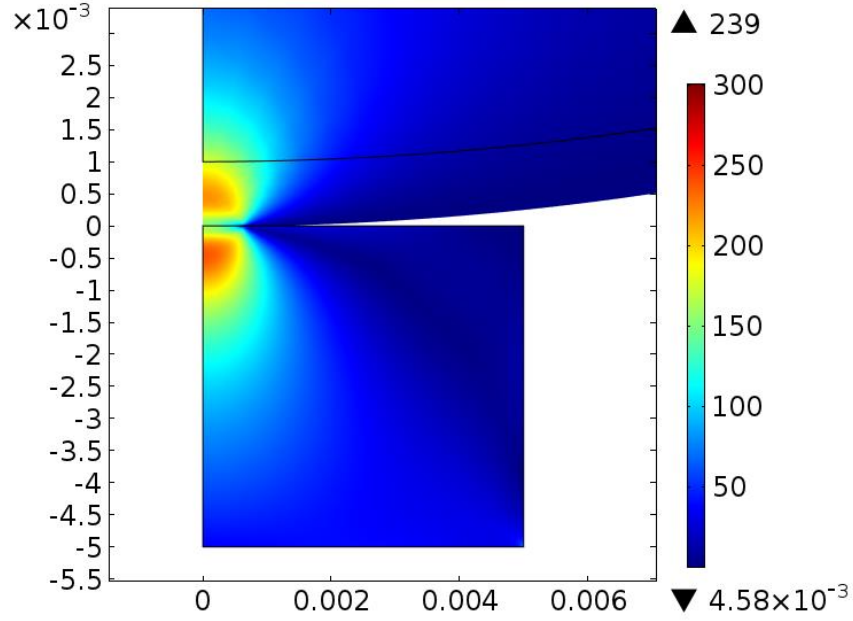


Figure 3.7: von Mises stress field for elastic contact FEA (Stress in MPa).

3.2.2.2 FEA Results (Plastic)

Because the von Mises stresses computed in the FEA were greater than the yield strength of the aluminum, a plasticity component was added to the FEA. The plasticity was implemented using the stress-strain curve associated with the aluminum foil material which characterizes the hardening behavior of the material past yield. This curve is shown in Figure 3.8. Plasticity analysis was performed using the same boundary conditions and loads applied in the elastic case.

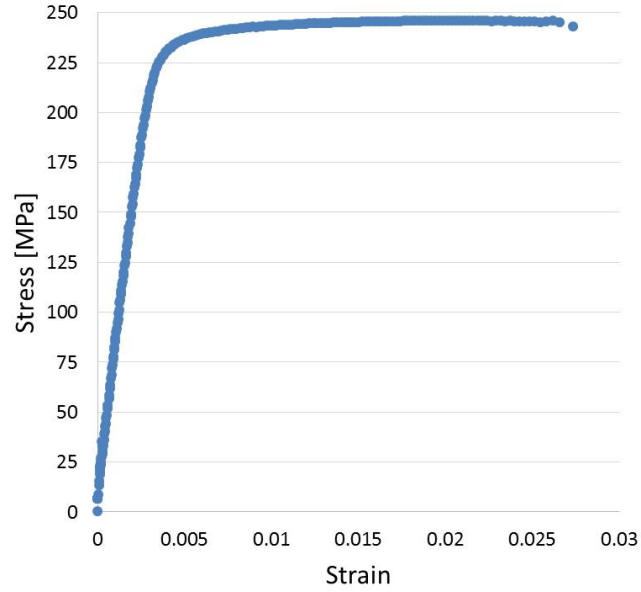


Figure 3.8: Stress-strain curve for Al 6061-H18 foil.

The von Mises stress field in the aluminum using plasticity is shown in Figure 3.9 while the zone of plastic deformation due to the contact is shown in Figure 3.10. As is seen, the plastic deformation covers a small, but non-negligible area. Figure 3.11 shows the amount of plastic deformation along the depth direction, indicating that an area of approximately 0.017 in. (0.4318 mm) experiences plastic deformation. This correlates to roughly three 0.006 in. thick foil layers.

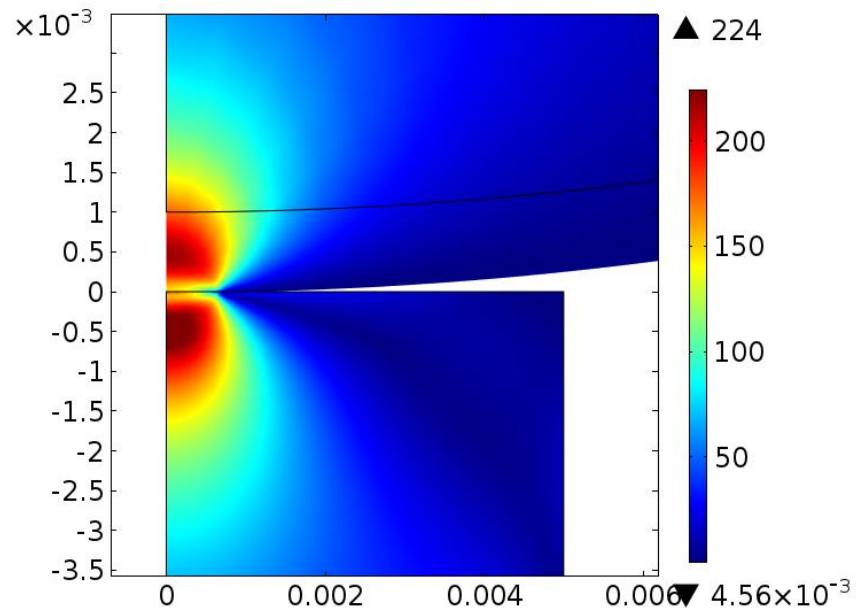


Figure 3.9: von Mises stress field with plastic deformation (Stress in MPa).

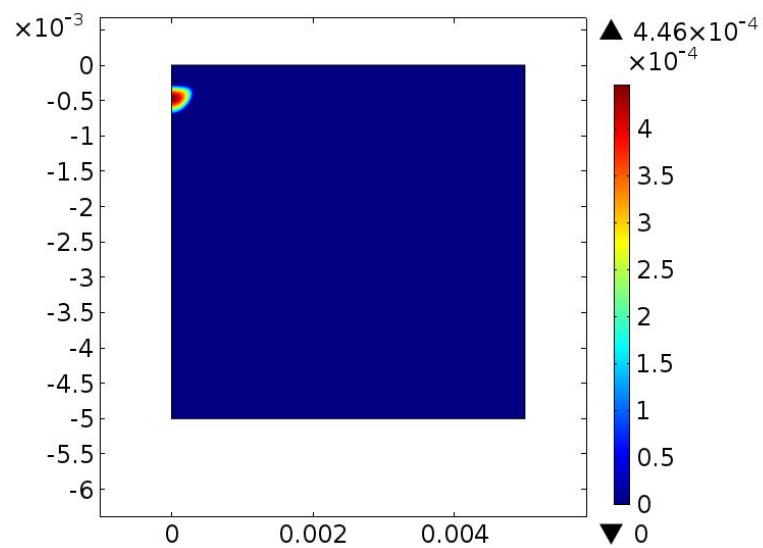


Figure 3.10: Zone of plastic deformation due to contact stresses.

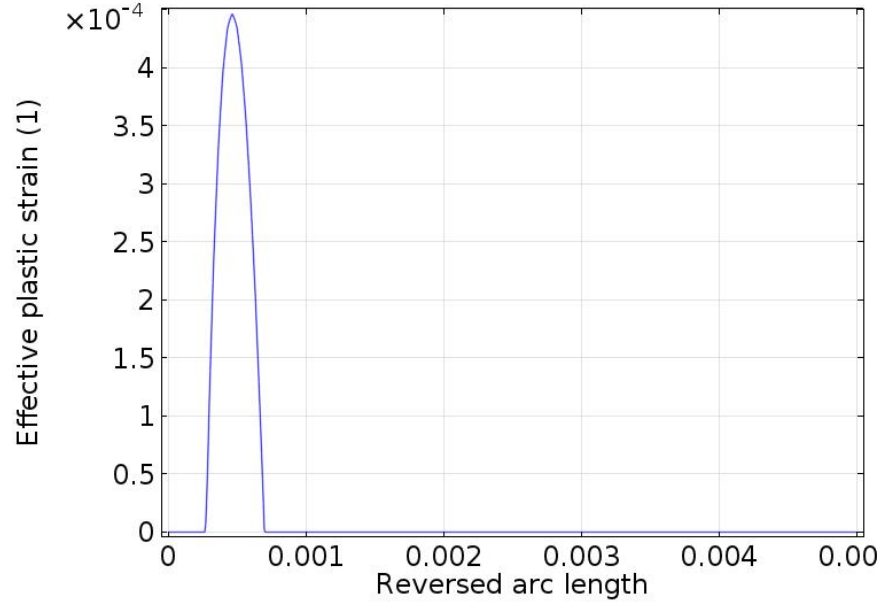


Figure 3.11: Plastic deformation along the depth of the baseplate.

3.2.2.3 Study on Reduced Normal Force

Contact modeling shows that applied normal forces of 5000 N result in sufficient stresses for plastic deformation to occur in aluminum. While 5000 N is a commonly used normal force in the 9 kW UAM process, it has been shown that normal force is largely insignificant to weld quality around this level. Therefore it is of interest to investigate other normal forces such that welding can be achieved without generation of plastic deformation due to contact stresses.

An FEA model was implemented with similar geometry and boundary conditions as presented previously using a 3000 N normal force, with the resulting von Mises stress field shown in Figure 3.12. As is shown, the stresses observed are less than the

225 MPa yield stress associated with the aluminum tape, indicating plastic deformation due to contact mechanics will not occur under these loads. The results show that lowering the normal load can eliminate plastic deformation in the bulk from contact mechanics alone.

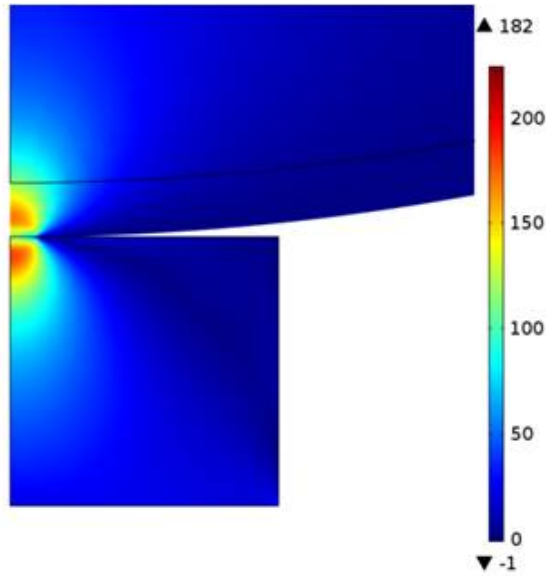


Figure 3.12: von Mises stress field under 3000 N normal force.

3.2.3 Discussion

Both the analytical solutions using Hertzian contact equations and the elastic FEA results indicate that plastic deformation occurs at 5000 N normal forces due to contact mechanics. These similar results substantiate that the mesh and boundary conditions applied in the FEA accurately represent the contact physics occurring in the UAM process. The plastic deformation was modeled further within the FEA construct by implementing plastic behavior in the aluminum. Results show that

plastic deformation of roughly 0.017 in. is occurring, or roughly three tapes deep into the build. The plastic deformation that occurs is expected to produce residual stresses in the foils which reduce the mechanical strength of UAM builds. It is therefore desired to minimize or eliminate stresses due to mechanical contact.

Analysis of 3000 N normal forces in the FEA construct shows that the stresses induced due to the contact mechanics do not induce plastic deformation. Welds of suitable quality have been shown by Hehr using 3000 N normal force [36]. Therefore future joints with aluminum should utilize lower normal forces such that plastic deformation due to contact does not occur. Similarly in other material systems, normal forces should be held to a minimum during the weld process to limit plastic deformation from contact mechanics. Of note, the analysis in this study does not include friction and was implemented in a static case at a single point of contact. The small area of plastic deformation shown would protrude through the length of the weld where contact was made.

The roughness of both the sonotrode and baseplate were ignored in the analysis, since bulk effects were the focus. Asperities on each surface are likely to deform and shear during the process, according to the bond theory of UAM. This asperity deformation was not modeled in this case but would be of interest in future studies.

3.3 UAM Applied Loads Model

To analyze the stress field due to the UAM loads applied during the process, an FEA solution was developed. The model applies normal loads and shear loads which are typically used for joining Al 6061-H18 foils. A schematic of the applied loads is shown in Figure 3.13. In the model, the normal and shear loads are applied to the

top surface of a UAM build, while the baseplate is fixed. The top rectangle in the model is Al 6061-H18 foil while the baseplate is Al 6061-T6.

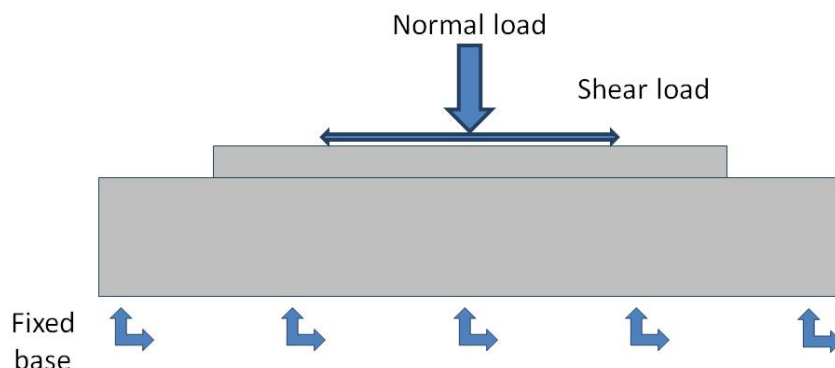


Figure 3.13: Schematic of applied loads from UAM applied to FEA analysis.

Modeling was performed in a pseudo-static configuration where the normal load and shear load for a single load cycle is applied. Dynamics and multiple loading cycles were not explored at this time. A normal load of 3000 N and a shear load of 2000 N was applied to the block. The shear loads used come from computed values from work by Hehr et al. and deVries [20, 35, 36]. A half cycle represents an applied load in the + x-direction only, while a full cycle is defined as shear loading to the right, and then to the left in the x-direction. The model investigates the effect of applied loads for the case of a single foil, as well as a 50 layer build.

3.3.1 Single Foil Model

For the case of a single foil, the von Mises stress is presented in Figure 3.14. As is shown, maxima in the stress field occur at the corners of the foil. A zoomed in

view of the plastic deformation which occurs on the left side of the foil is shown in Figure 3.15, where a small area of plastic deformation occurs at the edge of the foil layer.

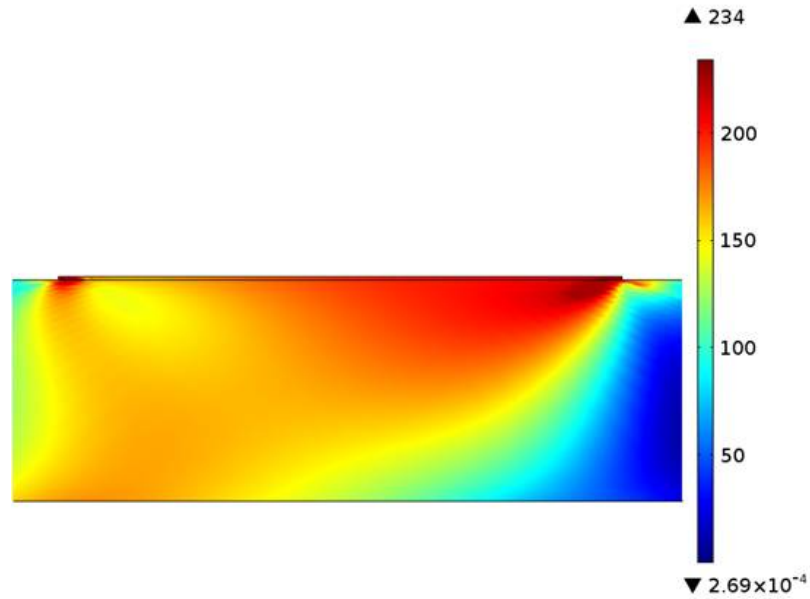


Figure 3.14: von Mises stress field for half cycle loading on single tape (Stress in MPa).

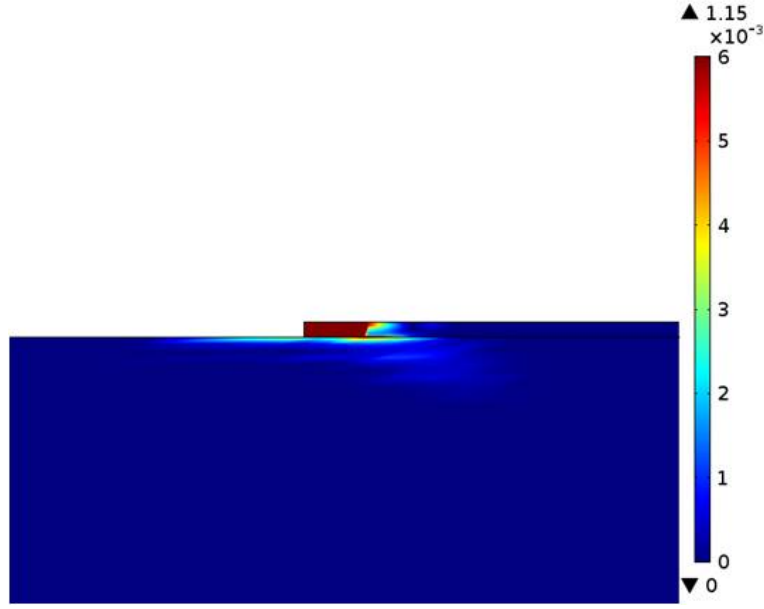


Figure 3.15: Plastic deformation zone for half cycle loading on single tape.

3.3.2 50 Layer Model

For the case of a 50 layer build the model is built similarly, with foil material representing the top rectangle in the model. Results of the von Mises stress induced by the applied loads for a half cycle with the shear load oriented to the right is shown in Figure 3.16. As is shown, a high stress occurs at the corners of the UAM build similar to the case of the single foil, consistent with a stress concentration at these points. The plastic deformation induced by this loading is shown in Figure 3.17 where significant plastic deformation occurs near these stress concentration zones, both in the aluminum foil, as well as marginally into the baseplate.

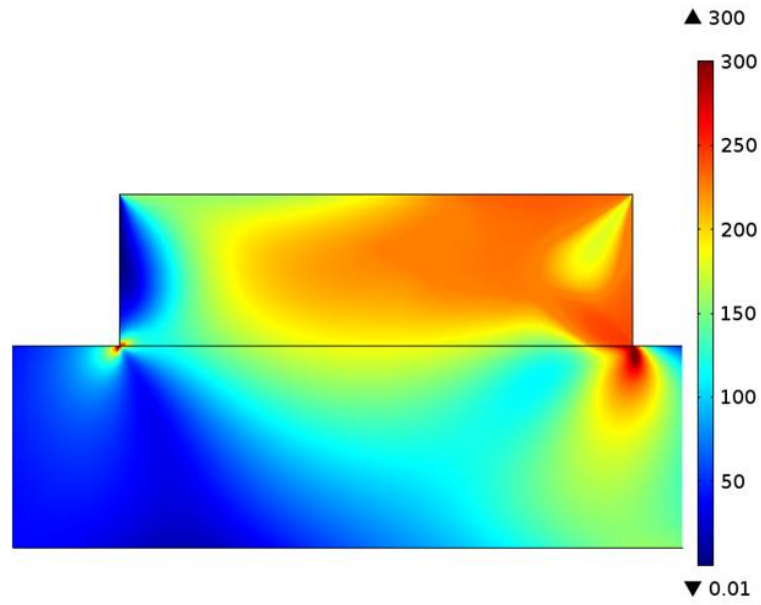


Figure 3.16: von Mises stress field for half cycle loading on 50 layer build (Stress in MPa).

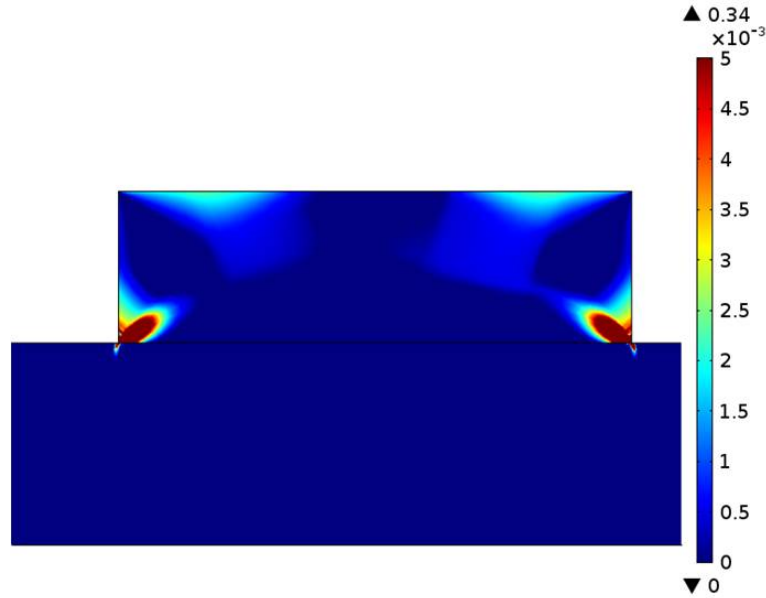


Figure 3.17: Plastic deformation zone for half cycle loading on 50 layer build.

To mitigate the stress concentration at build corners, fillets can be formed in the UAM build during trim processes by utilizing ball nosed end mills. The effect of fillets on the von Mises stress field is shown in Figure 3.18. While the stress is still high, especially in the fillet regions, the fillet can mitigate the stress concentration in these areas. Figure 3.19 shows the plastic deformation which occurs in this configuration. As is shown, the plastic deformation in the UAM build decreases significantly when using a fillet at the build edges.

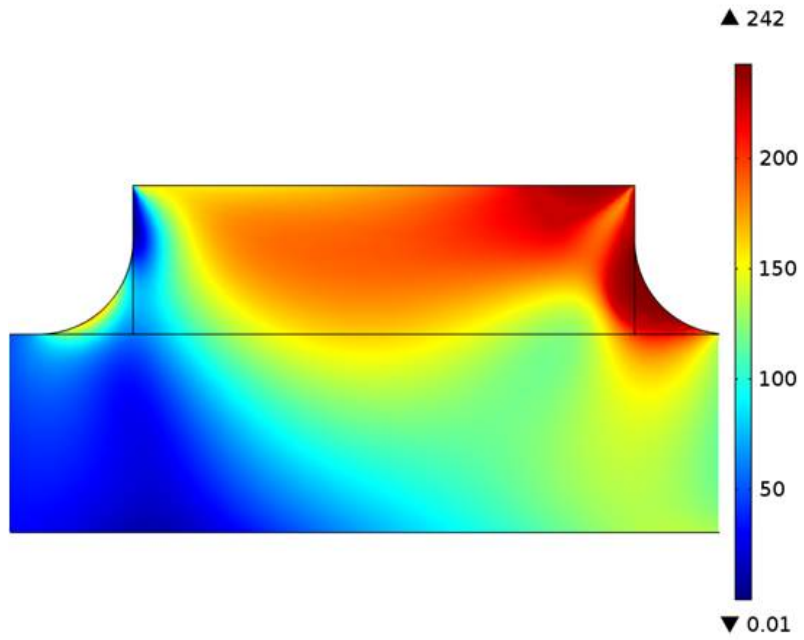


Figure 3.18: von Mises stress field for half cycle loading on 50 layer build with fillet.

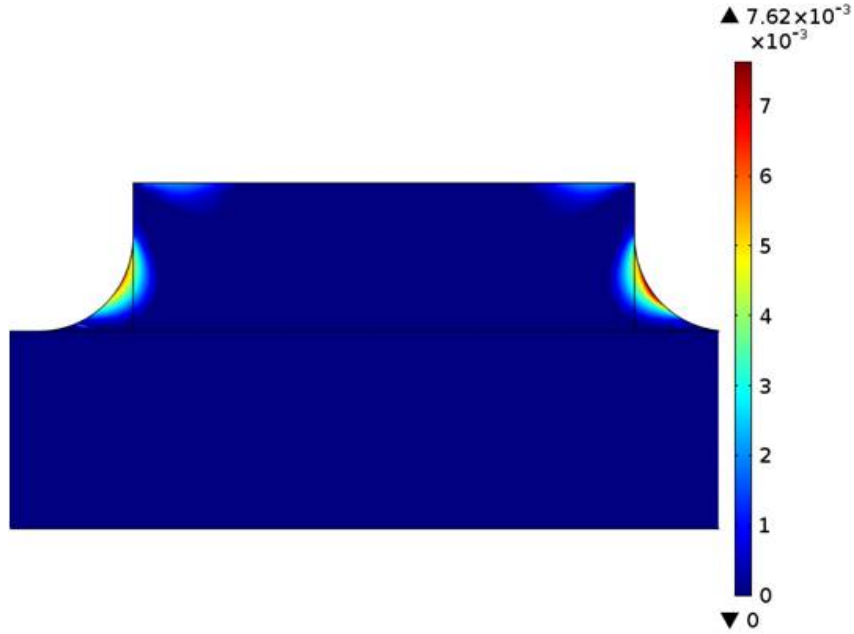


Figure 3.19: Plastic deformation zone for half cycle loading on 50 layer build with fillet.

3.3.3 Discussion

The applied normal and shear loads during the UAM process were modeled using FEA and shown to induce plastic deformation in aluminum UAM builds. The deformation was present in both the single foil case, as well as a 50 layer build. This plastic deformation due to applied loading could cause significant reduction in mechanical strength of UAM builds, through the residual stresses and strains that remain in the material through the build process. In addition, the continued application of UAM loads through building up consecutive layers could lead to further degradation of mechanical properties.

Further, strain rate effects were not examined in detail due to the static loads applied. Because the UAM process operates at 20 kHz, high strain rates occur which could influence the behavior of the material and therefore effect the modeling. These effects were not investigated but would be of further interest.

In the case of a 50 layer build, significant stress and plastic deformation was shown to occur at a square edge. Investigation of fillets at edge locations indicates that the stress can be significantly reduced. Therefore in UAM operations, trim passes should be conducted periodically using ball nosed end mills, which produce stress mitigating fillets.

While studying contact modeling alone, it was shown that reduction of the applied normal force can reduce stresses such that plastic deformation is eliminated. However, in the UAM process, normal and shear forces are applied together to achieve welding. While reduction of normal forces can likely reduce the bulk plastic deformation that occurs, modeling of the UAM applied loads shows that the stresses remain high enough for plastic deformation. Future UAM builds will require tailoring of processing parameters such that adequate bonding can occur while minimizing the bulk plastic deformation that can reduce overall mechanical strength.

3.4 Microstructural Analysis of Heat Treated Foil

While much work has been conducted to investigate the microstructure at the bond interface of UAM built structures, little attention has been given to the bulk of the tape. Specifically, it has been believed that the bulk of the foil is unchanged during the UAM process, while deformation and recrystallization occur at the bond

interface region. To examine the effects of the UAM process on the bulk of the foils, microstructural analyses were performed.

The typical tapes used for the UAM process have been cold rolled to final dimensions, with significant work hardening and residual strain present in the material. This can make it difficult to distinguish the strains applied solely by the UAM process. To investigate a previously unstrained microstructure, Al 6061 tapes were solutionized to the T4 condition via heating to 530 °C for one hour and quenching in water. This removes any rolling strain from the microstructure, while providing a tape with similar tensile strength to as-rolled foils of 240 MPa. In addition, the investigation of solutionized tape is appealing because it offers significant elongation to failure compared to the H18 condition tapes often used (20% vs. 3%). Significant increases in tape elongation are expected to improve the durability of UAM builds, as they are less prone to brittle failure. To examine the effects the UAM processing loads have on the bulk foil microstructure, aluminum foils were investigated using electron microscopy.

3.4.1 Microstructural EBSD

Two sets of measurements were performed to investigate the material microstructure, each conducted using electron back scatter diffraction (EBSD) with a Quanta scanning electron microscope (SEM). One set of measurements was performed on T4 heat treated tapes prior to welding, providing a baseline for the initial microstructure. The other set of measurements was performed on T4 treated tapes which had undergone the UAM welding process. The purpose of these measurements is to determine the initial and welded grain structure through the thickness of a foil layer. Given the

microstructure of each, a determination of any changes due to the weld process can be examined, and a metric of the strain induced in the foil can be determined.

For the welded sample, welds were performed using the parameters determined in Chapter 2 given in Table 2.7. Using these parameters, a six tape stack was produced for investigation. The stack was then sectioned with an abrasive saw, hot mounted in conductive carbon, and polished using a diamond suspension. Final polishing was conducted with colloidal silica solution on a vibropolisher for 18 hours. The unwelded foil was prepared using similar methods, though sectioning was performed using a shear. Following polishing, each sample was lightly etched to expose the grain structure for the EBSD measurements.

EBSD was performed on the samples using a 25 keV beam voltage in the Quanta microscope. The welded sample used a 300 nm step size while the unwelded foils were examined with a 500 nm step size. Each scan was conducted such that the full thickness of a single foil layer was examined.

3.4.1.1 EBSD Results

The grain map for the welded sample is shown in Figure 3.20, where the foil thickness is shown between the two areas containing black points, or no data. The color map provided with the EBSD results indicates crystallographic orientations parallel to the normal of the sample surface for each of the grains measured. Colors are assigned to each of the $\langle 100 \rangle$, $\langle 110 \rangle$, and $\langle 111 \rangle$ directions. In the case of intermediate orientations, a combination of the colors is assigned. As is shown, in the bulk of the tape, grains with a color gradient across the length of the grain are shown, indicating crystal rotation and plastic deformation has occurred.

Post-processing of the image was conducted to clean up areas of noise in the data using a nearest neighbor approach. Points of less than 5% confidence were omitted from the analysis and are shown in black. Unprocessed images for the EBSD analysis are provided in Appendix C. Areas of low confidence were found both at the top and bottom of the foil layer, at areas of high deformation due to the texture of the sonotrode. These are well known areas of significant deformation because of contact with the roughened sonotrode, or contact with previously deformed layer.

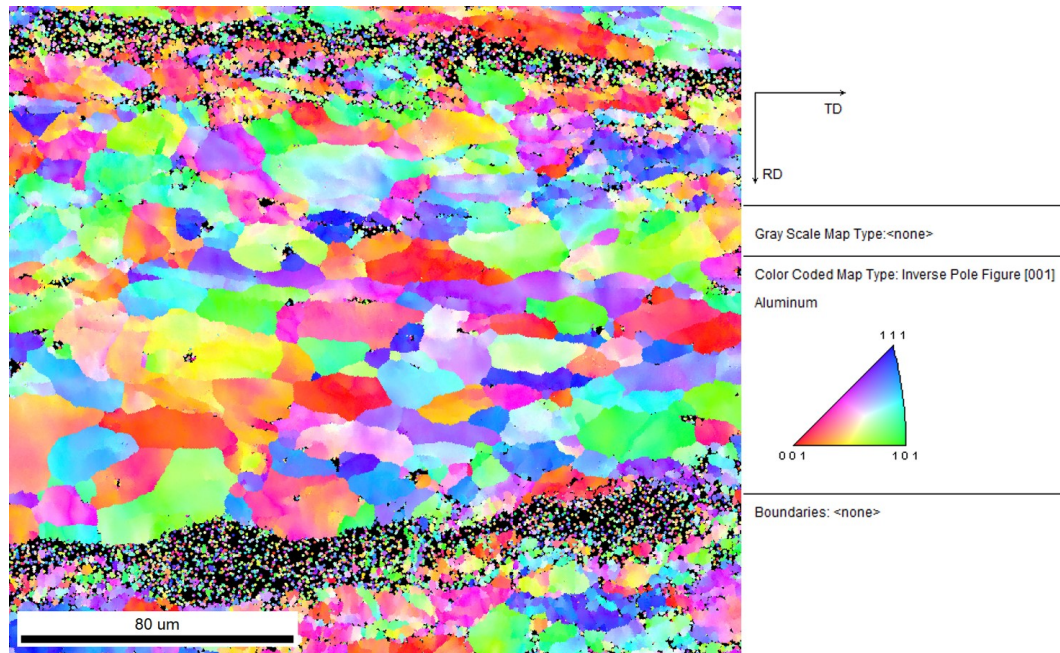


Figure 3.20: Grain map colored via inverted pole figure of the welded 6061-T4 foil.

The grain map for the unwelded sample is shown in Figure 3.21. A similar clean up procedure was conducted and all points of less than 5% confidence were omitted and shown in black. Areas of low confidence are found toward the bottom of the foil,

likely due poor signal detection in these areas from imperfect polishing. In contrast to the welded foils, the grains within the bulk of the unwelded case show mostly consistent coloration throughout each grain. This indicates qualitatively that little to no plasticity has occurred in the grain structure.

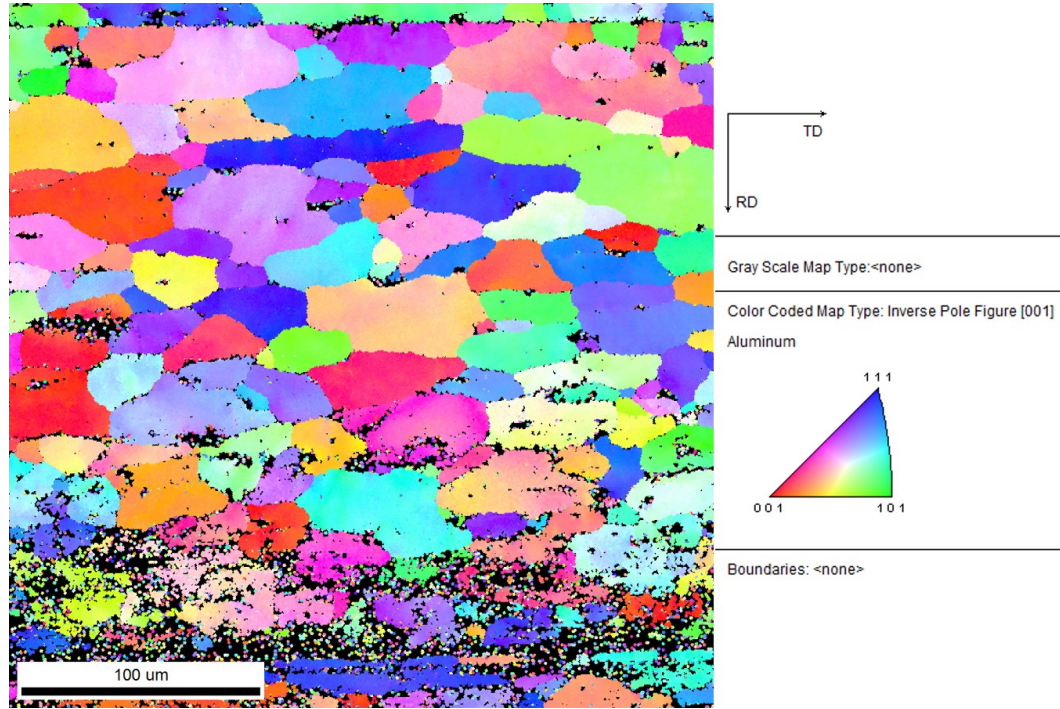


Figure 3.21: Grain map colored via inverted pole figure of the unwelded 6061-T4 foil.

To further analyze the existence of plastic deformation in each condition, a grain orientation spread (GOS) analysis was conducted. GOS is a technique which compares the orientations at each point within a grain, to the average orientation of the grain. By conducting such comparisons, a measurement of the grain rotation can be achieved. Low GOS values are indicative of lower amounts of crystal rotations, while

higher GOS numbers indicate more crystal rotation is present. The degree of crystal rotation provides a metric of the plastic deformation in the grain. GOS results for the welded case are shown in Figure 3.22. As is shown, high GOS measurements are shown throughout the foil thickness, indicative of significant plastic deformation. White and black areas are indications of no data in the analysis.

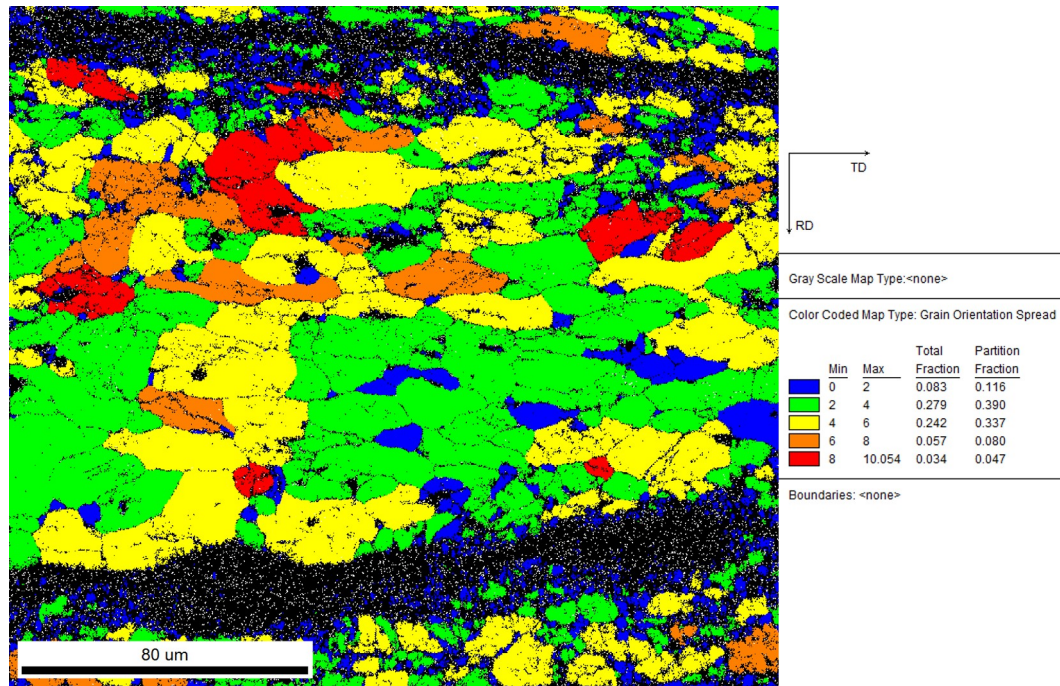


Figure 3.22: Grain orientation spread analysis of welded 6061-T4 foil.

A similar analysis of the GOS for the unwelded foil is shown in Figure 3.23, presented with the same color scale. As is shown, the majority of the analysis shows low GOS values, indicated in blue, signifying that little crystal plasticity is present in the foil.

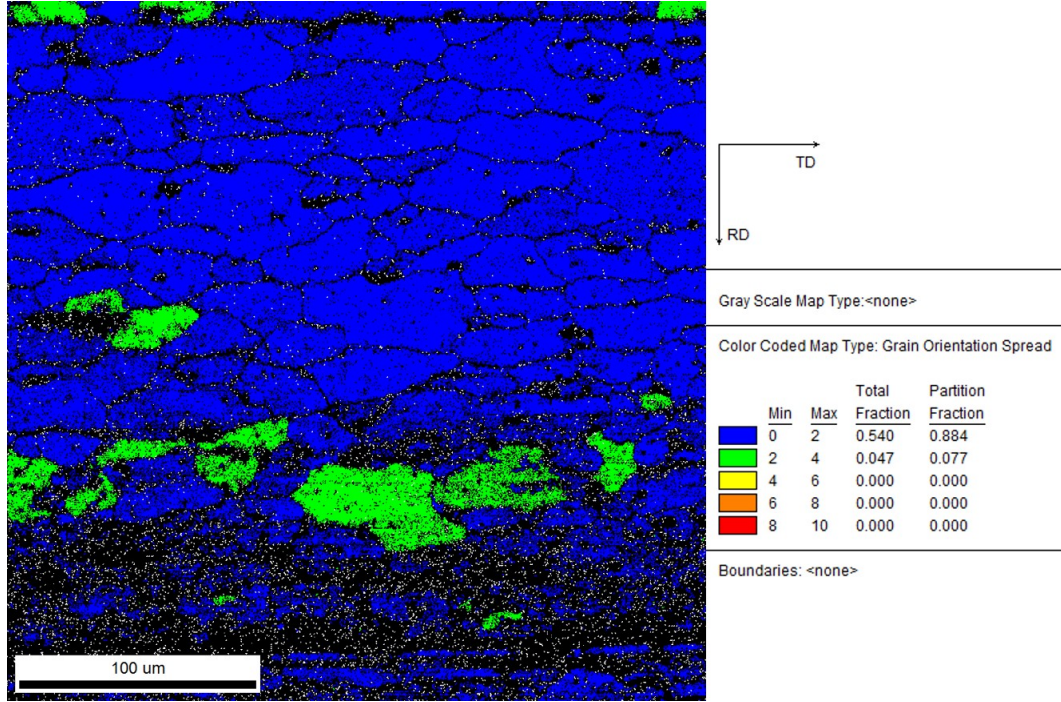


Figure 3.23: Grain orientation spread analysis of unwelded 6061-T4 foil.

3.4.2 Discussion

EBSD analysis of welded and unwelded solutionized foils shows indications of plastic deformation in the bulk of the welded foil, while the unwelded foil shows little to no plastic deformation. This conclusion is based on both the grain maps and the GOS analyses performed. In the colored grain maps, the welded grains in the bulk indicate a color gradient across the grain, indicating slight curvature in the lattice structure. The GOS analysis confirms these results through comparisons of the grain orientations to the average within the grain. In each case, the welded foil indicates significant plastic deformation is occurring, especially when compared to the unwelded condition.

UAM bond theories suggest that plastic deformation occurs at the faying surfaces, leading to metallic bonding. Previous examinations of the welded microstructure have mostly supported this concept, with a recrystallized zone observed at the interface region and a bulk microstructure mostly unchanged. This work however, shows that the deformation of the bulk foil structure cannot be ignored, since large amounts of plastic deformation occur through the tape thickness after welding.

This plastic deformation could lead to degradation of the UAM build properties, especially under accumulated load conditions as the build progresses. The mechanism of this property degradation will require further work to determine if it occurs due to a Bauschinger-like effect of reversed loading, accumulative loading leading to fatigue failure, or by some other mechanism.

Compared to traditionally manufactured structures, the bulk deformation in the UAM process produces parts with a higher proportion of residual stress due to the plastic deformation. This could lead to the significantly reduced strength when compared to traditionally manufactured components. The use of heat treatments, as described in Chapter 2, are shown to significantly increase the as-built properties of UAM builds. This indicates that the mechanism causing the reduction in strength can be eliminated or reduced following heat treatment and that when possible, heat treatments should be applied to UAM structures to maximize strength. The use of higher ductility aluminum foils such as those in the T4 condition would be of future interest to reduce these effects and allow heat treatment for strengthening at temperatures of 160 °C.

These results confirm the findings of modeling efforts presented in Sections 3.2 and 3.3 indicating that the UAM process induces plastic deformation in the bulk

of Al 6061 foil builds. While both the sonotrode contact mechanics and the UAM applied loads models predict plastic deformation, it cannot be determined from these experiments whether the plastic deformation is driven by either cause in this case.

Analysis of the welded foil resulted in poor signal quality near the top and bottom of the foil layer, in areas of high deformation due to sonotrode contact. It cannot be determined with certainty from these measurements whether the poor resolution in these areas is due to high plastic deformation, or due to nanocrystalline grain sizes which are difficult to resolve with EBSD. In either condition, the data cleanup procedure must be conducted carefully, so as to avoid misrepresenting the data in areas of poor resolution.

3.5 Summary

UAM builds were produced using process parameters that were optimized individually. Using these optimized parameters, builds were produced which resulted in significantly reduced mechanical strength compared to initial properties. Investigations of the effects of contact mechanics and the UAM applied loads were performed to determine the effect of these mechanical loads on build quality. It was shown that the contact mechanics under a 5000 N normal force produce stresses that cause plastic deformation in aluminum builds. Reducing the normal force to 3000 N was shown in the analyses to eliminate plastic deformation due to contact mechanics.

The applied normal and shear loads in the UAM process were modeled in FEA indicating that plastic deformation is produced in aluminum. These applied loads will require further investigation to provide suitable weld conditions without generating plastic deformation. Using a straight build edge results in significantly higher loads

at the base of the builds due to a stress concentration. Utilizing fillets through trim passes with ball-nosed end mills can significantly reduce the stresses and plastic deformation in these areas.

Analysis of the foil microstructure in welded and unwelded conditions indicates that plastic deformation occurs in the foil bulk during the UAM process. This confirms the results of modeling efforts which predict bulk plastic deformation for Al 6061 foil. The existence of plastic deformation in the bulk indicates that the applied loads in the UAM process can be detrimental to UAM builds, especially under accumulating load conditions as builds progress. Further work will be necessary to minimize and control the bulk plastic deformation occurring in the process.

Chapter 4: SHEET METAL JOINT DESIGN AND IMPLEMENTATION WITH UAM SYSTEM

Introduction

This chapter focuses on the development and characterization of a sheet metal joint constructed using an ultrasonic additive manufacturing system. Construction of the joint utilizes traditional UAM equipment in a new configuration to achieve joints one order of magnitude thicker than commonly used with UAM. Following development of a joint configuration, measurements were taken to characterize the room temperature tensile strength, elevated temperature tensile strength, and room temperature fatigue strength. Additionally, the effect of post-process heat treatments on mechanical strength was examined. Examinations of sheet metal joints are conducted for Al 6061-T6 and Al 2219-T31 material.

4.1 Joint Design with Al 6061

4.1.1 Thickness Scoping Trials

To begin the design of a sheet metal joint using ultrasonic welding, it is necessary to determine the weldable thickness range. Existing state of the art for UAM built structures uses foils on the order of 0.006 in. (0.152 mm) thick [4], while ultrasonic

seam welding of 1100 aluminum alloys has been successfully conducted on 0.3 mm thick material [83]. The goal of such pilot testing is to determine the maximum weld thickness possible, identifying the envelope of geometries for joint design. Pilot test welds were performed to determine the weldable envelope for Al 6061-T6 employing a range of foil thicknesses. The various foil thicknesses were machined from thicker stock to create the desired dimensions. The strips were ultrasonically welded to an aluminum 6061-T6 baseplate using the Fabrisonic SonicLayer 4000 UAM system, with all tests performed at room temperature. A successful weld was determined as one which stuck to the baseplate and could not be easily peeled off manually, while also not welding directly to the sonotrode.

Initial attempts were performed using a knurl patterned sonotrode, pictured in Figure 4.1. This knurl pattern is more aggressive than the typical 7 or 14 μm R_a roughness sonotrodes normally used in UAM and the contact width on is 0.5 in. (12.7 mm) wide, increasing the weld pressure per weld attempt compared to a 1 in. (25.4 mm) wide horn. Therefore weld forces during the trials were decreased to compensate for this increased pressure. Weld attempts at thicknesses of 0.016 in. (0.406 mm) were unsuccessful with this sonotrode in achieving a suitable weld without subsequent joining to the sonotrode itself. Attempts to increase parameters such as the amplitude led to significant sticking to the sonotrode without viable welding.

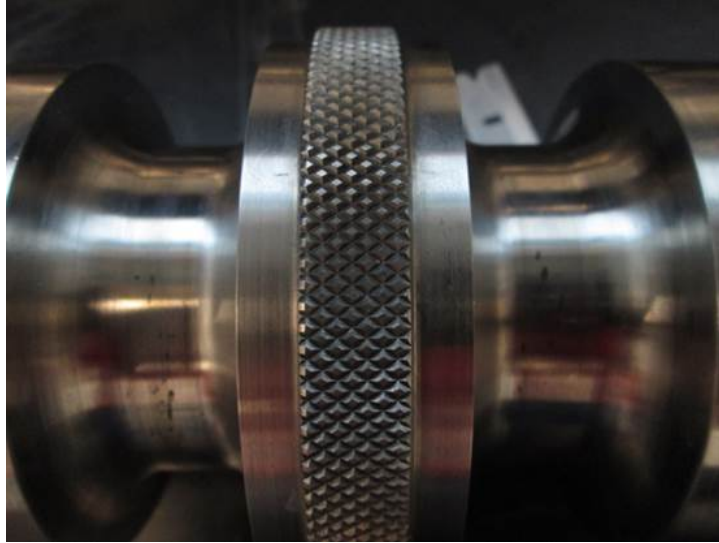


Figure 4.1: Knurl patterned sonotrode.

Following unsuccessful attempts with the knurl patterned sonotrode, attempts were performed with a $7\text{ }\mu\text{m R}_a$ roughness sonotrode, shown in Figure 4.2. The texture on this horn is achieved using electronic discharge machining (EDM). With this horn, weld trials were performed varying the amplitude, weld speed, and weld force until a weld was achieved or it was clear a weld was not possible under this configuration. Foil thicknesses including, 0.006 (0.152), 0.016 (0.406), 0.020 (0.508), 0.025 (0.635), 0.030 (0.762), 0.032 (0.813), and 0.035 (0.889) in. (mm) were attempted. An image of a trial using 0.016 in. thick aluminum is shown in Figure 4.3. A maximum thickness of 0.032 in. was identified as viable. Attempts to exceed this thickness resulted in inadequate welding or direct welding to the sonotrode, regardless of parameter levels tested. The weld parameters for the 0.032 in. (0.813 mm) thickness pilot welds are

shown in Table 4.1. These parameters indicate levels at which a weld can be achieved, but do not represent an optimized set.

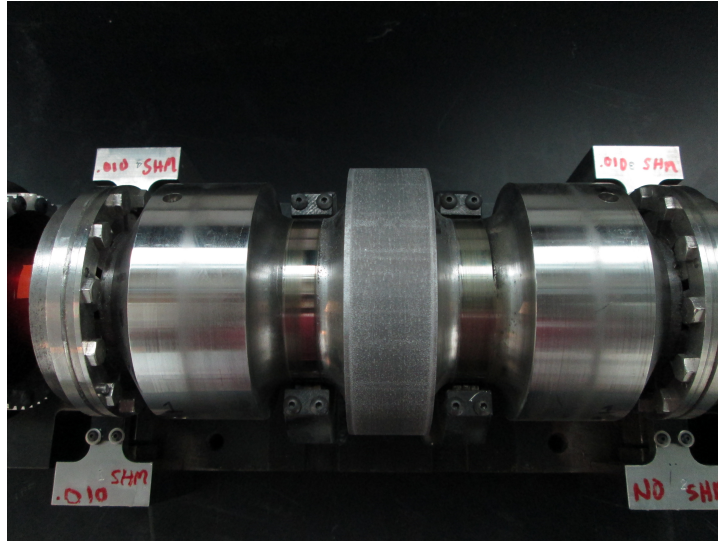


Figure 4.2: Image of 7 μm horn.

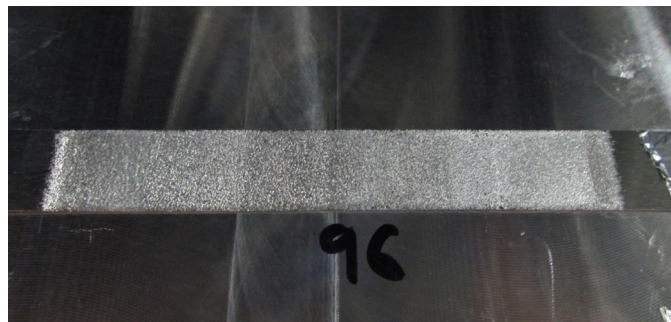


Figure 4.3: Image of 0.016 in. (0.406 mm) thick scoping trial.

Table 4.1: Welding parameters for 0.032 in. (0.813 mm) thick welds using Al 6061-T6.

Process Variable	Set Value
Weld Force (N)	1500
Weld Speed (in/min)	30
Amplitude (μm)	41.4
Spot Time (ms)	225
Sonotrode Surface Texture, Ra (μm)	7
Oscillation Frequency (kHz)	20

Following thickness scoping, an aluminum sheet was joined to a baseplate to verify the process parameters and boundary conditions are feasible when joining larger stock. An image of this weld is shown in Figure 4.4. Dimensions of the the sheet are 12 in. x 6 in. x 0.032 in. (304.8 x 152.4 x 0.813 mm) This joint successfully welded to the baseplate and could not be pulled up manually.



Figure 4.4: Weld trial using aluminum sheet stock.

4.1.2 Design Configuration Development

Using the maximum weld thickness of 0.032 in. (0.813 mm), joint designs were investigated for sheet material 0.063 in. (1.6 mm) thick. A 0.063 in. thickness was chosen because it is roughly twice the thickness of the maximum thickness identified as weldable, providing a good starting point for joint development. One design considered uses a lap layout as shown in Figure 4.5a. To create a flush surface finish, the concept uses an initial weld, followed by a machining step (Figure 4.5b), and a final weld pass which uses foil material to fill in the machined layer and provide a flush surface finish (Figure 4.5c).

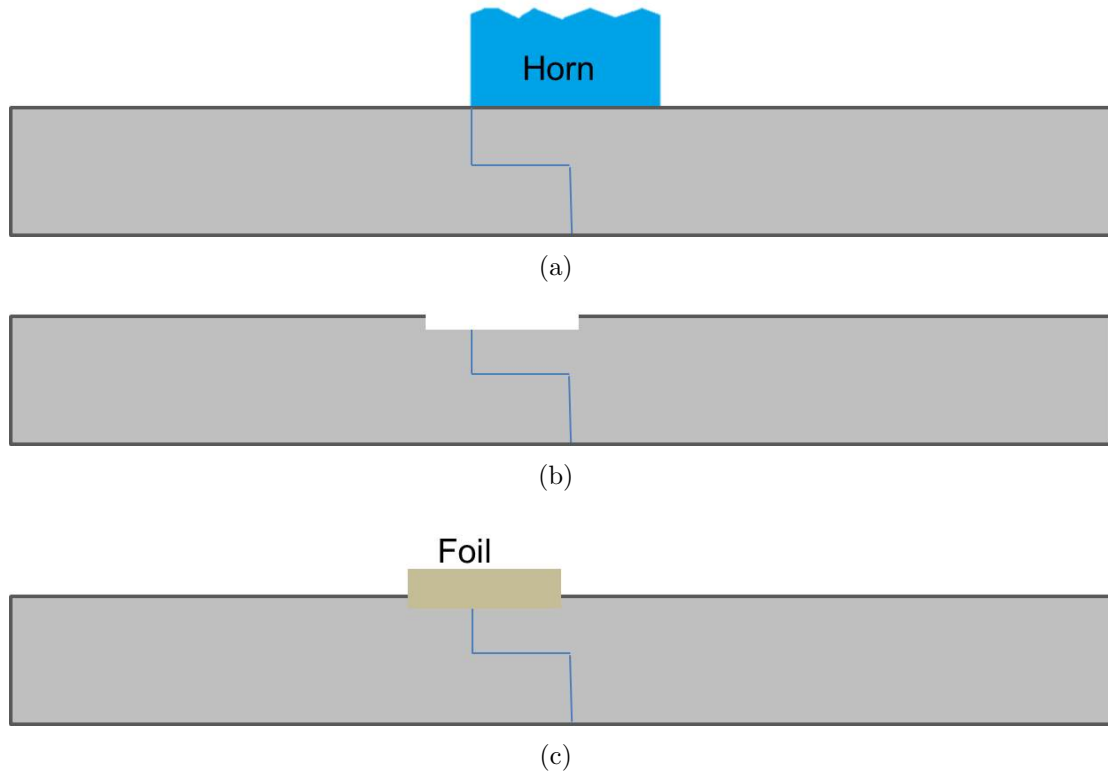


Figure 4.5: (a) Layout for lap joint (b) joint with machined surface and (c) joint with flush surface using foil.

Weld trials were attempted on a vacuum chuck, which fixtured each sheet of material. While successful in joining the lap configuration (Figure 4.6), suitable joining of tape material was not achieved. An image of an attempt to join foil material is shown in Figure 4.7. As is shown, significant tape tearing occurs in the center of the joint, which indicates non-uniform support underneath the weld. This can occur due to poor mating between the sheets, and weld support surfaces that are not level.



Figure 4.6: Lap joint showing joining of two sheets.



Figure 4.7: Weld trial using foil to fill in machined section exhibiting tape tearing due to poor support.

While the lap joint was successful in joining the aluminum sheets, significant deformation of the sheet material occurs due to the channels in the vacuum chuck. An image of the vacuum chuck with its channels is shown in Figure 4.8a and a deformed sheet after welding onto the chuck is shown in Figure 4.8b.



(a)



(b)

Figure 4.8: Vacuum chuck and deformed sheet material pressed into chuck channels.

To prevent the deformation of the sheet material into the vacuum chuck, an adapter plate was designed to provide a solid base beneath the weld area. This adapter plate is shown in Figure 4.9. Welds are conducted over the center portion of the plate, away from any channels, removing the possibility of forming into the channels while also providing adequate fixturing of the two sheets during welding. To achieve suitable flatness, the adapter plate is Blanchard ground to maintain flatness and parallelism.

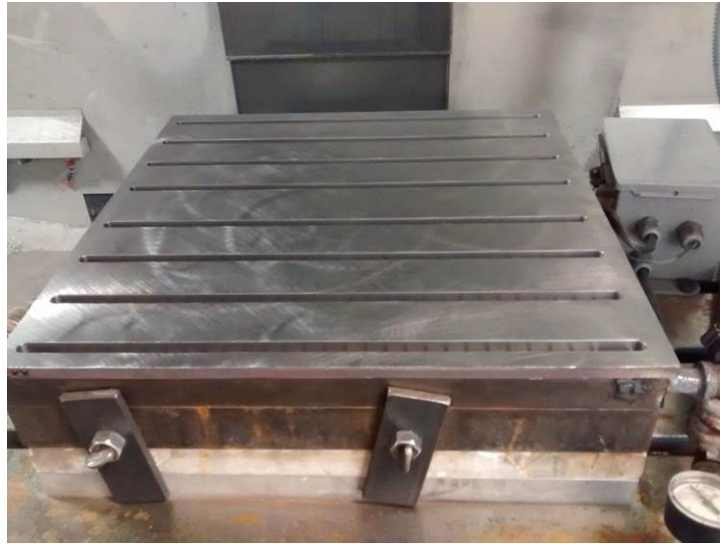


Figure 4.9: Adapter plate for vacuum chuck.

Using this adapter plate a lap configuration was attempted consisting of two separately machined sheets, with matching steps that are welded over to create the joint. The concept is shown in Figure 4.10 and is similar to that shown in Figure 4.5a. In this configuration, channels are machined on each side of the joint to control the horn

contact area during development. In a final application, a designated horn geometry would eliminate the need for such a step.

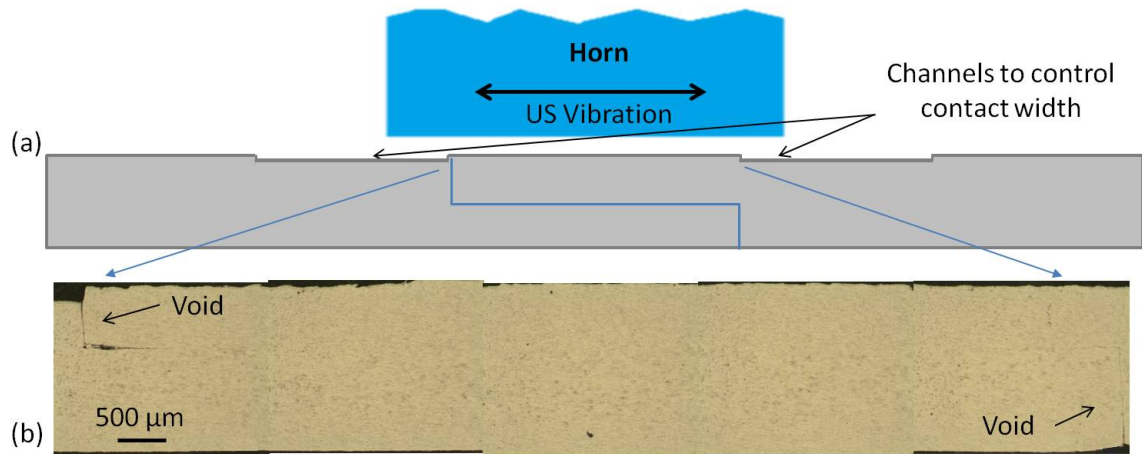


Figure 4.10: Lap joint (a) schematic and (b) cross section.

Reasonably successful joints can be achieved using this design. Specifically there are no indications of voids in the horizontal portion of the joint, but there is a lack of bonding in the vertical portions, as shown in Figure 4.10b. It is expected that the lack of bonding is due to the lack of relative sliding motion and normal force between the two sheets in those areas. Because the ultrasonic vibrations are applied normal to the vertical mating surfaces, scrubbing does not occur, which is necessary for bonding. Therefore, in order to achieve complete bonding throughout, the joint design must allow relative sliding motion between all mating surfaces.

Following these principles, other joint designs were considered. Of specific interest are designs that utilize an angle, or scarf joint configuration. This type of design allows the mating surfaces to move relative to one another while remaining relatively

simple to manufacture. To test this concept a joint was created with an angle on one side and a lap joint mating on the other. The angled portion was machined using a chamfer end mill and the flat portion was machined using a square end mill. The joint schematic and a cross section of the joint is shown in Figure 4.11. As shown in the cross section, while voids are present around the vertical mating surface, there are no voids in the angled portion of the joint. This indicates that the angle allows sufficient relative scrubbing action for joining to occur.

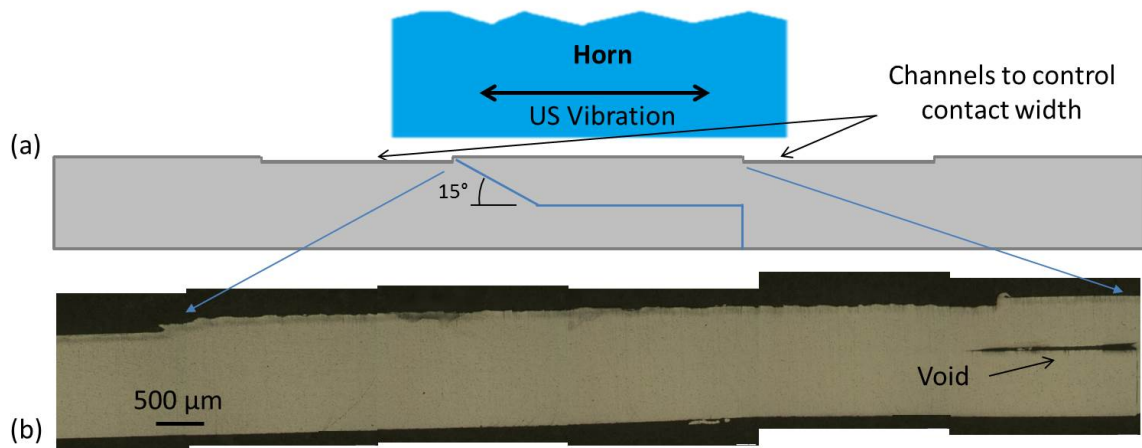


Figure 4.11: Angled lap joint (a) schematic and (b) cross section.

Attempts to use this concept along the entire length of a 0.076 in. (1.93 mm) thick joint shows some improvement in void content, however voids still persist at the deepest portions of the joint. A schematic and cross section of the full angle joint is shown in Figure 4.12.

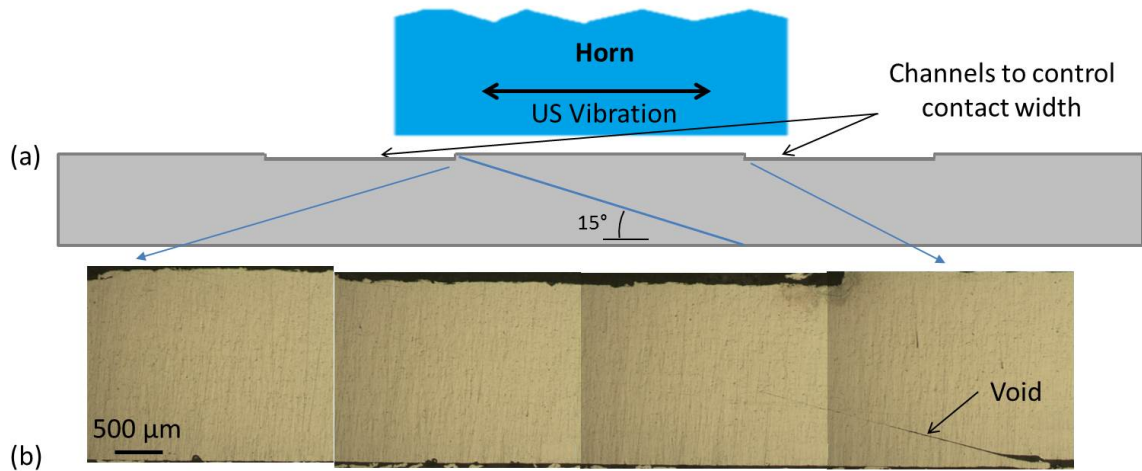


Figure 4.12: Scarf joint (a) schematic and (b) cross section.

Due to the presence of voids in the scarf joint design, as shown in Figure 4.12b, the use of a second weld pass was considered. A first attempt was conducted using two welds on the same side of the sheet, while staggering the contact area of the horn on the sheets. A concept of this weld and a cross section of the joint are shown in Figure 4.13. As is shown, a void still exists at the deepest section of the joint while the remainder of the joint exhibits no voids near the top.

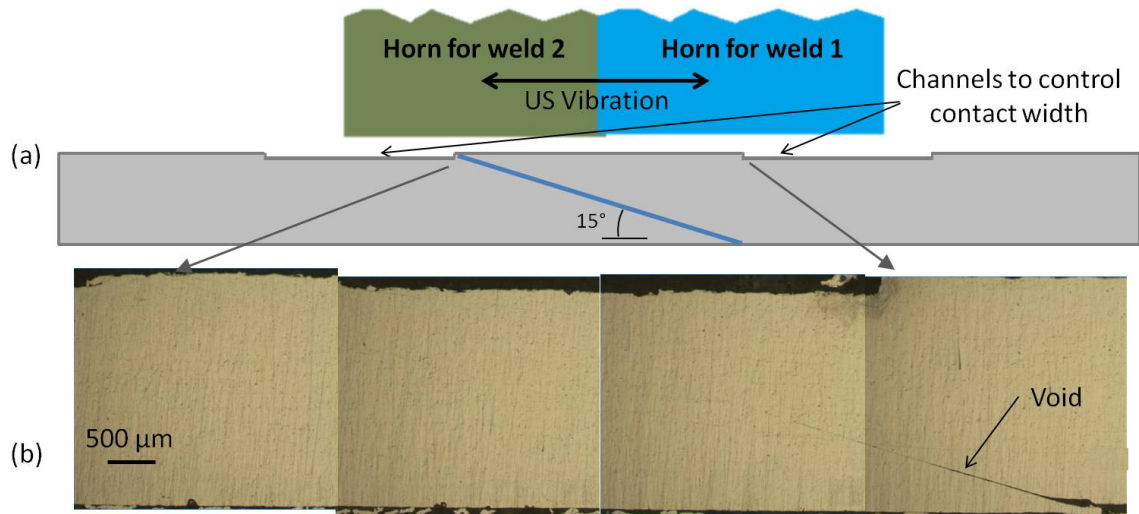


Figure 4.13: Scarf joint with side by side welding: (a) schematic and (b) cross section.

To eliminate voids throughout the length of the build, welds on each side of the sheet were considered. This approach was implemented by turning the sheet over after an initial weld pass and performing a second weld pass on the opposite side of the joint, as illustrated in Figure 4.14. As is shown, there are no apparent voids along the length of the joint; the faint lines in the image are an artifact of the polishing process.

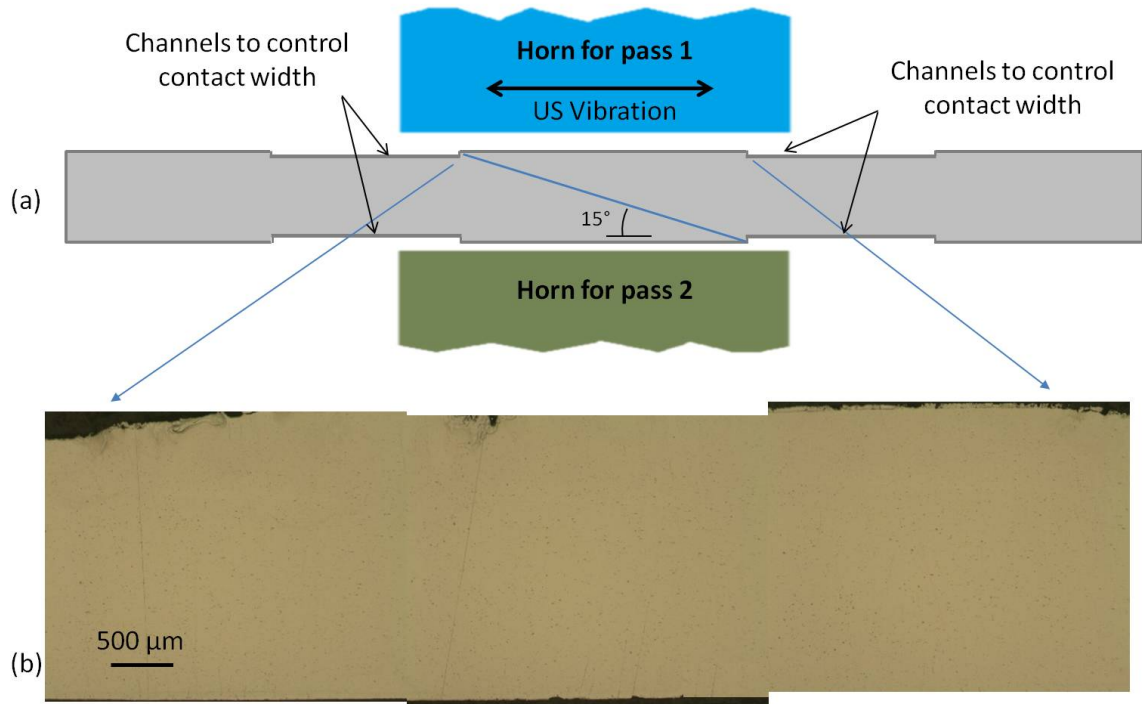


Figure 4.14: Scarf joint with welding on both sides: (a) schematic and (b) cross section.

4.1.2.1 Horn Film

In joining thicker sheet material, a thin film of aluminum is deposited on the horn. An image of the film is shown in Figure 4.15. It is believed that this film occurs due to the sonotrode scrubbing against the sheet during the weld process, creating a friction affect where aluminum is deposited onto the horn. While not prohibitive during the conceptual research stages, this phenomenon will require further investigation in the future to determine its effect on welding over time.

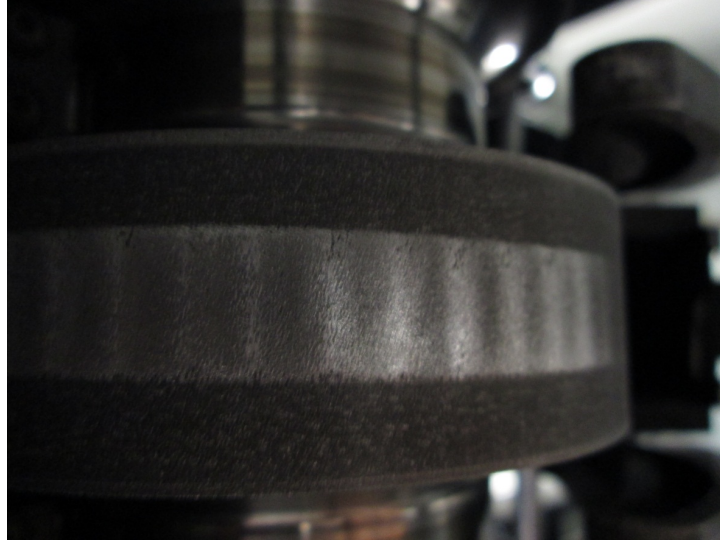


Figure 4.15: Image of aluminum film deposited onto horn after joining 0.020 in. (0.508 mm) thick stock material.

4.1.3 Design of Experiments for Joint Optimization

A lack of voids does not guarantee maximum strength for the joint. Therefore a design of experiments (DOE) study was performed to gain a better understanding of the effects of welder vibration amplitude, weld speed, and weld angle on joint strength. This study investigated five different weld angles, two levels of horn vibration amplitude, and two weld speeds for a scarf joint with welding on both sides of 0.076 in. (1.93 mm) thick Al 6061-T6 sheet. The experimental design is shown in Table 4.2.

For a constant joint thickness, if the angle varies, the width of the weld varies significantly, from 0.88 in. (22.35 mm) at 5° to 0.165 in. (4.19 mm) at 25° . Therefore, a constant normal force would apply varying levels of pressure to mating joint surfaces, confounding the process parameters being examined. To maintain constant

Table 4.2: Design of experiment for angle, amplitude, and weld speed

Angle (°)	Amplitude	Weld Speed (in/min) [mm/s]
5	High, Low	29 [12.28], 25 [10.58]
10	High, Low	29 [12.28], 25 [10.58]
15	High, Low	29 [12.28], 25 [10.58]
20	High, Low	29 [12.28], 25 [10.58]
25	High, Low	29 [12.28], 25 [10.58]

pressure for different angles, the applied normal force was varied based on the joint width. Additionally, the relative vibration amplitude applied along the mating joint surfaces changes with angle according to a cosine relationship. Due to this relationship, the amplitude was also compensated based on the angle during the study. The compensated weld parameters are provided in Table 4.3.

Table 4.3: Compensated weld parameters for low and high levels of amplitude.

Angle	Joint Width (mm)	Weld Force (N)	Low Amplitude (μm)	High Amplitude (μm)
5	22.35	5759	38.028	39.968
10	11.10	2924	38.468	40.43
15	7.29	2000	29.22	41.22
20	5.38	1556	40.315	42.371
25	4.19	1305	41.8	43.93

Due to the availability of angled end mills at the various angles desired, a vertical geometry was utilized for machining. Conceptually this is shown in Figure 4.16. Two aluminum backing plates were clamped around the sheet to be machined and clamped to angle plates on a 3-axis mill. These plates provide rigidity and minimize vibrations

during machining operations. Grinding was also tested as a manufacturing method, though took more time and was hindered by aluminum build up on the grinding disks.

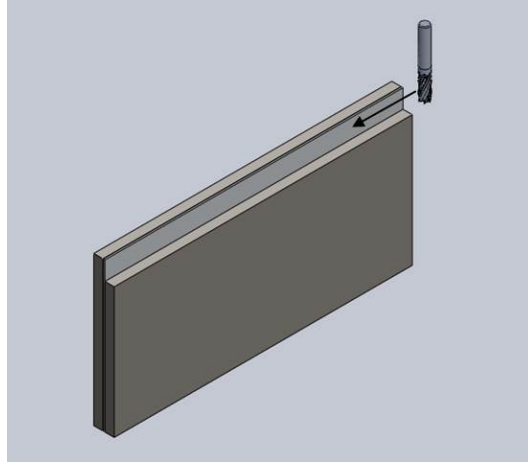


Figure 4.16: Method for machining plates at various angles.

To conduct the DOE, ultrasonically welded joints were manufactured for each of the parameters outlined in Table 4.3. Tensile tests were performed on the constructed joints using an Interlaken load frame with a 0.05 in/min (0.02 mm/s) displacement rate, measuring the load and displacement. Of note, elongation measurements were taken using the linear variable differential transformer (LVDT) within the load frame which includes deflection of the frame itself along with the sample. While inducing some error into the measurements, using elongation as a comparative response is viable. For all tests, samples were machined to a uniform thickness of 0.065 in. (1.651 mm), removing the channels machined during joint manufacturing, followed by machining to final dimensions. The sample dimensions are shown in Figure 4.17. Three tensile tests were performed for each of the build combinations.

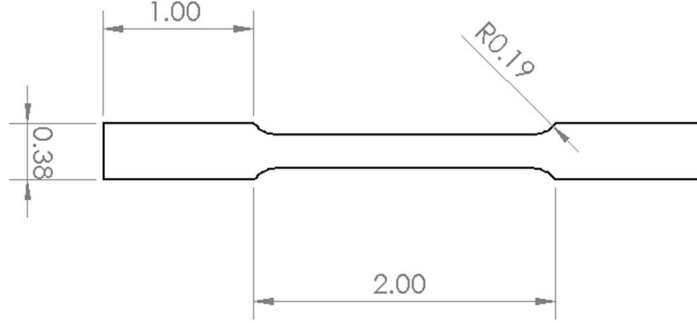


Figure 4.17: Schematic test specimen for tensile testing (dimensions in inches).

In addition to tensile testing, cross sections were prepared for each treatment combination. Sections were hot-mounted, ground, and polished using standard preparation techniques. The cross sections for each of the 20 trials are shown in Appendix B. Cross sections, while useful in determining whether voids exist, are insufficient in determining weld viability. Therefore the focus of the DOE study is on the mechanical test results, with cross sections used as supplemental information.

4.1.4 Analysis of Design of Experiments Study

Following the DOE, statistical analyses including analysis of variance (ANOVA) were conducted on the resulting data. ANOVA is used to compare three or more variables for their statistical significance on an examined process. The analysis uses a generalized linear model to describe the behavior, with the following form:

$$Y_{ijkt} = \mu + \alpha_i + \beta_j + \gamma_k + \epsilon_{ijkt}. \quad (4.1)$$

The linear equation (4.1) describes dependence of the response variable Y on the various treatment factors. In this case, Y is the tensile strength and μ represents

the overall mean of Y . The treatment factors α , β , and γ represent the main effects of the process parameters, with α_i denoting the effect of angle at the i th level while the other factors are fixed, β_j representing the effect of amplitude at the j th level, and γ_k representing the effect of weld speed at the k th level. The error variable ϵ represents any nuisance response in the model and exhibits a normal distribution with zero mean. All ϵ_{ijkt} are mutually independent with respect to i , j , k , and t . The statistical studies were performed using Minitab statistical software.

The ANOVA results for tensile strength are shown in Table 4.4. In the ANOVA table, the p-value represents the probability of obtaining a result at least as extreme as the observation, under the assumption that a null hypothesis of no effect is true. Lower p-values are indicative of stronger evidence against the null hypothesis. In this study, p-values of <0.05 are considered indicative of significant evidence against the null hypothesis. As shown in Table 4.4, p-values for both angle and amplitude are <0.05 , indicating that angle and amplitude have significant effects on ultimate tensile strength (UTS), while weld speed with a p-value of 0.946 does not have a significant effect over the range of speeds tested.

The main effects plots shown in Figure 4.18 reinforce these conclusions. In each plot, lower angles yield higher tensile strength. Likewise, for amplitude, high levels of amplitude lead to higher levels of tensile strength.

Table 4.4: ANOVA table for tensile strength.

Source	DF	Seq SS	Adj. SS	Adj. MS	F	p-value
Angle	4	1860.76	1860.76	465.19	49.26	<0.001
Amplitude	1	116.47	116.47	116.47	12.33	0.001
Speed	1	0.04	0.04	0.04	0	0.946
Error	53	500.55	500.55	9.44	-	-
Total	59	2477.8				

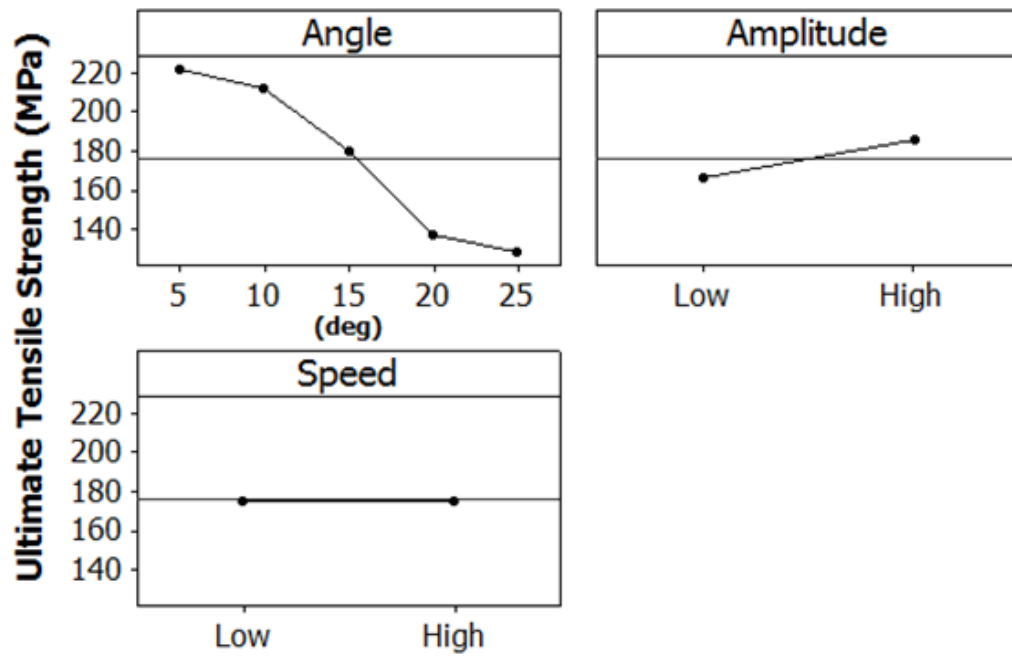


Figure 4.18: Main effects plot for ultimate tensile strength.

Similar trends are observed when considering elongation as the response variable. In the ANOVA table for elongation (Table 4.5), the effects of both angle and amplitude have p-values less than 0.05. Trends in the main effects plots show similar results,

whereby lower levels of amplitude result in higher elongation and high levels amplitude result in higher elongation.

Table 4.5: ANOVA table for elongation.

Source	DF	Seq SS	Adj. SS	Adj. MS	F	p-value
Angle	4	0.0257929	0.0257929	0.0064482	51.29	<0.001
Amplitude	1	0.0010532	0.0010532	0.0010532	8.38	0.006
Speed	1	0.0001216	0.0001216	0.0001216	0.97	0.33
Error	53	0.0066636	0.0066636	0.0001257	-	-
Total	59	0.0336312				

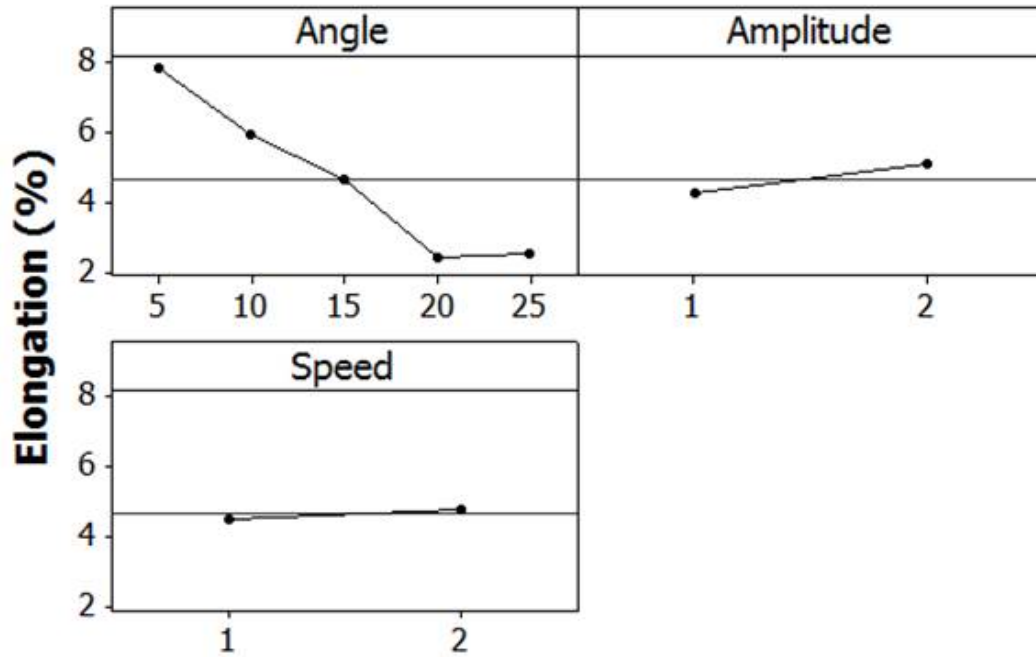


Figure 4.19: Main effects plot for elongation.

Residual plots for the responses of strength and elongation are provided in Figures 4.20 and 4.21. Each of the sets of plots shows no indications of trends, bias, or significant outliers in the data, indicating that the assumption of a normal distribution of residuals is met and that the general linear model used is appropriate.

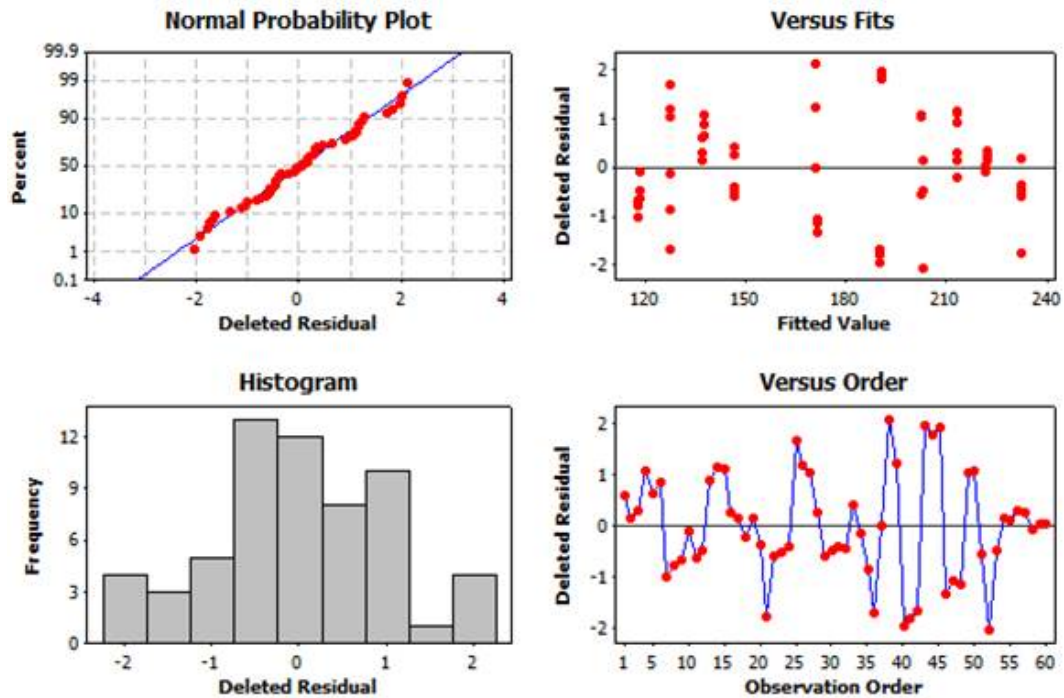


Figure 4.20: Residual plots for UTS.

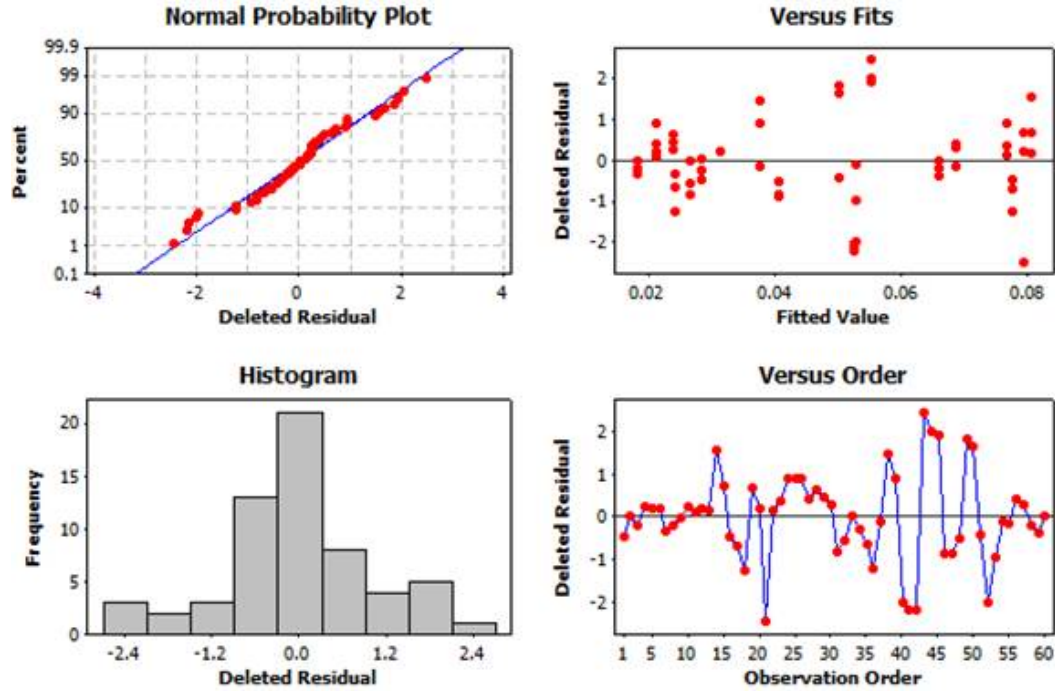


Figure 4.21: Residual plots for elongation.

To test whether interaction effects are present in the model, the various 2-factor interactions were investigated individually. Interaction effects for the strength results are shown in Figure 4.22. As is seen, no strong indications of interaction effects are observed. Figure 4.23 likewise shows little indications of interaction effects occurring in the elongation results. The associated ANOVA tables for the UTS and elongation responses with an angle-amplitude interaction are provided in Tables 4.6 and 4.7. Similarly, these results show that only the main effects of angle and amplitude are significant to a 0.05 level. The angle-amplitude interaction shown resulted in the lowest p-value at 0.084, statistically insignificant at the 0.05 level. All other interactions examined resulted in similarly insignificant p-values and are not presented for brevity.

These results are consistent with previous analyses in ultrasonic welding, which found interaction effects to be mostly insignificant on the process [41, 42, 87].

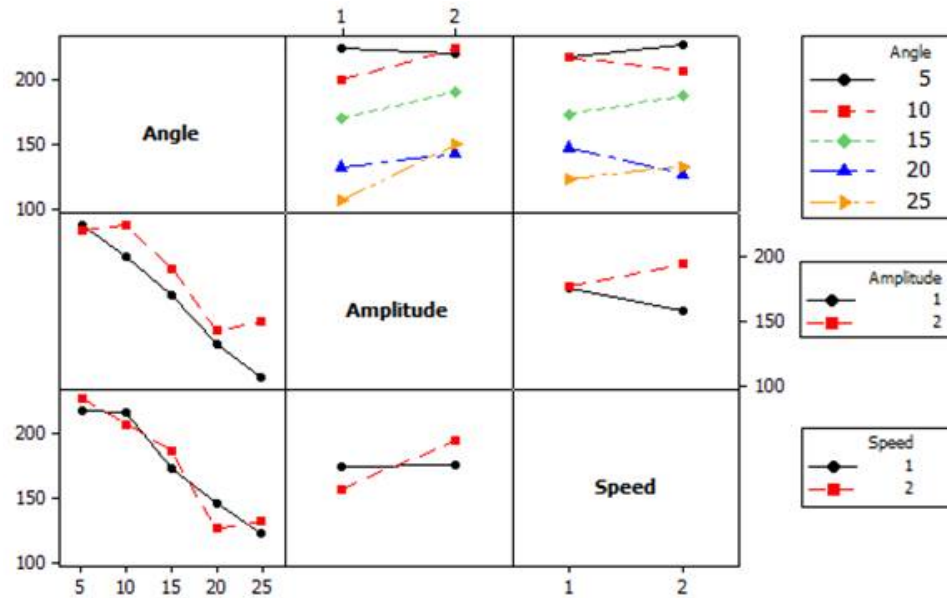


Figure 4.22: Interaction plots for UTS.

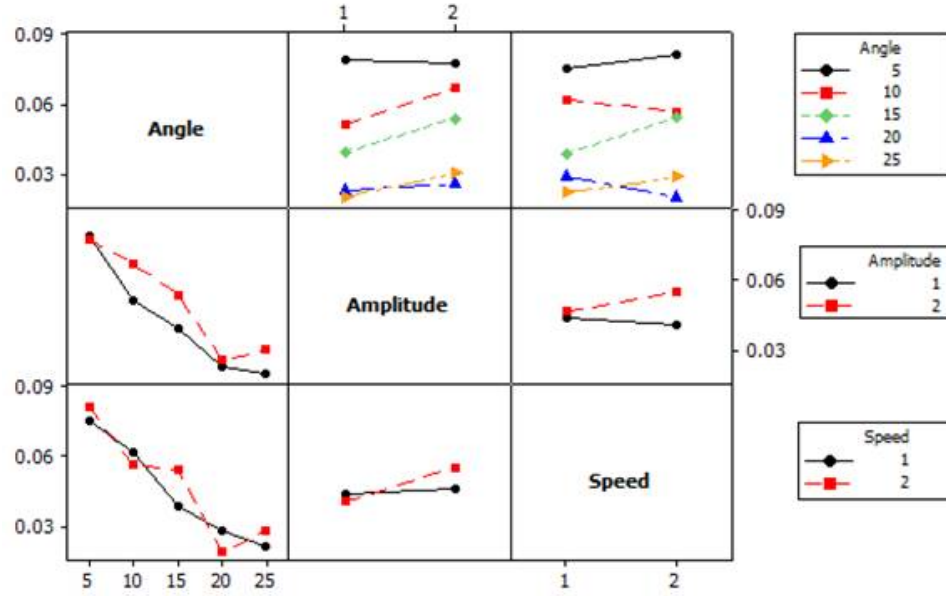


Figure 4.23: Interaction plots for elongation.

Table 4.6: ANOVA table for UTS including interaction effects.

Source	DF	Seq SS	Adj. SS	Adj. MS	F	p-value
Angle	4	1860.76	1860.76	465.19	53.67	<0.001
Amplitude	1	116.47	116.47	116.47	13.44	0.001
Speed	1	0.04	0.04	0.04	<0.00	0.946
Angle*Amp.	4	75.84	75.84	18.96	2.19	0.084
Error	49	424.71	424.71	8.67	-	-
Total	59	2477.81				

Optimal conditions for strength can be determined using Tukey pairwise comparisons to compare the significance of variation from one level to the next [18]. The Tukey comparisons follow the equation,

Table 4.7: ANOVA table for elongation including interaction effects.

Source	DF	Seq SS	Adj. SS	Adj. MS	F	p-value
Angle	4	0.0257929	0.0257929	0.0064482	52.59	<0.001
Amplitude	1	0.0010532	0.0010532	0.0010532	8.59	0.005
Speed	1	0.0001216	0.0001216	0.0001216	0.99	0.324
Angle*Amp.	4	0.0006561	0.0006561	0.00001640	1.34	0.269
Error	49	0.0060075	0.0060075	0.0001226	-	-
Total	59	0.0336312				

$$\tau_i - \tau_s \in (\bar{y}_i - \bar{y}_s) \pm \omega_T \sqrt{msE\left(\frac{1}{r_i} + \frac{1}{r_s}\right)}, \quad (4.2)$$

where ω_T is taken from a studentized distribution depending on the data set. When interpreting Tukey pairwise comparison tables, if a comparison range from the lower to higher value includes zero, it is not considered statistically significant. If the comparison range does not include zero, it indicates that a statistically significant difference between two levels is observed at a 95% confidence.

Tukey pairwise comparisons between the levels of angle and the levels of amplitude are presented in Tables 4.8 and 4.9 for the ultimate tensile strength data. From Table 4.8, it can be seen that the levels for the 5° and 10° angles are not statistically different, while the differences between 5° and all other angles are significant. Because there is no statistically significant difference between 5° and 10°, this study indicates that either of these angles is acceptable for maximizing mechanical strength. Pairwise comparisons for the two levels of amplitude, shown in Table 4.9, confirm the ANOVA results that the low and high levels are significantly different statistically.

Based on the results and analyses of the DOE study, the best weld parameters for these joints within the levels tested are presented in Table 4.10. A 10° scarf joint

Table 4.8: Tukey 95% pairwise comparisons among levels of angle compared with Angle = 5°.

Angle	Lower	Center	Upper
10	-5.07	-1.53	2.01
15	-9.66	-6.12	-2.58
20	-15.99	-12.45	-8.91
25	-17.32	-13.78	-10.24

Table 4.9: Tukey 95% pairwise comparisons among levels of amplitude compared with low level of amplitude.

Amplitude	Lower	Center	Upper
High	1.195	2.786	4.378

angle was selected because its strength was statistically equivalent to the 5° joint angle while being easier to machine. Of note, these are optimized parameters within the levels tested and may not represent a global optimum.

Table 4.10: Optimal levels for seam welding as determined by DOE.

Parameter	Level
Weld Force	2924 N
Weld Speed	25 in/min
Amplitude	41 μm
Angle	10°

4.1.5 Finite Element Modeling of Scarf Joint Angles

To better understand the effect of the weld angle on bonding, a finite element analysis was performed using COMSOL Multiphysics. The geometry modeled uses

one side of the joint, configured in a 2D plane strain approximation. The loading conditions applied are shown in Figure 4.24. The weld amplitude is applied via static displacement at the top of the sheet, similar to how the weld force is applied. Along the bottom of the sheet, a roller condition is used for the first inch (2.54 cm) away from the angle and a fixed condition is used after that, representing the fixturing conditions of the vacuum chuck. To simplify the model, a condition of no y-direction displacement is used along the angled weld surface. This simplification emulates the effect of the second sheet, while eliminating the need for contact elements. All five angle conditions were modeled separately, according to the compensated amplitudes and forces used in the DOE study (Table 4.3).

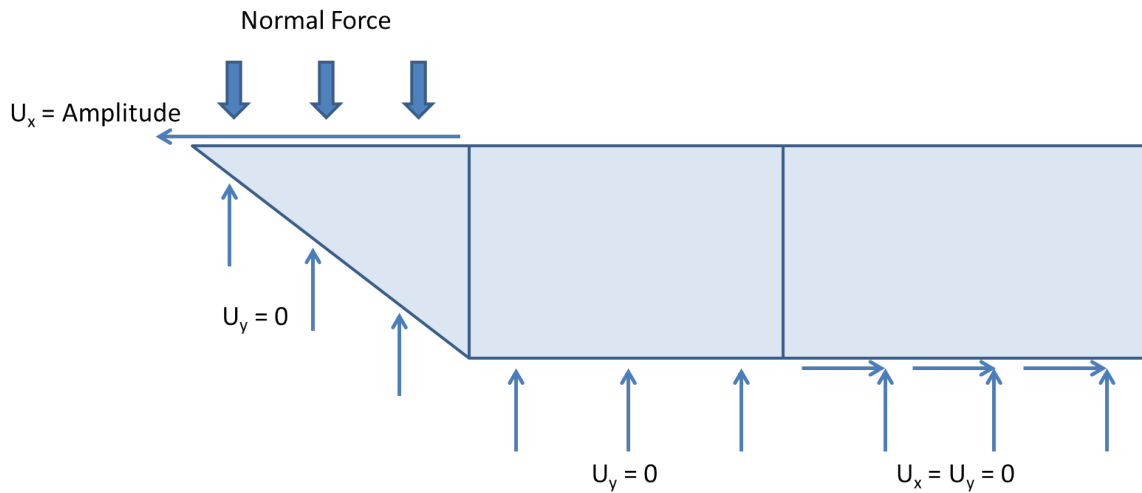


Figure 4.24: Boundary conditions and loads applied to FEA model.

The model results showing the x-displacement for each condition are presented in Figure 4.25. The x and y dimensions are presented in millimeter units and the

x-displacement units are in microns. As the angle increases, the location where the displacement decreases moves higher on the angled portion of the joint. Comparison of the 5° condition with the 25° condition shows this clearly, where the $38\text{ }\mu\text{m}$ contour for the 25° case is 0.559 mm from the bottom of the joint while this contour is 0.279 mm from the bottom of the joint for the 5° case. Because the ultrasonic welding process is based on relative motion, the differences in relative displacement could explain the relative differences in strength observed between the various angles.

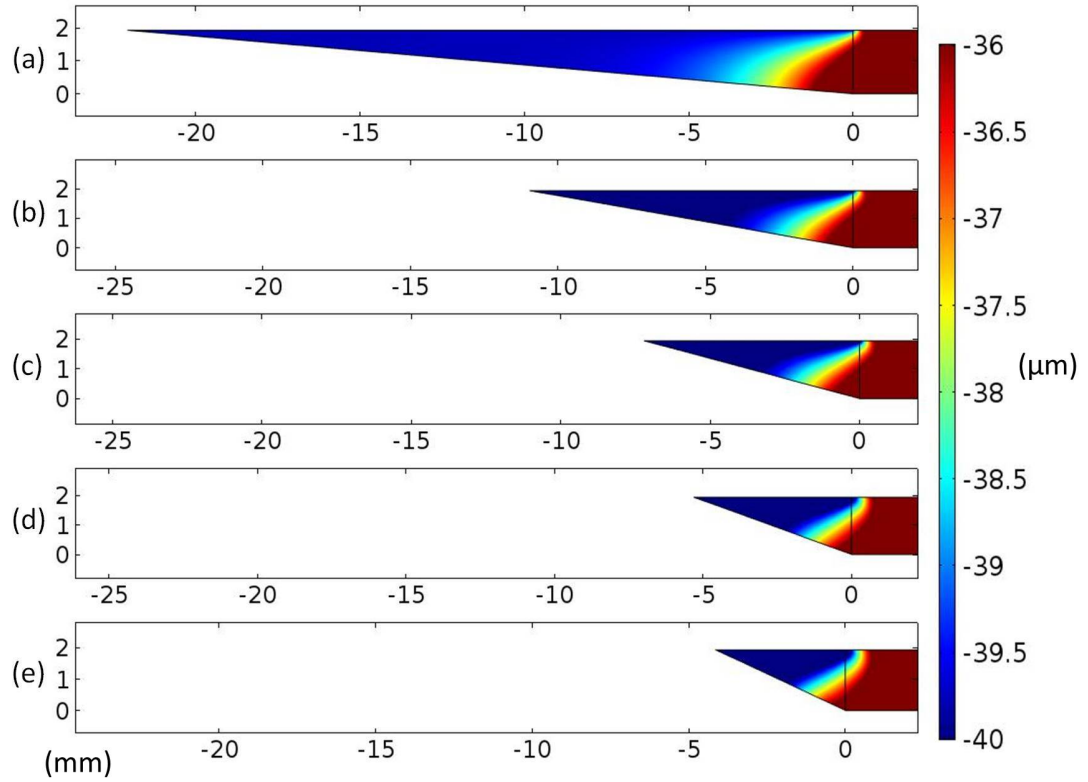


Figure 4.25: Horizontal displacement results for each of the five angles modeled (a) 5° (b) 10° (c) 15° (d) 20° and (e) 25°

4.2 Mechanical Characterization of Optimized Joints

Using the optimized values determined via the DOE study (Table 4.10), scarf joints of 0.076 in. (1.931 mm) thick Al 6061-T6 sheets were welded for mechanical testing. Room temperature tensile tests high temperature tensile tests at 210 °C, and room temperature fatigue tests were conducted to characterize the joint strength.

4.2.1 Room Temperature Tensile Testing

Room temperature tensile tests were performed using an Interlaken load frame, with load measured using a load cell with a 5000 lb. (22,241 N) range and displacement measured via the linear variable differential transformer built into the frame. Tests were performed using a displacement rate of 0.05 in/min (0.02 mm/s). Test results for the three as-built joints are presented in Table 4.11. The resulting average tensile strength is 221.3 MPa while the tensile strength of bulk aluminum 6061-T6 is 310 MPa [3].

Table 4.11: Room temperature ultimate tensile strength (UTS) test results for as-built Al 6061 joints

Sample	UTS (MPa)
1	220.0
2	222.2
3	221.5
Avg.	221.3
St. Dev.	1.1

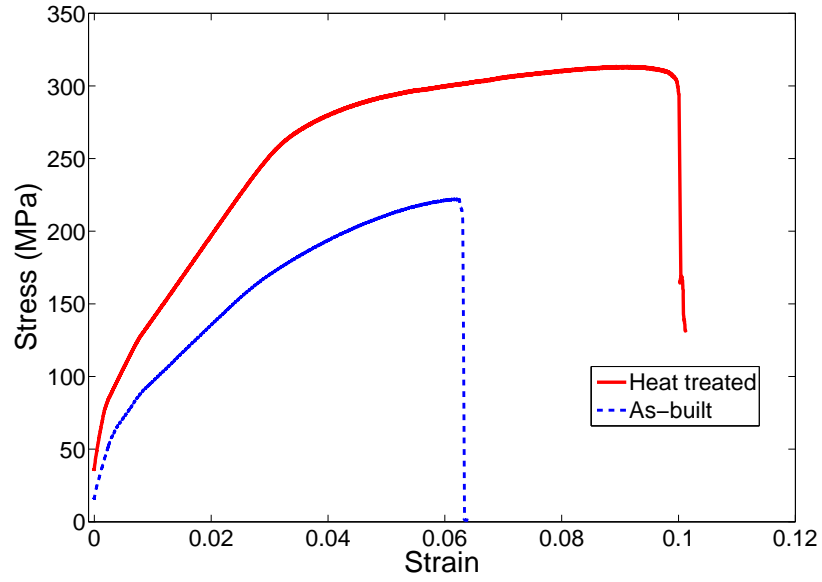
Heat treatments were investigated as a means to improve the tensile properties following joining. Joint samples were prepared following the T6 treatment for aluminum 6061, by solutionizing at 530 °C followed by aging at 160 °C for 18 hours [2]. Test results for the three joints are presented in Table 4.12. The tensile strength of the heat treated samples increases from an average of 221.3 MPa to 311.0 MPa, matching bulk material [1]. These results indicate that tensile strength of the joints can be maximized and that bulk material properties can be achieved using a post-process heat treatment.

Table 4.12: Room temperature ultimate tensile strength (UTS) test results for heat treated Al 6061 joints

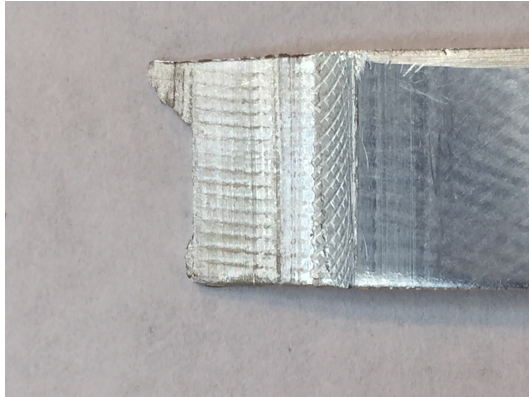
Sample	Room Temp. UTS (MPa)
1	313.0
2	297.9
3	322.0
Avg.	311.0
St. Dev.	12.2

Representative stress-strain curves for the as-built and heat treated material are shown in Figure 4.26. As is shown, the curves and tabulated data indicate that post-process heat treatments can provide significant enhancements in the tensile strength and elongation. Representative fracture surfaces for the as-built and heat treated samples are shown in Figure 4.26b and c. For the as-built sample, failure occurs along the joint, with little ductility, as shown by the relatively straight edge along the failure line. The heat treated sample, in contrast, shows much higher ductility, with

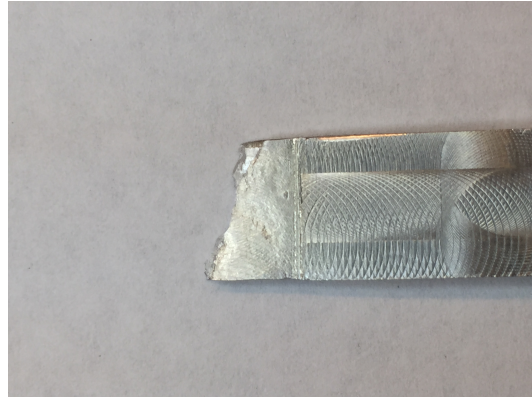
the failure surface traveling throughout the bond zone with a failure line traveling diagonally through the joint.



(a)



(b)



(c)

Figure 4.26: (a) Representative room temperature tensile test results for as-built and heat treated joints (b) Fracture surface of as-built joint (c) Fracture surface of heat treated joint.

4.2.1.1 Age-Only Heat Treatment

The effect of using an age-only heat treatment was investigated using similarly produced joints. In this case, the heat treatment used is the aging treatment of 160 °C for 18 hours. This treatment is used to investigate whether the drop in strength in the as-built joints is due to a resolutionization or migration of the strengthening precipitates away from the interface during welding. Similarly, removing the solutionizing step in the heat treatment can significantly increase production and lower costs in a final application. Room temperature tensile tests were performed similarly on these samples; with results from the three samples presented in Table 4.13. As is shown, similar performance is achieved for the samples that were only aged, and not resolutionized.

Table 4.13: Room temperature tensile test results of aged-only Al 6061-T6 joints.

Sample	UTS (MPa)	Elongation (%)
1	311.6	6.5
2	304.7	5.7
3	328.2	7.8
Avg.	315.1	6.7
St. Dev.	12.4	1.1

4.2.2 High Temperature Tensile Testing

To characterize the high temperature tensile behavior of the joints, tensile tests were performed at 210 °C within a thermal chamber on a Test Resources load frame with a displacement rate of 0.05 in/min (0.02 mm/s). Samples were heat treated to the T6 condition, then subjected to 210 °C for 30 min. prior to initiating the tests. Results of the six tests are shown in Table 4.14. The results compare favorably with

bulk material, with an average tensile failure strength of 184.1 MPa, similar to bulk material strengths of 186.2 MPa [1].

Table 4.14: High temperature tensile test results of heat treated Al 6061-T6 joints.

Sample	UTS (ksi)	% Room Temperature UTS	Elongation (%)
1	193.1	62.2	14.1
2	196.5	63.3	14.1
3	164.8	53.1	23.1
4	179.3	57.8	26.1
5	195.8	63.1	11.8
6	175.1	56.4	23.1
Avg.	184.1	59.3	18.7
St. Dev.	13.1	4.2	6.1

Reference curves from MMPDS data are shown in Figure 4.27 along with superimposed results from welded joints in Figure 4.28. As is shown graphically, results of welded and heat treated joints show similar mechanical strength under elevated temperature tensile testing conditions.

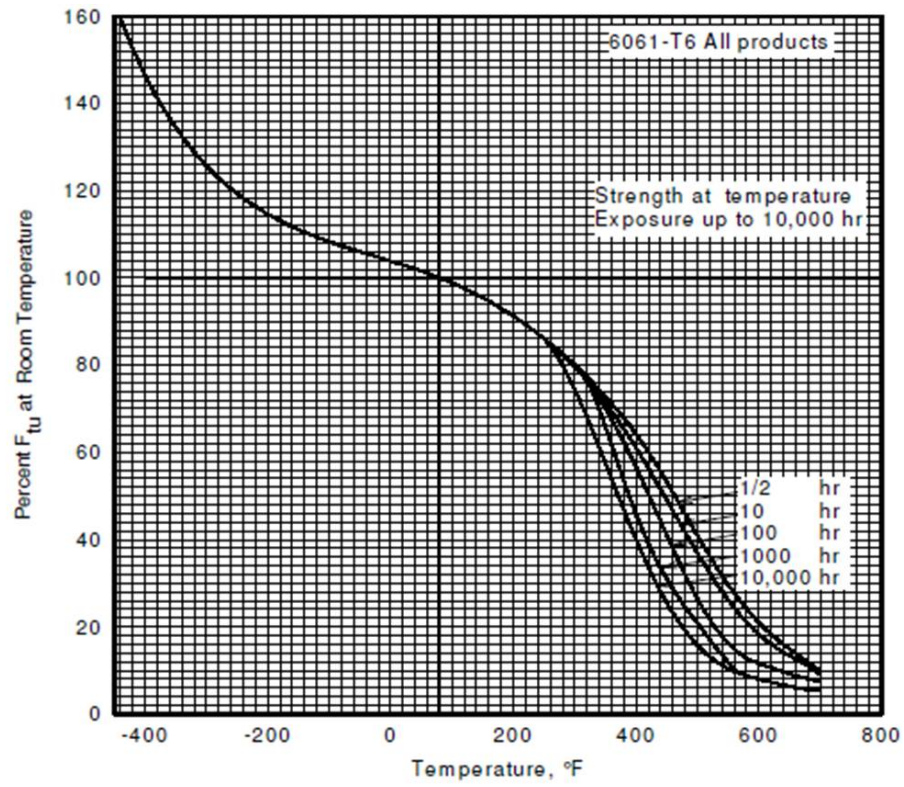


Figure 4.27: Reference data from MMPDS for elevated temperature tensile strength of Al 6061-T6 [1].

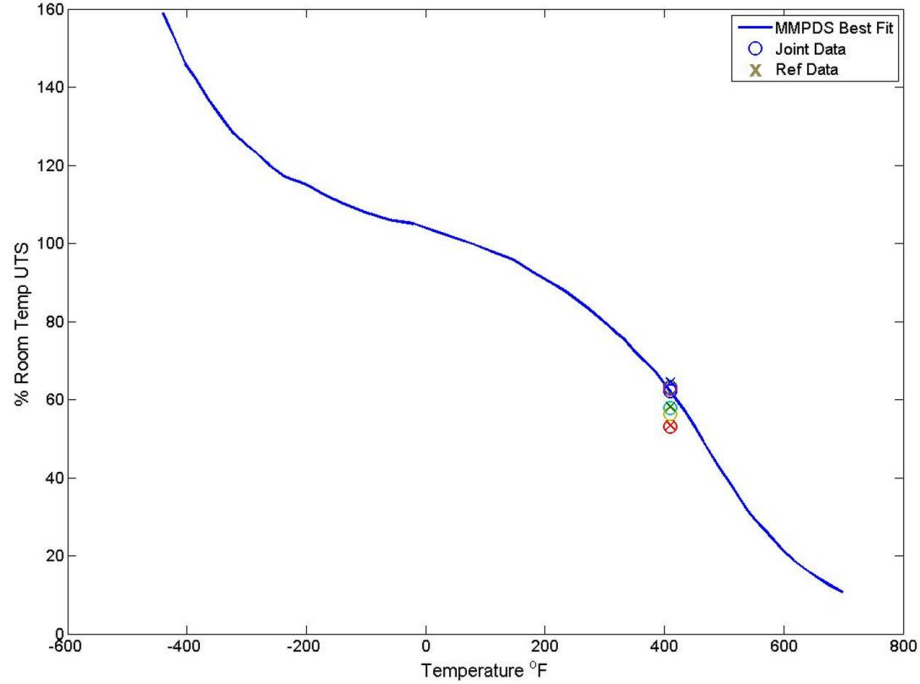


Figure 4.28: Comparison of high temperature tensile strength of welded test samples to reference and MMPDS data.

4.2.3 Room Temperature Fatigue Testing

To characterize the cyclic performance of the joints, room temperature fatigue testing was conducted on samples that were heat treated to the T6 condition. An MTS 831 test frame was used to apply a cyclic load with a maximum stress of 32 ksi (220.63 MPa) and a minimum stress of 1.6 ksi (11.03 MPa), resulting in an R-ratio of +0.05. The sinusoidal load was applied to the samples at 50 Hz until failure and the number of cycles to failure was recorded for each test. The results of the six tests are shown in Table 4.15. On average, the number of cycles to failure is approximately 190,000. Bulk aluminum material was tested under the same conditions, resulting in failure after 250,000 cycles. Published values for bulk aluminum 606-T6 indicate

failures after roughly 700,000 cycles using cylindrical samples, but otherwise similar test conditions [1]. The MMPDS data for the cylindrical geometry samples is shown in Figure 4.29, with superimposed data from the joints tests shown in Figure 4.30. As is shown graphically, despite a rectangular sample design that creates stress concentrations at the corners, resulting fatigue strengths are on the same order as bulk aluminum.

Table 4.15: Cycles to failure for room temperature fatigue testing.

Sample	Cycles to Failure
1	169437
2	265556
3	168265
4	158542
5	184063
6	217324
Avg.	193864

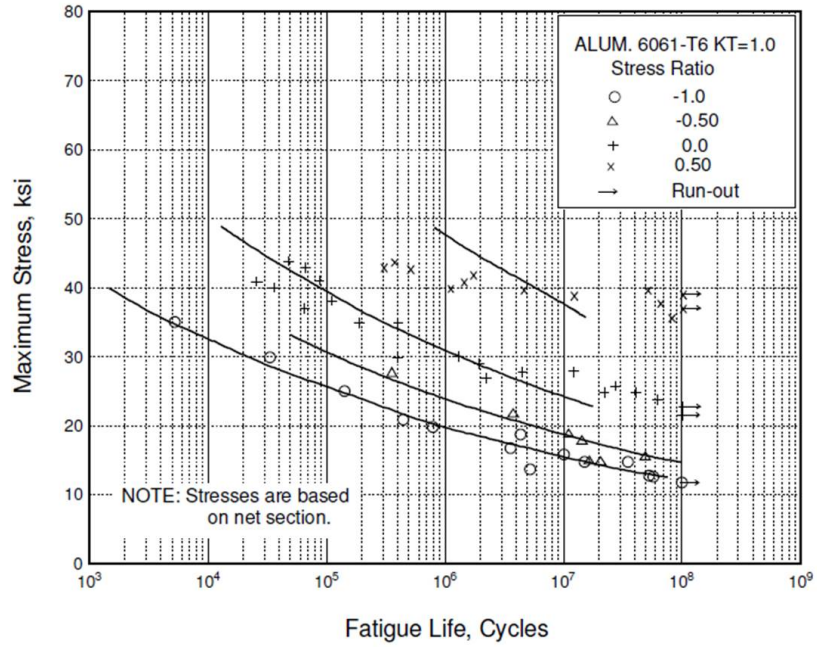


Figure 4.29: Reference data from MMPDS for fatigue testing of Al 6061-T6 material.

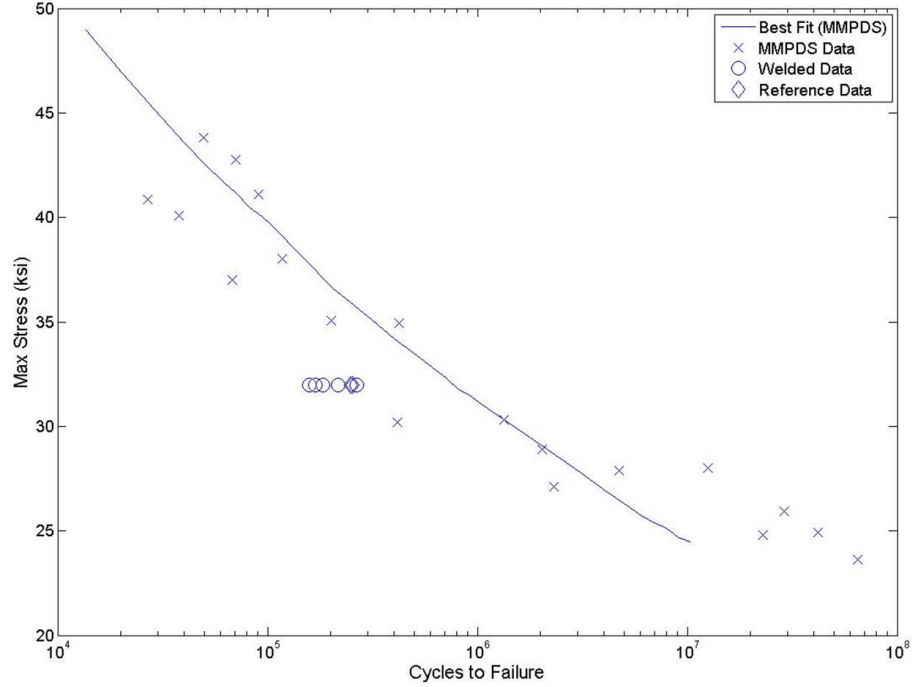


Figure 4.30: Comparison of fatigue performance of welded test samples to reference and MMPDS data.

4.3 Discussion

A design of experiments study found that lower scarf joint angles produce higher ultimate tensile strengths within the levels tested. Finite element analysis indicates that higher relative displacements are occurring throughout the low angle joints. Because relative motion is the basis for ultrasonic joining, this likely produces the higher bond strength observed for lower angles.

Tensile tests on as-built scarf joint samples yielded an average tensile strength of 221.3 MPa, which is 29% lower than the UTS of bulk Al 6061-T6. Microsections of the joint do not indicate the presence of voids; therefore other explanations for the decrease in strength are necessary. Aluminum 6061 is an age-hardenable material

relying on solid solution and precipitation hardening as mechanisms for improving strength. During the ultrasonic joining process, the precipitates at the interface may be resolutionizing or migrating away from the interface, resulting in a decrease in strength. The strength of fully solutionized material is 241.3 MPa [3], similar to the as-built samples, supporting this hypothesis. Post-process heat treatments have been successful in improving joint strength, indicating that the heat treatment is reintroducing precipitates at the interface that provide strengthening. Additionally, age-only heat treatments produce strengths similar to bulk material, indicating that the aging treatment is reintroducing the strengthening precipitates to the weld interface. To confirm this hypothesis within the microstructure, high resolution microstructural evaluations, including nanoindentation at the joint interface, would be required.

High temperature tensile tests show that heat treated joints provide strengths similar to bulk material. This provides further evidence of the joint quality achievable using a post-weld heat treatment. Similarly, the fatigue performance approaches that of bulk material with joint failures occurring after 190,000 cycles on average compared to bulk material failures after 250,000 cycles. These values are less than published bulk material results, which may be a result of differences in test specimen geometry. The rectangular shape of the specimens can influence fatigue performance due to stress concentrations at sharp corners, which could be mitigated by using circular specimens [24]. Comparison of the sheet specimens welded in this study to the cylindrical samples presented in MMPDS data, therefore is not a direct comparison.

The use of UAM equipment in the non-traditional configuration presented here is an expansion of the capabilities of the technology. With UAM, multiple foils are typically built up to a desired dimension; however the methodology presented here

enables 0.076 in. (1.9304 mm) thick sheets to be joined with a single weld joint, increasing throughput. Using these joining concepts, it may be possible to integrate the ultrasonically joined scarf joints with traditional UAM applications and other manufacturing methods to increase the speed and reduce the cost of part fabrication. For example, part of a structure with embedded features such as cooling channels, sensors, electronics, or reinforcements could be built using UAM and then joined with sheets or parts produced using conventional processes.

4.4 Seam Joining using Al 2219

Following the successful weld joints created using Al 6061 sheet material, attempts were performed to join Al 2219 sheet material. A 10° scarf joint configuration was used based on the optimized results from the study on Al 6061. Initial weld parameters followed those successful for Al 6061. A cross section of the first weld trial with the 2219 material is shown in Figure 4.31. As is seen, a void is present in the center of the joint. Following this trial, subsequent weld trials were performed with increasing weld energy applied to the joint. The parameters used for the trials are summarized in Table 4.16. Within the trials, weld force, weld speed, and weld amplitude were varied with amplitude increasing significantly from the optimal values found for Al 6061. Cross sections of the weld trials are presented in Figures 4.32-4.36. As is shown, despite significant increases in applied weld energy, voids remain in the center of each joint.

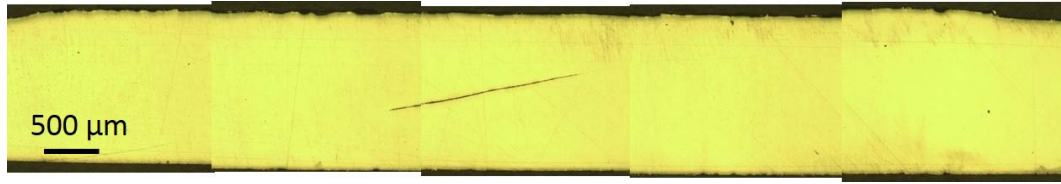


Figure 4.31: Cross section of trial 1 with Al 2219.

Table 4.16: Weld trials process parameters for Al 2219 material.

Weld Trial	Weld Force (N)	Weld Speed (in/min)	Weld Amplitude (μm)
1	3000	25	41
2	3000	25	43.66
3	4000	25	44.7
4	3000	20	46.83
5	3500	20	48.94
6	3500	20	52.11

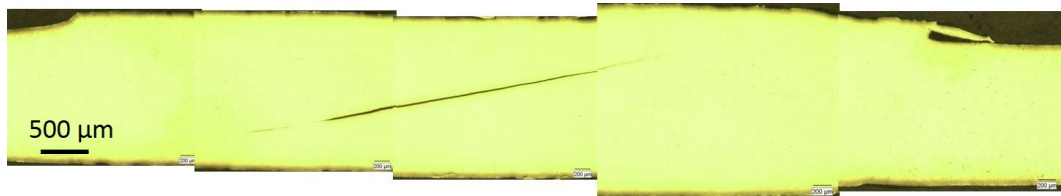


Figure 4.32: Cross section of trial 2 with Al 2219.

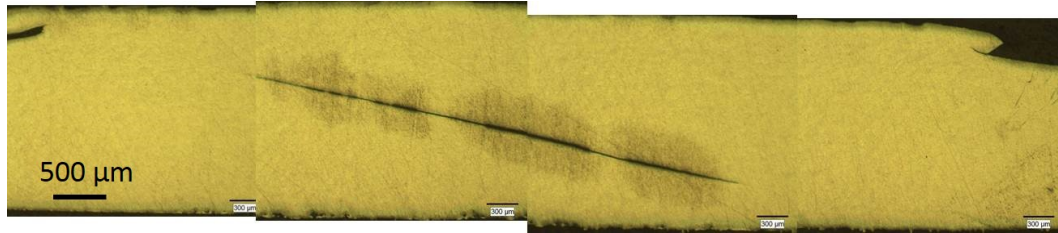


Figure 4.33: Cross section of trial 3 with Al 2219.

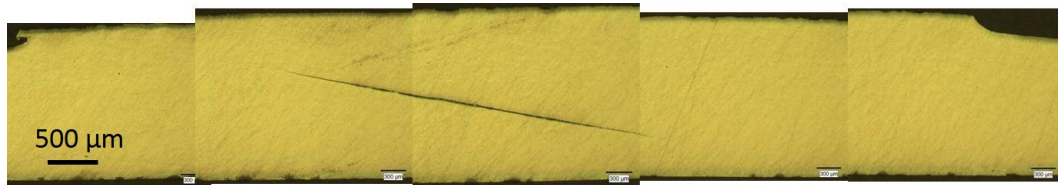


Figure 4.34: Cross section of trial 4 with Al 2219.

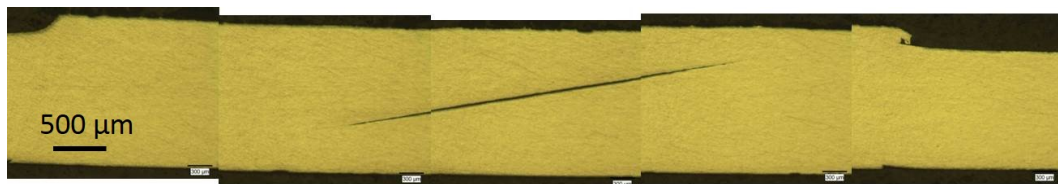


Figure 4.35: Cross section of trial 5 with Al 2219.

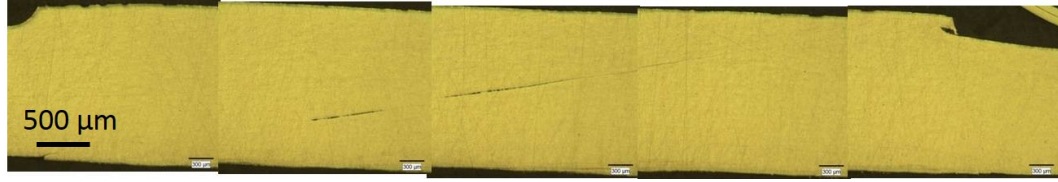


Figure 4.36: Cross section of trial 6 with Al 2219.

4.4.1 Discussion

Attempts to join Al 2219-T31 sheet material have shown that the material can be welded. However, voids in the center of the joint indicate incomplete joining through the thickness and an associated decrease in mechanical strength. It is hypothesized that differing material properties and varying responses to cold work explain the differences in the joining behavior of 2219 and 6061. While 6061-T6 and 2219-T31 each have yield strengths of 250 MPa, their ultimate tensile strengths vary significantly, from 310 MPa for 6061-T6 to 360 MPa for 2219-T31 [1]. The UAM process imparts significant cold work during processing, thus the larger cold work strengthening exhibited by 2219 may explain the lack of complete welding along the thickness of the joint. It may be possible to achieve a complete weld along the length of the joint in thinner material stock, where any losses or joint compliance could be minimized.

Future work will be necessary to achieve a complete joint, including the investigation of additional process conditions such as heating the baseplate during welding, material temper, and surface roughness of mating sheets, in addition to fine tuning weld force, weld speed, and joint angle. Similar studies could likewise be performed on thinner material stock as well.

4.5 Summary

A methodology was developed for joining aluminum 6061 sheets of 0.076 in. (1.93 mm) thickness using ultrasonic welding. The joint design uses a scarf joint configuration and ultrasonic joining on both sides of the sheet to achieve successful welding. A design of experiments approach identified a 10° angle as optimal for joining with an amplitude of 41 μm and weld speed of 25 in/min as optimal welding parameters. Resulting as-built joints yielded tensile strengths of 220 MPa, 90 MPa less than solid material. Therefore a heat treatment process was applied to the joints, resulting in room temperature tensile strengths of 310 MPa, matching solid material. High temperature tensile testing yielded results similar to solid material. Likewise, the cyclic fatigue behavior of the heat treated joints approaches that of solid material. While joints can be achieved using Al 2219-T31 material future work will be required to achieve fully dense joints.

Chapter 5: DISSIMILAR MATERIAL JOINING WITH UAM

Introduction

Joining of material combinations including aluminum and titanium, aluminum to steel, steel to aluminum, and steel to steel are examined in this chapter. Examinations include developments to achieve suitable welds through pilot studies. Material combinations are then examined via mechanical strength and microstructural techniques.

5.1 Al/Ti Joining

5.1.1 Experimental Methods

5.1.1.1 Sample Manufacturing

Aluminum and titanium dissimilar joints were examined using the Fabrisonic 4000 9 kW UAM system. Al 1100 foils and commercially pure titanium foils 0.005 in. (0.127 mm) thick were investigated. Nominal compositions and ultimate tensile strengths for these materials are given in Table 5.1. During joining, a bilayer arrangement is used where titanium on top of aluminum is welded in one step. This is shown schematically in Figure 5.1. In this arrangement, the sonotrode is in contact with the

titanium layer only, limiting the potential for welding aluminum foil to the sonotrode. All samples were built onto a solid aluminum 6061-T6 baseplate with the Al 1100/Al 6061 interface as the first layer.

Table 5.1: Nominal composition (wt%) and ultimate tensile strength (UTS) of materials.

Material	C	H	O	N	Fe	Ti	UTS (MPa)
Cp Ti	0.10	0.015	0.25	0.03	0.25	balance	343
	Si	Cu	Mn	Zn	Residuals	Al	UTS (MPa)
Al 1100-O	1.0	0.05-0.20	0.05	0.10	0.15	99.0 min	90

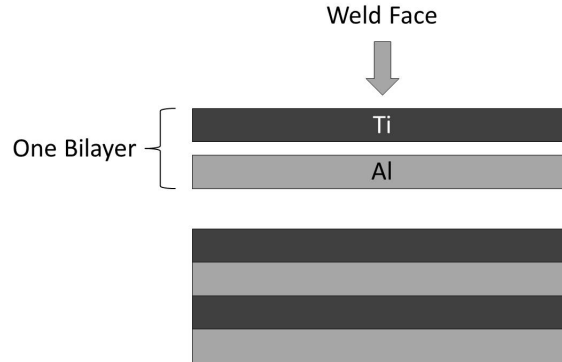


Figure 5.1: Arrangement for Al/Ti bilayers.

Previous work in 1 kW UAM proved joining of Al/Ti builds and identified optimal build parameters using a design of experiments approach for Cp Ti and Al 1100 [41]. With the developments associated with 9 kW UAM, specifically increases in applied amplitude, it is necessary to reexamine these parameters, as 9 kW UAM has exhibited

improvements in bond quality for other material systems [87]. Weld amplitude has been shown to provide increased bond strength for both 1 kW and 9 kW UAM [41, 42, 87].

Pilot studies were performed to identify the viable weld parameters for Al/Ti builds with 9 kW UAM. Weld trials were conducted using the bilayer arrangement on an aluminum 6061-T6 baseplate while varying process parameters including weld force, weld amplitude, weld speed, and baseplate temperature. Weld trials were considered successful when the material bonded to the baseplate and could not be pulled off manually. In most trials, Al 1100 would bond well to the Al 6061 baseplate, however achieving a successful bond of titanium to Al 1100 was more difficult. Successful process parameters for Al/Ti from pilot studies is shown in Table 5.2. These parameters were used for all builds performed in this study. The parameters produce suitable welds, but do not necessarily represent a globally optimized set.

Table 5.2: Weld parameters used for Al/Ti joints.

Parameter	Level
Weld Force	3500 N
Weld Speed	60 in/min
Amplitude	41.55 μm
Temperature	200 °F
Horn Texture	7 μm , R_a

5.1.1.2 Joint Characterization

Following the process parameter trials, builds were examined for their mechanical performance as well as microstructure. Mechanical performance was investigated via push-pin and shear testing. The push-pin test is a comparative test that provides a

metric of bond strength via delamination of a build. The test was originally proposed by Zhang [89], and has proven viable in other studies [82, 87]. This test is used instead of a traditional tensile test because it provides a measurement of the bond strength in a relatively small number of layers, significantly reducing costs. Likewise the samples are easily machined using the UAM system and three-axis mill. More details on the test can be found in work by Zhang et al. [89] and in Chapter 1.

Buils for the tests were constructed using five Al/Ti bilayers, 10 total layers, with a hole machined through the base layer to the first layer of aluminum. This is the first layer tested, though as the test progresses, the pin presses through to other layers as well. Push-pin tests were performed in a Gleeble 3800 thermo-mechanical test frame at room temperature. During the test, a pin is pressed through the sample at 0.2 mm/sec with the load and displacement being recorded. The maximum force during the pushout as well as the area under the curve, or mechanical work, are the two metrics used to analyze the results of the test.

Following push-pin sample construction, designated builds were heat treated to examine the effect of heat treatments on mechanical and microstructural properties. Heat treatments were performed in a conventional induction furnace in an air atmosphere at 600 °C for one hour, following previous work [26, 50]. Work by Fuji and Kim in friction welding of Al/Ti combinations has shown that this treatment produces optimized tensile strength and elongation, as well as material failures away from the joint interface.

Shear testing was conducted on samples with 16 bilayers, 32 total layers, sectioned into 5 x 5 mm samples and mounted in a specially designed test module. The test

setup ensures that shear occurs within the layered structure and not through the aluminum baseplate material. Specimens were tested using a 50 kN Lloyd mechanical test frame with load applied until failure. Figure 5.2 shows the sample, the loading conditions, and the sample within the test fixture. Shear testing was conducted on as-built and heat treated samples. The heat treatment used is the spark plasma sintering process (SPS) which consists of increased temperature and pressure, under inert atmosphere. The technique is commonly used for sintering powders, however has been used in joining of dissimilar material joints of Ti and steel [59, 60]. SPS treatment in an FCT System was conducted at 500 °C for 600 s under argon atmosphere (10^{-2} torr) and uniaxial pressure of 15 MPa. All shear testing and related SPS heat treatments were performed in collaboration with Ben-Gurion University.

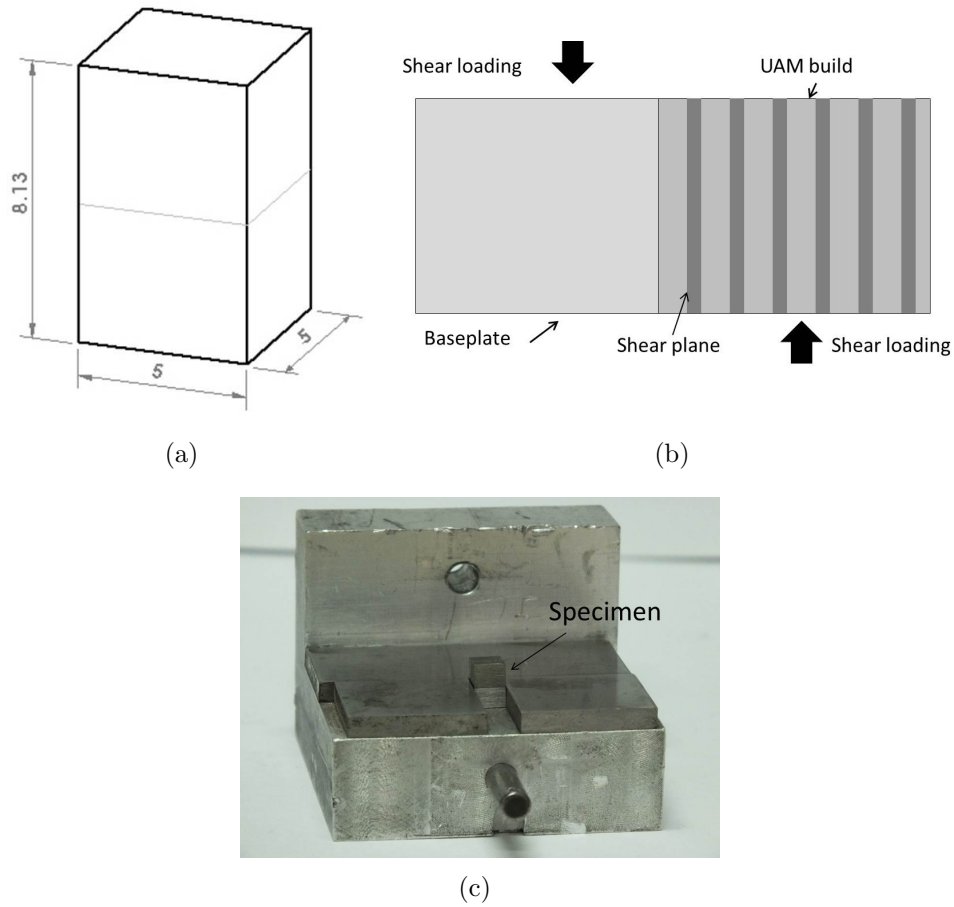


Figure 5.2: Setup for shear test including (a) shear specimen drawing (in mm) (b) schematic of shear test loading conditions (not to scale) and (c) image of shear fixture.

In addition to mechanical testing, microstructural evaluations were performed on the as-built and heat treated joints. Optical microscopy was used to determine if significant voids were present in the builds. Scanning electron microscopy (SEM) was used to further examine the builds including a chemical analysis to measure diffusion while electron back scatter diffraction (EBSD) was used to investigate the grain structure of the resulting joints. All electron microscopy was performed in

collaboration with University of Tennessee researchers. Samples for microstructural analyses were sectioned perpendicular to the welding direction and mounted in epoxy. Grinding was performed using 180, 320, 400, 600, 800 and 1200 grit papers. Polishing was performed with 3 μm and 1 μm diamond pastes; final polished with a 0.05 μm colloidal silica solution.

5.1.2 Mechanical Characterization

5.1.2.1 Push-pin Testing

A summary of the results of push-pin testing is presented in Table 5.3, including both as-built and heat treated samples. The individual curves for each of the tests are shown in Figure 5.3. The maximum force during delamination and the mechanical work, or area under the force-displacement curve were used as metrics for examining the results. As can be seen, the heat treated samples yield much higher values of delamination force, approximately 2.4 kN vs. 5.8 kN on average. Similarly the mechanical work for failure is significantly higher for heat treated samples, roughly 3.5 kN-mm vs. 12.7 kN-mm on average. These results indicate that heat treatment significantly increases the mechanical strength of Al/Ti bonded samples. The variation within the as-built and heat treated test groups is attributed to variations in machining and heat treatment, causing slight changes in the mechanical strength within a specific group.

Table 5.3: Results of push-pin testing for as-built and heat treated Al/Ti joints.

Sample	Force (kN)	Integral (kN-mm)
As-built 1	2.3	2.7
As-built 2	2.5	4.4
Heat-treated 1	5.1	12.1
Heat-treated 2	6.5	13.4

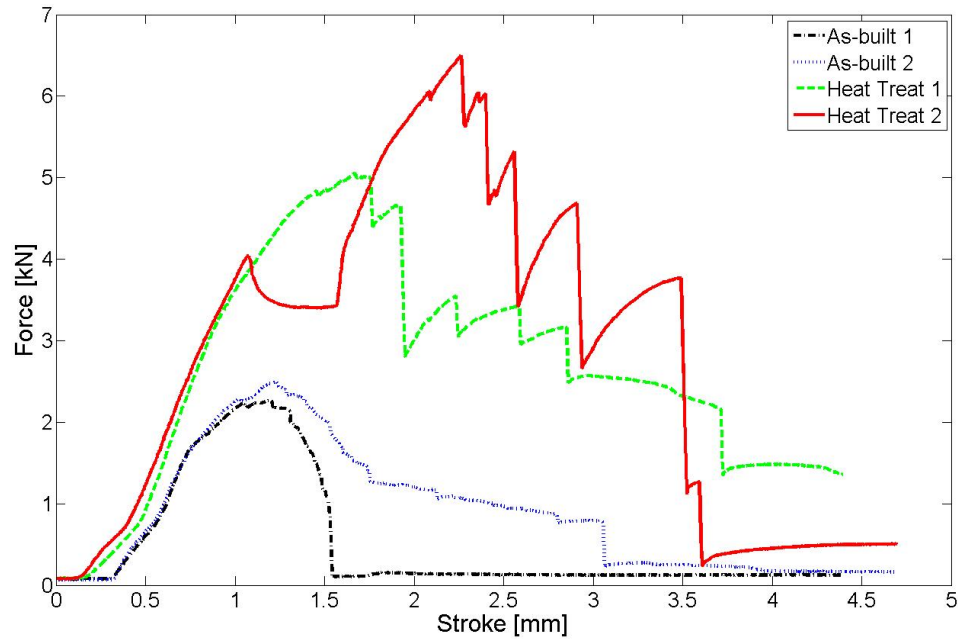
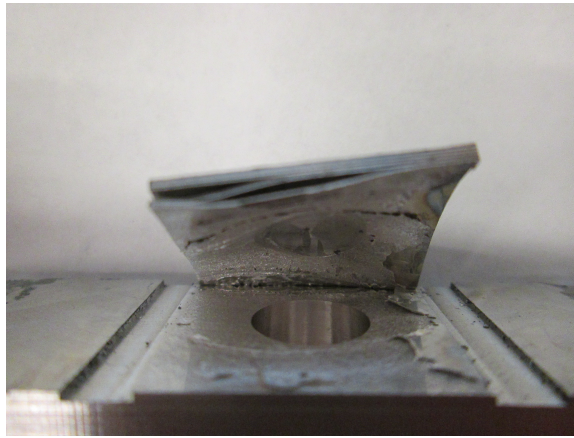


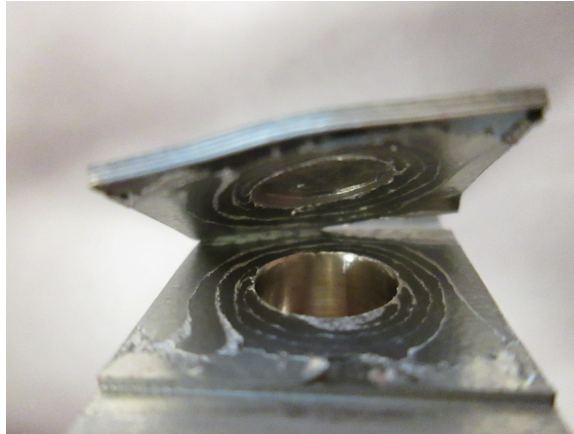
Figure 5.3: Push-pin data for as-built and heat treated Al/Ti joints.

Images of the failed push-pin samples are shown in Figure 5.4. As can be seen, the as-built samples fail by delamination of a single layer along the entire bonded area with some delamination in the higher layers, indicating that the bond strength is lower than the material strength. The heat treated samples by contrast, fail through multiple layers as shown by the concentric rings in Figure 5.4b, indicating the bond

can withstand significant loading prior to failure of the tape material. These failure rings are likewise more consistent and uniform than the small amounts of delamination in the as-built samples. The discrete jumps in the load-displacement curves in Figure 5.3 correlate with the fracture of specific layers within the bonded sample. These jumps are present in both heat treated samples but are absent in the as-built samples, indicating a difference in their failure behavior.



(a)



(b)

Figure 5.4: Failure surfaces of Al/Ti push-pin samples for (a) as-built and (b) heat treated samples.

An SEM image of the fracture surface of an as-built push-pin sample is shown in Figure 5.5(a). The image shows some degree of ductile failure surrounded by areas of material contact, without ductile failure. Energy dispersive spectroscopy (EDS) maps of the aluminum and titanium content are provided in Figure 5.5(b) and (c) showing the elemental content in these areas. While the failure is primarily in the aluminum, areas of titanium are present surrounding the ductile failure indicating a material transfer is occurring during bonding.

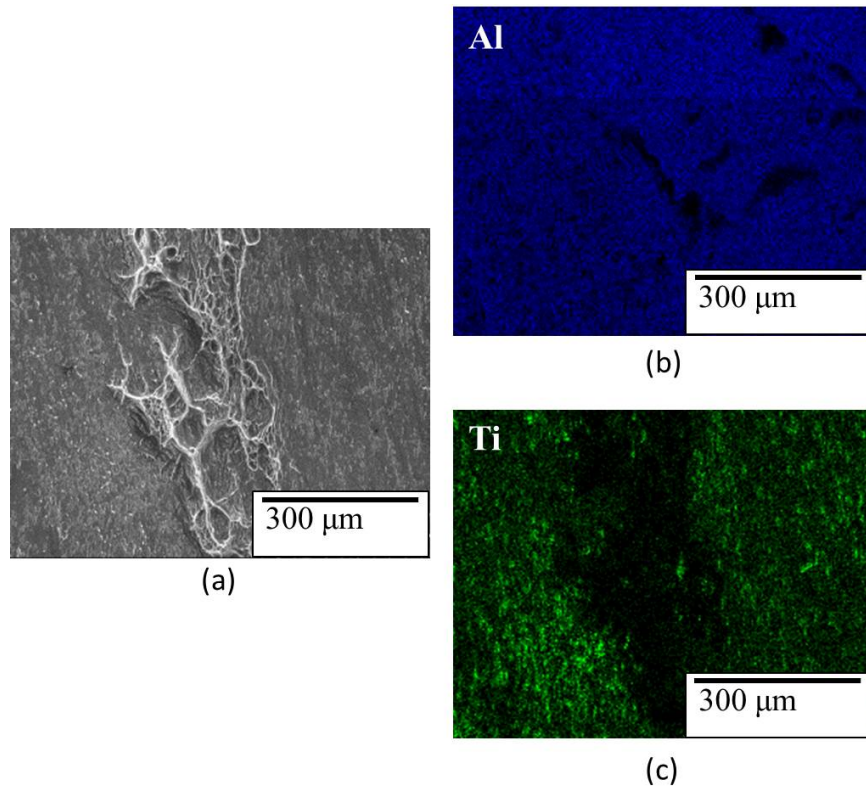


Figure 5.5: (a) SEM image of failure surface of as-built push-pin sample (b) EDS mapping of aluminum (c) EDS mapping of titanium.

5.1.2.2 Shear Testing

Results of shear testing are summarized in Table 5.4 showing the average ultimate shear stress (USS) and standard deviation of the tests. As is shown, the shear strength of the SPS treated samples exhibits ultimate shear strengths over two times that of the as-built samples with strengths of 102.4 MPa vs. 46.3 MPa. Additionally, the failure characteristics of the as-built and heat treated samples exhibit contrasting behavior. Figure 5.6 shows failed shear specimens for each case. The as-built sample broke into separate parts while the heat treated samples exhibited a more ductile failure.

Table 5.4: Results of shear testing for Al/Ti joints.

Condition	Avg. USS (MPa)	St. Dev. (MPa)
As-built	46.3	2.6
Heat Treated	102.4	7.4

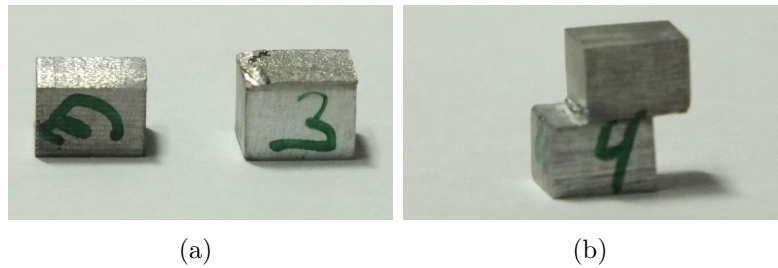


Figure 5.6: Failed Al/Ti shear test specimens (a) as-built and (b) heat treated.

The surfaces of fractured specimens were examined under optical microscopy; shown in Figure 5.7. The textured surface exhibited by the as-built sample is indicative of brittle failure, whereas the gliding texture shown by the heat treated sample is indicative of a more ductile failure mechanism. The striations seen in Figure 5.7b indicate a smearing or sliding action is occurring during loading, which is due to the ductile nature of the failure, while the brittle failures shown in Figure 5.7a lack these striations. These results, along with the shear strength results, indicate that heat treatment can significantly increase the strength and ductility of Al/Ti joints.

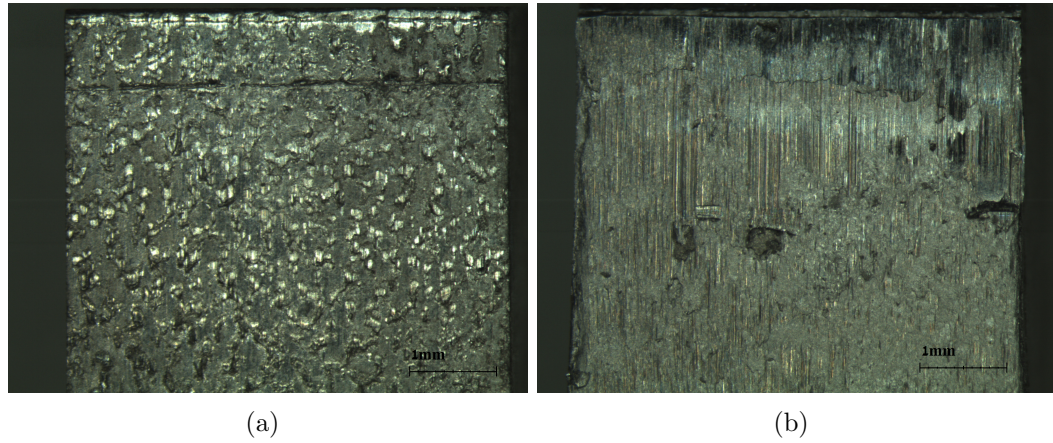


Figure 5.7: Failed shear test specimens (a) as-built and (b) heat treated.

5.1.3 Microstructural Evaluations

Evaluation of the cross-section of an as-built Al/Ti sample is shown in Figure 5.8a, where no indications of large voids are present in the sample. In addition, it can be seen that the top of the titanium layers have an imparted roughness from the sonotrode, while the bottom of each titanium layer contains a smooth to smooth

interface with the aluminum. This imparted roughness could play a role in how the two materials are joining, especially if the bond mechanism is mechanical interlocking, which has been shown in previous studies [41].

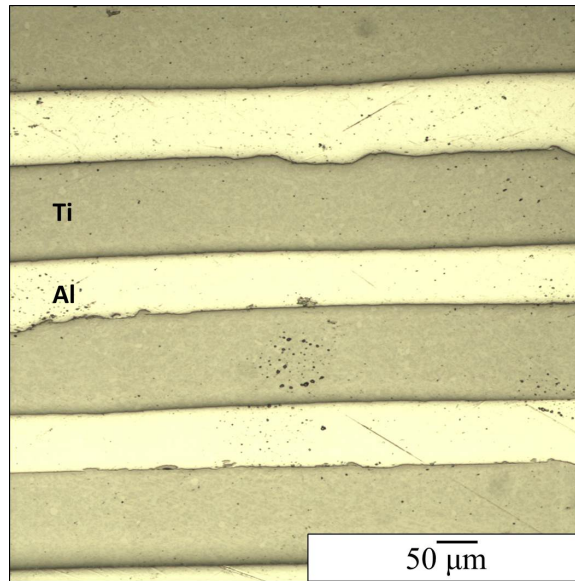


Figure 5.8: Optical image of Al/Ti bilayers.

To investigate the chemistry along the interfaces, a diffusion profile was measured along the line shown Figure 5.9a via EDS. The diffusion profile for the first Al/Ti interface layer is shown in Figure 5.9b and c. As can be seen, there is no large scale diffusion of aluminum or titanium into the adjoining material.

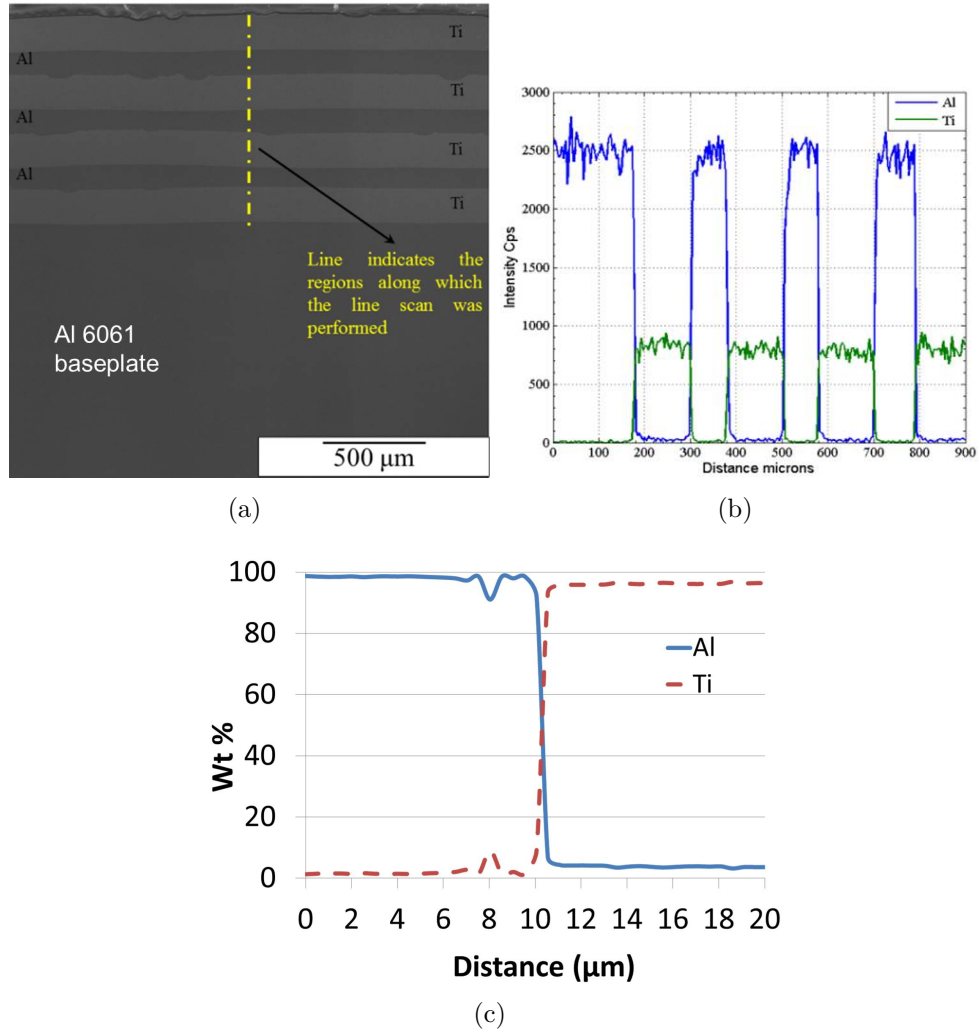


Figure 5.9: (a) SEM image of as-built Al/Ti sample showing diffusion line scan results at multiple scales (b) and (c).

Figure 5.10 shows the EBSD scan of an as-built Al/Ti build. Results show significant deformation in the aluminum layers at the titanium-aluminum interfaces. The aluminum layers have a nominal thickness of 127 μm prior to welding, which is reduced to approximately 70 μm after the UAM process. By contrast, the titanium layers are nominally 127 μm prior to welding and 125 μm after welding. The layers

lower in the build show more grain refinement and deformation than layers further up the build. Figure 5.11 shows the grain structure of the aluminum and titanium foils prior to welding. Comparing this with Figure 5.10, it appears that the microstructure in the titanium is unchanged during the welding process, with all deformation and refinement occurring in the softer aluminum layers.

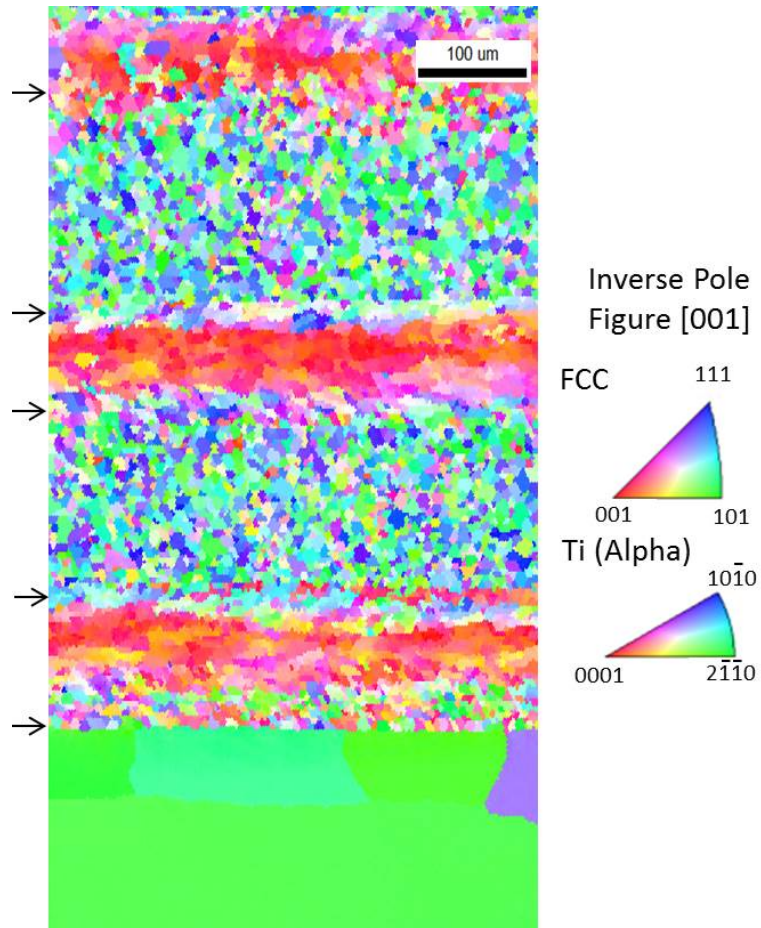


Figure 5.10: Electron back scatter diffraction image of Al/Ti joint, arrows indicate approximate location of material interfaces.

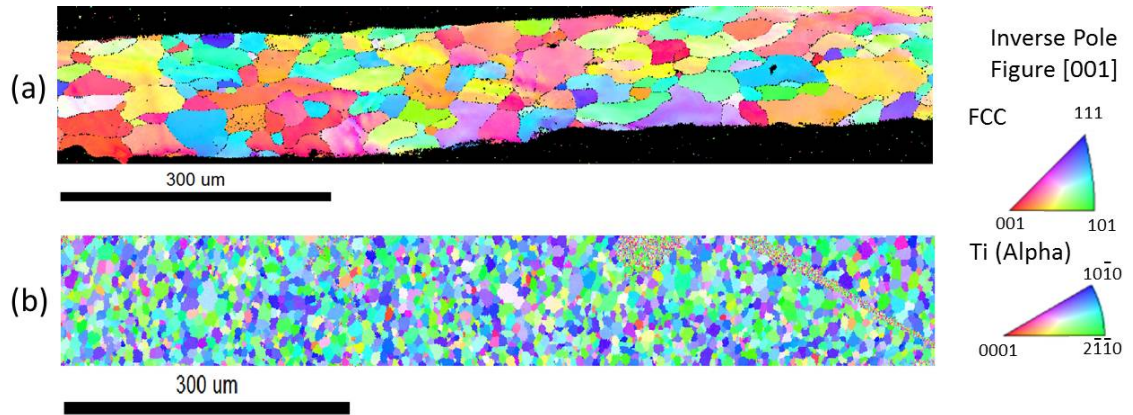
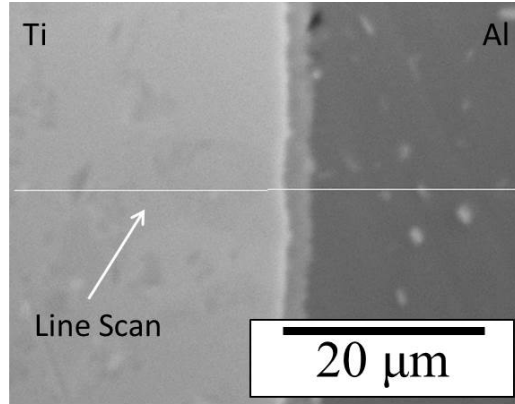
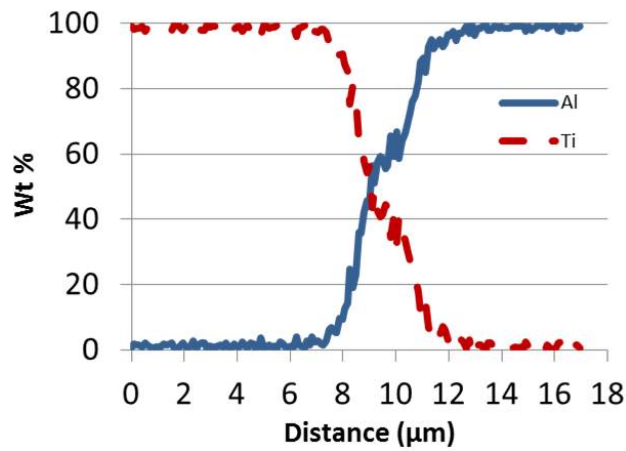


Figure 5.11: Electron back scatter diffraction image of (a) aluminum foil and (b) titanium foil, prior to welding.

Heat treated samples were also investigated for their microstructure. An SEM image of a smooth interface in a heat treated Al/Ti sample is shown in Figure 5.12a, where a transition zone exists between the aluminum and titanium. To investigate the chemistry within this zone, a diffusion profile was measured; shown in Figure 5.12b. These results show significantly more diffusion is occurring in the heat treated sample than in the as-built samples, with a diffusion zone of roughly $5\text{ }\mu\text{m}$.



(a)



(b)

Figure 5.12: Diffusion line scan for Al/Ti after heat treatment along smooth interface.

EBSD measurements for a heat treated Al/Ti sample are shown in Figure 5.13. The grain structure in the titanium layers appears unchanged compared to the as-built samples, while the aluminum layers show significant grain growth. In each of the aluminum layers, it appears the heat treatment has caused preferential grain growth into only a few grains for each layer. Minimal grain growth appears in the baseplate material, while the aluminum foil material shows significant growth. This is likely

indicative of the high strain energy in the foil from the UAM process leading to a high driving force for recrystallization.

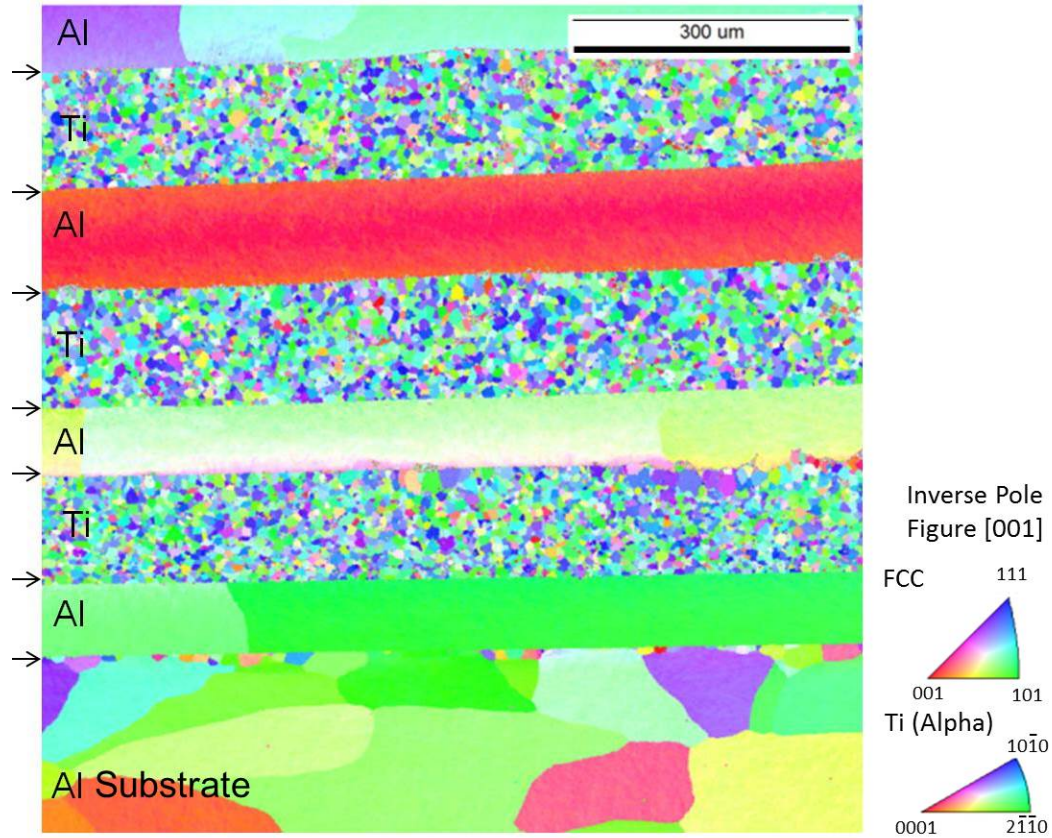


Figure 5.13: Electron back scatter diffraction image of Al/Ti joint after heat treatment, arrows indicate approximate location of material interfaces.

5.1.4 Discussion

Push-pin testing shows that post-process heat treatment of Al/Ti builds produces significant increases in mechanical strength, as measured by the mechanical work for failure. Increases from 3.5 kN-mm to 12.7 kN-mm were exhibited when applying a post-process heat treatment. Differences were present in the failure surfaces as well

showing increased ductility for heat treated samples. The complex stress states of the push-pin test can make it difficult to differentiate the exact loading conditions during and immediately prior to failure, making it challenging to discern the local failure behavior. However failure through multiple layers indicates strong bonding is occurring which can withstand the push-pin load until fracture of the material occurs. After failure, the load is redistributed to the layers above and continued until the sample completely fails. When weaker bonding is occurring, as in the as-built case, delamination occurs because the weak bonding in a given layer is unable to withstand the push-pin forces; indicating that the bond strength along the layer is weaker than the material itself.

Similarly, shear tests show a strength increase of 46.3 MPa to 102.4 MPa for as-built and heat treated samples respectively. Microstructural investigations show that an intermetallic layer of approximately 5 μm is forming between the titanium and aluminum layers after heat treatment. It is hypothesized that this thin intermetallic layer is biaxially constrained by the layers on each side of the interface. Conceptually this is similar to what can occur during brazing where a thin braze layer constrains the interface, preventing plastic deformation in the braze zone, increasing mechanical strength [74]. In this case, the intermetallic layer acts similarly to the thin braze layer and the biaxial stress state leads to increases in mechanical strength. This strengthening effect from an intermetallic layer has been observed in the joining of Al/Cu samples [38, 82] and this phenomenon is expected to be the cause of the increases in shear strength and push-pin strength observed.

Previous studies have examined various aspects of Al/Ti joining using 1 kW UAM. Using a shear test and 1 kW UAM, Hopkins et al. [41] measured as-built shear

strengths of 63 MPa on average, slightly above the average value of 46 MPa for 9 kW UAM as-built shear strengths measured. Studies by Obielodan et al. [67] using CpTi and Al 3003 exhibited as-built shear strengths of 34 MPa. Following a heat treatment of 480 °C for 30 min, shear strengths of 73 MPa were measured while exhibiting diffusion of approximately 5 μm . This diffusion zone was said to provide solid solution strengthening at the interface, not present in the as-built samples. The study presented here proves shear strengths of 102 MPa on average are possible when using 9 kW UAM and a post-process heat treatment which generates a similar 5 μm diffusion zone. However in this case, this diffusion zone is theorized to provide a biaxial constraining action at the interface which provides the strengthening. Weld amplitudes of 41.55 μm are expected to increase the plastic deformation at the bond interfaces, thus increasing the driving force for recrystallization at the interface and improving bonding as compared to the studies using 1 kW UAM. As-built samples in all three cases lack indications of diffusion which, based on results of heat treated specimens, is necessary for maximizing mechanical strength.

EBS of the as-built microstructure shows deformation in the aluminum layers while the titanium appears unchanged. This is likely due to the deformation characteristics of each. The aluminum 1100 alloy is much weaker than the titanium layer, with ultimate tensile strengths of 90 MPa and 343 MPa respectively [3]. Therefore the much weaker aluminum layers are more likely to deform under load than the titanium layers. Upon heat treatment, the aluminum grains grow significantly, to the extent that each layer appears to contain only a few grains while the heat treatment does not appear to alter the grain structure of the titanium. The plastic deformation in the aluminum increases the driving force for recrystallization to occur, and when

heated to within 60 °C of melting, recrystallization and grain growth occur. Because there is little strain energy retained in the titanium and the heat treatment temperature is well below the melting temperature of titanium (1668 °C), there is little driving force for recrystallization to occur in the titanium layers. This preferential grain growth in the aluminum layers is consistent with previous research in Al 1100 alloys, where annealing treatments led to significant grain growth at temperatures approaching 600 °C [54].

5.2 Al-Steel Joining

5.2.1 Experimental Methods

Sample Manufacturing

Joints of Al 6061 and 4130 steel were constructed using the Fabrisonic SonicLayer 4000 UAM machine. The joint configuration used a direct welding of Al 6061 layers onto a 4130 steel baseplate. Al 6061-H18 foil, 0.006 in. (152.4 μm) thick and a 4130 steel baseplate 0.1 in. (2.54 mm) thick were used and iterative testing was conducted to determine the viable weld parameters for joining the materials. Stress-strain curves for the materials are given in Figures 3.8 and 5.14 respectively. Table 5.5 shows the weld parameters used in the study. Of note, these parameters represent those where bonding was achieved and the foil could not be pulled off manually. These parameters do not necessarily represent an optimal set.

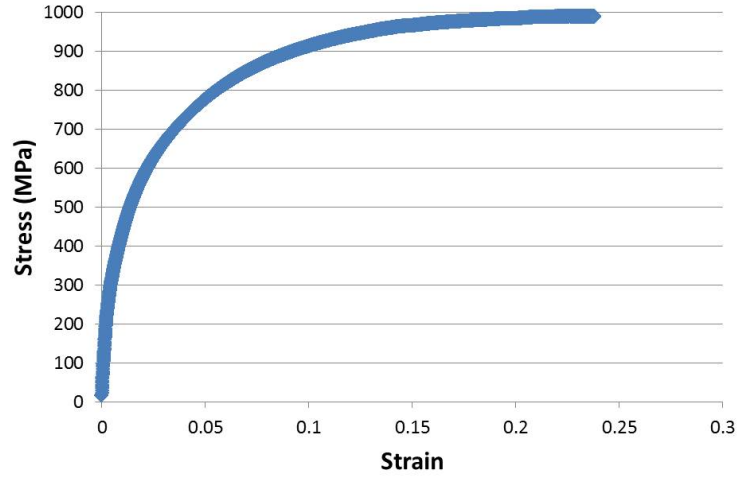


Figure 5.14: Stress-strain curve for as-received 4130 foil.

Table 5.5: Weld parameters used for Al 6061 onto 4130 steel joints.

Parameter	Level
Weld Force	5000 N
Weld Speed	100 in/min
Amplitude	23 μm
Temperature	300 °F
Horn Texture	7 μm , R_a

In addition to aluminum onto steel, welds of as-received 4130 steel foils 0.005 in. (0.127 mm) thick were attempted onto aluminum 6061 baseplates. Similar iterative testing was conducted to determine a viable set of weld parameters for joining the materials. Table 5.6 shows the viable weld parameters from the study. Similarly, these parameters do not represent an optimized set. Of note, most of the parameters

are the same between the two sets, however the required amplitude for joining is significantly higher ($41.6 \mu\text{m}$ vs. $23 \mu\text{m}$) for the case of steel onto aluminum.

Table 5.6: Weld parameters used for 4130 steel onto Al 6061 joints.

Parameter	Level
Weld Force	5000 N
Weld Speed	100 in/min
Amplitude	$41.6 \mu\text{m}$
Temperature	300 °F
Horn Texture	$7 \mu\text{m}$, R_a

Joint Characterization

Characterization of aluminum onto steel joints was conducted using push-pin and microstructural analyses. Push-pin samples, similarly to studies of Al/Ti combinations, utilized 10 foil layers for the sample dimensions. Because the focus of this work is the Al/steel interface, samples were machined such that the push-pin was pressing directly on this interface. Test setup and conditions were similar to those for Al/Ti combinations described in Section 5.1.

5.2.2 Mechanical Characterization

Results of the push-pin testing are presented in Figure 5.15 and Table 5.7. Because the first layer is of interest in this case, the maximum pushout force is the most useful response variable for the push-pin test. With an average pushout force of 2.85 kN, these results indicate a slightly stronger first layer bonding is occurring in these materials as compared to the Al/Ti combination which have an average, as-built pushout force of 2.38 kN. This is likely due to the strength of the parent materials

used in these combinations where Al 1100 is used for Al/Ti combinations while Al 6061 is used in the joints to steel. The lower ultimate tensile strength of the Al 1100 is attributed to the lower strength in those push-pin results.

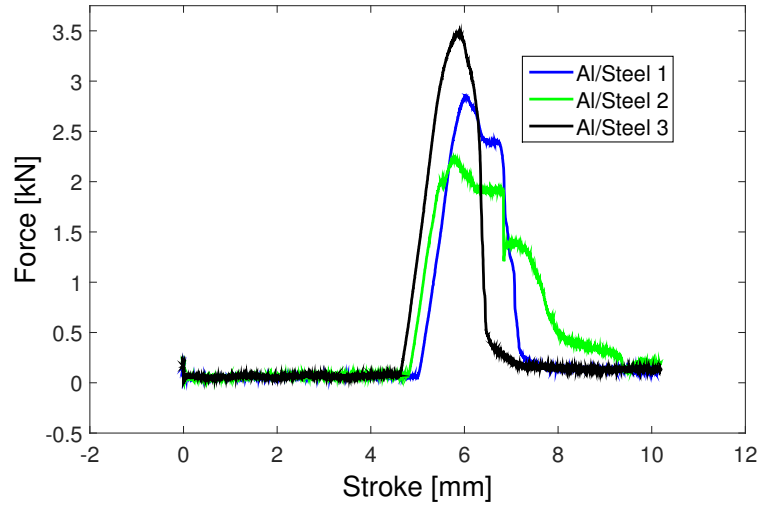


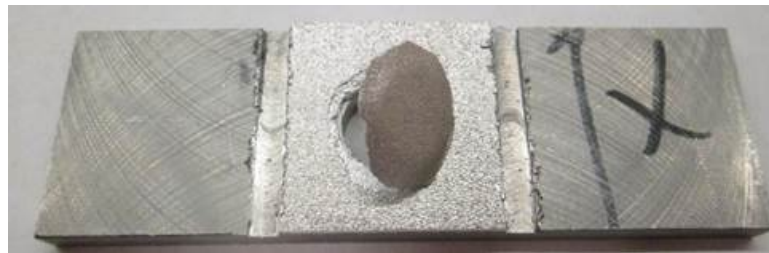
Figure 5.15: Push-pin results for Al 6061 onto 4130 steel.

Table 5.7: Results of push-pin testing for aluminum onto steel joints.

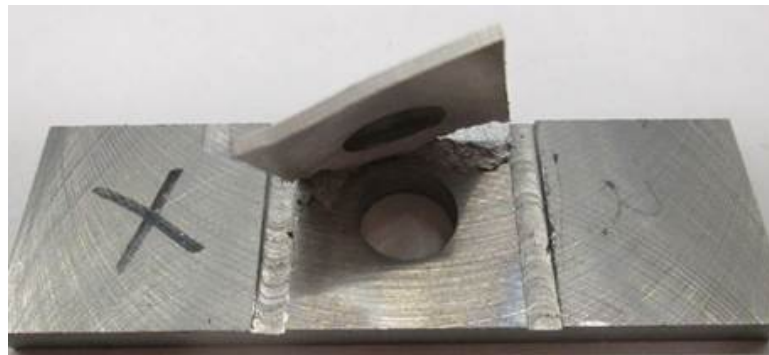
Sample	Force (kN)	Integral (kN-mm)
1	3.47	5.06
2	2.24	5.64
3	2.85	4.74
Avg	2.85	5.15

Analysis of the failure surfaces of the samples gives some indication of their bond characteristics. Shown in Figure 5.16, the failure surfaces of samples 1 and 2 differ.

Sample 1 shows failure through the aluminum layers, with little delamination, while sample 2 shows a failure mostly by delamination of the first layer bond. This indicates a difference in the first layer bond characteristics, despite similar processing conditions. Sample 2 was sectioned near the beginning portion of the weld, while sample 1 was sectioned further along the weld. At the beginning portion of the weld, it is possible that the weld amplitude had yet to reach its steady state value. This would indicate that less displacement and plastic deformation is occurring in this portion of the weld, leading to poorer bonding. This hypothesis will require further investigation.



(a) Sample 1



(b) Sample 2

Figure 5.16: Failure surfaces of aluminum onto steel samples.

5.2.3 Microstructural Characterization

Evaluation of the Al/steel interface indicates no large voids exist, as shown in Figure 5.17. Similar results are shown in the steel onto aluminum joint interface shown in Figure 5.18. In each case, the interface appears voidless and each micrograph is representative of the entire joint interface.

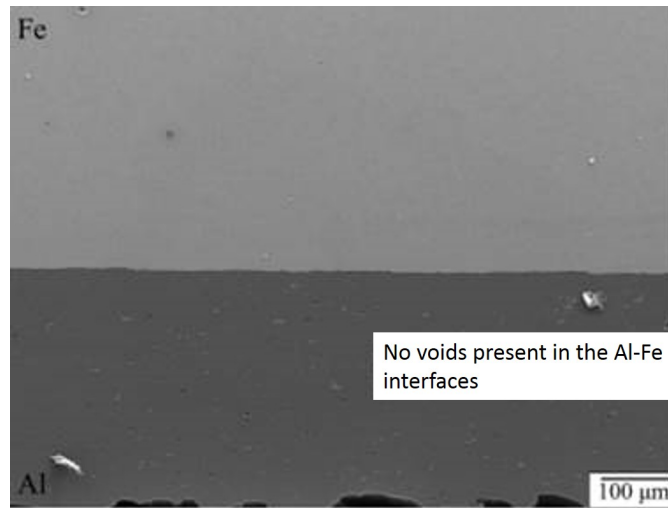


Figure 5.17: Scanning electron microscopy image of aluminum onto steel joint interface.

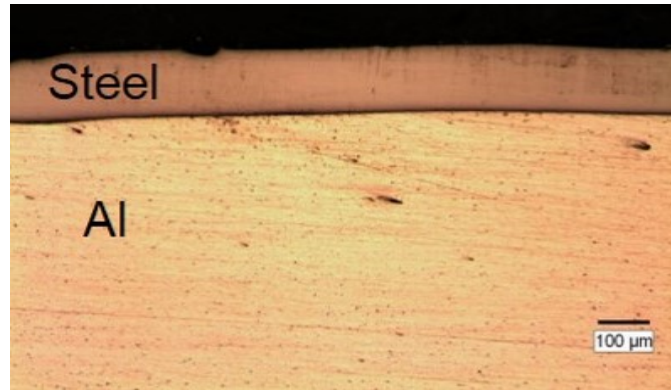


Figure 5.18: Optical image of steel onto aluminum joint interface.

Diffusion scan results along the interface of the aluminum onto steel joints using EDS indicate a small amount of diffusion across the interface, as shown in Figure 5.19. However, beam-sample interactions may account for the approximately $1\ \mu\text{m}$ band of diffusion across the interface. Studies in Al/Cu dissimilar systems show that the accelerating voltage can produce diffusion scans which indicate interdiffusion based solely on beam-sample interactions [61]. EDS using an electron beam therefore does not have the spatial resolution to determine the exact diffusion at this scale, but can provide a broader understanding of diffusion at the interface.

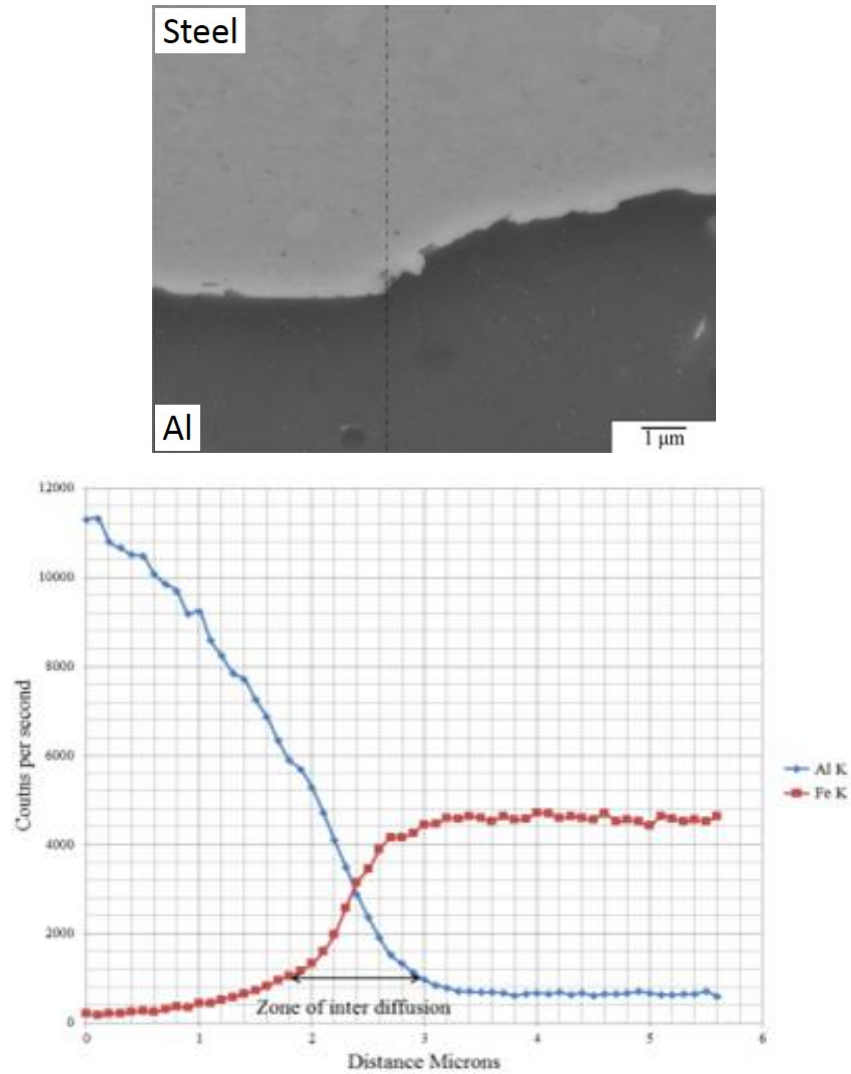


Figure 5.19: (a) SEM image and (b) diffusion line scan results for Al/Steel joints.

EBSD measurements are provided in Figure 5.20. Results indicate a recrystallized zone exists at the interface, where small, equiaxed grains are formed in the steel material. The grains in the aluminum layers in certain zones indicate an elongated structure, normal to the steel interface. This could indicate that thermal gradients

which occur during cooling are producing a grain growth phenomena at the interface after recrystallization is occurring, though further work will be required to validate this hypothesis.

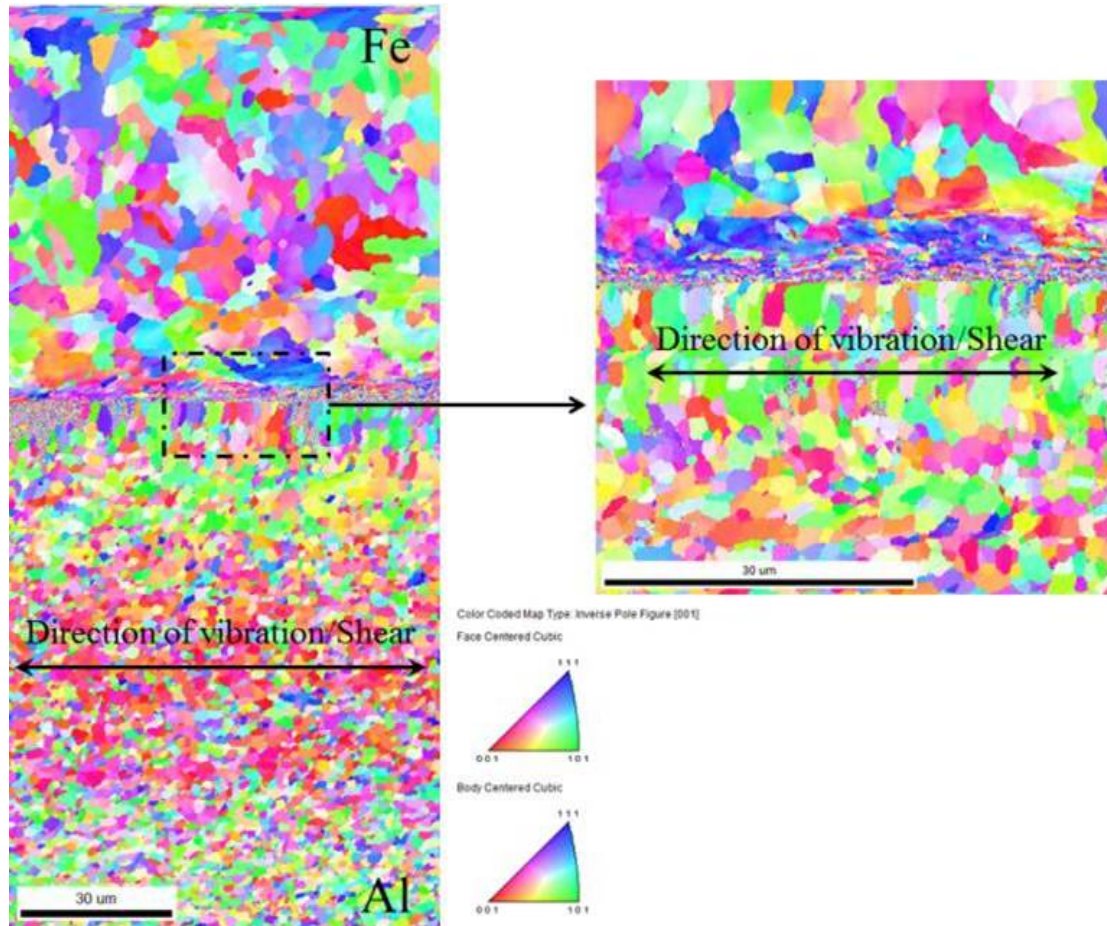


Figure 5.20: EBSD of Al/steel interface.

Grain orientation spread (GOS) image mapping is shown in Figure 5.21 for the Al/Steel joints. GOS is a technique which can provide a qualitative representation of the plastic deformation in the observed material. The GOS map for this system shows

5.2.4 Discussion

Aluminum/steel joints were achieved using the 9 kW UAM system with joint strengths greater than that of aluminum/aluminum joints, indicating a strong metallurgical bond is achieved. Microstructural analyses show that deformation exists in the interface steel layer for an aluminum onto steel joint. This is expected to be due to the kinetics for recrystallization of the two materials. For aluminum, with a lower melting point and yield strength, the driving force for recrystallization is higher at the process temperatures. As is seen in the EBSD analyses, the aluminum grains near the interface no longer exhibit an elongated structure parallel to the weld interface, rather the grains are equiaxed, or in some cases near the interface, elongated normal to the weld interface. This indicates that a recrystallization phenomena has occurred, both at the interface and throughout the bulk of the tape. It is therefore hypothesized that the aluminum layer undergoes significant deformation during the bonding process, overcoming the thresholds of deformation and temperature for recrystallization to occur. The preferential grain growth normal to the interface is potentially caused by a retention of heat in the steel baseplate, which provides heating to the interface grains over a longer period of time, allowing grain growth in this direction.

For the steel baseplate, deformation is present near the bond interface, while recrystallization has not appeared to occur. The driving force for recrystallization in the steel has therefore not likely been met. Baseplate temperatures for joining are relatively low, at 300 °F and the UAM process is known to generate little heat during welding. Therefore under the given conditions, the steel is much less likely to recrystallize than the aluminum.

5.3 Steel-Steel Joining

5.3.1 Experimental Methods

5.3.1.1 As-Received Foils

Joining of as-received 4130 steel foils to annealed 4130 steel baseplates was attempted using the Fabrisonic SonicLayer 4000 UAM system. Multiple sets of weld trials were attempted to achieve bonding with suitable weld quality. Initial trials utilized 4130 steel foils, 0.005 in. (0.127 mm) thick with UTS of 965 MPa, while annealed 4130 steel 0.1 in. (2.54 mm) thick baseplates with UTS of 550 MPa were used. Iterative studies were performed varying the weld force, weld speed, and weld amplitude to generate a viable weld. Viable weld parameters for foil to baseplate welds are presented in Table 5.8, while an image of a weld between the foil and baseplate is shown Figure 5.22. Welds achieved using these parameters cannot be pulled apart manually. Of note, welds using a 7 μm R_a roughness horn were unable to generate suitable welds while horns with 14 μm R_a roughness were able to achieve good welds.

Table 5.8: As-received 4130 steel foil to annealed 4130 steel baseplate welding parameters for direct welds to the baseplate.

Parameter	Level
Weld Force	8000 N
Weld Speed	85 in/min
Amplitude	38.76 μm
Temperature	300 °F
Horn Texture	14 μm , R_a



Figure 5.22: Steel to steel directly to baseplate.

4130 foil to baseplate welds require significant input energy in the form of weld force, speed, amplitude, and temperature. Slight variations in the processing conditions for amplitude would often lead to nuggetting, or the formation of a weld between the foil material and the sonotrode. Examples of these nuggets are shown in Figure 5.23, where steel foil has welded to the sonotrode. Welding of foils in this manner also effects the surface characteristics of the foil. Figure 5.24 shows an image of a welded foil that has undergone tempering at the surface in contact with the sonotrode. This is likely due to the pressure and relative sliding motion between these two pieces. Bonds between as-received 4130 steel foils were unable to be achieved under the conditions tested, likely due to the high strength of the steel foil material. Attempted welds exhibit poor bonding, or weld to the sonotrode.

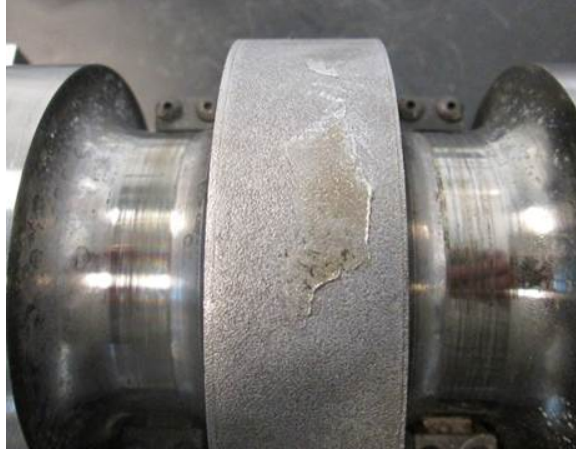


Figure 5.23: Nugget formations on horn from direct as-received steel foil joining.

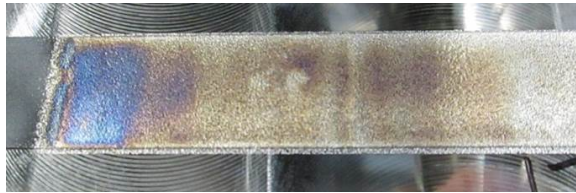


Figure 5.24: Steel to steel weld with significant surface coloration.

5.3.1.2 Steel Joining with Interlayers

Due to the inability to produce suitable welds using as-received 4130 steel foils directly, the use of interlayering structures was investigated. The configuration of joints with interlayers is similar to the aluminum and titanium configuration. A schematic of the layout in this instance is provided in Figure 5.25. A 0.001 in. (0.0254 mm) thick nickel 201 layer is laid manually onto the 4130 steel baseplate and the 4130 steel material is welded on top. The sonotrode therefore only contacts

the 4130 steel layer. Using this approach requires less energy at the weld surfaces to generate bonding, thus reducing possibility of nugget formations on the sonotrode. An iterative process parameter study determined the viable weld parameters shown in Table 5.9. As is shown, welds can be generated at lower temperatures and at higher deposition rates than the direct steel foil to steel baseplate configuration. An image of a successful weld using the Ni interlayer concept is shown in Figure 5.26. These initial welds, while successful, show some unevenness along the weld surface.

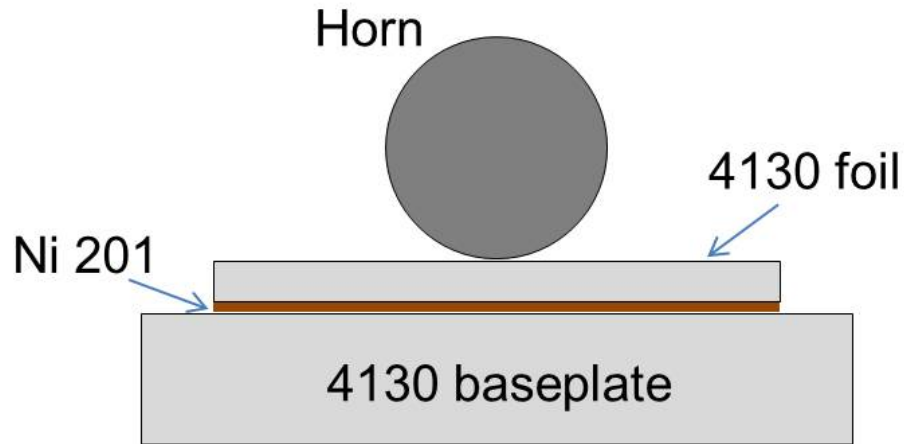


Figure 5.25: Weld schematic for joining steel to steel using Ni interlayer.

Table 5.9: Weld parameters for steel to steel with nickel interlayer.

Parameter	Level
Weld Force	5000 N
Weld Speed	100 in/min
Amplitude	40.14 μm
Temperature	200 °F
Horn Texture	7 μm , R_a



Figure 5.26: Steel to steel joint with nickel interlayer.

Increasing the applied weld force from 5000 N to 9000 N and utilization of a 14 μm roughness horn leads to a more uniform weld, as shown in Figure 5.27. The weld parameters for this joint are shown in Table 5.10. While normal force is a mostly insignificant parameter for aluminum joints according to previous work, the increased stiffness of steel compared to aluminum may make normal force more significant. An even weld surface is essential for uniform bonding to occur. Therefore normal force may require further investigation as to its effect on weld quality for steels.



Figure 5.27: Steel joining with nickel interlayer and increased normal force.

Table 5.10: Weld parameters for steel to steel with nickel interlayer.

Parameter	Level
Weld Force	9000 N
Weld Speed	100 in/min
Amplitude	37.13 μm
Temperature	200 °F
Horn Texture	14 μm , R_a

Welds utilizing a 0.001 in. (0.0254 mm) thick 1010 steel interlayer, in a similar configuration to the Ni 201 interlayer, were similarly successful. An image of a successful weld is provided in Figure 5.28. The weld parameters for this joint are given in Table 5.11. Of note, the successful weld with the 1010 steel interlayer uses a 40 in/min weld speed and 300 °F baseplate temperature. The required increase in weld energy applied is likely due to the properties of the nickel compared to the steel.

Nickel, with an FCC crystal structure, is more easily deformable than steel, requiring less weld energy to induce plastic deformation at the surface for bonding.



Figure 5.28: Steel joining with 1010 steel interlayer.

Table 5.11: Weld parameters for steel to steel with nickel interlayer.

Parameter	Level
Weld Force	7000 N
Weld Speed	40 in/min
Amplitude	38.58 μm
Temperature	300 °F
Horn Texture	14 μm , R_a

5.3.1.3 Steel Joining Following Annealing

While welds using interlayering concepts have proven successful, certain applications require use of a single tape material throughout the structure, prohibiting the use of interlayers. However, early attempts at direct welding of as-received 4130 foils were largely unsuccessful, due to insufficient bond strength and nuggetting to the

sonotrode during welding. Therefore pre-processing of the tapes through heat treatments to improve weldability were pursued. Annealing of the as-received 4130 foil strips was conducted in a controlled atmosphere furnace using argon gas. Attempts to heat treat in air were unsuccessful due to significant surface oxide and rust formation. Annealing was performed at 1550 °F (845 °C) for two hours and furnace cooled, following ASM standards [43]. A stress-strain curve for the annealed foil material is shown in Figure 5.29. As is shown, compared to the as-received properties shown in Figure 5.14, the annealed foil exhibits significantly lower strength, making it more weldable.

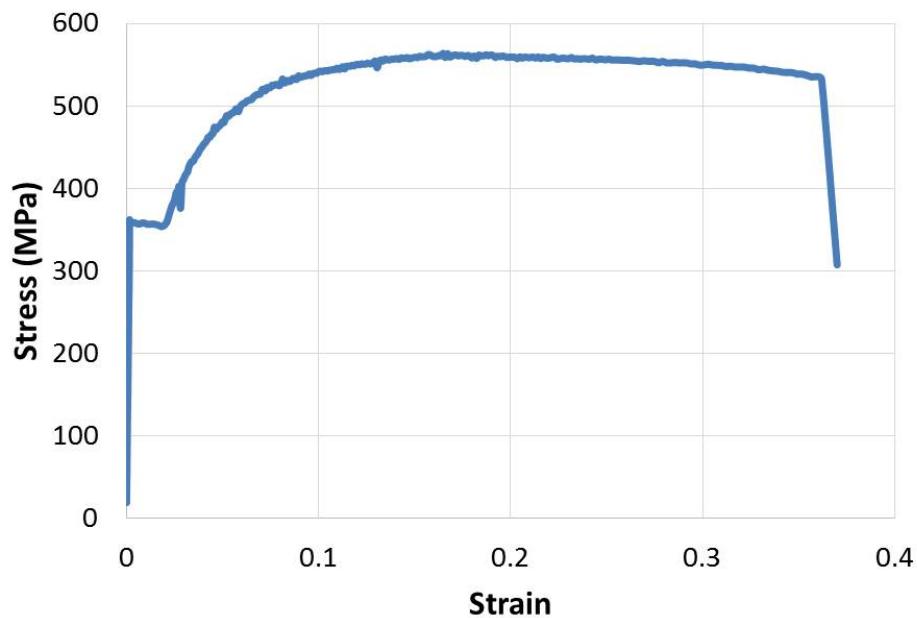


Figure 5.29: Stress-strain curve for annealed 4130 foil.

Attempts to weld the annealed foil to A36 hot rolled steel baseplates followed iterative process parameter weld trials through variations of weld force, weld amplitude, weld speed, and baseplate temperature. The successful weld parameters using the annealed foil are presented in Table 5.12. An image of a successful six layer build using the annealed foil is shown in Figure 5.30.

Table 5.12: Weld parameters for steel to steel using annealed 4130 steel foil.

Parameter	Level
Weld Force	5500 N
Weld Speed	60 in/min
Amplitude	36.2 μm
Temperature	300 °F
Horn Texture	14 μm , R_a

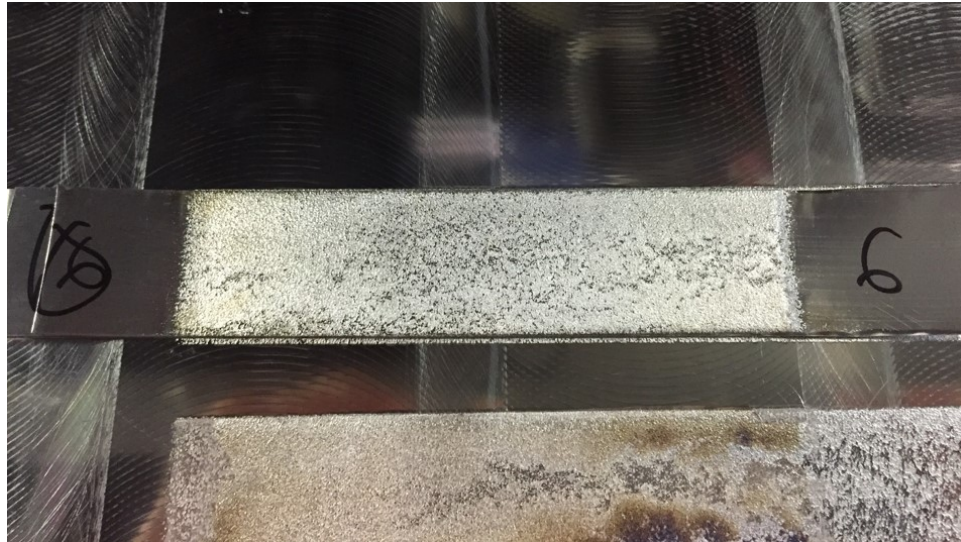


Figure 5.30: Successful layered build using annealed 4130 foil.

5.3.2 Microstructural Characterization

5.3.2.1 Steel Joining with Interlayers

Following the successful joining trials using interlayers, cross sections of the joints were examined under optical microscopy to determine whether voids were present. Example images of a six layer build using a Ni 201 interlayer are shown in Figure 5.31. As is shown, no voids exist along the weld interfaces. The nickel foil appears to heavily deform under the UAM loads, while the steel layers show moderate deformation.

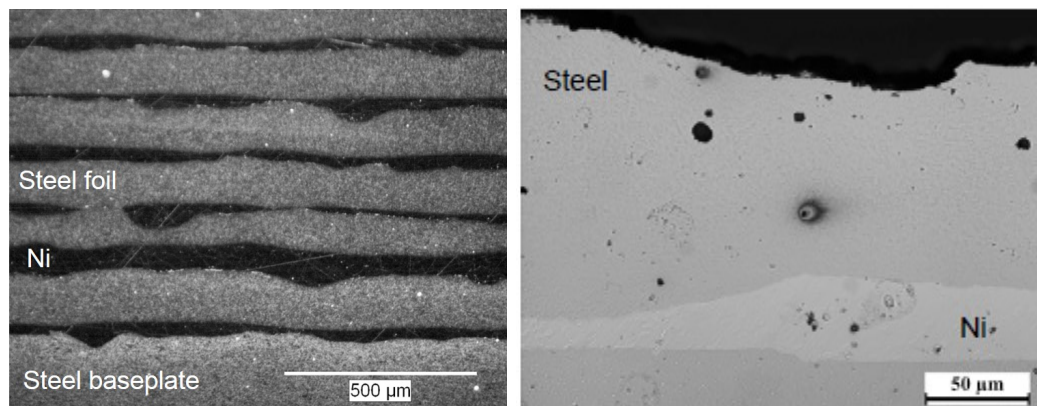


Figure 5.31: Successful layered build using annealed 4130 foil.

EBSD of the as-received 4130 foil texture is presented in Figure 5.32. EBSD analysis of steel interlayer joints using nickel are shown in Figures 5.33 and 5.34. As is shown, a small grain structure is observed in the interface between the Ni foil and the 4130 substrate. Extensive deformation appears in both the steel baseplate and nickel layers. Additionally, it does not appear that the bulk of the 4130 foil has deformed much, compared to the as received foil in Figure 5.32.

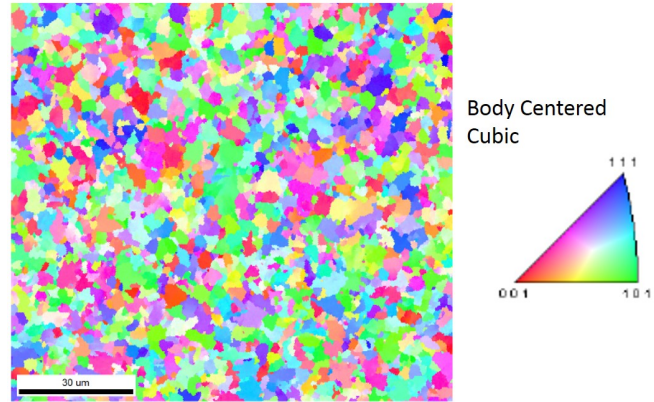


Figure 5.32: EBSD of as-received 4130 foil.

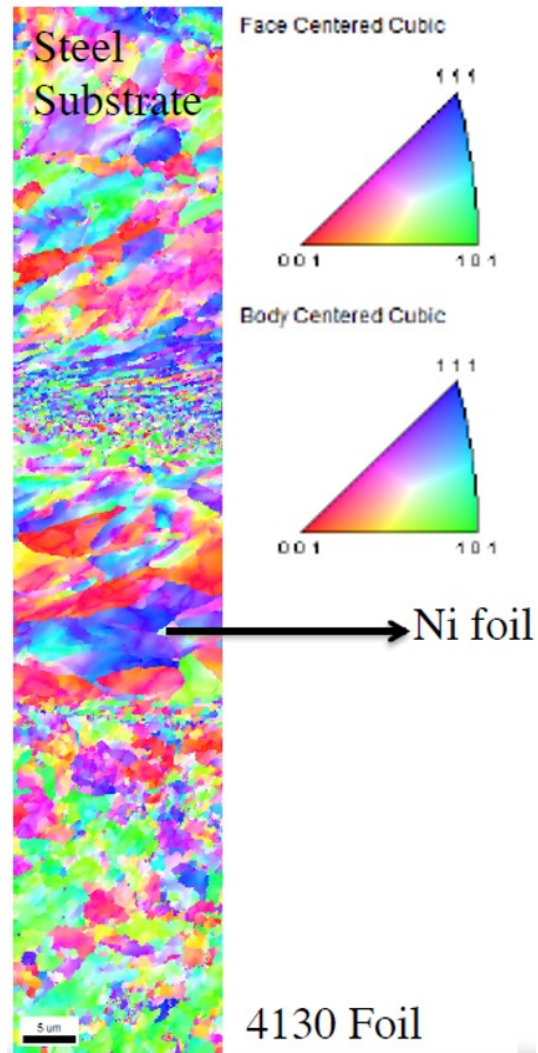


Figure 5.33: EBSD of steel joints using Ni interlayers.

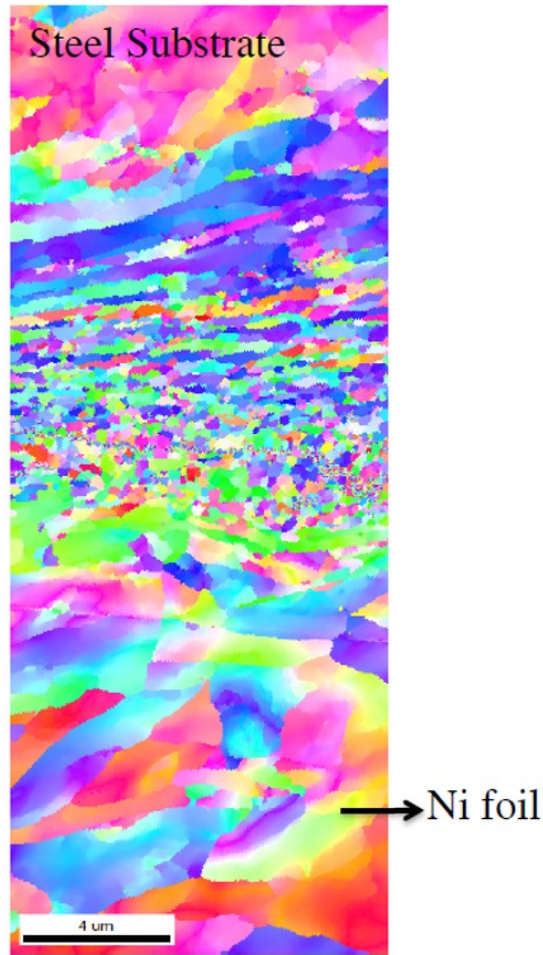


Figure 5.34: EBSD of steel joints using Ni interlayers zoomed in to closer length scale.

For steel joining with 1010 steel interlayers, optical images of the joints are shown in Figure 5.35. Within the optical image, small areas of voids can be seen, especially near the baseplate/1010 steel interface. This indicates a lack of uniform bonding can occur in this configuration. An EBSD scan of the same interface is shown in Figure 5.36. As is shown, the 4130 foil is largely unchanged from the original microstructure, while grain refinement appears to have occurred in the 4130 baseplate.

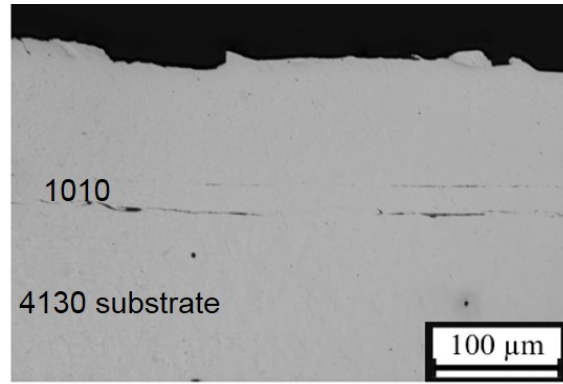


Figure 5.35: Optical microscopy image of steel joint with 1010 interlayer.

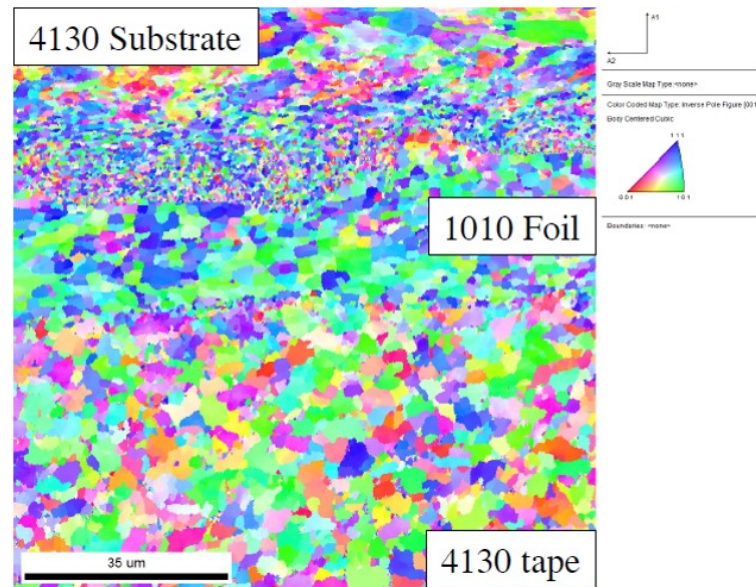


Figure 5.36: EBSD scan of steel joint with 1010 interlayer.

5.3.2.2 Direct Steel Joining with Annealed Foil

Optical microscopy of steel to steel joints using annealed foils are presented in Figure 5.37. As is shown in the image, areas of complete bonding were achieved for this configuration. However, complete bonding did not occur in all cases. Figure 5.38 shows the edge of the build where small cracks or voids exist between the foil layers, and a crack propagates into the baseplate material.

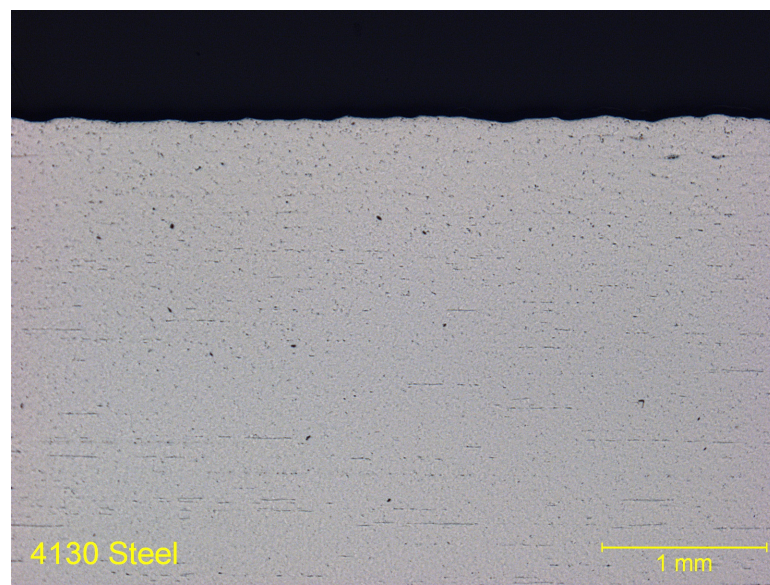


Figure 5.37: Optical image of six annealed 4130 foil layers welded to steel baseplate.

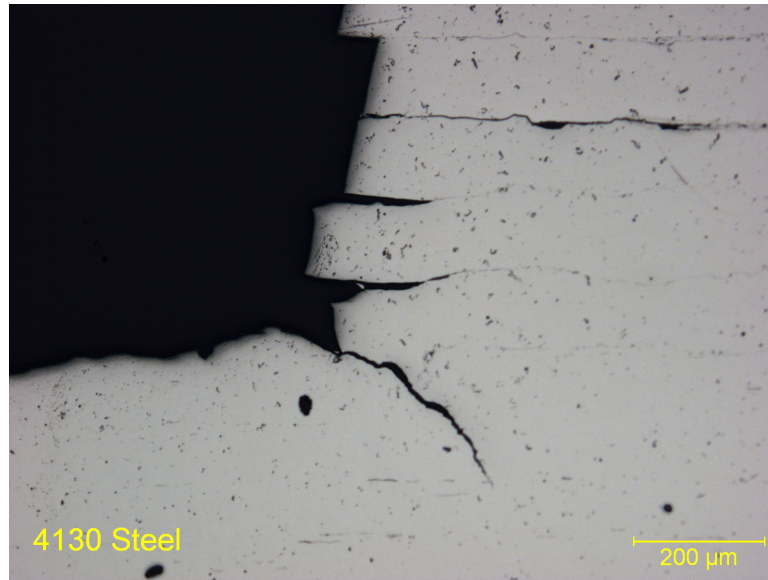


Figure 5.38: Optical image crack in annealed 4130 foil welds.

5.3.3 Discussion

Steel to steel joints were attempted using as-received 4130 steel foil stock. While successful welds were achieved to annealed baseplates, joints could not be achieved to successive foils. It is expected that this is due to the high strength of the as-received material, with a tensile strength of 965 MPa. Due to this high tensile strength, plastic deformation is likely not occurring at the surface to the extent necessary for bonding to occur.

Therefore interlayering concepts were investigated, using Ni 201 and 1010 steel as an interlayer between the steel foils. This concept achieved successful welds with both materials. Examination of welds using the Ni interlayer show no voids. Analysis of the grain structure of these welds through EBSD shows that deformation is limited to the substrate and interlayers, while the 4130 does not undergo much deformation. A

similar explanation is used in this case where the high strength in the foil compared to the substrate and interlayer drives the deformation in the weaker layers.

Welds with the 1010 steel show some indications of voids. It is expected that these voids can be minimized or eliminated with further optimization of weld parameters. Some grain refinement is shown in the substrate which is likely due to the fact that this layer is the weakest. Because the baseplate is the weakest, it undergoes more plastic deformation resulting in stored strain energy. This strain energy and the moderate temperature increase in the process lead to a driving force for recrystallization in the baseplate layer.

In addition to successful welds with interlayers, direct welds were achieved using annealed foils. These joints show areas of uniform, complete bonding. However, cracks or voids appear at the edges of the builds and cracks appear to form into the baseplate. Further investigation will be necessary to control the process such that these cracks do not form. It is possible that these cracks originate due the stress concentration at these areas. Further, the cyclic loading due to the UAM applied loads, may lead to crack formation and growth in these areas. Further investigation of the microstructure will be necessary to fully characterize these joints. However, the ability to joint steel directly should open new possibilities for component design using the UAM process.

5.4 Summary

Titanium-aluminum dissimilar material joints were achieved using 9 kW ultrasonic additive manufacturing. As-built and post-process heat treated samples were investigated for mechanical and microstructural properties. Heat treated samples show

two fold increases in mechanical strength as compared to as-built samples for both push-pin and shear strength tests; achieving ultimate shear strengths over 100 MPa. Microstructural evaluations show no indications of voids or intermetallic formations in as-built samples and that the deformation and grain refinement is restricted to the aluminum layers. Diffusion and significant grain growth is seen in heat treated samples, and a small intermetallic layer is formed between the titanium and aluminum layers. This 5 μm intermetallic layer is hypothesized as responsible for the increases in mechanical strength of the samples.

Aluminum-steel joints were achieved using the UAM process both in the aluminum to steel and steel to aluminum configurations. The joints indicate little residual strain in the aluminum, indicating recrystallization has occurred. Steel portions of the joint indicate strain present in the material, which indicates that the driving forces of deformation and temperature for recrystallization have not been met.

Steel to steel joints have been proven using both interlayer configurations as well as directly with annealed foils. Further work will be required to fully characterize and apply these joints in given applications.

Chapter 6: CONCLUSIONS AND FUTURE WORK

6.1 Summary

Optimization of weld parameters for Al 6061 was conducted via a design of experiments study. Based on the results of this study, weld amplitude and weld speed were determined as significant parameters for weld strength while weld force and temperature were not significant among the levels tested. Specific levels for optimization include weld amplitudes of 32.8 μm and weld speeds of 200 in/min. Further optimization studies were performed to determine the optimal stacking methodology for creating large scale builds. This work indicates that builds should use at least 0.0035 in. (0.0889 mm) overlap from foil to foil and use a randomized stacking pattern to maximize mechanical properties. Further work has indicated that performing roughening passes following machining for flattening can increase strength. Finally, it was shown that post-process heat treatments to aluminum builds can significantly increase tensile properties and should be applied in structural applications when possible.

A modeling effort was pursued to develop an understanding of the low mechanical strength that can occur in UAM builds. Modeling of the contact mechanics in the UAM process was conducted using analytical Hertzian equations as well as finite element analyses. Both analytical and FEA solutions applying 5000 N normal forces

indicate that plastic deformation is occurring in the bulk of the foil. No plastic deformation is predicted to occur under 3000 N loads from the FEA model. Examination of the applied forces in the UAM process via FEA indicates that the normal and shear forces applied in the process result in plastic deformation in the foil as well. This plastic deformation increases as the build height increases, especially for configurations with a sharp corner. Fillets at corner locations significantly reduces stress in these areas. Microstructural examinations of the grains in the foil bulk confirm that plastic deformation occurs. Previous studies only identified microstructural changes to the interface region.

A scarf joint was identified as a viable configuration for joining aluminum sheet material using ultrasonic welding on UAM equipment. A design of experiments study was performed to determine the optimal weld configuration and weld parameters for creating the joints. Results of this study indicate that the scarf angle and weld amplitude are significant parameters for weld quality, while weld speed is insignificant within the levels tested. The final joint design uses a weld force of 2900 N, weld speed of 25 in/min, weld amplitude of 41 μm , and scarf angle of 10°. Following this methodology, as-built joints can be produced without voids, with a tensile strength of 220 MPa. Through application of a post-process heat treatment, joint tensile strengths are 310 MPa, comparable to bulk material. Similarly the high temperature tensile strength and room temperature fatigue strength are comparable to solid material. It is expected that this design construct can be further applied to other material systems.

Finally, the weldable material combinations viable in the UAM process has been expanded with combinations investigated including Al/Ti, Al/steel, and steel/steel. It

was shown that post-process heat treatments can significantly improve the mechanical properties of Al/Ti joints through development of a controlled intermetallic layer that constrains the interface, adding strength. Joints of aluminum and steel were achieved with similar success. Microstructural investigations indicate that limited voids exist in such builds and that residual deformation is present in the steel material while the aluminum appears to have undergone recrystallization. Joining of 4130 steel to itself was more challenging to achieve, likely due to the significant mechanical strength of the alloy. While steel to steel joints were proven, further work is required to improve joint consistency and allow larger structures to be built.

6.2 Contributions

A fundamental understanding of the process-property relationships as related to the UAM process was developed in this dissertation. Using this understanding, the UAM process can be extended to more applications, moving the technology from a niche lab scale to a more applications based scale with relevance to aerospace, automotive, and other industries.

- Determined optimal build parameters for UAM Al 6061 material
 - Optimized weld parameters for Al 6061 UAM builds including amplitude, weld speed, normal force, and baseplate temperature
 - Developed a methodology for stacking of foils to eliminate voids and maximize mechanical strength
 - Showed that the effects of heat treatments on UAM builds can significantly improve mechanical strength

- Examined the applied loads in the UAM process through models which identify potential causes for reductions in mechanical strength
- Developed a methodology for joining 0.076 in. (1.93 mm) thick aluminum 6061 sheet material using UAM equipment
 - Examined various joint designs with resulting design using scarf joint configuration
 - Determined the optimal joint angle and weld parameters using design of experiments study
 - Tested room temperature and elevated temperature tensile strength, and room temperature fatigue of scarf joints with resulting joints comparable to bulk material
- Demonstrated the weldability of dissimilar material combinations using UAM
 - Al/Ti
 - * Al/Ti combinations tested in as-built and heat treated conditions. Heat treated joints produce shear strength twice that of as-built joints.
 - * Microstructural investigations show deformation limited to aluminum layers. Heat treatment results in significant grain growth in aluminum layers and formation of thin intermetallic layer.
 - Al/Steel
 - * Weldability of aluminum to steel and steel to aluminum proven successful

- * Microstructural investigations indicate that recrystallization occurs in the aluminum layers, while the steel layers show residual strain
- Steel to steel
 - * Steel to steel joints were proven successful in direct welding configurations and with interlayers of 1010 steel and nickel 201
 - * Direct joining achieved for annealed 4130 steel foil, however more work is required to fully realize steel structures with UAM

6.3 Future Work

While the work conducted here significantly extends the understanding of the properties of UAM built structures, more work is necessary to fully realize the capabilities of the technology. Significant work was conducted to optimize the process conditions of the UAM process to maximize mechanical strength. Using this work as a basis, further characterization of these optimized structures is necessary to design components using the UAM process. Of note, the out of plane tensile and fatigue strength in each of the material directions is necessary. With this information, further engineering design decisions can be conducted and comparisons can be made to existing literature on homogeneous material. This testing, while costly, will provide engineers considering the UAM process with comparative data from which to make design decisions.

An initial modeling effort was conducted to determine the effect applied loads have on UAM builds. It was shown that contact mechanics alone can induce plastic deformation in a UAM aluminum build under certain loading conditions. Similarly, when the applied normal and shear loads were investigated in an FEA model, the

UAM build undergoes significant plastic deformation in the bulk at the build edges due to these loads. While mitigating steps can be introduced which reduces the stress at these corners, such as fillets, further work is necessary to limit these loads. Further, the effect of continued cyclic loading, or fatigue, during the build process must be investigated. The application of high loads in shear appear to be necessary for optimal bonding, but must be considered when high cyclic loads are applied to the build such that fatigue failure of the build itself occurs due to the processing conditions.

Investigation of the effect of surfaces roughness shows that higher roughness sonotrodes and utilization of texturing passes following machining improves mechanical strength. The UAM process involves many tribological aspects which can play a key role in the process. One aspect that will require further work is the investigation of consistent surfaces through the bond process. Following machining, a smooth surface with tooling marks which have a characteristic texture is created. The effect of texturing onto this type of surface must be further investigated such that consistency is achieved when comparing welded foils and texturing following machining. Further, the tribological aspects of sonotrode/foil coupling have not been formally investigated, and could be of interest as related to inadvertent welding of foils to the sonotrode.

The majority of understanding and decision making regarding the UAM process is based on experimental data. Some models exist, however they lack the predictive capability to determine material properties based on process parameter inputs due to an inadequate representation of the multi-scale physics of the process. While some models explain the structural aspects, they lack an accurate connection to the material microstructure. Other models, while somewhat characterizing the microstructure, do

not account for structural modes of vibration during the process. A more multi-scale framework is necessary to connect the various physics occurring during the process to provide a comprehensive representation. While continued experiments will be required, they are less economical than computational iterations, especially in design. A predictive model would allow process developments to happen more quickly and span a larger design space than the currently used experimental methods.

The majority of research conducted in the UAM field relates to aluminum alloys. While this work has expanded the viable material combinations for the process, additional characterization of the microstructure and mechanical properties of such builds is necessary. Further, an understanding of the similarities and differences in the bond mechanisms is crucial to expanding the weldable materials envelope. While 4130 steel was used as the focus of this work, a multitude of other ferrous alloys are used in industry. Developing an understanding of the differences in the bonding characteristics of ferrous alloys, with specific interest in the required crystallographic alignments for joining, is necessary to expand the viable applications with the technology.

The development of a ceramic or ceramic coated horn is ongoing work that is critical for dissimilar material and ferrous joints. Because the current horn is made of steel, when attempting to weld steel the similar affinity for welding foil to the sonotrode and foil to foil makes direct joints difficult. A ceramic horn, which has a lower chemical affinity for joining to the foil, could improve ferrous joints.

In addition to ferrous materials, other more exotic alloys may prove useful in further studies. The capabilities of the UAM process for cladding applications makes it a viable choice for layering thin amounts of valuable alloys onto lightweight structures. UAM could prove to be an economical method of creating heterogeneous composite

structures with such clads. Further work in joining such alloys could prove beneficial in applying the process in other industries.

Finally, a methodology was proposed for joining sheet material using the UAM process. The methodology proved that sheet joints could be created using the UAM process, with mechanical properties similar to that of bulk material. Applications of this technology in the automotive and aerospace industry should be further developed to implement the technology. Potential applications include body panels in automotive structures and wing or fuselage skins in aerospace structures. The joint design investigated used Al 6061, however an understanding of the challenges posed when attempting other alloys or other material systems is necessary to enhance the viable applications of the sheet joining process.

Appendix A: DESIGN OF EXPERIMENTS DATA FOR UAM AL 6061

Table A.1: Push-pin results for design of experiments study.

Set	Sample	Temp.	Force	Amp.	Speed	Peak Force (kN)	Mech. Work (kN*mm)
1	1.1	1	1	1	1	2.89	3.81
1	1.2	1	1	1	1	3.50	4.84
1	1.3	1	1	1	1	3.42	4.06
1	1.4	1	1	1	1	3.22	4.85
2	2.1	1	1	2	2	4.18	5.06
2	2.2	1	1	2	2	3.51	3.97
2	2.3	1	1	2	2	3.17	3.97
2	2.4	1	1	2	2	4.53	5.18
3	3.1	1	1	3	3	3.81	5.07
3	3.2	1	1	3	3	3.57	5.39
3	3.3	1	1	3	3	3.85	4.65
3	3.4	1	1	3	3	3.59	2.74
4	4.1	1	2	1	1	3.56	3.79
4	4.2	1	2	1	1	3.02	2.73
4	4.3	1	2	1	1	3.08	2.99
4	4.4	1	2	1	1	3.27	3.50
5	5.1	1	2	2	2	3.19	4.25
5	5.2	1	2	2	2	2.99	4.17
5	5.3	1	2	2	2	3.33	4.16
5	5.4	1	2	2	2	3.40	4.21
6	6.1	1	2	3	3	3.30	4.34
6	6.2	1	2	3	3	3.53	2.89
6	6.3	1	2	3	3	3.75	4.44
6	6.4	1	2	3	3	4.04	5.33

Table A.1 Continued:

7	7.1	1	3	1	2	2.64	2.39
7	7.2	1	3	1	2	2.99	3.14
7	7.3	1	3	1	2	2.64	2.87
7	7.4	1	3	1	2	2.94	2.57
8	8.1	1	3	2	3	3.58	5.13
8	8.2	1	3	2	3	3.31	3.76
8	8.3	1	3	2	3	3.48	3.73
8	8.4	1	3	2	3	3.21	3.34
9	9.1	1	3	3	1	3.84	4.94
9	9.2	1	3	3	1	3.78	4.50
9	9.3	1	3	3	1	3.70	4.74
9	9.4	1	3	3	1	3.96	5.44
10	10.1	2	1	1	3	2.78	2.53
10	10.2	2	1	1	3	2.47	2.43
10	10.3	2	1	1	3	2.85	2.59
10	10.4	2	1	1	3	3.00	3.98
11	11.1	2	1	2	1	3.35	4.40
11	11.2	2	1	2	1	3.28	4.76
11	11.3	2	1	2	1	3.17	4.16
11	11.4	2	1	2	1	3.53	4.29
12	12.1	2	1	3	2	3.24	4.27
12	12.2	2	1	3	2	3.20	3.39
12	12.3	2	1	3	2	3.80	5.02
12	12.4	2	1	3	2	3.91	4.84
13	13.1	2	2	1	2	3.51	4.19
13	13.2	2	2	1	2	3.36	4.31
13	13.3	2	2	1	2	3.07	4.00
13	13.4	2	2	1	2	3.62	4.66
14	14.1	2	2	2	3	3.46	4.59
14	14.2	2	2	2	3	3.63	4.38
14	14.3	2	2	2	3	3.43	4.56
14	14.4	2	2	2	3	3.34	3.88
15	15.1	2	2	3	1	4.35	5.35
15	15.2	2	2	3	1	3.84	4.41
15	15.3	2	2	3	1	4.29	5.54
15	15.4	2	2	3	1	3.69	4.89
16	16.1	2	3	1	3	2.93	2.99
16	16.2	2	3	1	3	3.13	2.98
16	16.3	2	3	1	3	3.02	3.23
16	16.4	2	3	1	3	2.98	3.23

Table A.1 Continued:

17	17.1	2	3	2	1	4.11	4.86
17	17.2	2	3	2	1	3.88	5.05
17	17.3	2	3	2	1	3.01	4.36
17	17.4	2	3	2	1	3.41	4.76
18	18.1	2	3	3	2	4.33	5.72
18	18.2	2	3	3	2	3.51	4.41
18	18.3	2	3	3	2	4.05	4.78
18	18.4	2	3	3	2	3.75	4.53

Table A.2: Shear test results for design of experiments study.

Set	Temp	Force	Amp	Speed	Stress (MPa)
1	1	1	1	1	89.8
1	1	1	1	1	58.0
1	1	1	1	1	66.2
1	1	1	1	1	91.6
2	1	1	2	2	87.2
2	1	1	2	2	88.7
2	1	1	2	2	86.6
2	1	1	2	2	31.7
3	1	1	3	3	80.9
3	1	1	3	3	22.1
3	1	1	3	3	64.4
3	1	1	3	3	84.8
4	1	2	1	1	8.2
4	1	2	1	1	40.6
4	1	2	1	1	83.5
4	1	2	1	1	95.5
5	1	2	2	2	73.4
5	1	2	2	2	80.6
5	1	2	2	2	97.0
5	1	2	2	2	7.7
6	1	2	3	3	55.8
6	1	2	3	3	39.8
6	1	2	3	3	47.2
6	1	2	3	3	84.9
7	1	3	1	2	66.7
7	1	3	1	2	70.0
7	1	3	1	2	80.1

Table A.2 Continued:

7	1	3	1	2	82.4
8	1	3	2	3	62.9
8	1	3	2	3	70.4
8	1	3	2	3	89.9
8	1	3	2	3	87.5
9	1	3	3	1	75.5
9	1	3	3	1	70.6
9	1	3	3	1	85.2
9	1	3	3	1	93.0
10	2	1	1	3	6.5
10	2	1	1	3	2.8
10	2	1	1	3	33.5
10	2	1	1	3	4.3
11	2	1	2	1	27.9
11	2	1	2	1	29.3
11	2	1	2	1	96.5
11	2	1	2	1	70.7
12	2	1	3	2	98.8
12	2	1	3	2	80.9
12	2	1	3	2	101.5
12	2	1	3	2	74.2
13	2	2	1	2	78.6
13	2	2	1	2	94.4
13	2	2	1	2	96.4
13	2	2	1	2	84.3
14	2	2	2	3	111.8
14	2	2	2	3	109.8
14	2	2	2	3	98.7
14	2	2	2	3	101.7
15	2	2	3	1	50.3
15	2	2	3	1	102.9
15	2	2	3	1	95.8
15	2	2	3	1	75.7
16	2	3	1	3	86.8
16	2	3	1	3	106.2
16	2	3	1	3	82.4
16	2	3	1	3	96.0
17	2	3	2	1	95.7
17	2	3	2	1	89.2
17	2	3	2	1	85.7

Table A.2 Continued:

17	2	3	2	1	95.9
18	2	3	3	2	83.4
18	2	3	3	2	93.3
18	2	3	3	2	84.1
18	2	3	3	2	87.8

Appendix B: SEAM JOINING CROSS SECTIONS AND DESIGN OF EXPERIMENTS DATA



Figure B.1: Cross section for weld trial 1.



Figure B.2: Cross section for weld trial 2.

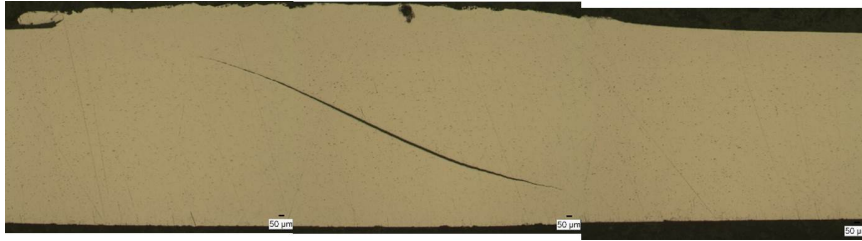


Figure B.3: Cross section for weld trial 3.

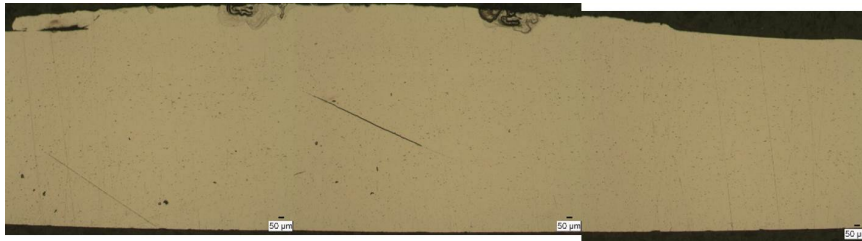


Figure B.4: Cross section for weld trial 4.

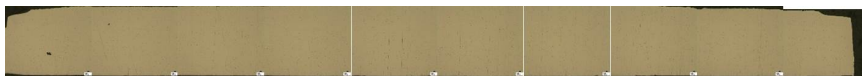


Figure B.5: Cross section for weld trial 5.



Figure B.6: Cross section for weld trial 6.



Figure B.7: Cross section for weld trial 7.



Figure B.8: Cross section for weld trial 8.



Figure B.9: Cross section for weld trial 9.



Figure B.10: Cross section for weld trial 10.



Figure B.11: Cross section for weld trial 11.

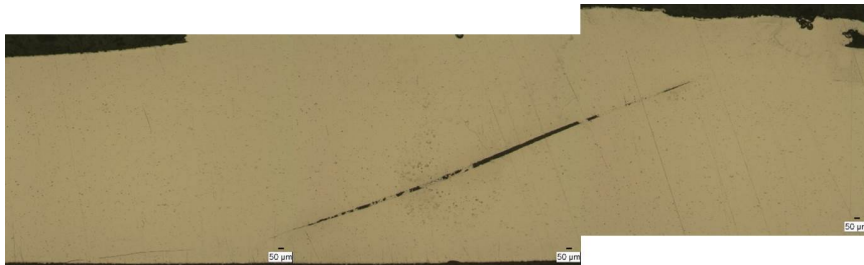


Figure B.12: Cross section for weld trial 12.

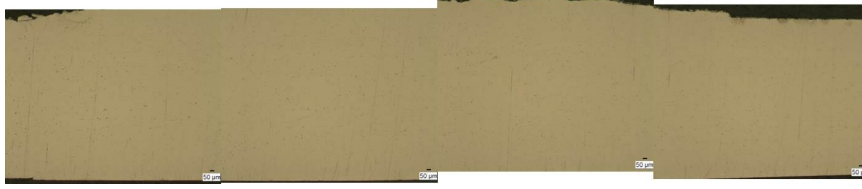


Figure B.13: Cross section for weld trial 13.

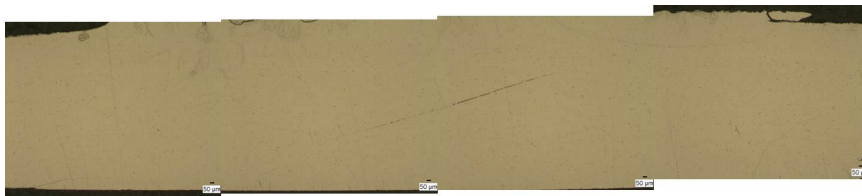


Figure B.14: Cross section for weld trial 14.



Figure B.15: Cross section for weld trial 15.

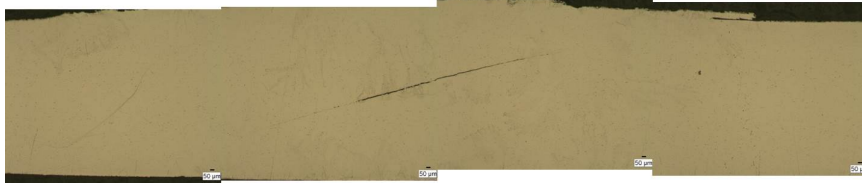


Figure B.16: Cross section for weld trial 16.



Figure B.17: Cross section for weld trial 1.



Figure B.18: Cross section for weld trial 18.

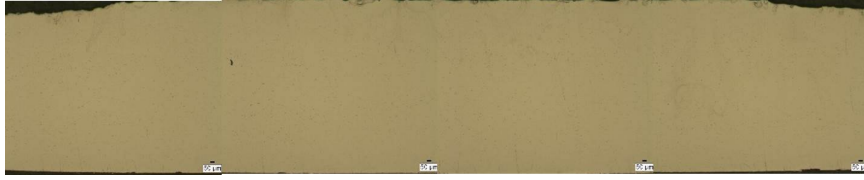


Figure B.19: Cross section for weld trial 19.

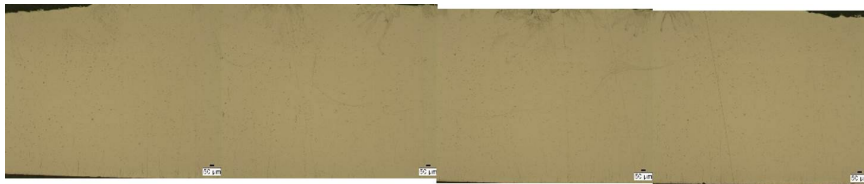


Figure B.20: Cross section for weld trial 20.

Table B.1: UTS test data for design of experiment study of seam welded joints

	UTS (ksi)				
Parameter Set	Sample 1	Sample 2	Sample 3	Average	Stdev
1	21.65	20.31	20.73	20.90	0.69
2	23.06	21.78	22.46	22.43	0.64
3	14.16	14.81	15.19	14.72	0.52
4	16.88	15.30	15.71	15.97	0.82
5	33.53	34.23	34.17	33.98	0.39
6	31.71	31.34	30.23	31.09	0.77
7	34.20	32.68	28.69	31.86	2.85
8	31.95	32.20	32.51	32.22	0.28
9	23.24	21.88	21.42	22.18	0.95
10	22.02	19.46	19.82	20.43	1.38
11	20.06	19.95	22.50	20.84	1.44
12	18.11	15.99	13.65	15.92	2.23
13	24.75	30.65	28.32	27.90	2.97
14	21.99	22.40	22.80	22.40	0.41
15	33.13	32.68	33.07	32.96	0.24
16	20.93	21.74	21.50	21.39	0.42
17	32.35	32.49	27.77	30.87	2.68
18	23.63	28.01	29.80	27.15	3.17
19	32.57	33.12	32.91	32.87	0.27
20	31.91	32.23	32.25	32.13	0.19

Table B.2: Elongation test data for design of experiment study of seam welded joints

	Elongation at Break				
Parameter Set	Sample 1	Sample 2	Sample 3	Average	Stdev
1	2.38%	2.86%	2.62%	2.62%	0.24%
2	3.35%	3.33%	3.34%	3.34%	0.01%
3	1.50%	1.64%	1.83%	1.66%	0.16%
4	2.36%	2.23%	2.34%	2.31%	0.07%
5	8.19%	9.55%	8.73%	8.82%	0.68%
6	7.28%	7.05%	6.49%	6.94%	0.41%
7	8.62%	8.14%	5.57%	7.45%	1.64%
8	7.80%	8.03%	8.55%	8.12%	0.39%
9	3.06%	3.04%	2.54%	2.88%	0.29%
10	3.02%	2.86%	2.68%	2.85%	0.17%
11	1.84%	2.10%	2.67%	2.21%	0.42%
12	2.11%	1.75%	1.19%	1.68%	0.46%
13	3.65%	5.24%	4.70%	4.53%	0.81%
14	3.29%	3.13%	3.14%	3.18%	0.09%
15	7.87%	7.48%	7.40%	7.58%	0.25%
16	3.19%	3.21%	3.52%	3.31%	0.19%
17	6.78%	6.64%	4.58%	6.00%	1.23%
18	3.33%	4.31%	5.18%	4.28%	0.93%
19	6.70%	7.27%	7.16%	7.04%	0.30%
20	6.39%	6.20%	6.57%	6.38%	0.18%

Appendix C: ADDITIONAL EBSD IMAGES

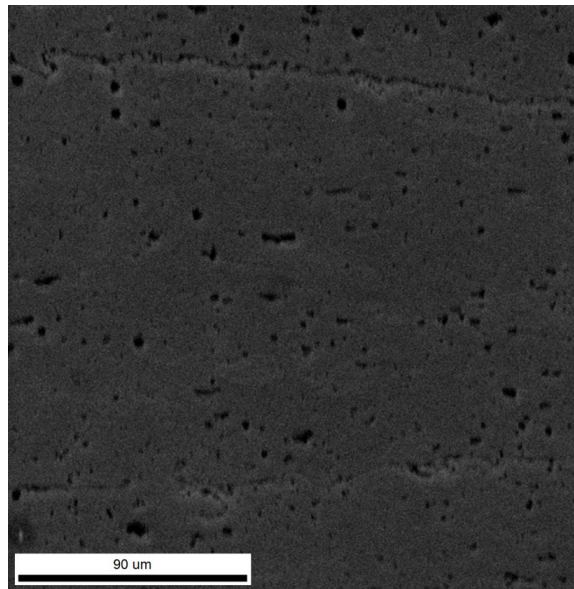


Figure C.1: SEM image of welded Al 6061-T4.

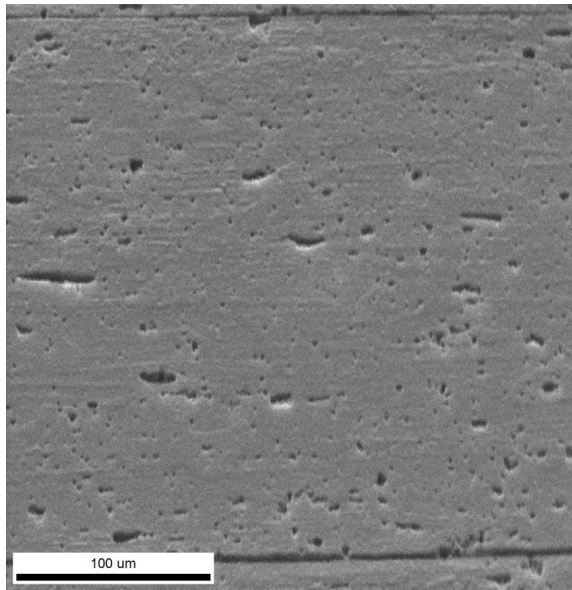


Figure C.2: SEM image of unwelded Al 6061-T4.

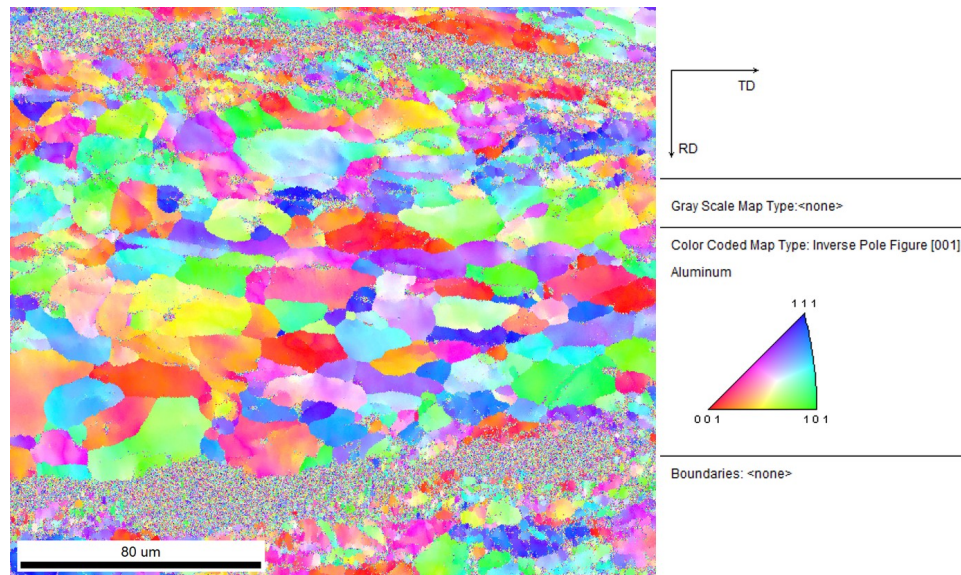


Figure C.3: Unprocessed grain maps colored via inverse pole figures for welded Al 6061-T4.

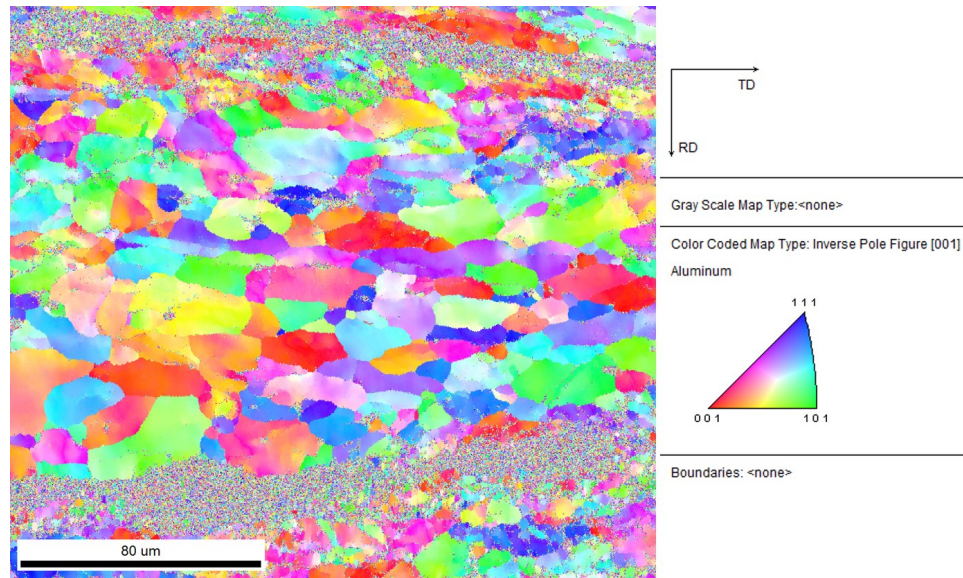


Figure C.4: Unprocessed grain maps colored via inverse pole figures for unwelded Al 6061-T4.

Bibliography

- [1] *Metallic Materials Properties Development and Standardization*. Battelle Memorial Institute, 2011.
- [2] ASM-International. *Heat Treating - Heat Treating of Aluminum Alloys, Vol. 4*. ASM International, 1991.
- [3] ASM-International. *Properties of Wrought Aluminum and Aluminum Alloys - Properties and Selection: Nonferrous Alloys and Special-Purpose Materials, Vol 2*. ASM International, 1992.
- [4] ASM-International. *Welding Fundamentals and Processes - Ultrasonic Additive Manufacturing, Vol. 6A*. ASM International, 2011.
- [5] ASM-International. *Welding Fundamentals and Processes - Ultrasonic Welding, Vol. 6A*. ASM International, 2011.
- [6] F. Balle, G. Wagner, and D. Eifler. Ultrasonic metal welding of aluminium sheets to carbon fibre reinforced thermoplastic composites. *Advanced Engineering Materials*, 11(1-2), 2009.
- [7] T.A. Barnes and I.R. Pashby. Joining techniques for aluminium spaceframes used in automobiles part II - adhesive bonding and mechanical fasteners. *Journal of Materials Processing Technology*, 99, 2000.
- [8] B. Bhushan. *Introduction to Tribology*. Wiley, 2002.
- [9] R. Borrisutthekul, P. Mitsomwang, S. Rattanachan, and Y. Mutoh. Feasibility of using TIG welding in dissimilar metals between steel/aluminum alloy. *Energy Research Journal*, 2, 2010.
- [10] G.E.P. Box and D.W. Behnken. Some new three level designs for the study of quantitative variables. *Technometrics*, 2:455–475, 1960.
- [11] G.E.P. Box and K.B. Wilson. On the experimental attainment of optimum conditions. *Journal of the Royal Statistical Society, Series B*, 13:1–45, 1951.

- [12] L.N. Brewer, D.P. Field, and C.C. Merriman. Mapping and assessing plastic deformation using EBSD. In A.J. Schwartz, M. Kumar, B.L. Adams, and D.P. Fields, editors, *Electron Backscatter Diffraction in Materials Science*. Springer Science and Business Media, New York, 2009.
- [13] R. Budnyas and K. Nisbett. *Shigley's Mechanical Engineering Design, 10th edition*. McGraw-Hill, 2014.
- [14] C.M. Chen and R. Kovacevic. Joining of Al 6061 alloy to AISI 1018 steel by combined effects of fusion and solid state welding. *International Journal of Machine Tools & Manufacture*, 44, 2004.
- [15] Y.C. Chen and K. Nakata. Microstructural characterization and mechanical properties in friction stir welding of aluminum and titanium dissimilar alloys. *Materials and Design*, 30, 2009.
- [16] P.H. Darji and D.P. Vakharla. Development of graphical solution to determine optimum hollowness of hollow cylindrical roller bearing using elastic finite element analysis. In F. Ebrahimi, editor, *Finite Element analysis - Applications in Mechanical Engineering*. InTech, European Union, 2012.
- [17] J. Davis. *Aluminum and aluminum alloys*. ASM International, 1993.
- [18] A. Dean and D. Voss. *Design and Analysis of Experiments*. Springer, New York, 1999.
- [19] R.R. Dehoff and S.S. Babu. Characterization of interfacial microstructures in 3003 aluminum alloy blocks fabricated by ultrasonic additive manufacturing. *Acta Materialia*, 58:4305–4315, March 2010.
- [20] E. DeVries. *Mechanics and Mechanisms of Ultrasonic Metal Welding*. PhD thesis, The Ohio State University, Columbus, OH, 2004.
- [21] D.J. Dingley and V. Randle. Microtexture determination by electron back-scatter diffraction. *Journal of Materials Science*, 27:4545–4566, 1992.
- [22] C.W. Dunnett. A multiple comparisons procedure for comparing several treatments with a control. *Journal of the American Statistical Association*, 50:1096–1121, 1955.
- [23] T. Dursun and C. Soutis. Recent developments in advanced aircraft aluminium alloys. *Materials and Design*, 56, 2014.
- [24] P.G. Forrest. *Fatigue of Metals*. Pergamon Press, 1970.

- [25] R.J. Friel, K.E. Johnson, P.M. Dickens, and R.A. Harris. The effect of interface topography for ultrasonic consolidation of aluminum. *Materials Science and Engineering A*, 527:4474–4483, 2010.
- [26] A. Fuji. Friction welding of Al-Mg-Si alloy to Ni-Cr-Mo low alloy steel. *Science and Technology of Welding and Joining*, 9(1), 2004.
- [27] H.T. Fujii, M.R. Sriraman, and S.S. Babu. Quantitative evaluation of bulk and interface microstructures in Al-3003 alloy builds made by very high power ultrasonic additive manufacturing. *Metallurgical and Materials Transactions A*, 42A:4045–4055, 2011.
- [28] J.M. Gibert, E.M. Austin, and G. Fadel. Effect of height to width ratio on the dynamics of ultrasonic consolidation. *Rapid Prototyping Journal*, 16, 2010.
- [29] R. Goehner and J. Michael. EBSD in the SEM for the identification of unknown crystalline phases. In *DXC 2004 Workshop Principles & Use of Microdiffraction & Microfluorescence*, Albuquerque, NM, 2004.
- [30] J. Goldstein, D. Newbury, D. Joy, C. Lyman, P. Echlin, E. Lifshin, L. Sawyer, and J. Michael. *Scanning Electron Microscopy and X-Ray Microanalysis*. 2003.
- [31] J.E. Gould. Joining aluminum sheet in the automotive industry - a 30 year history. *Welding Journal*, 91, 2012.
- [32] I.E. Gunduz, T. Ando, E. Shattuck, P.Y. Wong, and C.C. Doumanidis. Enhanced diffusion and phase transformations during ultrasonic welding of zinc and aluminum. *Scripta Materialia*, 52, 2005.
- [33] R. Hahnlen and M.J. Dapino. NiTi-Al interface strength in ultrasonic additive manufacturing composites. *Composites B*, 59, 2014.
- [34] G.M. Hamilton and L.E. Goodman. The stress field created by a circular sliding contact. *Journal of Applied Mechanics*, pages 371–376, 1966.
- [35] A. Hehr and M.J. Dapino. Dynamics of ultrasonic additive manufacturing: Part i: System model and FRF estimation. *Journal of Sound and Vibration*, In Review.
- [36] A. Hehr and M.J. Dapino. Dynamics of ultrasonic additive manufacturing: Part ii: Welder shear force and efficiency. *Journal of Sound and Vibration*, In Review.
- [37] A. Hehr, P.J. Wolcott, and M.J. Dapino. Effect of weld power and build compliance on ultrasonic consolidation. *Rapid Prototyping*, In Press.
- [38] G. Heness, R. Wuhrer, and W.Y. Yeung. Interfacial strength development of roll-bonded aluminium/copper metal laminates. *Materials Science & Engineering A*, 483-484, 2008.

- [39] H. Hertz. On the contact of elastic solids. *Journal für die reine und angewandte Mathematik*, 92:156–171, 1881.
- [40] E.T. Hetrick, J.R. Baer, W. Zhu, L.V. Reatherford, A.J. Grima, D.J. School, D.E. Wilkosz, S. Fatima, and S.M. Ward. Ultrasonic metal welding process robustness in aluminum automotive body construction applications. *Welding Journal*, 88, 2009.
- [41] C.D. Hopkins, S.A. Fernandez, and M.J. Dapino. Statistical Characterization of Ultrasonic Additive Manufacturing Ti/Al Composites. *Journal of Engineering Materials and Technology*, 132:041006–1–041006–9, 2010.
- [42] C.D. Hopkins, P.J. Wolcott, M.J. Dapino, A.G. Truog, S.S. Babu, and S.A. Fernandez. Optimizing ultrasonic additive manufactured Al 3003 properties with statistical modeling. *Journal of Engineering Materials and Technology*, 134:011004–1–011004–10, 2012.
- [43] ASM International. Properties and selection: Irons, steels, and high-performance alloys. 1, 2010.
- [44] ASTM International. ASTM E 466-07: Standard practice for conducting force controlled constant amplitude axial fatigue tests of metallic materials, 2007.
- [45] ASTM International. E 8/E 8M-08: Standard test method for tension testing of metallic materials, 2008.
- [46] R. Jahn, R. Cooper, and D. Wilkosz. The effect of anvil geometry and welding energy on microstructures in ultrasonic spot welds of AA6111-T4. *Metallurgical and Materials Transactions A*, 38A, 2007.
- [47] G.D. Janaki Ram, Y. Yang, J. George, C. Robinson, and B. Stucker. Improving linear weld density in ultrasonically consolidated parts. In *Proceedings of the 17th Solid Freeform Fabrication Symposium, Austin, Texas*, 2006.
- [48] R. Jiangwei, L. Yajiang, and F. Tao. Microstructure characteristics in the interface zone of Ti/Al diffusion bonding. *Materials Letters*, 56, 2002.
- [49] K. Johnson. *Interlaminar Subgrain Refinement in Ultrasonic Consolidation*. PhD thesis, Loughborough University, Loughborough, UK, 2008.
- [50] T.H. Kim, J. Yum, S.J. Hu, J.P. Spicer, and J.A. Abell. Process robustness of single lap ultrasonic welding of thin, dissimilar materials. *CIRP Annals - Manufacturing Technology*, 60, 2011.

- [51] C.Y. Kong and R.C. Soar. Fabrication of metal–matrix composites and adaptive composites using ultrasonic consolidation process. *Materials Science & Engineering A*, 412(1-2):12–18, 2005.
- [52] C.Y. Kong, R.C. Soar, and P.M. Dickens. Characterisation of aluminum alloy 6061 for the ultrasonic consolidation process. *Materials Science & Engineering A*, 363(1-2):99–106, 2003.
- [53] C.Y. Kong, R.C. Soar, and P.M. Dickens. Optimum process parameters for ultrasonic consolidation of 3003 aluminum. *J. of Materials Processing Tech.*, 146(2):181–187, 2004.
- [54] C. Kwan and Z. Wang. Microstructure evolution upon annealing of accumulative roll bonding (ARB) 1100 Al sheet materials: evolution of interface microstructures. *Journal of Materials Science*, 43, 2008.
- [55] Dezhi Li and Rupert Soar. Influence of sonotrode texture on the performance of an ultrasonic consolidation machine and the interfacial bond strength. *Journal of Materials Processing Technology*, 209:1627–1634, 2009.
- [56] G. Liu, Z. Lin, and Y. Bao. Improving dimensional accuracy of a u-shaped part through an orthogonal design experiment. *Finite Elements in Analysis and Design*, 39, 2002.
- [57] M.W. Mahoney, C.G. Rhodes, J.G. Flintoff, R.A. Spurling, and W.H. Bingel. Properties of friction-stir-welded 7075 T651 aluminum. *Metallurgical and Materials Transactions A*, 29A, 1998.
- [58] E. Mariani and E. Ghassemieh. Microstructure evolution of 6061 O Al alloy during ultrasonic consolidation: An insight from electron backscatter diffraction. *Acta Materialia*, 58, 2010.
- [59] A. Miriyev, D. Barlam, R. Shneck, A. Stern, and N. Frage. Steel to titanium solid state joining displaying superior mechanical properties. *Journal of Materials Processing Technology*, 214, 2014.
- [60] A. Miriyev, A. Stern, E. Tuval, S. Kalabukhov, Z. Hooper, and N. Frage. Titanium to steel joining by spark plasma sintering (SPS) technology. *Journal of Materials Processing Technology*, 213, 2013.
- [61] J.E. Mueller, J.W. Gillespie, and S.G. Advani. Effects of interaction volume on x-ray line-scans across an ultrasonically consolidated aluminum/copper interface. *Scanning*, 35, 2013.
- [62] S. Nemat-Nasser and Y. Li. Flow stress of FCC polycrystals with application to OFHC Cu. *Acta Materialia*, 46(2), 1998.

- [63] Mark Norfolk and Hilary Johnson. Solid-state additive manufacturing for heat exchangers. *JOM*, 67(3):655–659, 2015.
- [64] J. Obielodan and B. Stucker. A fabrication methodology for dual-material engineering structures using ultrasonic additive manufacturing. *International Journal of Advanced Manufacturing Technology*, 70, 2013.
- [65] J.O. Obielodan, A. Ceylan, L.E. Murr, and B.E. Stucker. Multi-material bonding in ultrasonic consolidation. *Rapid Prototyping Journal*, 16(3):180–188, 2010.
- [66] J.O. Obielodan, G.D. Janaki Ram, B.E. Stucker, and D.G. Taggart. Minimizing defects between adjacent foils in ultrasonically consolidated parts. *Journal of Engineering Materials and Technology*, 132, 2010.
- [67] J.O. Obielodan, B.E. Stucker, E. Martinez, J.L. Martinez, D.H. Hernandez, D.A. Ramirez, and L.E. Murr. Optimization of the shear strengths of ultrasonically consolidated Ti/Al 3003 dual-material structures. *Journal of Materials Processing Technology*, 211, 2011.
- [68] E. Ollerton. Elastic stresses between curved bodies in rolling contact. *Strain*, pages 80–87, 1971.
- [69] C. Robinson, C. Zhang, G.D. Janaki-Ram, E. Siggard, B.E. Stucker, and L. Li. Maximum height to width ratio of free-standing structures built by ultrasonic consolidation. In *Proceedings of the 17th Solid Freeform Fabrication Symposium*, Austin, TX, August 2006.
- [70] H. Scheffe. *The Analysis of Variance*. John Wiley and Sons, New York, 1959.
- [71] D. Schick, S.S. Babu, D.R. Foster, M. Dapino, M. Short, and J.C. Lippold. Transient thermal response in ultrasonic additive manufacturing of aluminum 3003. *Rapid Prototyping Journal*, 17, 2011.
- [72] S. Shimizu, H.T. Fujii, Y.S. Sato, H. Kokawa, M.R. Sriraman, and S.S. Babu. Mechanism of weld formation during very-high-power ultrasonic additive manufacturing of Al alloy 6061. *Acta Materialia*, 74, 2014.
- [73] E. Siggard. Investigative research into the structural embedding of electrical and mechanical systems using ultrasonic consolidation. Master’s thesis, Utah State University, Logan, UT, 2007.
- [74] M.H. Sloboda. *Design and Strength of Brazed Joints*. Johnson Matthey Metals, London, 1961.

- [75] K. Sojiphan, S.S. Babu, X. Yu, and S.C. Vogel. Quantitative evaluation of crystallographic texture in aluminum alloy builds fabricated by very high power ultrasonic additive manufacturing. In *Solid Freeform Fabrication Symposium*, Austin, TX, 2012.
- [76] H. Somekawa, H. Watanabe, T. Mukai, and K. Higashi. Low temperature diffusion bonding in a superplastic AZ31 magnesium alloy. *Scripta Materialia*, 48, 2003.
- [77] V. Songmene, J. Kouam, I. Zaghibani, N. Parson, and A. Maltais. *Global Machinability of Al-Mg-Si Extrusions - New Trends in Fabrication and Applications*. InTech, 2012.
- [78] M.R. Sriraman, S.S. Babu, and M. Short. Bonding characteristics during very high power ultrasonic additive manufacturing copper. *Scripta Materialia*, 62:560–563, January 2010.
- [79] M.R. Sriraman, M. Gonser, H.T. Fujii, S.S. Babu, and M. Bloss. Thermal transients during processing of materials by very high power ultrasonic additive manufacturing. *Journal of Materials Processing Technology*, 211, 2011.
- [80] E. Taban, J.E. Gould, and J.C. Lippold. Dissimilar friction welding of 6061-T6 aluminum and AISI 1018 steel: Properties and microstructural characterization. *Materials and Design*, 31, 2010.
- [81] G. Taguchi. Quality engineering (taguchi methods) for the development of electronic circuit technology. *IEEE Transactions on Reliability*, 44:225–229, 1995.
- [82] A.G. Truog. Bond Improvement of Al/Cu Joints Created by Very High Power Ultrasonic Additive Manufacturing. Master’s thesis, The Ohio State University, Columbus, OH, 2012.
- [83] J. Tsujino, T. Ueoka, T. Kashino, and F. Sugahara. Transverse and torsional complex vibration systems for ultrasonic seam welding of metal plates. *Ultrasonics*, 38:67–71, 2000.
- [84] J.W. Tukey. *The problem of multiple comparisons*. Department of Statistics, Princeton University, Princeton, NJ, 1953.
- [85] T. Watanabe, H. Takayama, and A. Yanagisawa. Joining of aluminum alloy to steel by friction stir welding. *Journal of Materials Processing Technology*, 178, 2006.
- [86] H. Van Wijk, G.A. Luiten, and P.G. Van Engen. Process optimization of ultrasonic welding. *Polymer Engineering and Science*, 36(9), 1996.

- [87] P.J. Wolcott, A. Hehr, and M.J. Dapino. Optimized welding parameters for Al 6061 ultrasonic additive manufactured structures. *Journal of Materials Research*, 17(29):2055–2065, 2014.
- [88] Y. Yang, G.D. Janaki Ram, and B.E. Stucker. An Experimental Determination of Optimum Processing Parameters for Al/ SiC Metal Matrix Composites Made Using Ultrasonic Consolidation. *Journal of Engineering Materials and Technology*, 129:538, 2007.
- [89] C. Zhang, A. Deceuster, and L. Li. A Method for Bond Strength Evaluation for Laminated Structures with Application to Ultrasonic Consolidation. *J. of Materials Engineering and Performance*, 18(8):1124–1132, 2009.
- [90] C.Y. Zhang, D.L. Chen, and A.A. Luo. Joining 5754 automotive aluminum alloy 2-mm-thick sheets using ultrasonic spot welding. *Welding Journal*, 93, 2014.
- [91] H. Zhao, D.R. White, and T. DebRoy. Current issues and problems in laser welding of automotive aluminium alloys. *International Materials Reviews*, 44(6), 1999.
- [92] B. Zhou, M.D. Thouless, and S.M. Ward. Predicting the failure of ultrasonic spot welds by pull-out from sheet metal. *International Journal of Solids and Structures*, 43, 2006.